NTNU

Norwegian University of
Science and Technology

Realization of a DDS/PLL Signal Source for W-band Radar Applications

Automotive FMCW Radar

Martin Rygh

Master of Science in Electronics

Submission date: June 2011

Supervisor: Jens F. Hjelmstad, IET

Co-supervisor: Stein Arne Askeland, IET

Norwegian University of Science and Technology
Department of Electronics and Telecommunications

Problem Description

Millimeter - wave technology is applicable for wide band communication and for sensor applications. The NTNU MMW project are thus focusing on the development of a wide band mm-wave front-end, utilizing phase steered antennas for reception and transmission, for use in automotive applications. An industry group (NORBIT, TRIAD) is currently developing a prototype system based on 3 commercial technologies, and this thesis will within the framework of the project participate in the following activities:

- Testing and characterization of the developed prototypes signal source.
- Realizing the provided signal source, as an appropriate FMCW waveform generator for automotive applications and further radar testing.
- Implementation of needed software, hardware and measurement tools for waveform analysis and circuit programming.
- Providing recommendations for further work related to the signal source, based on the experiences obtained during the thesis work.

Assignment given: 15. January 2011
Supervisor: Jens F. Hjelmstad, IET

Abstract

This thesis presents a realization process, of how a programmable DDS/PLL signal source were made suitable as an linear FMCW waveform generator for automotive W-band radar applications. The dissertation describes the specific background theory that were used to complete the implementation and substantiate the discoveries during the development process. Hence is an outline of FMCW basic properties, automotive radar implementations, applied waveforms and the fundamental radar ambiguity function presented and threated. Moreover are vital background theory for basic FMCW design problems presented, including degradation of range resolution due to loss of effective bandwidth, nonlinearities in chirp modulation and limitations of the receiver resolution. Additionally is the inevitable problem of FMCW transceiver noise leakage briefly described, along with the general concept of choosing the right beat frequency for maximal FMCW sensitivity and maximal range-Doppler resolution. The specific circuit design is then presented, together with the full radar design which the signal source is intended for.

The realization process starts with an initial test of circuit performance, seen in relation to the radar documentation and set the fundament for the further investigation and development. Hence does this part include measurements and discussion of output power achievements, spectral purity, spectral waveform appearance and phase noise. The thesis does then set further focus to more specific methods of measuring and evaluating the circuits LFM waveform, in aspect of a combined frequency and time characterization, chirp linearity achievements and waveform beat frequency evaluation. The dissertation does further describe how the first hand waveform generation were erroneous and how this problem was investigated and solved through radar documentation/source code corrections. As a last part of the realization process is then the final and successive implementation of waveforms described, along with the main results presented as waveform spectrograms and selected beat frequency spectrum plots. The working process and the main results are then summarized in a final summary discussion.

The major results and conclusions of the thesis are that the tested NORBIT DDS/PLL signal source could be realized as an linear FMCW waveform generator with overall good linear properties. Two basic LFM waveforms, the up-chirp and triangular waveform were implemented and tested. However were there discovered nonlinearities within the up-chirp waveform, due to the transient response of the total circuit. Hence most likely caused by the limited PLL frequency lock time. This was proven through a specific beat frequency analysis of the most affected waveform, with fitted W-band LFM characteristics. Nevertheless were the isolated chirp generation within the waveforms considered more than sufficient, since both windowing technics and selective sampling could be used in the future radar implementation. Three specific waveform realizations were specially recommended for the initial further use. Further were also a specific region

of desirable waveform chirp-rates recommended, that enables a good trade off between close target radar sensitivity and digital acquisition system complexity. Additionally did the thesis work conclude with that the NORBIT signal source design, enabled a flexible and easy control of the waveform generation through the microcontroller interface. Further more had also the thesis work resulted in the implementation of two good methods for waveform measurements and analysis. By the use of the spectrogram- and the beat frequency-method, could accurate waveform properties be extracted. Hence were also these methods recommended for further waveform developments in the experimental radar project.

Furthermore was it recommended that future effort should be put in to the development of more applicable waveforms, to achieve full multiple range-Doppler target extraction. Hence since the overall signal source proved to have the nessesary waveform agility. It was in addition proposed that the future full radar implementation should utilize the accessabillity of the microcontroller to achieve synchronization of signal source modulation and future sampling solution. Thus to enable beneficial beat frequency sampling for the quadrature radar receiver. Since the mapping of the phase noise influence and the chirp linearity were seen as non-optimal, was it additionally suggested that future studies should yield better methods for such characterization. It was finally put forward that an intermediate simple test radar could be implemented to enable sampling system testing and FMCW signal processing of real measurements, if the millimeter part of the radar is further postponed.

Acknowledgements

I would first like to thank my supervisor Jens F. Hjelmstad at the Norwegian University of Science and Technology, for letting me be apart of the Millimeter Wave NTNU research project during the work on the thesis and providing me the assignment. I would also much like to thank Stein Arne Askeland for his guidance and support. I will further like to thank NORBIT for giving me the opportunity to work with the radar signal source and providing me with additional circuit related documentation and equipment. In addition would I specially like to thank Laurens de Brujiin at NORBIT for his eminent help with hardware related issues and helpful discussions.

Contents

Nomenclature

ADC	.....	**Analog to Digital Converter** *Device that converts an analog signal to an digital signal*
AF	.....	**Radar Ambiguity Function**
Bistatic	.....	**Bistatic Radar** *Radar system where the transmit and receive antennas are located at different locations as viewed from the target*
CL	.....	**Mixer Conversion Loss**
DAC	.....	**Digital to Analog Converter** *Device that converts a digital signal to an analog signal*
DAS	.....	**Digital Acquisition System** *System that samples, stores and pre-processes an analog Rx radar signal*
DDS	.....	**Direct Digital Synthesis/Synthesizer**
EMC	.....	**Electromagnetic Capability** *The study of unintentional unwanted EM effects and how to avoid such effects in electronic equipment*
FMCW	.....	**Frequency Modulated Continuous Wave**
FDW	.....	**Falling Delta Word**
FSRR	.....	**Falling Sweep Ramp Rate**
Ku-band	.....	**IEEE Frequency Band Category** *Describing the band from 12-18 GHz*
LFM	.....	**Linear Frequency Modulation**

LO ..... **Local Oscillator**
Reference to the local oscillator it self or where the system reference frequency is generated

LRR ..... **Long Range Radar**

MF ..... **Matched Filter**

MMW ..... **Millimeter Waves**
Defined by IEEE as wavelengths in the range of 3mm to 1mm (110 - 300 GHz), or as Millimetric Waves in range of 11mm to 1mm (27 - 300 GHz)

Monostatic ..... **Monostatic Radar**
Radar system where the transmitter and receiver are co-located as viewed from the target, typical when the same antenna is used for both Tx and Rx

PLL ..... **Phase Locked Loop**

PN ..... **Phase Noise**

PSU ..... **Power Supply Unit**

Quasi-Bistatic ..... **Quasi-Bistatic Radar**
Radar system where the transmit and receive antennas are slightly separated but appears to be at the same location as viewed from the target

RADAR ..... **Radio Detection And Ranging**

RAF ..... **Radar Ambiguity Function**

RBW ..... **Resolution bandwidth**

RCS ..... **Radar Cross Section**
Electromagnetic backscatter form an object, given in m^2

RDW ..... **Raising Delta Word**

RMSE ..... **Root Mean Square Error**

RSRR ..... **Raising Sweep Ramp Rate**

RSS ..... **Square Root of Sum of Squares**

Rx	.....	**Receiver/ Receiving**
SNR	.....	**Signal-to-Noise Ratio**
Tx	.....	**Transmitter/ Transmitting**
UWB	.....	**Ultra Wide Band**
W-band	.....	**IEEE Frequency Band Category** *Describing the band from 75-110 GHz*
X-band	.....	**IEEE Frequency Band Category** *Describing the band from 8-12 GHz*
μ**C**	.....	**Microcontroller**

1. Introduction

Over the last two decades have the demands for car safety and reduction of fatal road accidents, been an enhanced focus for governments world wide. This has lead to an increased focus on driver assistance and on-board safety systems, for the global car manufacturers as the right technology have become more available. One component often used in such systems, is the *automotive radar*, which provides an all-weather sensor capability to the overall driver assistance or car safety system. As a part of a typical multi-sensor solution, can the radar in this matter provide various information to the cars sensor data fusion processor, dependent of the desired application. Hence can the radar yield sensor data that could be used for car/human/object detection and tracking. More detailed applicative use of the automotive radar is hence presented in section 2.1 to illustrate the typical sensors agility and corresponding background information of such radar utility.

As a result of the above mentioned situation have governmental and international authorities like EU, funded research programs that focuses on car safety technology. Two offspring's from this is effort have been the *SARFA*- and *ADOSE* projects, which the MMW NTNU project group have been a involved in, along with its two main industry partners, NORBIT and TRIAD. While the SARFA project were focused on RF MEMS steerable antennas for automotive radar and future wireless applications, are the ADOSE project currently running, doing research and applying specific automotive sensor solutions. As a part of this project have thus an attribute to the automotive radar solution been purposed to detect low radar cross section targets as humans, within the high clutter environment seen by the radar. The use of a harmonic radar (HR), with corresponding body-worn active/passive reflector tags, have in that matter been purposed as a solution for avoiding car-human collisions within the noisy environment. Within this effort and the NTNU's desire for an experimental MMW sensor, have the collaboration of NTNU, TRIAD and NORBIT, resulted in the development of a W-band FMCW radar. The radar is hence designed to function as both a automotive long range radar (up to 150 m) and as a harmonic radar, within the allocated band at 77GHz given by the European Telecommunication Standard Institute (ETSI). NTNU's role in this project is to work with the system level integration and the application of the radar. The long term goal is further to include the radar in an multi sensor platform to achieve a complete sensing solution, for automotive applications. Such a technology platform with several sensors will insure redundancy, higher detectabilliy, extended features of car safety and possible military applications. A combination of sensors have been purposed to include a 77GHz steerable wide angle radar, a low frequency sector radar, a wide angle high resolution imaging sensor, infrared line scanners, SICK laser scanner, GPS-trackers. All integrated with a common car-based CAN-bus architecture.

Nevertheless are the millimeter part of the experimental W-band radar, currently under test and evaluation at the supplying industry partner. Thus were this thesis assigned to investigate the finished programmable signal source of the radar, that had only been initially tested for design-specific RF and waveform achievements. Hence had this essential part of the radar, to be further optimized for full radar implementation and automotive FMCW sensing capability.

1.1. Assignment Approach

The specific purpose of this thesis was to realize and evaluate a combined DDS/PLL signal source, designed for W-band automotive radar applications. Hence by the use of the following hypothesis, were the thesis work committed:

> *To what extent can the NORBIT DDS/PLL signal source be realized as a fundamental FMCW waveform generator for automotive radar applications.*

It was initially decided to demarcate the thesis to investigate the signal sources ability to generate waveforms suited for automotive long range radar and moreover spesificlly study its ability to generate *basic linear FMCW waveforms*. Thus in order to yield a fundament for further waveform developments and signal source applications.

To investigate the hypothesis and hence realize the circuit for further use, were a plan worked out, based on lesson was learned from a previous radar project. The previous project had involved testing of a partially unknown circuit design and had in that matter revealed the great importance of fundamental circuit understanding, together with thorough fundamental testing of basic circuit performance, before any real implementation should be conducted. At last but not least had the project also implied the necessity of radar documentation confirmation.

The thesis was then to be conducted in the following steps according to the plan:

1. Establish general understanding of the FMCW radar fundamentals, its possible problematic implementations and main sources of errors.
2. Further studies of the desirable basic FMCW waveform implementations.
3. Fundamental studies of the specific signal source components and design, within the frame of the total radar design.
4. Initial measurements and evaluation of fundamental circuits spectral, power and noise properties, compared to the radar documentation.
5. Developing a method for combined frequency/time measurements, for analysis of the typical FMCW waveform properties and chirp linearity. Hence to enable easier confirmation of delivered circuit performance and waveforms, but also to confirm consistency between delivered circuit source code and real waveform output, for further waveform development and possible de-bugging.

6. Developing a laboratory setup for measurements of the resulting beat frequency, for additional waveform confirmation of the preprogrammed and possible new waveform implementations.
7. Implementation of software and interface to enable reprogramming and realization of desirable waveforms.
8. Final realization and analysis of desired waveforms recommended for further use.

The thesis had then, within the described framework, to evaluate the finds and achievements up against the work hypothesis and yield recommendations for further work.

It is clear that the thesis had to be conducted in small steps in order to reveal what could be done in the next and thus reuse possible good methods derived in the proceeding development. Hence does the main chapters 4, 5 and 6 describe how the way towards the final goal were conducted, with the reuse of several points of the plan and the ongoing considerations that had to be made successively though out the thesis. Based on how the real realization was performed are the three main chapters organized similarly to show the whole long process of circuit realization.

1.2. Outline of the Thesis

- **2 Specific Background** - Presents the fundamental FMCW radar scheme and the specific background theory that were used to complete the thesis.
- **3 Circuit Design** - Description of the signal source circuit and the outline of the full radar design.
- **4 Initial Circuit Performance** - Describes how the initial measurement were conducted, presents the obtained results and discusses the initial finds in relation to full radar implementation and next step of the thesis developments.
- **5 Waveform Evaluation Methods and Waveform Measurements** - Describes the fundamental methods that were used to measure the waveform and its corresponding beat frequency. In addition does this chapter also describe the methods that were used to process the obtained measument data and how the initial waveform were analyzed. Moreover does this chapter additionally present the analysis of the initial waveform and discusses how the modulation were found to be erroneous.
- **6 Solving Erroneous Waveform Generation and Development of New Waveforms** - This chapter of the thesis describes how a solution to the erroneous waveform generation were found. It also describes how the realization of new waveforms were decided upon and explains how the new waveforms were programmed to circuit. Further does this chapter present measurement results and analysis of the new waveforms, along with the discussion to this part of the thesis.
- **7 Summary Discussion** - This chapter summarize the whole working process and discusses the most important finds of this thesis.

- **Appendix A: Theoretical fundamentals** - Presentation of fundamental radar and microwave theory that lay beneath the specific theory presented in chapter 2 radar. Additionally are some derivations that are presented in the specific part shown in this chapter.
- **Appendix B: Waveform Evaluation Methodesand Waveform Measurements** - Presentation of used MATLAB code, simulation results and additional measurement results that are used and discussed in chapter 5.
- **Appendix C: Solving Erroneous Waveform Generation and Development of New Waveforms** - Presentation of the performed microcontroller program modifications and the additional measurement results, obtained in chapter 6.

2. Specific Background

To day many types of radars are in use for different types of applications and purposes. In appendix A.1 some of these are introduced. But why should it be perfereable to use the FMCW radar for some applications, compared to others?

Generally the FMCW radar benefits the advantages of the continuous wave radars. Which is first of all the ability to employ high procentage duty cycles, that will yield high average transmitted power, but low peak power. Compared to pulsed systems, must such insted utilize high peak power to obtain the same detection performance, due to their low average power. Consecuently can FMCW radars be utilized as low power radar systems that can implement inexpensive solid-state transmitters and reduce the overall costs. Additionally will this property combined with a high time-bandwidth product, yield a LPI capability compared to pulsed radars with the same detection performance.

Further more will FMCW radars in contrast to pure CW radars, have the ability to sense both target range and Doppler. This capability is realized by the use of frequency modulation, to obtain a imparted bandwidth for good range resolution. Hence by using a 'long' time-varying FM modulation in an homodyne or heterodyne configuration, can a large bandwidth be achieved and by matched filtering yield good signal compression on reception. By correlating the transmitted waveform with an equivalent copy of the transmitted waveform, a baseband/IF-signal known as the *beat frequency*, reveals information of both range and Doppler of the target. Normally would FMCW scheme enable very good range resolution, good target discrimination and good target-to-clutter ratio. Moreover is the FMCW waveforms highly deterministic, which in turns can be advantageous because it allows predictions, to what form the real Rx signal should be like. Thereby will interference be uncorrelated to the expected return and hence be suppressed by the radar receiver.

Compared with pulsed systems that receive target range information from pulse timing, does FMCW radars receives its range information in frequency domain. The advantage here is that it enables use of digital FFT processing of the baseband beat signal. By applying a simple low pass filter, so it matches the desired spectral range, the FFT processing length can be severely limited. Thereby yield fast processing and low processing complexity, compared with pulsed systems [13], [36] and [26].

Although several modulation schemes can be utilized to impart bandwidth in FMCW radars, the linear frequency modulation (LFM) is often perfered for its simplicity upon information extraction and transceiver designs. Figure 2.1 illustrates how the basic linear FMCW can be implemented as an monostatic homodyne transceiver.

Besides revealing a basic design approach, the figure also illustrates the concept of

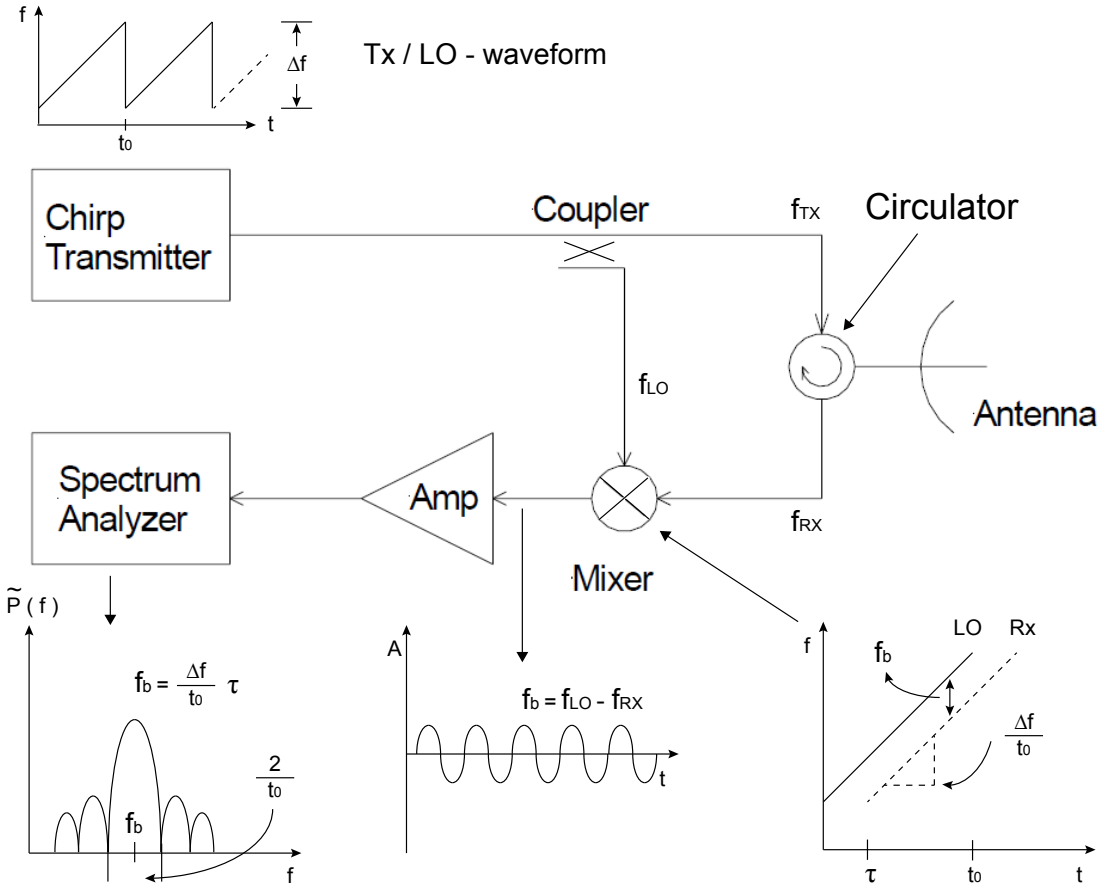

Figure 2.1.: Basic concept of a monostatic FMCW radar system

generating an beat frequency f_b that is proportional to the round-trip-time τ. Thus can the range to target, further be estimated through reversing the beat frequency relation. It has been stated that;

> *It is a feature of FMCW radars that almost any range resolution can be easily obtained by varying the frequency sweep [13, p.70]*

, which is certainly not true for pulsed radars. Nevertheless does such feature acquire a high agility signal source.
Note however also from figure 2.1 that there will be a duality to FMCW waveforms, where the spectral resolution will be inversely proportional to the *sweep time*. Likewise will the range resolution be inversely proportional with the *swept bandwidth*. This would be further explained in the waveform analysis, section 2.3.

To analyze the FMCW radar for detectability, the general CW radar equation [16, p. 121] can be used, which is an extension of the basic radar equation A.25.

$$SNR = \frac{P_{CW}\, T_{Dwell}\, G^2\, \lambda^2\, \sigma}{(4\pi)^3\, R^4\, kT_0\, F_n\, L_{sys}\, L_{win}} \tag{2.1}$$

A CW radar uses a FFT-filter bank, to obtain Doppler frequencies. The FMCW radar is used in a similar way, but utilizes both Doppler and range in the frequency spectrum.

The CW/FMCW radar equation differs from the basic radar equation with the *dwell time* T_{Dwell}, which is the observed time in each narrow band filter or FFT bin. The dwell time is defined as the inverse of the frequency resolution ΔF, ($T_{Dwell} = 1/\Delta F$). Hench will ΔF give the receivers effective noise bandwidth per FFT bin. Further can the dwell time then be defined as $T_{Dwell} = N_{FFT}/2f_{max}$, where N_{FFT} is the FFT filter size. f_{max} is the maximum resolvable frequency by the FFT and 2 is due two obtain the double side spectrum of both positive and negative Doppler shifts. If a *spectrum analyzer* is used to analyze the frequency spectrum, will the dwell time be the inverse of the *resolution bandwidth*, which is likewise related to the FFT implementation. It is worth noticing that windowing technice of a general analyzer will not be optimalized for the utilized waveform and received signal can suffer from large side lobes. In other implementations of a FMCW radar windowing loss needs to be taken into account. The windowing loss L_{win} will then be the loss in SNR to the ideal matched filter when other filter or windowing technices is used. Windowing-techniques are used in FMCW radars mainly to lower the natural sidelobes of the beat frequency. Hence so large RCS targets not will mask small targets by their additional sidelobes. Such amplitude modifications of the signal would however yiled some signal reduction and spectral widening, dependent of the used window.
In equation 2.1 the diverse gain of two antenna CW approach have been switched with a single squared gain for a monostatic case. In addition to the other factors the P_{CW} is the average power received over the dwell time and L_{sys} vil compensate for all system losses, transmission lines, waveguides, conversion loss of mixers etc.

There are a lot different derived radar equations that fit specific FMCW schemes. Commonly are they rearranged to study the maximum range in relation to the minimum detectable SNR, however not used in this thesis. Another radar equation that has a more applied approach to LFM waveform, is the version given by Jankiraman [13, p.6] (figure), where the equation is related to the waveform's modulation frequency f_m and not seen in relation to the FFT filter bin. This equation is also threated as a bistatic case, were it approximates the receivers bandwidth, matched to the waveforms bandwidth and combines the system loss in one factor.

$$SNR_{R_0} = \frac{P_{CW}\, G_{Tx}\, G_{Rx}\, \lambda^2\, \sigma}{(4\pi)^3\, R^4\, kT_0\, F_R\, L_{sys}\, f_m} \tag{2.2}$$

Although there are a lot of advantages that speaks for the use of FMCW radars, is this implementation not without problems. The most severe problem that needs to be threated with respect, is problems that come from the simultaneous receive and transmit property of CW type radars. This yield that a relatively large portions of transmitted power would leak into the receiver through the circulator or between antennas in the bistatic approach. Hence may this cause damage to the receiver circuit or saturate active components. Sufficient isolation needs therefore to be insured, by the circulator/coupler or the use of separate Tx and Rx antennas, with low connected side-lobes to one another. The easiest way to insure sufficient isolation is the use of a bistatic or quasi-bistatic design,

alone or in combination with a *reflected power canceler* [42, sec. 6.1 & 6.2]. In addition do the FMCW waveforms suffer from a range-Doppler coupling, describe further in section 2.3. This yield that a non-static target will bias the beat frequency output by the amount of Doppler shift. Hence is range measurements of Doppler targets always erroneous in FMCW systems and the ambiguity needs to be solved for correct range and track information. Further will the typical Sinc(X)-output of the beat frequency, seen in figure 2.1, suffer from high sidelobe levels, making the system highly sensitive to close clutter. To counter this sensitivity are often amplitude weighting in form of digital windowing technices is used to reduced side-lobe levels to the trade off of range resolution. In addition are there several more conventional clutter cancellation technincs that can be used for this purpose like narrowbeam receive antennas and MTI or MTD processing of FMCW signals [42, sec.3]. Although the excessive use FFT processing in FMCW radars is normally beneficial, can it also impose a threat to the computation time or DAS circuit costs, when there are high demands to both range resolution and maximum range. In section 2.4 and 2.5 will it also be shown how the FMCW radar performance also rely on the fundamental waveform parameters, as chirp bandwidth and sweep time, but additionally how the waveforms are processed and how chirp nonlinearity effects it. Hence imposing several trade-off-consiterations, to the design of FMCW systems.

Summarized will the main limiting factors to FMCW sensitivity be the general receivers thermal noise, its Tx power leakage through circulator/ coupler or divers antennas, the degree of LO-to-IF mixer leakage and the amount of near-field clutter. Additionally should it be noted that FMCW systems heavily rely on the degree of phase noise (FM noise) added to the frequency modulated signal by the signal generating oscillator and additionally how well the PN between Rx and LO is correlated at the mixer input [42]. With a high correlation between the FM noise in LO and RX signal at mixer, would the PN spectral desnsity at the beat frequency region, be substantially reduced. However does this cancellation of FM noise relay on the degree of match between the signal path lengths of LO and RX, and the specific frequency offset from carrier. Since the RX path-length will be dependent of range to target, would these two components normally not be sufficiently correlated to yield cancellation. However have Stove [42] shown that the unavoidable power leakage could be beneficial to reduce the PN influence by aligning the signal path lengths of the LO and the Tx leak signal. Hence would a high degree of PN correlation be achieved at the Rx mixer, thereby limiting the loss of sensitivity around zero frequency after down-conversion. This performance will of course be degraded if strong near clutter or near targets dominant power to the leakage. Nevertheless would a FM noise cancellation, yield that AM noise plays a more significant role in the overall system noise performance. Hence would the FMCW system sensitivity, also be limited by the degree of cancellation of both AM and FM noise in the system. Further theory of this specific subject will be presented in section 2.6.

2.1. Automotive FMCW Radar

As stated in the last section, are there a lot of advantages that speaks for the use of FMCW radars, but why is it perfreable also in Automotive applications?

In the last 20 years there has been an increased interested for using FMCW radars as driver assistance sensors. The background for the interest have been the FMCW's relatively simple design, with a typical single RF source as transmitter and reference oscillator, thereby enabling the use of soil-state-amplifiers. Hence can production costs be cut drastically compared with similar pulsed systems. Because the FMCW waveforms are continuous, can the radar yield high average output power, which in comparison with pulsed radars of the same sensitivity, could be quite difficult to achieve. Similarly will the nature of the waveforms be beneficial in achieving large bandwidths, thereby permitting very good range resolution and Doppler processing. These properties will hence be a premise for use in high density target environments like a road. Likewise will the the large bandwidth product also contributes to the reduction of interference from other radars at the same frequency band, making it applicable for *all-car* implementation. Additionally can the FMCW radar also yield good short range performance, making it usable for several automotive sensor applications, both at short and long range. In further relation to pulsed systems, is another very important advantage the low measurement time and low computational complexity. Intuitively is this highly preferable in the complex road environment and if the sensor is to be used for car safety applications, thereby insuring a faster 'threat' assessment.
In addition does the high frequency allocation for such radars at 24 and 77 GHz, also allow system and antenna designs to be very small and integrated. Thus making an easier fit into the vehicle body, as one or several sensors. The high allocated frequencies will though yield high atmospheric attenuation. Nevertheless does the confined observation range of 100 - 150 m for vehicle application, highly limit the influence from such attenuation. Compared with optical sensors, will MMW radars have greater penetration through the normal atmosphere, fog, smoke, and dust. Compared with lower frequency radars, will MMW radars on the other hand experience relatively high free-space loss and lower transparency through adverse weather and obstacles [4], [36] , [42], [32]. Due to the use of MMW in automotive radars along with typical high desity target situations, is it common to use windowing techninques like described in the latter section. Typical windows used for automotive radar is the *Hamming*-, *Taylor*- and *Chebyshev*-window. More considerations to the use of window-techniques will be presented in section 2.4.

Today several FMCW systems at both 24 and 77 GHz are implemented as *driver assistance* sensors like *adaptive cruise control* (ACC) and *parking assistance* (PA). The vehicle systems must hence obtain the targets range, azimuth angle and the radial velocity simultaneously, with high resolution and accuracy in high density target situations.
Recently some few car manufactures also have started to implement FMCW sensors in *car safety* applications like *collision avoidance* (CA) and *precrash detection* (PC). However must a car safety sensor-system compared to a driver assistance system, yield significantly higher requirements for target detection reliability , measurement accuracy, measurement time, signal processing and threat assessment, to insure short reaction time

of the safety system. Thus must the radar yield very high performance to give reliable target information to the fusion of all vehicle sensor data. These high demands must also be incorpored together with additional integrity systems, if *autonomous driving* (AD), like the *MIG* autonomous vehicle [1], should be implemented as common car application in the future [33].

Figure 2.2 shows a typical automotive sensor scheme for LRR FMCW radar. Normally a wide Tx antenna beam is used to illuminate the desired wide region in front of the car. Typically a phased array antenna is used at Rx to synthesize a scanning pencil beam in the azimuth plane. The adversity of the Rx array can be used to incorporate angle measurement schemes like *monopulse* together width the general range and Doppler sensing, thereby enabling the best possible situation awareness in the region of interest.

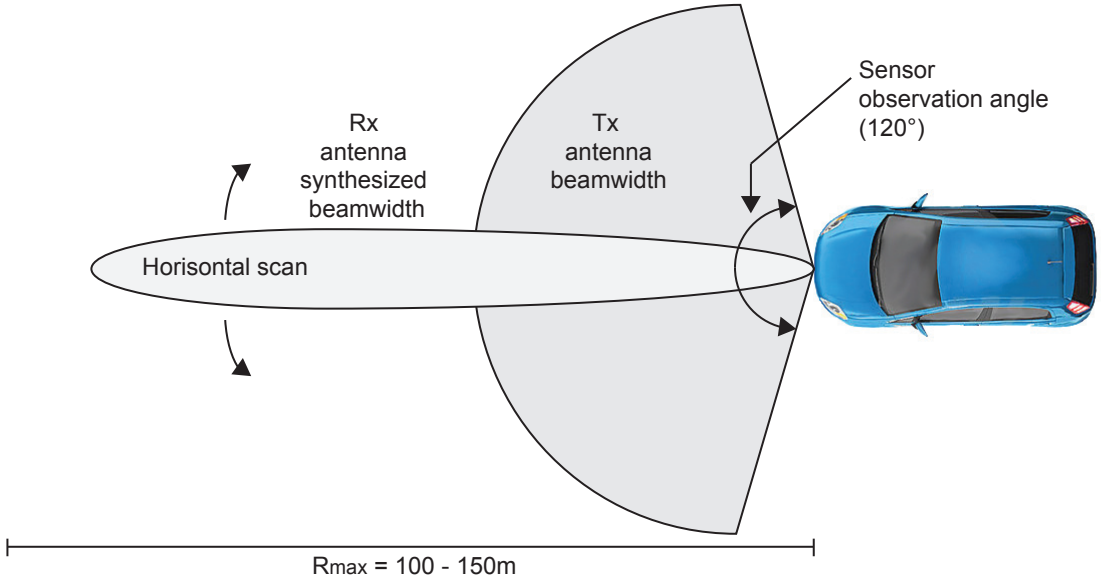

Figure 2.2.: Conceptual FMCW automotive sensor for long range detection and tracking

2.2. Applied Waveforms

In order to test a experimental radar, one approach is to make use of the simplest waveforms that could be generated by the system. Hence to use them as references to other more advanced waveforms as the radar development proceeds. However can this practical approach only be used if one utilizes a high agility system, that can change waveforms easily without big recalibration or hardware tuning. In this thesis is such a agile system implemented through utilization of a DDS as a fundamental part of signal source. Hence can different waveforms theoretically be implemented and thereby starting of with the easiest, most fundamental for comparison if other more advanced schemes are preferable later in the development. Although such an approach is applicable, must there still performed a theoretical analysis of fundamental waveform properties to see how the desired waveforms applies to the system. Hence will some general FMCW waveforms

be presented in this section and analytically examined further in the next, by the use of the radar ambiguity function.

The simplest waveform implementation for FMCW radars is the continuous LFM waveforms. In FMCW-LFM does the radar sweep the frequency linearly from a start frequency f_0 up to a maximum frequency $f_0 + \Delta f$. Hence defining the FM *bandwidth* of the sweep, Δf. In some cases can the sweep intentionally be made nonlinear to correct waveform errors or to minimize sidelobes (*NLFM-waveforms*). However does section 2.5.2 show that, nonlinearities to the waveform, normally introduce unwanted effects in the signal processing. Hence if a linear sweep is originally intended and the processing is similarly suited.
Compared to a single LFM-pulsed sweep, the FMCW-waveform sweeps the bandwidth repeatedly within the modulation time which is given by the modulation frequency f_m. Four typical linear FMCW waveforms are shown in figure 2.3.

In figure 2.3 is the *up-chirp* waveform made of one positive frequency sweep, hence will the modulation time $(1/f_m)$ be the same as the *chirp time* (t_0). The ratio of the bandwidth of the sweep and chirp time will give the rate of frequency change (α). This rate is the proponallity constant that will set the properties for the resulting *beat frequency* (f_b), together with the target range and target Doppler shift. The triangular waveform is made up of both a *up-chirp* and a *down-chirp*. This configuration will utilize the possibility to extract both range and Doppler shifts with reduced ambiguity in Doppler. For instance, if an up-chirp will experience a positive Doppler shift from a target this will add a positive bias to the beat frequency. Hence can the radar not know whether the target is at a specific range with no Doppler or if the target is at a longer range with a Doppler shift. The third and fourth waveform , *Triangular with hold*, is used to simplify the detection of multiple Doppler targets. Here will the hold-region will yield the ability to detect different Doppler shifts at the constant CW region. The problem however, is to link the different Doppler frequencies back to the different f_b's. Thus are several types of different modulations used to day, to ease Doppler extraction for multiple targets and resolve the range-Doppler ambiguity simultaneously. Examples of such is the LFM-FH [33] and triangular waveforms with different chirp rates. To illustrate the applied waveforms in time domain, an up-chirp and a triangular waveform is shown respectively in figure 2.4 and 2.5. The waveforms have a swept bandwidth of $100\ \mathrm{MHz}$ over a period of $3\mu s$ / $6\mu s$, generated in MATLAB from equation 2.3 and 2.3 (Appendix B.1.1).

The waveforms can be described mathematically as complex time-domain functions over one period [16, sec. 5.3]. The above waveforms are displayed in equation 2.3, 2.4, 2.5 and 2.6 with frequency rate $\alpha = \frac{\Delta f}{t_0}$. The amplitude A will be proportional to the output power and antenna gain in Tx and in addition target RCS, antenna gain('s) and range attenuation in Rx.
Up-chirp waveform as a complex function:

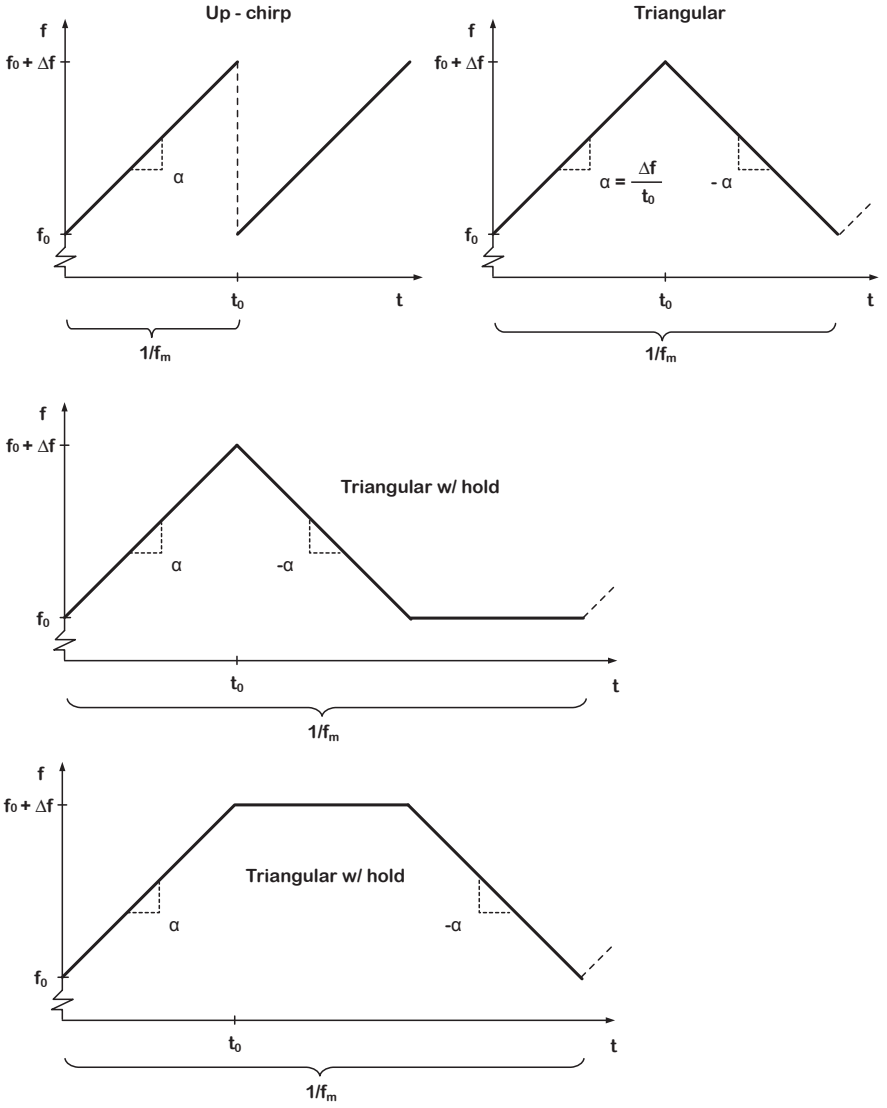

Figure 2.3.: Typical FMCW waveforms

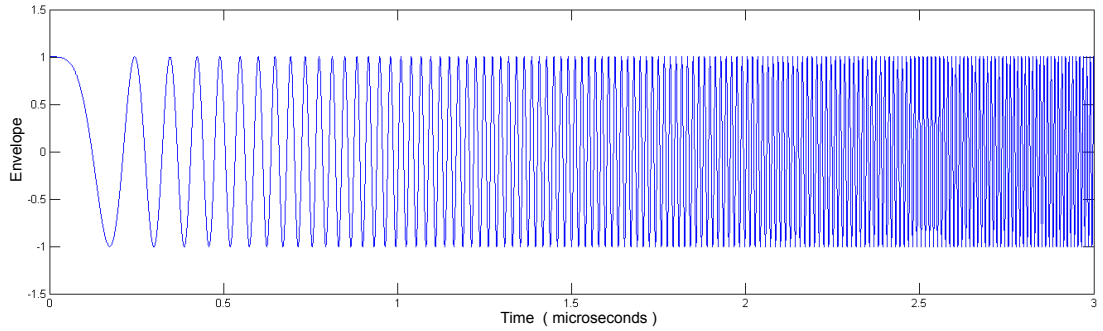

Figure 2.4.: Time signal 'up-chirp', $100\ \mathrm{MHz}$ and $3\mu s$

$$s(t)_1 = A\, e^{j2\pi(f_0 t + \frac{\alpha}{2}t^2)} \qquad [0 < t < t_0] \tag{2.3}$$

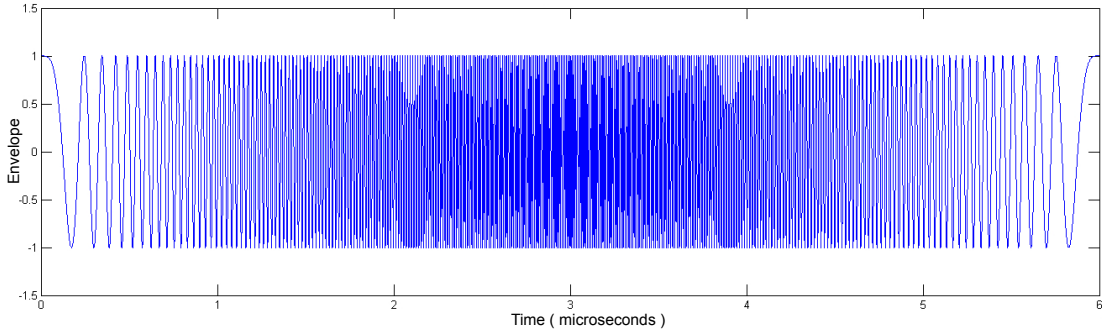

Figure 2.5.: Time signal 'triangular', $100\ \mathrm{MHz}$ and $6\mu s$

Triangular waveform as a complex function:

$$s(t)_2 = \begin{cases} A\, e^{j2\pi(f_0 t + \frac{\alpha}{2}t^2)} & [0 < t < t_0] \\ A\, e^{j2\pi(f_0 t + \Delta f t - \frac{\alpha}{2}t^2)} & [t_0 < t < 2t_0] \end{cases} \tag{2.4}$$

Triangular waveform with hold as a complex function:

$$s(t)_3 = \begin{cases} A\, e^{j2\pi(f_0 t + \frac{\alpha}{2}t^2)} & [0 < t < t_0] \\ A\, e^{j2\pi(f_0 t + \Delta f t - \frac{\alpha}{2}t^2)} & [t_0 < t < 2t_0] \\ A\, e^{j2\pi(f_0 t)} & [2t_0 < t < 3t_0] \end{cases} \tag{2.5}$$

Second triangular waveform with hold as a complex function:

$$s(t)_4 = \begin{cases} A\, e^{j2\pi(f_0 t + \frac{\alpha}{2}t^2)} & [0 < t < t_0] \\ A\, e^{j2\pi(f_0 t + \Delta f)} & [t_0 < t < 2t_0] \\ A\, e^{j2\pi(f_0 t + \Delta f t - \frac{\alpha}{2}t^2)} & [2t_0 < t < 3t_0] \end{cases} \tag{2.6}$$

These expressions can be obtained from the time integral of the instantaneous frequency. A linear up-chirp is expressed intuitively in frequency as an linear function and converted

to instantaneous phase by integration

$$\begin{aligned} f(t) &= f_0 + \alpha t \qquad [0 \le t \le t_0] \qquad (2.7) \\ &\Downarrow \\ \psi(t) &= 2\pi \int_0^t (f_0 + \alpha t)\, du \\ &= 2\pi \left(f_0 t + \frac{\alpha}{2} t^2 \right) \qquad (2.8) \end{aligned}$$

When the instantaneous phase is found the complex time signal can be obtained by insertion

$$\begin{aligned} s(t)_1 &= A\, e^{j\psi(t)} \qquad [0 \le t \le t_0] \\ &= A\, e^{j2\pi(f_0 t + \frac{\alpha}{2} t^2)} \end{aligned}$$

The frequency spectrum can be obtained by the Fourier integral, over one modulation period, of the time signal. Since the waveforms in FMCW are preferably matched on reception, will one period of the signal be sufficient, for analysis in the frequency domain. Hence equal to a pulsed chirp. This assumption is also normally done in studies of the FMCW waveform ambiguity function as well.

$$s(t)_1 = A\, e^{j2\pi(f_0 t + \frac{\alpha}{2} t^2)} = s(t) \cdot e^{j2\pi(f_0 t)}$$

Where s(t) is the complex envelope

$$\begin{aligned} s(t) &= A\, e^{j\pi(\frac{\alpha}{2} t^2)} \qquad [0 \le t \le t_0] \\ \mathcal{F}\{\cdot\} &\Downarrow \\ S(f) &= A \int_0^{t_0} \left(e^{j\pi(\frac{\alpha}{2} t^2)} \right) e^{-j2\pi f t}\, dt \end{aligned}$$

To obtain the detailed Fourier expression the further derivation involves identification of *Fresnel* integrals $S(x)$ and $C(x)$), which can be pursued in detail in [13, p.37]. The *Fresnel* integrals are odd functions $-S(x) = S(-x)$ and $C(-x) = -C(-x)$, giving the frequency domain expression

$$S(f) = \tau \sqrt{\frac{1}{\Delta f \tau}} \cdot e^{-j \left(\frac{(2\pi f)^2 \tau}{4\pi \Delta f} \right)} \left\{ \frac{[C(x_2) + C(x_1)] + j[S(x_2) + S(x_1)]}{\sqrt{2}} \right\}$$

The expression shows a symmetrical property, yielding $S(f) = S(-f)$. Thus giving spectral components in both sides of spectrum with a amplitude of the *Fresnel*-ripple,

which again will increases with low values of the time bandwidth product $(\tau\ \Delta f)$. The two-side and positive-side spectrum of a $100\ \mathrm{MHz}$, $40\mu\mathrm{s}$ up-chirp waveform generated by FFT estimation in MATLAB, is given in figure 2.6 as an typical FMCW frequency spectrum. It is important to note that this will not be the case for quadrature Rx processing, were the spectrum will be of the one-side type, dependent of the chirp modulation.

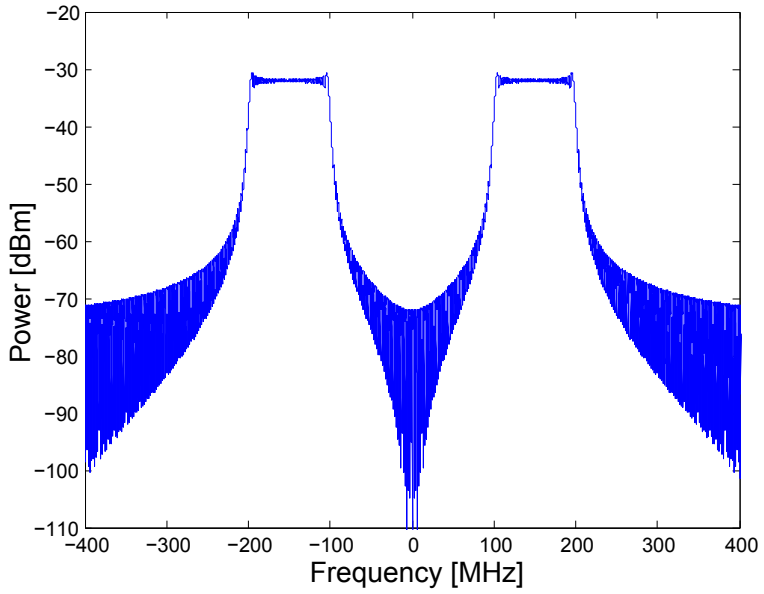

(a) Two-side spectrum

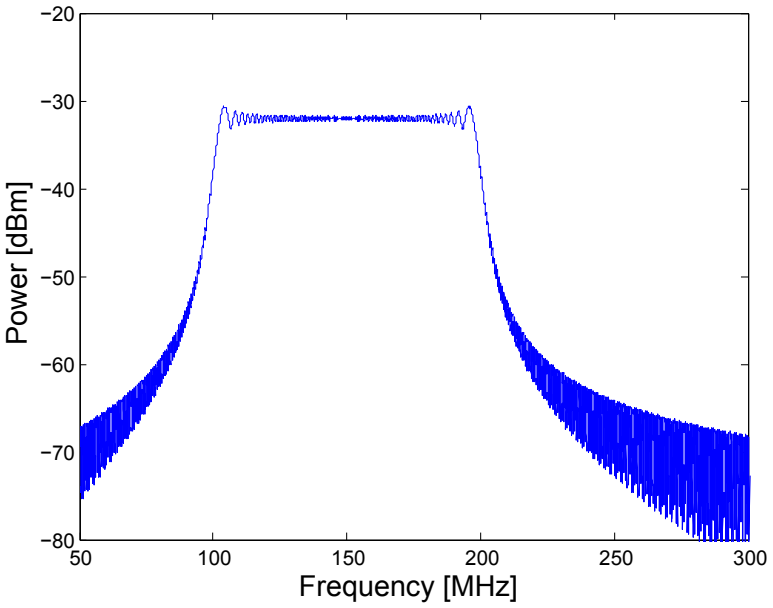

(b) One-side spectrum

Figure 2.6.: Typical FMCW spectrum, up-chirp, $\Delta \mathrm{f} = 100\ \mathrm{MHz}$, $\mathrm{t}_0 = 4\mu\mathrm{s}$

2.3. Waveform Ambiguity Function

As described in the previous chapter, have this thesis limited its focus to the study of LFM-CW waveforms in this radar application. But how will the choice of waveform affect the radar ambiguity function and how will then the continuous FMCW waveform apply to the analysis? Luckily does the ambiguity functions normally apply for analysis on a single pulse basis. Therefore can the FMCW waveforms be studied theoretically as single LFM-pulses without any errors being made [13, p.43]. Intuitively will this yield since it is desirable to correlate the full Tx and LO waveforms in the downconversion-mixer within the modulation period, hence on a 'pulse' basis and thus act as a *matched filter*.

By applying the perfered waveform to equation A.45 the radar ambiguity function can be derived [16, p.251]. The RAF of the up-chirp waveform is given in equation 2.9 as an example. Note however that pulse duration $\tau^{'}$ is the same as the FMCW sweep period t_0 in the previous section.

$$|\chi(\tau, f_d)|^2 = \left| \left(1 - \frac{|\tau|}{\tau^{'}}\right) \frac{\sin\left(\pi\tau^{'}(\mu\tau + f_d)\left(1 - \frac{|\tau|}{\tau^{'}}\right)\right)}{\pi\tau^{'}(\mu\tau + f_d)\left(1 - \frac{|\tau|}{\tau^{'}}\right)} \right|^2 \qquad |\tau| \leq \tau^{'} \tag{2.9}$$

Figure 2.7 show the RAF of a LFM up-chirp pulse of bandwidth $\Delta f = 5Hz$ and sweep time/ pulse width $\tau = 1\ second$

In general is it possible to make some intuitive observations about the LFM RAF.

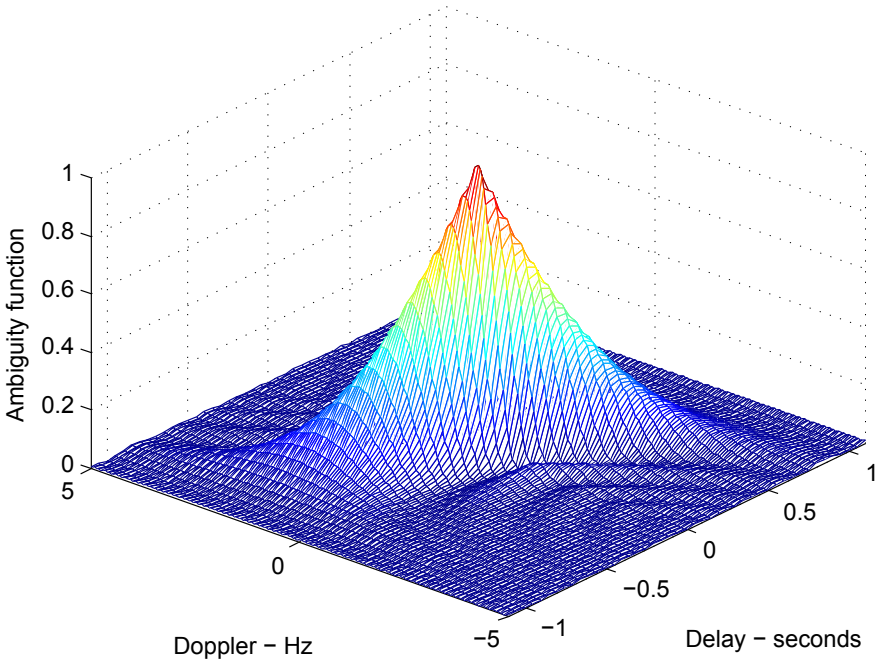

Figure 2.7.: The radar ambiguity function of a LFM/FMCW-pulse, $\Delta f = 5Hz$ and $\tau = 1\ second$

The most obvious difference compared to the CW-pulse RAF (figure A.20) is the new

range-Doppler coupling, which gives different range and Doppler resolutions and new ambiguity interpretations. In addition will the general RAF properties (A.46-A.49) yield that the constant volume of the LFM-RAF, will be constant. Hence will attempts to increase the range and Doppler resolution by generating at narrow mid-point peak result in increased side-lobe levels, because of the volume will be distributed. Additionally will a possible windowing of the compressed LFM-pulse decrease the sidelobe levels but widthen the pulse main lobe. Similarly will slope-form-altering be inherited by the RAF-shape from property 4.
To investigate the resolution properties, will the Zero-delay and -Doppler cuts of the uncertainty function, be helpful to look at the resolution in respect to the pulse-length and bandwidth.
The Zero-delay $|\chi(0, f_d)|$ cut, will then represent the Doppler resolution between the first nulls of the main lobe. By insertion the corresponding uncertainty function will yield

$$|\chi(0, f_d)| = \left| \frac{sin(\pi \tau^{'} f_d)}{\pi \tau^{'} f_d} \right| \qquad |\tau| \leq \tau^{'}$$

Evaluated for $sin(Arg)/Arg = 0$, will the first null will occur at $Arg = n\pi,\ n = 1$, resulting in $\tau^{'} f_d = 1$, thereby achieving the same Doppler resolution as a single CW pulse, given by the pulse length / FMCW sweep time

$$f_d = \pm \frac{1}{\tau^{'}} \tag{2.10}$$

$$\Delta f_d = \frac{1}{\tau^{'}} \tag{2.11}$$

Note that the Doppler resolution can be easily coupled to the radial velocity by $v = \alpha_0 / 2\tau^{'}$, but this yield only for the coaxial direction of the radar antenna. This relation is therefore left out of the notation since it is often the relative speed to the radar platform that is desired, however depended of the radar configuration.

The Zero-Doppler $|\chi(\tau, 0)|$ cut, will correspondingly represent the range resolution between the first nulls

$$|\chi(\tau, 0)| \ = \ \left| \left(1 - \frac{|\tau|}{\tau^{'}}\right) \frac{sin\left(\pi \tau^{'} \mu \tau \left(1 - \frac{|\tau|}{\tau^{'}}\right)\right)}{\pi \tau^{'} \mu \tau \left(1 - \frac{|\tau|}{\tau^{'}}\right)} \right| \qquad |\tau| \leq \tau^{'} \tag{2.12}$$

Similarly will the $sin(Arg)/Arg = 0$ give the delay/range resolution for $n = 1$, were $\mu = \Delta f / \tau^{'}$ and τ is evaluated for positive values, defining the delay resolution.

$$
\begin{aligned}
\tau^{'}\mu\tau\left(1-\frac{|\tau|}{\tau^{'}}\right) &= 1 \\
\Delta f\left(\tau-\frac{\tau^2}{\tau^{'}}\right) &= 1 \\
\tau^2-\tau\tau^{'}+\frac{\tau^{'}}{\Delta f} &= 0 \\
\tau &= \frac{\tau^{'}}{2}\left(1-\sqrt{1-\frac{2}{\tau^{'}\Delta f}}\right) \\
\sqrt{1-Arg} &\approx 1-\frac{Arg}{2} \qquad [Arg << 1] \\
\tau &\approx \frac{\tau^{'}}{2}\left(1-\left\{\sqrt{1-\frac{2}{\tau^{'}\Delta f}}\right)\right) \\
& \qquad [\tau^{'}\Delta f >> 1] \\
& \Downarrow \\
\tau &\approx \frac{1}{\Delta f}
\end{aligned}
\tag{2.13}
$$

This derivation show that the LFM-upchirp waveform has an increased range resolution compared with the single CW pulse from section A.10. Hence the the range resolution will be given in equation 2.14 as long the receiver bandwidth match the sweep bandwidth.

$$\Delta R = \frac{c}{2}\cdot\tau \approx \frac{c}{2\Delta f} \tag{2.14}$$

Consecuently does this prove that the LFM-waveform will be compressed in Rx through the matched filter. Therefore the compressed output of MF will be given by the sweep bandwidth Δf, which again must be equal the radar receiver bandwidth B. Generalized can the LFM-RAF properties be seen in figure 2.8 for both an up-and down-chirp pulse, showing an axial symmetry of the two closely related waveforms.

Compared with the uncompressed CW pulse the LFM waveform will have compression ratio (time-bandwidth product) accordingly

$$\epsilon = \frac{\tau^{'}}{(1/\Delta f)} = \tau^{'}\Delta f = \tau^{'}B \tag{2.15}$$

As a result will the compression ratio increase with increased bandwidth. However can a large frequency sweeps result in non-linearities of the waveform, degradating the resolution by slope-shape inheritage. Such Non-linearity can arise from using free-running VCO's in signal generation, which will have a monotonic frequency-to-voltage relation and therefore be linear only within portions of the utilized bandwidth.

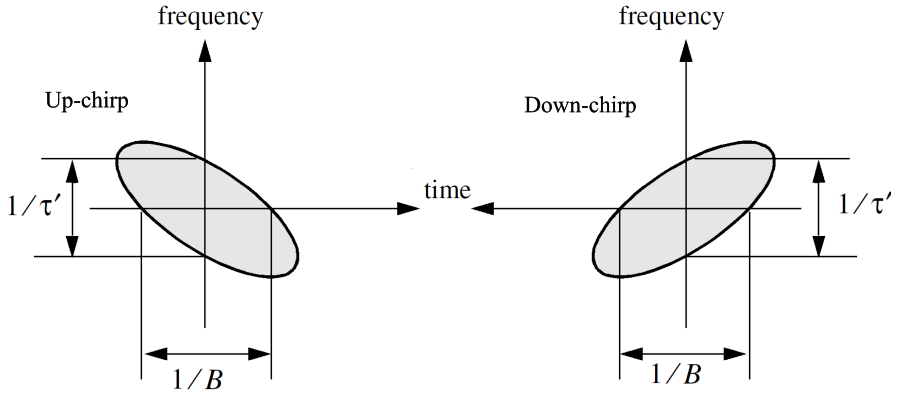

Figure 2.8.: The generalized radar ambiguity function contour of LFM up/down-chirp

The above derivations show that, isolated in range and Doppler domain, will it be preferable to have large sweeping bandwidth for good range resolution and long sweep time to increase the signal energy and Doppler resolution. This arise from the $Sinc(Arg)$ output of the matched filter along each isolated domain. It can be said that it is preferable to have the time-bandwidth product as high as possible. However does figure 2.8 reveal that the ambiguity function (uncertainty function) is skewed between the two domains, giving a *range-Doppler coupling*. As RAF property 2 stated, will the total volume of the RAF be constant and consecuently high time-bandwidth product have increased side-lobes in the skew which can lead to great ambiguity confusion. If the radar ambiguity function (equation 2.9) is investigated, the peak value will appear when the output $Sinc(Arg)$ have $Arg = 0$ and yield

$$(\mu\tau + f_d) = 0$$

$$(\frac{\Delta f}{\tau^{'}}\tau + f_d) = 0$$

$$\tau_{peak} = -\frac{f_d\tau^{'}}{\Delta f} \tag{2.16}$$

Hence gives equation the linear range-Doppler coupling and the linear shift. This proves that a non-Doppler target will have a maximum at $|\chi(0,0)|$, but a Doppler target will shift the peak in the skew diagonal $f_d = -\mu\tau^{'}$, creating a error in the delay/range domain and vice versa. Note here that the shift, will be dependent of the relation between Δf and $\tau^{'}$, giving the corresponding range error

$$\delta R = \frac{c\tau}{2} = \frac{c\tau^{'}f_d}{(2\Delta f)} = \frac{cf_d}{(2\mu)} \tag{2.17}$$

In addition to the shift in the dual domain, will the amplitude of the peak will be reduced according to the RAF magnitude. However would shifts within $f_d = 1/\tau^{'}$, make an acceptable reduction in peak values. Thereby making the LFM waveforms *Doppler*

invariant/ Doppler-tolerant inside the limit [16, p.321]. The ambiguity relation shows that there will only be unambiguous non-coupled relation, along the Zero-cut axis.
To illustrate the range-Doppler coupling, figure 2.9 show the contour plots of two low range resolution LFM pulses with pulse width $1\ second$ and corresponding bandwidths of $10Hz$ and $100Hz$. The figure exemplify how the increased bandwidth, will result in better range resolution. But also increased sidelobe levels with distinct peaks, revealed by the circular color contours

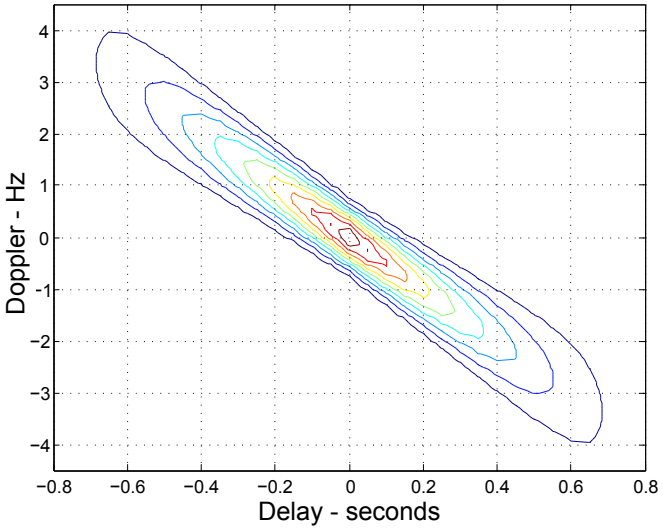

(a) LFM-pulse, $\tau^{'} = 1\ sec$ and $\Delta f = 10Hz$

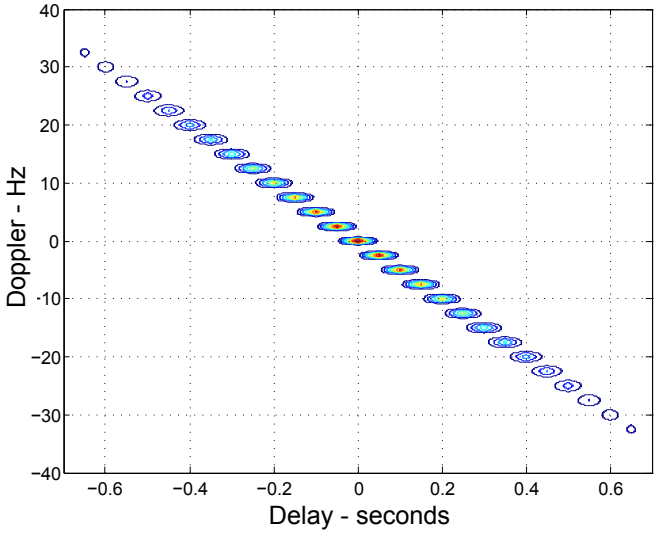

(b) LFM-pulse, $\tau^{'} = 1\ sec$ and $\Delta f = 100Hz$

Figure 2.9.: The radar ambiguity contours with a $\times\ 10$ increase in bandwidth

All figures are generated by implementations of the RAF in MATLAB, with the source code given in appendix D. Further is the LFM-pulse/waveform of a typical automotive radar application, shown in figure 2.10 for comparison. The radar parameters are taken form a practical implementation of a $77\ \mathrm{GHz}$ LRR/SRR done by Rohling [32]. The

figure show the domain view of delay and Doppler for the uncertainty function. Similarly with figure 2.9(b) will the higher time-bandwidth ($20e^6$) product create several narrow peaks in the diagonal, but much more narrow. The domain-view will give an idea of the diagonal form of the uncertainty function, since the peaks are just barely visual in the contour plot. Note the good resolution at the origin of the RAF. A $1\,\mathrm{GHz}$ bandwidth will give $\Delta\mathrm{R} = 0.15\,\mathrm{m}$ ($\Delta\tau = 1\ ns$) and $\Delta\mathrm{v} = 3.6\,\mathrm{km/h}$ ($\Delta\mathrm{f_d} = 500\,\mathrm{Hz}$). However should it be pointed out, that the volume property of the RAF gives big sidelobe levels in range for Doppler-shifted targets. Nevertheless can these shifts be sensed and resolved in Doppler domain, within the $f_d = 1/\tau^{'}$ limit. Hence can the range error be corrected if the Doppler-shift, not exceeds this decorrelation limit. Summarized can it be said that a LFM up-chirp of this kind will have a eminent response to high density fast moving targets.

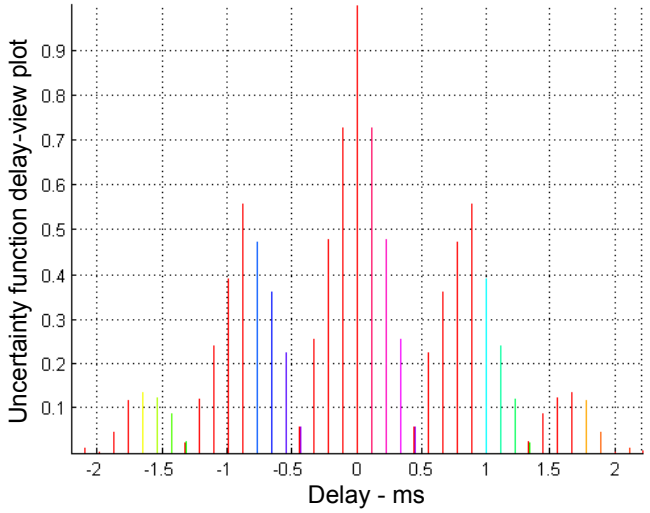

(a) LFM-pulse, $\tau^{'} = 2\,ms$ and $\Delta f = 1\,GHz$

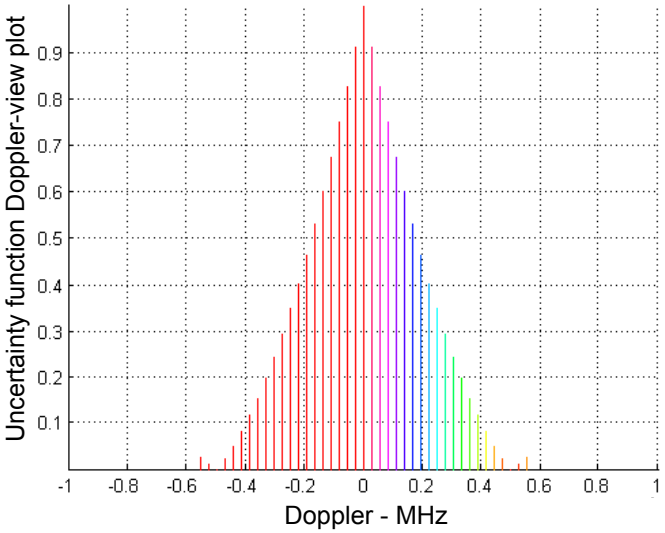

(b) LFM-pulse, $\tau^{'} = 2\,ms$ and $\Delta f = 1\,GHz$

Figure 2.10.: Domain views of the uncertainty function of a typical LFM automotive waveform

The LFM pulse/waveform will generally suffer form the range-Doppler coupling, creating confusion when both domains are equally desirable. This property can however be important when detecting Doppler targets. Compared with a single pulse of equal duration, will a LFM pulse create a significant output peak power, over a much broader range of Doppler-shifts. Hence is targets to be more likely detected and a single matched filter can be realized instead of a filter bank. Thus is the LFM waveform more *Doppler-tolerant* than the single pulse [30, p.197].

2.4. FMCW Beat Frequency Synthesis

When the FMCW radar receives the echo signal, the Rx waveform will be mixed with the reference LO waveform. Hence will the signal be demodulated in the mixer and produce a difference frequency, known as the *beat frequency*, which will be a offset in baseband proportional to the range and Doppler shift of the target. The mixing between the reference waveform and the echo waveform will make an approximate matched filter, with a $Sinc(X)$ output in frequency domain as described in the last chapter.

A typical FMCW transceiver design for range and Doppler extraction would be similar to the one in figure 2.11. The figure show how the mixing of high frequency waveforms will be down-converted to baseband, creating a low frequency output. Further will a LP-filter insure rejection of higher harmonic outputs from the mixer. Additionally can the filter act as an anti-aliasing filter for the ADC-circuit, hence insuring that targets and clutter beyond the maximum range are not aliased back at baseband creating *ghost* targets. The LP-filter bandwidth should also set to the maximal beat frequency, thereby limiting the FFT-length. A bandpass filter could be implemented instead of the LPF to remove the noisy 1/f-region, however must such a implementation be matched to the minimum beat frequency of interest to avoid masking of desired close targets.
Further will the baseband signal be amplified to match the dynamical region of the ADC. After sampling/detection the signal is normally applied to amplitude weighting for side-lobe reduction, before the signal is transformed to the frequency domain by the FFT algorithm. Then the frequency signal can be interped bin-wise, where each frequency bin in the FFT will correspond to a range bin and thereby giving the theoretical limit for the obtainable range-resolution given by the number of FFT-bins in the positive part of spectrum.

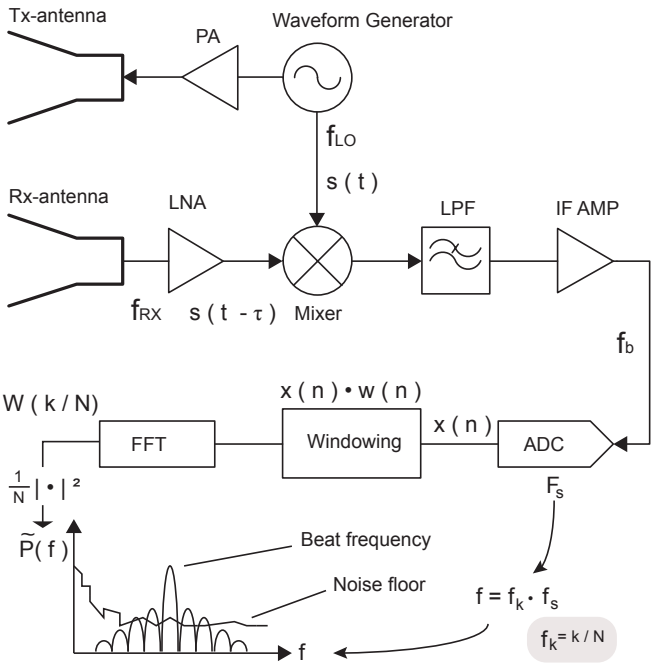

Figure 2.11.: Typical FMCW bistatic transceiver with estimated power spectrum output

Response to Static Targets

If a LFM up-chirp echo signal come from a static target, the mixing-process down to baseband can be described mathematically in time domain as

$$\begin{aligned} s(t)_{bb} &= s(t)^*_{LO} \cdot s(t-\tau)_{Rx} \\ &= A_{LO}\, e^{-j2\pi(f_0 t + \frac{\alpha}{2}t^2)} \cdot A_{Rx}\, e^{j2\pi(f_{rx}(t-\tau) + \frac{\alpha}{2}(t-\tau)^2)} \\ &= A_{LO}\, A_{Rx}\, e^{-j2\pi\left(f_{rx}\tau + \alpha\tau t - \frac{\alpha}{2}\tau^2\right)} \end{aligned}$$

Substituting τ and α into standard chirp parameters, the equation yield

$$= A_{LO}\, A_{Rx}\, e^{-j2\pi\left(f_{rx}\frac{2R}{c} + \frac{\Delta f}{t_0}\frac{2R}{c}t - \frac{\Delta f}{2t_0}\left(\frac{2R}{c}\right)^2\right)}$$

Since the sweep time, $t_0 >> \frac{2R}{c}$ last term of the phase term can be neglected

$$= A_{LO}A_{Rx}\, e^{-j2\pi\left(f_{rx}\frac{2R}{c} + \frac{\Delta f}{t_0}\frac{2R}{c}t\right)}$$

The beat frequency spectrum can only be studied practical for positive spectral components, hence can the real value of the complex expression be taken.

$$\begin{aligned} s(t)_{real} &= Re\left\{s(t)_{bb}\right\} \\ &= A_{LO}A_{Rx}\,\cos\left(2\pi\left(f_{rx}\frac{2R}{c}+\frac{\Delta f}{t_0}\frac{2R}{c}t\right)\right) \end{aligned}$$

The instantaneous frequency/ *beat frequency* is then given by

$$\begin{aligned} &\Downarrow \\ f_b(t) &= \frac{1}{2\pi}\frac{d}{dt}(\Psi(t)) \\ f_b(t) &= \frac{1}{2\pi}\frac{d}{dt}\left(2\pi\left(\frac{2f_{rx}R}{c}+\frac{\Delta f}{t_0}\frac{2R}{c}t\right)\right) \\ f_b &= \underline{\underline{\frac{\Delta f}{t_0}\frac{2R}{c}}} \end{aligned} \tag{2.18}$$

Equation 2.18 show the beat frequency relation to static targets, and its proportionality to the chirp rate and the targets range (round-trip-time). The current relation is shown on the left side of figure 2.12 in both the combined RF frequency-time domain and in baseband frequency-time domain. Note how the Rx offset in time will give the resulting beat frequency, but also limit the time were beat frequency is consistent. The time distribution of the beat will hence give the amount of power obtained at this frequency in relation to the intermediate time, shown as thick lines in the figure. However normally the time offset is very short compared to the offset seen in figure 2.12 and therefore will most of the power be distributed over the wanted beat. For instance will a automotive target at 150 m, give a round-trip time of $1\ \mu s$. If the chirp sweep time is 1 ms, the offset will be only 0.1% of the total chirp and yield that practically all power distributed at the beat. This derivation also proves the vailidity of the cancelation of the last phase term in the beat frequency derivation.

Response to Doppler Targets

Like the derivation of the beat frequency for static targets, the similar can be done for Doppler targets with constant velocity. Hence can the range be inserted into the derivation as $R(t) = R_0 + vt$, where R_0 is the initial range at $t = 0$.

After the new substition of the chirp parameters in $\tau(t)$ and α, the equation yield

$$s(t)_{bb} = A_{LO}\,A_{Rx}\,e^{-j2\pi\left(f_{rx}\frac{2R(t)}{c}+\frac{\Delta f}{t_0}\frac{2R(t)}{c}t-\frac{\Delta f}{2t_0}\left(\frac{2R(t)}{c}\right)^2\right)}$$

The signal instantaneous phase term is then

$$\Psi(t) = 2\pi\left(f_{rx}\frac{2(R_0+vt)}{c}+\frac{\Delta f}{t_0}\frac{2(R_0+vt)}{c}t-\frac{\Delta f}{2t_0}\left(\frac{2(R_0+vt)}{c}\right)^2\right)$$

Rearranging the phase term as

$$= \left(\frac{2R_0}{c}f_{rx}-\frac{\Delta f}{t_0}\frac{2R_0^2}{c^2}\right)+\left(\frac{2vf_{rx}}{c}+\frac{\Delta f}{t_0}\frac{2R_0}{c}\left(1-\frac{v}{c}\right)\right)t+ \\ +\left(\frac{\Delta f}{t_0}\frac{2v}{c}\left(1-\frac{v}{c}\right)\right)t^2$$

The first term is then identified as a constant constant phase term, while the last phase term can then be effectively left out for non relativistic velocities [12, App. A3].
The real signal then yield

$$s(t)_{real} = Re\left\{s(t)_{bb}\right\}$$

$$= A_{LO}A_{Rx}\cos\left(\Psi(t)\right)$$

The instantaneous frequency/ *beat frequency* is then

$$\Downarrow$$

$$f_b(t) = \frac{1}{2\pi}\frac{d}{dt}(\Psi(t))$$

$$f_b(t) = \frac{1}{2\pi}\frac{d}{dt}\left(2\pi\left(\left(\frac{2vf_{rx}}{c}+\frac{\Delta f}{t_0}\frac{2R_0}{c}\left(1-\frac{v}{c}\right)\right)t+\left(\frac{2R_0}{c}f_{rx}-\frac{\Delta f}{t_0}\frac{2R_0^2}{c^2}\right)\right)\right)$$

For automotive application that yield, $R_{max} < 200\,m$, $\Delta f \approx 1\,GHz$,
$v_{rel} < 300\,m/s$ and $t_0 > 100\,ms$, the negative contribution to the beat frequency proportial term could be effectively left out. Additionally will the constant phase term diminish due to time-derivation and the FMCW response to Doppler targets be given by

$$\underline{\underline{f_b = \frac{\Delta f}{t_0}\frac{2R}{c}+\frac{2vf_{rx}}{c}}} \tag{2.19}$$

Equation 2.19 show that the beat frequency for automotive applications will be proportional to both range and the Doppler frequency of the target. This relation also prove the range-Doppler ambiguity described with the radar ambiguity function of the up chirp waveform, which lead to that Doppler targets can be interpreted as a static targets another range. Figure 2.12 summarize the up-chirp waveform response to both static and Doppler targets in the combined time-frequency domain. In order to resolve the range-Doppler ambiguity down-chirps or hold periods needs to be added to the waveform.

To use the current proven relations they must be rearranged as range-equations which is the parameter that is desirable in this case. Extraction of range from the Doppler

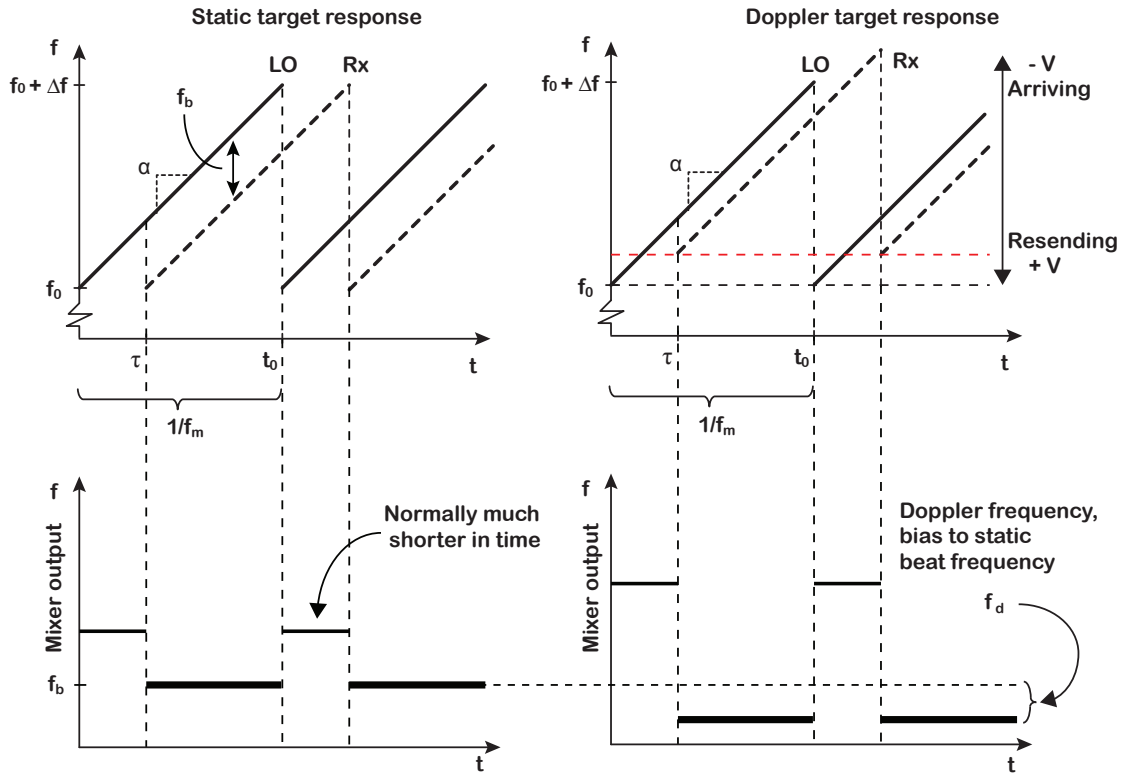

Figure 2.12.: Beat frequency synthesis for single static and Doppler target

frequency is intentionally left out since the thesis will only study static target responses in relation to spectral purity and use the up-chirp as waveform basis. However the derivation of the specific Doppler-relation to beat frequency in the automotive context is relevant since, the above simplifications does not yield for all FMCW applications. Similarly will the expression be were helpful when setting chirp parameters in relation to expected target Doppler-shifts and max/min range, to decide upon an reasonable region for the observable beat frequency.

The range can thus be given as [26]

$$\boxed{R = \frac{t_0\, c}{2\, \Delta f} f_b} \tag{2.20}$$

Additionally will the maximum- or *unambiguous range* always be an important relation, in order to understand the radars range-capability without *ghosting*. Since FMCW radars mostly use the FFT-algorithm to obtain its beat frequency spectrum it is convenient to express the unambiguous range in relation to the FFT implementation. This will then give a persitant maximum range in relation to obtainable hardware and its sampling frequency and FFT presicion. In order to do so two fundamental conditions must be meet.
First the Nyquist criteria, must be for filled to not loose any spectral information

$$\boxed{f_s \geq 2 \cdot f_{b,\,max}} \tag{2.21}$$

Secondly, to maintain the matched filter characteristics the processed samples $(NFFT)$ must match the modulation period, which in the case of the up-chirp is equal to the chirp sweep time (t_0). This also defines the FMCW *coherent processing interval* (CPI), which is normally insured by a timing and control circuit which synchronizes the sampling window in the DAS with the sweep start-up in the waveform generating circuit. To meet the Radix-based algorithm the FFT presicion should be on the form 2^n for fast computing.

$$\boxed{t_0 = \frac{NFFT}{f_s} = \frac{2^n}{f_s}}$$

Inserted in the range equation for $f_{b,\,max}$, yielding R_{max} the relations combine to

$$\boxed{NFFT \geq \frac{4\,\Delta f\,R_{max}}{c}} \tag{2.22}$$

which also makes and appropriate rule for setting the NFFT for cases were R_{max} must be meet.
Thereby the unambiguous range is given as

$$\boxed{R_{max} = R_{un} = \frac{NFFT\,c}{4\,\Delta f} = \frac{t_0\,c}{2\,\Delta f} f_{b,\,max}} \tag{2.23}$$

Another very important parameter for ranging radar systems is the *range resolution*. From the range equation(2.20) the resolution will be given by the delta component of the beat frequency.

$$\boxed{\Delta R = \frac{t_0\,c}{2\,\Delta f}\Delta f_b} \tag{2.24}$$

when meeting the CPI demand it reduce to the resolution obtained from the radar ambiguity function

$$\boxed{\Delta R = \frac{c}{2\,\Delta f}} \tag{2.25}$$

The resolution can also be a interpreted from the above relations to the theoretical FFT-bin resolution

$$\Delta R_{bin} = \frac{R_{max}}{NFFT/2}$$

and in terms of the bin-wise spectral response

$$\Delta f_b = \frac{f_{b,\,max}}{NFFT/2}$$

It should be noted that this theory only holds for the ideal case and that real implementation would suffer more limiting factors that that could degrade the overall FMCW performance. Note also that the NFFT is divided by two to give the one-side spectrum relation, since the FFT must be twice the size of the real signal length to obtain all available power. Similarly these relations show the FFT precision will be a big limiting

factor of FMCW systems [26, pp. 169-171], [13, pp.71-74].

2.5. Degradation of Range Resolution

Although the beat frequency equation show that the beat frequency is a function of both range and velocity, it reveals not all about the real range resolution. More factors than the basic chirp bandwidth, play an important part of the FMCW range resolution. In general FMCW range resolution depends both on the transmitted bandwidth, the effective processed bandwidth from the overlap between the LO reference and the received signal, the receiver frequency resolution (sampled bin resolution) and the frequency sweep linearity [27]. Additionally the use of windowing technices will reduce sidelobe levels, but also broaden the beat frequency spectral resolution. Further more, may also the Doppler shift relative to the radar smear out the beat frequency, since no real motion can be considered to be at exactly constant velocity. In this section the influence upon the range resolution of the effective processed bandwidth, waveform nonlinearities and receivers frequency resolution, will be closer examined.

2.5.1. Effective Processing Bandwidth

When the a FMCW radar synthesize the beat frequency, from the mixer correlation between the reference LO waveform and the Rx waveform, there will be a horizontal displacement in time-frequency-domain. Hence offset by the round-trip-time. The displacement would then in fact limit the effective processing bandwidth, since the beat will only produced over a part of the available chirp bandwidth [13, p. 74] and [27]. Figure 2.13 show how the mismatch due to the echo delay of the Rx waveform would reduce the effective bandwidth $\Delta f^{'}$ when using the up-chirp waveform. Note however that the echo-delay is made exceptional large in relation to the total sweep-time, in order to show the current relation. Normally the delay is much shorter and Piper [26] states that a common rule to avoid most of the current effect, is to insure that the modulation period (sweep-time in up-chirp) is at least 5 times the transit time. Thereby insuring that 80% of the total bandwidth is used for its right purpose.

The reduced effective bandwidth would then be given by the difference between full chirp bandwidth and the ratio of the echo-delay τ and the total modulation period t_m.

$$\Delta f^{'} \;=\; \Delta f \left(1 - \frac{\tau}{t_m}\right) \tag{2.26}$$

In the relation to the the perfect up-chirp waveform, t_m equals t_0. The *degraded range resolution* would then yield

$$\Delta R_{eff} \;=\; \frac{c}{2\,\Delta f \left(1 - \frac{\tau}{t_m}\right)} \tag{2.27}$$

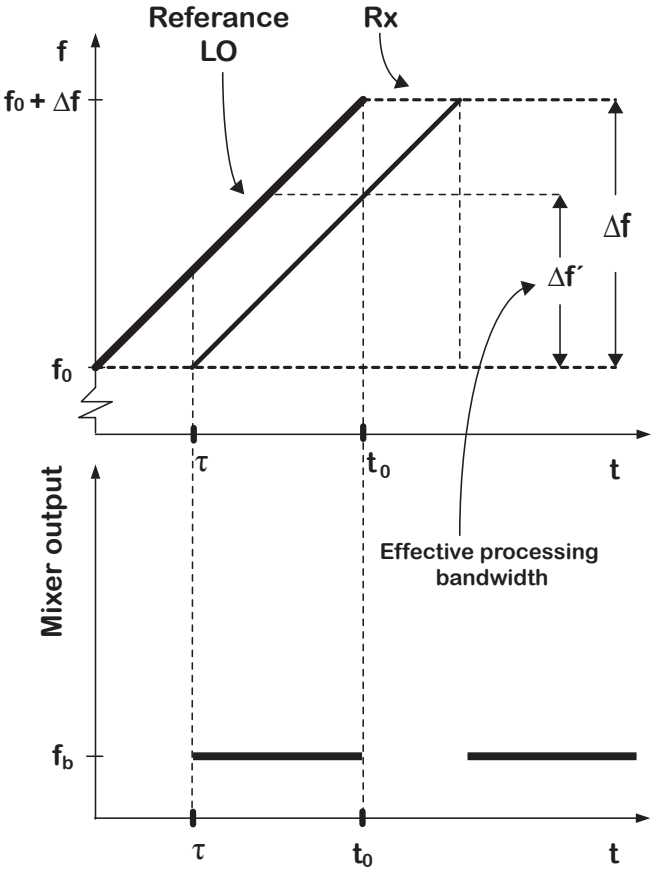

Figure 2.13.: Reduction of effective bandwidth to round-trip-time delay

If the generation of the chirp also contains a slew to new sweep or for instance a DDS settle time, the horizontal displacement in figure 2.13 will be even longer. Hence will the *effective modulation time* $t_m^{'}$ be reduced by the *sweep recovery time* t_{sr} and the echo-delay

$$t_m^{'} = t_0 - \tau - t_{sr}$$

The *degraded range resolution* will thus finally yield

$$\Delta R_{eff} = \frac{c}{2\,\Delta f\left(1 - \dfrac{\tau + t_{sr}}{t_m^{'}}\right)} \tag{2.28}$$

From the above equation it can be concluded that: *The range resolution in FMCW radar will decrease with increased range and be at its minimum at the maximum range* [13, p.75]. When this phenomena is seen in relation to *effective processed power*, figure 2.13 show how the wanted beat frequency would not be processed continouslly in time. Hence would there be a loss of the total available power processed over the full bandwidth, given by.

$$L_{sr} = \frac{\tau + t_{sr}}{t_m^{'}}$$

Although the property in equation 2.28 normally yield, giving coarser frequency and range resolution in the beat spectrum, some preventive actions could be taken to minimize

the bandwidth reduction. One approach is to match the processed number of samples to the effective modulation period $t_m^{'}$. However does this require changing the sample rate in accordance with the time-delay (range), making the scheme difficult to implement for practical applications with normally fixed sample frequencies. Perhaps a better scheme is then to synchronize the processing interval with the modulation frequency [26, p. 171]. Likewise could also a large echo-delay compared to the effective modulation time, be countered by a fixed delay of the LO signal. Hence would the error be minimized, but traded for a lower beat frequency and enhanced demands for the delay element insuring a non-dispersive performance for the wanted waveform.

The above equations show that the effective processing bandwidth is a important property for FMCW radars in general, but how does this apply for automotive radars? If the maximum range of automotive FMCW radars is set to approximately 200m, the general sweep-time rule purposed by Piper (described at the start of the section) could be used to insure minimum influence.

$$\tau = \frac{2\,R_{max}}{c} = 1.3\,\mu s$$

By applying Pipers rule, the chirp sweep time t_0 for automotive radars could be set by

$$\boxed{t_0 \geq\ 5\ \times\ \tau >\ 7\,\mu s} \tag{2.29}$$

to insure minimum reduction of effective bandwidth. Thus can reduction of processed bandwidth and range resolution caused by the target delay, normally be ignored for most automotive applications, where the sweep time in range of ms.
However must also the processing interval be taken into account, insuring that the the sweep recovery time is less than the echo-delay.

2.5.2. Non-linear Chirp

In order to achieve ranging capability in FMCW radars, the frequency must be swept over a large bandwidth in order to achieve a good range resolution. Thus will the quality of the chirp over the bandwidth be of the most importance. In case of LFM-waveforms, the figure of merit will the *chirp linearity*, which will determine the stability of the resulting beat frequency when the Rx and LO waveform is correlated in mixer. However will a ideal linearity never be achieved, because of the natural phenomena of circuit/transmission *dispersion* and non-ideal chirp waveform generation.

To day many FMCW radars uses DDS signal sources to generate highly controllable and linear chirps. However will also such implementation yield portions of non-linearity. Firstly the this arise from the fact that the DDS would produce a step-wise chirp at its output resulting from the digital-to-analog conversion (section A.11). Hence must the output be smoothen and anti-aliased with a LP-filer, minimizing the analog step-like structure in the combined frequency-time-domain. Although this technice will normally yield low non-linearity on chirp the signal generation would always suffer from non-ideal

effects as limited presicion in phase/frequency-accumulator, phase reading circuit, sine look-up table and DAC representation values, but also filter quality. All these effect will contribute either to phase mismatch or added spurious component to generated chirp [13, pp.299-310]. However have investigations of linearity of single DDS based W-band sensors proven to be minimal, close to ideally linear [15]. Thus making DDS based chirp generating circuits the obvious choice for FMCW applications. Nevertheless will there be a uncertainty to the up-conversion scheme to RF/Radar-band, since the todays DDS's are limited to a maximum output in the region of a few GHz.

Different schemes of up-conversion will therefore theoretically add a amount of distortion to the frequency sweep. If for instance a PLL circuit is used for high frequency up-conversion, with the DDS implemented as signal reference to the PLL's PFD, the loop needs to insure high frequency agility. Hence must the loop filter be designed very wide-banded, which will be a trade-off for increased phase noise and reference spurs appearance at chirp output [44]. Resultingly would a test of the chirp linearity be of the most importance, insuring that the circuit- or waveform design not violates the beat spectral purity.

Figure 2.14 show how a non-linear chirp will produce a *beat frequency ambiguity* at the output beat spectrum. Resultingly would f_b vary width time, increasing its spectral width over the processing period and degrading the range resolution. In a good radar design the spectral variation of $f_b(t)$ should however be kept mainly within the receivers frequency resolution bin, making the range and Doppler estimation independent of non-linearity of chirp [13, p.81].

Although it is obvious that non-linear LFM waveform will influence the resulting beat frequency spectral width, its figure of merit, *non-linearity*, is not easiest parameter to derive and consistently describe. A number of derivations and descriptions have been purposed for different designs and implementations, hence [13, pp.79-83], [15], [44], [27], [20] and [25].

Besides measuring the real spectral width of the beat frequency main lobe, which will also be dependent of other factors, the frequency error from ideal chirp slope to real measured slope and deviation of beat frequency to ideal beat frequency seems to be the most intuitive, figure of merits, of non-linear waveform behavior [15].

$$NL = \frac{\delta Slope}{Slope} = \frac{\delta f_b}{f_b}$$

Note that the nonlinearity described in this manner would be a function of echo delay (τ) and hence range (R), since the variations in beat frequency would depend on the relative mismatch between the NL in reference waveform to the NL in echo return waveform (figure 2.14). Thus can the resulting range resolution be estimated by the *square root of the sum of squares* (RSS), between theoretical resolution and the nonlinearity of range.

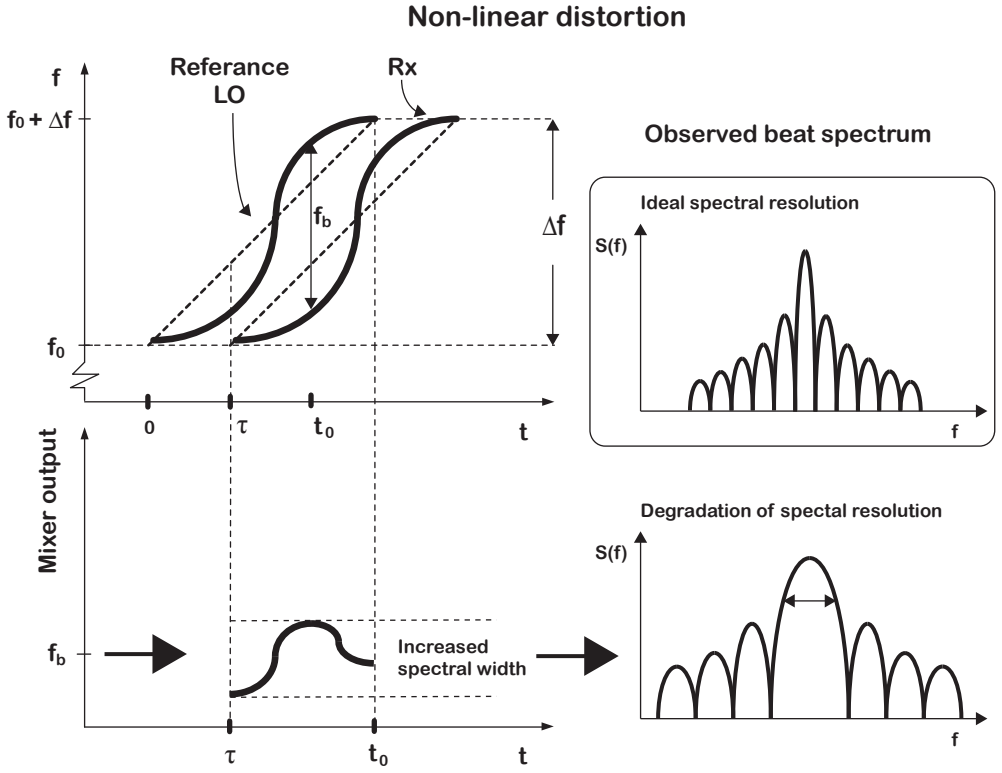

Figure 2.14.: Degradation of spectral resolution due to non-linear frequency sweep

$$\Delta R = \sqrt{\left(\frac{c}{2\Delta f}\right)^2 + (NL \cdot R)^2} \tag{2.30}$$

Figure 2.15 show how non-linearity can be seen in respect to the deviation from ideal chirp. Where the differences could be described as *root mean square error* (RMSE) or maximum chirp deviation $e_{chirp}(max)$. The reason why RMSE could be used for slope deviation description and not the normally used, *standard deviation* (SD), is that it gives a sample-wise comparison of residuals. While on the other hand SD compares with a mean value, which will not give meaning to a slope comparison. However would the standard deviation be good figure of merit, to compare the resulting beat frequency deviation.

Mathematically the chirp frequency error could be described as the frequency difference between ideal chirp and measured chirp

$$e_{chirp}(t) = f_{theo}(t) - f_{meas}(t) \qquad [0 < t < t_0] \tag{2.31}$$

Thus would the maximum deviation and RMSE be given as

$$e_{chirp}(max) = |e_{chirp}(t)|_{max} \tag{2.32}$$

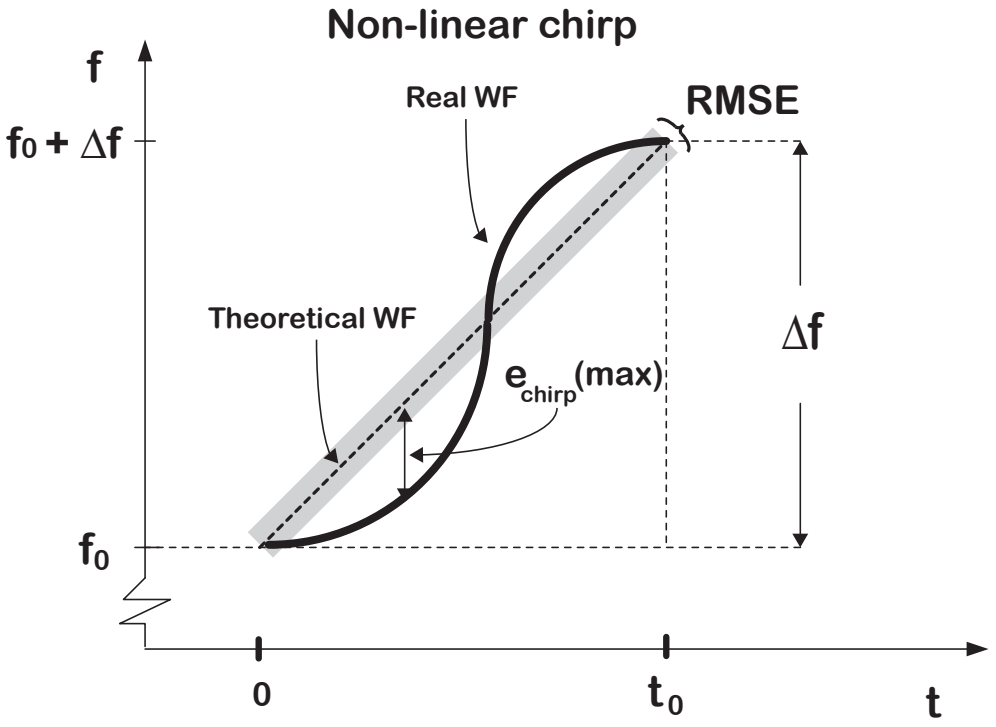

Figure 2.15.: Non-linear frequency sweep waveform

$$RMSE = \sqrt{\frac{1}{t_0}\int_0^{t_0} |e_{chirp}(t)|^2 \, dt} \tag{2.33}$$

or as measured discrete samples

$$= \sqrt{\frac{1}{N}\sum_{n=1}^{N} |e_{chirp}(n)|^2} \tag{2.34}$$

In order to get comparable figures of merit between designs, it is common to normalize RMSE or SD in relation to the total swept bandwidth, since non-linearity in waveforms will be more severe at longer frequency sweeps. Hence could the maximum error and RMSE be given as *effective maximum instantaneous linearity* (L_{me}) and *effective mean square root linearity* (L_{se}) [25].

$$L_{me} = \frac{e_{chirp}(max)}{\Delta f} \cdot 100 \qquad [\%] \tag{2.35}$$

$$L_{se} = \frac{RMSE}{\Delta f} \cdot 100 \qquad [\%] \tag{2.36}$$

Although these parameters will give numbers to the nonlinearity of a single waveform, it is however important to realize that the observed spectral width of the beat frequency

will depend on the mismatch nonlinearities create between LO and Rx waveform when they are correlated in the receive mixer.
When linearity is studied as beat frequency deviation, the relation apply as follows

$$
\begin{aligned}
f_{LO}(t) &= f_0 + \alpha t + e_{chirp}(t) \\
f_{Rx}(t) &= f_0 + \alpha(t-\tau) + e_{chirp}(t-\tau) \\
&\Downarrow \\
f_b(t) &= f_{LO}(t) - f_{Rx}(t) \\
&= \alpha\tau + (e_{chirp}(t) - e_{chirp}(t-\tau)) \\
&= f_b(ideal) + \delta f_b(t)
\end{aligned} \tag{2.37}
$$

The above equation show that the ideal beat frequency would be ambiguous to the *beat frequency error* caused by the convolved frequency error of LO reference waveform and target echo waveform. To interpret the actual error one need to measure the instantaneous deviation of beat frequency for several periods to get good statistics or to measure the error on both LO reference and real target echo return, and make an estimation of variance [25],[15]. Clearly these methods demand lot of instrumentation and large measurement datasets in order to create good statistics for estimates of beat frequency spectral distortion.

A more analytical approach have therefore been purposed by Piper, studying non-linearity as Sinusoidal non-linearity on waveform due to non-ideal linearizers [27]. This analyzing technice was generally intended for FMCW implementations that uses linearizer circuits. Such implementations would normally reduce peak non-linearity errors and increase the error frequency, making the error more sinusoidal and analyzable. However does such a analysis of error periodicity give a general understanding of how the non-linear chirp nature affects the beat frequency in spectrum.

According to Piper the transmitted waveform (up-chirp) could be described by the periodicity (f_n) and frequency deviation amplitude (A_n) of the non-linearity

$$f_{LO}(t) = f_0 + \alpha t + A_n \, sin(2\pi f_n t)$$

hence as complex signal

$$s(t)_{LO} = A_{LO} \, e^{-j2\pi \left((f_0 t + \frac{\alpha}{2} t^2) + \frac{A_n}{2\pi f_n} (1 - cos(2\pi f_n t)) \right)}$$

mixing to base band with target echo

$$s(t)_{bb} s(t)^*_{LO} \cdot s(t-\tau)_{Rx}$$

simplifying and obtaining beat frequency form time derivation, yield

$$\Downarrow$$

$$f_b(t) = \frac{\Delta f}{t_0} \frac{2R}{c} + \frac{A_n}{2\pi f_n} \left(sin(2\pi f_n t) - 2\pi f_n sin\left(2\pi f_n \left(t - \frac{2R}{c} \right) \right) \right) \quad (2.38)$$

Equation 2.38 show how the beat frequency spectral width from the target return, will depenten on both the periodicity(bandwidth) of the chirp error and the effective processing time of the nonlinearity, relative to target range (echo delay). Hence is a ambiguity added to the beat frequency, caused by the sinusoidal fluctuation around the ideal beat frequency. If the nonlinearity is long term stable, would a long processing interval/ correlation time relative to the target delay, decrease the nonlinear influence on the spectral resolution. The parameters of the sinusoidal nonlinearities would give the spectral apparence around the beat frequency. Thus will the frequency of the nonlinearity f_n imply were the frequency sidelobes appear in relation to the beat frequency. Likewise would the amplitude of the nonlinearities give the sidelobe amplitude [27]. Figure 2.16 show the concept of how a ideal target spectrum would be influenced by two types of chirp nonlinearities.

2.5.3. Range Resolution in Relation to Receiver Frequency Resolution

Although it has been shown in this chapter that nonlinearities will degrade the spectral resolution of the beat frequency, the real observed resolution will also be dependent on the receivers frequency resolution/ range-bin resolution by the convolution of the target beat frequency spectral width (Δf_{tar}) and the receiver filter bandwidth (Δf_{rec}) [26]. Hence can the observed resolution be estimated by the square root of the sum of squares (RSS).

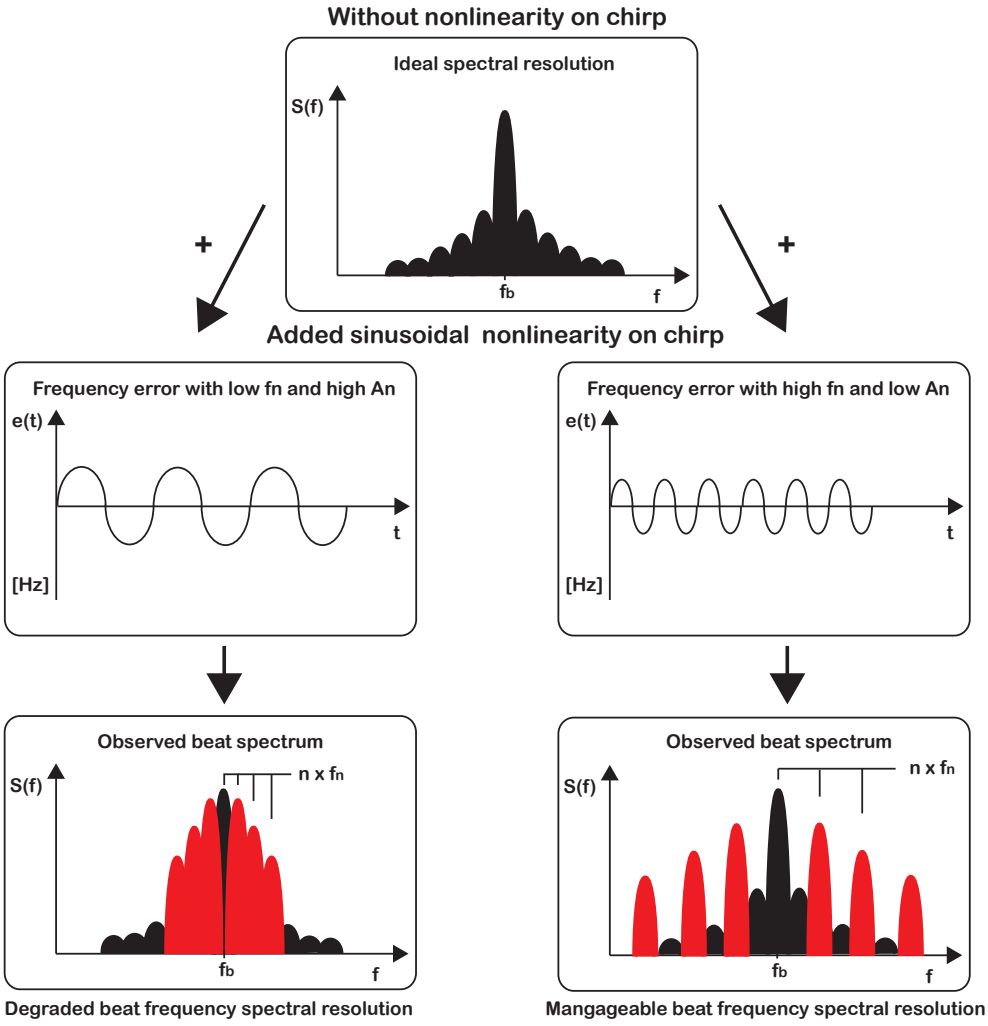

Figure 2.16.: Added beat frequency ambiguity by sinusoidal nonlinearities on chirp waveform

$$\boxed{\Delta f_b = \sqrt{\Delta f_{tar}^2 + \Delta f_{rec}^2}} \qquad [Hz] \tag{2.39}$$

where Δf_{tar} would be the beat frequency spectral width to the ideal point target or spectral width to the degradation of nonlinearities on chirp, given as correspondingly

$$\Delta f_{tar} = \frac{1}{t_m - \tau - t_{sr}}$$

or as nonlinearity

$$\Delta f_{tar} = \frac{NL}{100} \cdot \Delta f \tag{2.40}$$

From equation 2.24 the beat frequency resolution can be transformed to range-bin resolution, by using the constant factor as a *scale factor* between the two domains

$$SF = \frac{t_0\, c}{2\, \Delta f} \qquad \frac{[m]}{[Hz]} \tag{2.41}$$

$$\text{multiplying } \Delta \text{f}_\text{b} \text{ by SF yield}$$

$$\Delta R = SF \times \Delta f_b \qquad [m] \tag{2.42}$$

By further applying equation 2.24 to 2.20 the convolved estimated range resolution becomes [13, p.77]

$$\boxed{\Delta R_{conv} = \frac{R}{f_b}\sqrt{\Delta f_{tar}^2 + \Delta f_{rec}^2}} \qquad [m] \tag{2.43}$$

In relation to Δf_{rec} the ideal receiver frequency resolution, will in the case of FMCW radars correspond to the range-bin resolution. Hence can the receiver resolution be given by

$$\Delta f_{rec} = \frac{1}{t_m} = \frac{1}{t_0} \qquad [Hz] \tag{2.44}$$

which further will in real implementation yield

$$\Delta f_{rec} = \frac{f_s}{NFFT} \qquad [Hz] \tag{2.45}$$

However as explained in the chapter start is the use of windowing technics common to reduce the beat frequency side-lobes. This would then be a trade-off for increased bin resolution and main-lobe reduction. For most ranging radar applications the Hamming-window would be the best choice for its balanced trade-off between SNR (1.34 dB reduction), side-lobe levels (-42.2 dB lowering) and spectral 6dB main-lobe resolution (1.81 bins), compared to the rectangular window [13, p.34]. Hence would the corrected Δf_{rec} be increased with 1.81 range-bins.

$$\Delta f_{rec} = 1.81 \cdot \Delta f_{rec} \qquad [Hz] \tag{2.46}$$

With all the current equations and relation in bound, Jankiraman have purposed a strategy for range resolution management [13, p.78], summarized in two factors that influence the range resolution:

1. Reduced range resolution due to loss of effective bandwidth [section 2.5.1]
2. Reduced range resolution due to the convolution of Δf_{rec} and Δf_{tar} [section 2.5.2 and 2.5.3]

Summarized could the range resolution be estimated by

$$\begin{aligned}\Delta R &= max\left\{\Delta R_{conv}\ ,\ \Delta R_{eff}\right\} \\ &= max\left\{\frac{R}{f_b}\sqrt{\Delta f_{tar}^2+\Delta f_{rec}^2}\ ,\ \frac{c}{2\,\Delta f\left(1-\frac{\tau}{t_m}\right)}\right\}\end{aligned} \tag{2.47}$$

From this equation three strategies could be used in order to enhance the range resolution, besides the obvious increase of bandwidth.

1. Increase the frequency sweep time t_m (t_0), which would reduce ΔR_{eff} and also Δf_{rec}.
2. Increase f_b by increasing f_s, thereby reducing ΔR_{conv}.
3. Decrease the nonlinearities in chirp, which would reduce Δf_{tar} and hence ΔR_{conv}.

2.6. Transceiver Noise Leakage

As presented in the introductory part of this chapter, the unavoidable leakage of transmitted power in to the receiver is a very important matter for FMCW system performance. The most obvious errors is of cours the power leak that damage system components or drive the low noise amplifier into saturation and thereby yield a nonlinear Rx output to mixer. Hence must always sufficient isolation between antennas or couplers be insured. However is the specific relation to amplitude noise (AM) and phase noise (PN) important to see how the beat frequency output will be affected by the inherited noise crated within the transceivers single signal source.

To describe the AM and PN noise relations, A.G Stove's paper on *Linear FMCW Technices* have been used to provide the fundamental theory for analysis of transceiver noise leakage [42].

Generally AM noise could be described as an quasi sinusoidal amplitude modulation (modulation index, α) on carrier (ω_0) within a narrow band region ($\pm\omega_m$) and separated as

$$A(t) = A_0(1-\alpha)sin(\omega_0 t)\ +\ A_0\frac{\alpha}{2}cos(\omega_0-\omega_m)t\ +\ A_0\frac{\alpha}{2}cos(\omega_0+\omega_m)t$$

Likewise could FM/PN noise could the be described as a narrow band modulation if the frequency deviation ($\Delta\omega$) is much smaller than the frequency offset((ω_m)).

$$A(t) = A_0 sin(\omega_0 t)\ +\ \frac{A_0}{2}\frac{\Delta\omega}{\omega_m}sin(\omega_0-\omega_m)t\ -\ \frac{A_0}{2}\frac{\Delta\omega}{\omega_m}sin(\omega_0+\omega_m)t$$

Note here the difference in the two expressions of the sidebands, thus yield opposite signs. However do the two expressions yield the same sidelobe level on both sides of carrier in the isolated cases. Further the expressions show that any arbitrary side bands could be created by adding arbitrary amplitude and phase. Thus could the two expressions be used for describing the noise sidebands of an an signal source oscillator, and be the fundament for noise level analysis. Since such a analysis is more appropriate to study as power noise, Stove have extracted the side band amplitudes of the above equations as maximum power expressions with assumed low modulation index.

$$P_{AM} \approx \frac{\alpha^2}{4} \qquad P_{FM} \approx \frac{(\Delta\omega/\omega_m)^2}{4}$$

In the case of single side FM noise the noise power would decrease as 20dB/decade for each offset m, if the frequency deviation at each frequency is constant for all frequency of interest.
When a leakage is supplied to RF port of the down-conversion mixer the signal will degrade the receivers noise figure. Generally would then a IF output, with basic input $A(t) = A_s sin(\omega t)$ yield

$$A^{'}(t) \approx kA_s\, cos((\omega - \omega_0)t + \phi)$$

where k is the conversion loss of mixer and ϕ is the relative signal phase to the local oscillator. Hence would the IF power be given by

$$P_s = \frac{(A_s k)^2}{2Z_0}$$

AM noise detection in mixer:
If the AM noise from oscillator is assumed to be sufficiently suppressed by a balanced mixer the local oscillator

$$A_L(t) = A_{LO} sin(\omega_0 t - \phi)$$

by applying the sideband AM noise relation to the RF leakage, an using the suppressed AM relation, the mixed simplified IF single sideband noise power output would yield

$$\boxed{P_{AM} \approx 4k^2 cos^2(\phi) = 4L\, cos^2(\phi)} \tag{2.48}$$

Equation 2.48 does express the detected IF AM noise power, as 4 times the single sideband RF noise power, to the relative phase between the RF leak and the LO signal, and the power conversion loss of mixer (L). The AM noise would then be detected when LO and leak are in phase.

FM noise detection in mixer:
In relation to FM noise detection the noise of oscillator can not be neglected, and oscillator can be expressed as

$$A_L(t) = A_{LO}[sin(\omega_0 t)\ +\ \frac{\Delta\omega}{\omega_m 2} sin(\omega_0 - \omega_m)t\ -\ \frac{\Delta\omega}{\omega_m 2} sin(\omega_0 + \omega_m)t]$$

Since FM signals will be dependent on the time relative relation to other signals, all RF signals would have to be described in relation to their time position, hence their relative delay to LO ($\delta\tau$). Hence must will all RF signals be expressed as

$$A_R(t) = A_0[sin(\omega_0(t-\delta\tau))+\frac{\Delta\omega}{\omega_m 2}sin((\omega_0-\omega_m)(t-\delta\tau))-\frac{\Delta\omega}{\omega_m 2}sin((\omega_0+\omega_m)(t-\delta\tau))]$$

After mixing and manipulation the expression yield

$$A_{IF} = 2k\frac{\Delta\omega}{\omega_m}A_0 \cdot sin(\omega_0\delta\tau) \cdot cos(\omega_0\frac{\delta\tau}{2}) \cdot sin(\omega_m(t-\frac{\Delta\tau}{2}))$$

The detected power relative to the single sideband RF level, after manipulation, would then yield

$$\boxed{P_{FM} \approx 4L\ sin^2(\phi)\ \cdot\ 4sin^2\left(\frac{\omega_m\delta\tau}{2}\right)} \tag{2.49}$$

From the above equation it can be seen that the FM/PM noise would be detected if the LO signal is in quadrature with the RF leak signal, showing that FM sidebands are in anti-phase whereas AM are in phase. The last term of equation 2.49 does also show that the FM noise would be canceled if the relative time delay ($\delta\tau$) of the RF signal is much less the modulation rate (f_m). Thus often called the noise cancellation term, referred to as C. If this relation is true, the signal variations on both LO and RF signal would be almost equal, hence having a strong correlation and minimizing the FM noise from output of mixer. On the other hand, would thus an increase of $\delta\tau$ yield less correlation and more observed FM noise at low IF spectrum.

The cancellation term for FM noise power could then help to insuring a radar design that minimizes the FM noise, seen in spectrum as 1/f-noise, descending from zero frequency. Hence could this be done by insuring that the signal path of the strongest source of leakage to mixer is approximately equal to the LO path to mixer. If such a design is implemented, a reduced 1/f spectrum would yield better sensitivity at low frequencies that would be beneficial for close target detection in FMCW radar (see figure 2.17).
To minimize FM noise by analysis in a bistatic or quasi-bistatic design, could the cancellation term be transformed to a length dependent expression. Hence where $\delta\tau = L_{TX}(L)/v$ and v is the propagation velocity for the specific material of interest.

$$C = 4sin^2\left(\frac{\pi f_m L_{TX}(L)}{v}\right)$$

For a specific level of wanted FM noise cancellation, $\delta\tau$ or $L_{TX}(L)$ could be determined from the above expressions as correspondinglly maximum leakage signal path delay or length. Figure 2.17 show the general concept of FM/PM noise cancellation in a bistatic FMCW radar, with resulting beat spectrum outputs for different levels of FM noise cancellation. If the two main signal paths of the figure are seen separately, the FM noise of the f_{RX} path (echo response) will at mixer be uncorrelated to f_{LO}, by the degree of mismatch of signal path length. Hence will the FM noise from the path $f_{TX}(L)$ be more correlated to f_{LO}, by less mismatch of signal path length. Note that the beat spectrum

will be the sum of both AM and FM noise, hence always more *noisy* for low frequencies related to the homodyne downconversion of oscillator overall noise.

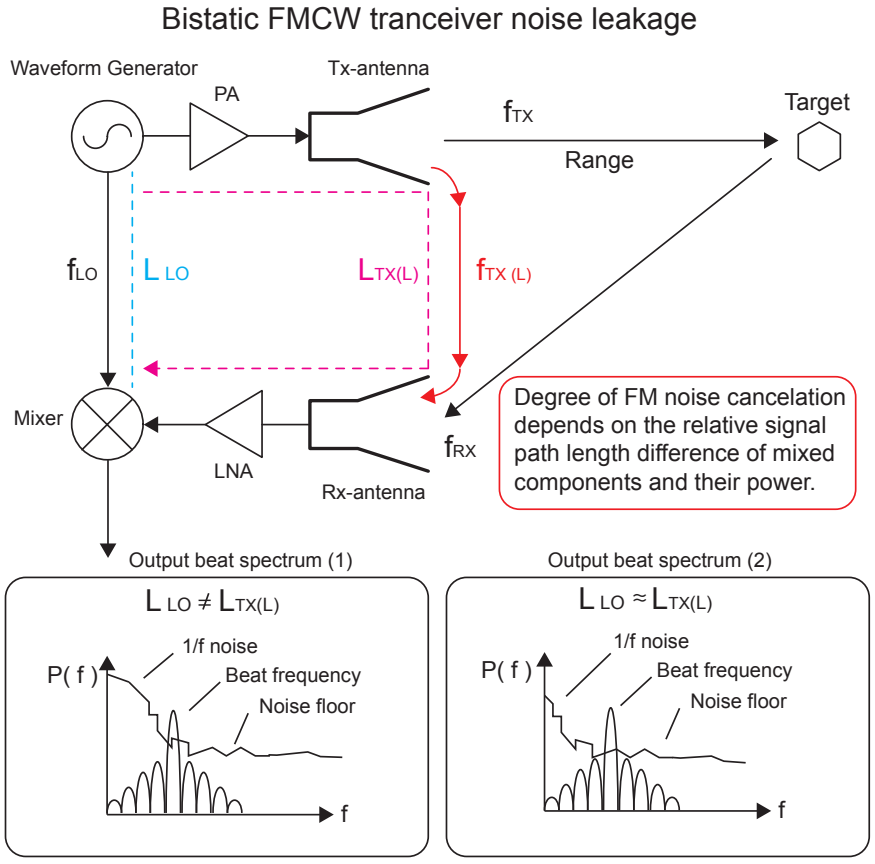

Figure 2.17.: Cancellation of FMCW FM noise due to leakage

Although the cancellation term can theoretically be matched to zero, the real cancellation will be limited by the degree of incidental FM-to-AM noise conversion, due to dispersion effects in propagation and target spectral response. Similarilly will also multiple sources of leakage, approximately equal in signal amplitude, also degrade cancellation [42]. Furthermore can near targets and strong clutter be superior to the leakage power-level, hence seen in mixer as the main source of FM noise. By the relative delay to LO signal, such cases would then increase the level of 1/f noise seen in beat spectrum [13, p.291].

The cancellation of FM noise is clearly beneficial to FMCW radar applications, however does the reduced FM noise now have to be considered in relation to the AM noise. Normally the AM noise from a standard oscillator is considered to be much less than its FM noise. However at IF spectrum after FM noise cancellation, this will no longer be true. Hence must AM noise have to be considered as plausible major noise source, for system degraded performance. Nevertheless would the weighting of noise sources in FMCW radar design be considered in relation to the systems sensitivity to either FM noise or AM noise.

Additionally must also the oscillators/VCO contribution to the output noise floor be determined, since its thermal noise will always be decorrelated and be a limiting factor to the receivers noise factor and hence SNR [44]. To make benefit of the noise power relations expressed in equation 2.48 and 2.49 in relation to allowable transmitter leakage power, Stove have presented two inequalities that could be used to approximate the needed level of isolation to minimize AM noise and FM noise.

In the case of AM noise, the resulting leakage of RF power (R) will be approximated by choosing the worst level of AM noise contribution of the system seen in relation to the thermal noise level as an offset (off). Hence could the inequality be expressed in dB as

$$P_t + P_{AM} + R \leq -174 + F_{rec} + off \tag{2.50}$$

For FM noise the similar expression yield, however must the degree of FM noise cancellation be taken into account

$$P_t + P_{FM} + R + C \leq -174 + F_{rec} + off \tag{2.51}$$

The easiest way of insuring sufficient TX/RX isolation is to use a bistatic/ quasi-bistatic design where isolation is insured by the separation of antennas. Which their separation could be derived from the above equations in form of the cancellation factor of FM noise (C). Although the antenna separation have been a much used scheme for sufficient TX-RX isolation, different types of coupler have also been used to do the same job but would normally yield lower isolation performance.

2.7. The General Choice of Beat Frequency

Since FMCW radar senses the environment and targets in the frequency domain through the *beat frequency*, need its dependencies to be considered carefully. The resulting LFM-FMCW beat frequency is as described, basicly dependent of the chirp-rate, target range and target Doppler-shifts. However must some kind of analysis be done to decide upon the right beat frequency region for the system. Hence how the chirp-rate parameters influence the beat frequency and how the beat frequency will fit the radar application, observed targets and available hardware.
Firstly if a design is not set, a design assessment should be made upon the general parameters and possible trade-offs between three basic domains:

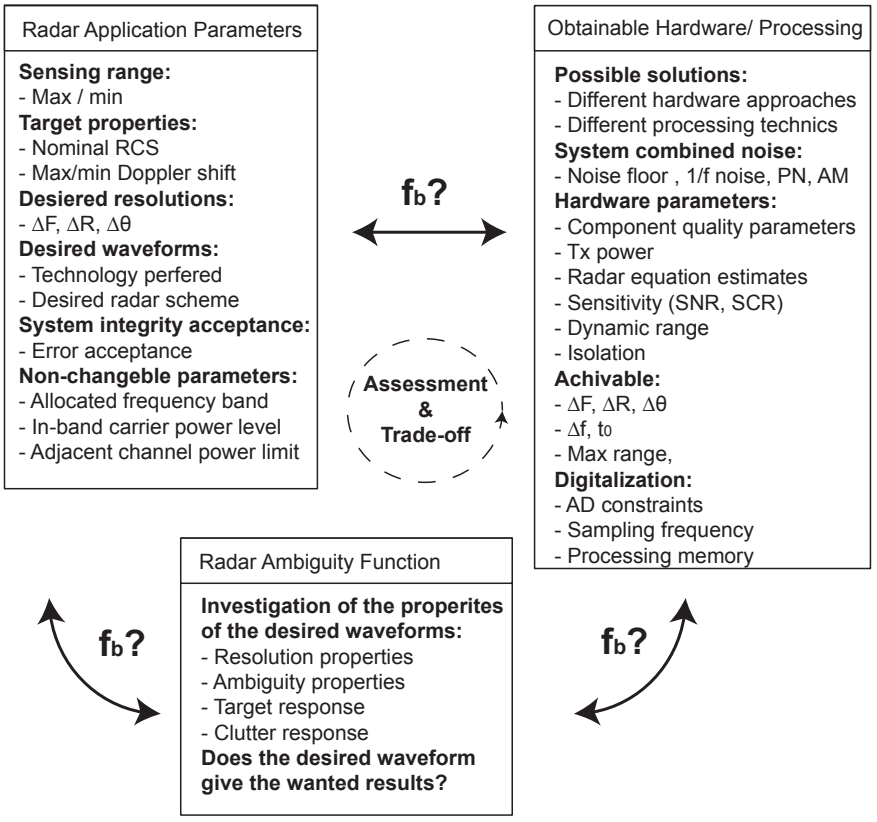

Figure 2.18.: General FMCW radar design assessment and trade-offs

Secondly when the fundamental assessments and trade-offs are made, will some parameters be more fixed than others and therefore give some limitations to the fundamental parameters for the further beat frequency setting. However it is important to note how the resulting beat frequency is affected during the general assessment and how an altering of it will reflect back at the three domains.
When a basic design analysis is made and the waveform is decided upon, can some general considerations to beat frequency setting be made [13, p.212].

- **Increasing** Δf: Improves range resolution, decreases the radiated power spectral density and shifts f_b up in frequency.
- **Decreasing** Δf: Enable better linearity control, enables higher output power.
- **Increasing** t_0: Yield longer range, increased Doppler resolution, makes the coherent processing interval longer and reduces the needed the sampling frequency by f_b reduction.
- **Increasing** f_b: Reduces influence from Zero/IF frequency 1/f-noise thereby increasing radar sensitivity, high f_b can impose difficulties in digitalization (need for high-speed samplers and improved processing capability), Doppler shifts from targets will be apparently shorter in range.
- **Decreasing** f_b: Reduces the bandwidth requirements for range-bin filters, improves conditions for PN-noise correlation (reduction) at the Rx mixer, lowers the requirements for digitalization and processing hardware.

In relation to practical beat frequency setting could the following method be used. However is it always important to note that each different FMCW radar design and application would be mostly limited by the systems non-changeable requirements, in respect to sensing range, resolution, hardware limitations and requirements of detectability. The FMCW system will also be overall limited by the radar equation, but also in respect to maximal possible radar range for detection. Moreover must also the parameters be considered in relation to costumers wanted performance. Nevertheless will all practical implementations yield trade-offs to some extent.

1. Basic parameters:

Initially the basic static beat frequency equation identify the tweakable parameters as chirp bandwidth Δf and chirp sweep time t_0.

$$f_b = \frac{\Delta f}{t_0}\frac{2R}{c}$$

For most FMCW application, would however Δf be less tweakable since the best *range resolution* is always desirable. Hence will Δf be maximized within the allocated bandwidth, regulated by for instance the stringent *ITU/ETSI* requirements, both in respect to power within allocated band and adjacent channels. However must the Δf maximation be considered in relation to chirp non-linearity. Never the less does this leave t_0 as the most tweakable parameter for beat frequency setting, although also constrained by system hardware capabilities.

2. Ranging systems:

When the radar is desired to sense static targets within a region of R_{min} and R_{max}, the first step is check if R_{max} is obtainable in respect to the radar equation.

f_b vs R_{min}:
If so, the the lowest beat frequency must be considered in relation to R_{min} and the intersection between 1/f noise and the noise floor observed in the beat spectrum. Hence to insure detectability for close targets. Additionally must also the radars response near clutter C_n be taken into account, which can be even more limiting to the minimal observable range and must hence be removed by high pass filtering. Thus need $\frac{\Delta f}{t_0}$ to match R_{min} so $f_{b,min} \geq f_{inter}$ or $f_{b,min} \geq C_n$, seen in figure 2.19.

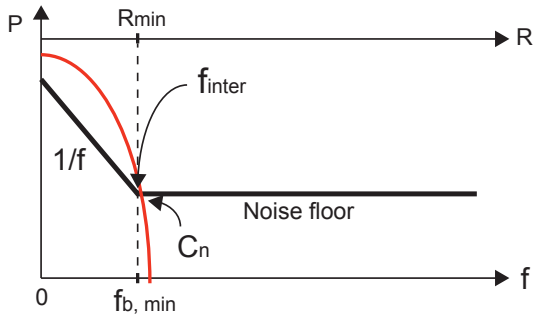

Figure 2.19.: Beat frequency setting in relation to sensitivity at minimum range

f_b vs R_{max}:
In the other end of the desired beat frequency spectrum, will $f_{b,\,max}$ be limited to the DAS capability and the Nyquist requirement. Hence in respect to obtainable f_s, $NFFT$ and the processing capability of effective data-rate. First must the following inequality always be for filled to satisfy Nyquist

$$f_s \geq 2 \cdot f_{b,\,max}$$

which can be expressed in relation to R_{max} as

$$f_s \geq 2 \cdot \left(\frac{\Delta f}{t_0} \frac{2\, R_{max}}{c} \right)$$

Thus must there be a weighting between f_s, chirp rate and the resulting $f_{b,\,min}$. However note that the sampling frequency could be lowered by the use of Quadrature detection, yielding ($f_s \geq f_{b,\,max}$), thus reducing the requirements for the DAS. In addition must also the chirp sweep period or modulation period (t_m), be seen in relation to the NFFT and sampling frequency, which dependently of the NFFT agility will influence the receivers range resolution.

$$NFFT = f_s \cdot t_0 \geq \frac{4\,\Delta f\; R_{max}}{c}$$

However constrains in one end of spectrum will change the other, so the best trade-off needs to be chosen. The above relations also illustrates that a well designed system with FM noise cancellation would be beneficial to increase the low frequency sensitivity to reduce the demands for the DAS system and reduced costs of full scale radar implementation. Note also that designs using BPF after downconversion need to match the filter to

the wanted region interest.

3. Range/Doppler systems:

The above relations would still yield for combined range-Doppler FMCW radars, but the added $\pm f_{d,\,max}$ for suspected Doppler targets of interest, increases the spectrum of interest in both ends. Either must the obtainable beat spectrum be accepted to be wider or must the static beat frequency region be sufficiently reduced in relation to range observability. This relation could hence be estimated by the expanded beat frequency equation.

$$f_b = \frac{\Delta f}{t_0}\frac{2R}{c} \pm f_{d,\,max}$$

Further must this equation then be interchanged with the static beat frequency relation in the equations of case 2. However does the induced limitations to the beat frequency spectrum caused by Doppler sensing, in many cases yield the need for other FMCW waveforms (section 2.2). While the pure chirp or the triangular waveform will detect Doppler by the linear offset from static beat frequency, FMCW waveforms with hold periods can sense speeding targets as a pure frequency outputs proportional to the radial velocity and carrier frequency. Hence will decision of waveform also be a part of this evaluation.

4. HRR systems:

The last consideration for the desirable beat frequency region, will be in respect to the range resolution or high range resolution systems (HRR). As derived in section 2.5.3, the convolved range resolution is given as

$$\Delta R_{conv} = \frac{R}{f_b}\sqrt{\Delta f_{tar}^2 + \Delta f_{rec}^2}$$

This relation show that the beat frequency in respect to range resolution needs to be set as high as possible and hence impose more demands to higher sampling frequency and the DAS performance. By increasing the sampling frequency this will additionally add a demand for a longer NFFT, in the Δf_{rec} term. If the nonlinearities of chirp are fixed, affected in Δf_{tar}, the equation would yield a never ending story of resolution demand and receiver complexity. Hence must the range resolution for HHR FMCW systems be specified for a wanted range resolution at a specific range, and weight up against the maximum affordable DAS system. Additionally must the setting of range resolution for a specific range be considered against the resulting reduction of effective bandwidth imposed by the relation between τ and t_0. The cases from 1 to 4 show the complexity of setting the right parameters for the best suited beat frequency spectrum. It is however obvious that the most desirable properties and hardware constraints needs to be identified early in the design process to tune the above parameters for best trade-off.

3. Circuit Design

This chapter presents the signal sources design and the radar system which it is fitted for. The fundamentals of DDS- and PLL-circuits, which is the two main components of the signal source, can be further reviewed in appendix A.11 and A.12. The specific circuit DDS and PLL components are described by application in chapter 6, but can be moreover examined in [10] and [9]. Estimates of spur levels and noise considerations have been completed by the radar designer, and can be examined in [5] and [7]. However are these topics threated by practical measurements and discussions, in the next chapters of the thesis.

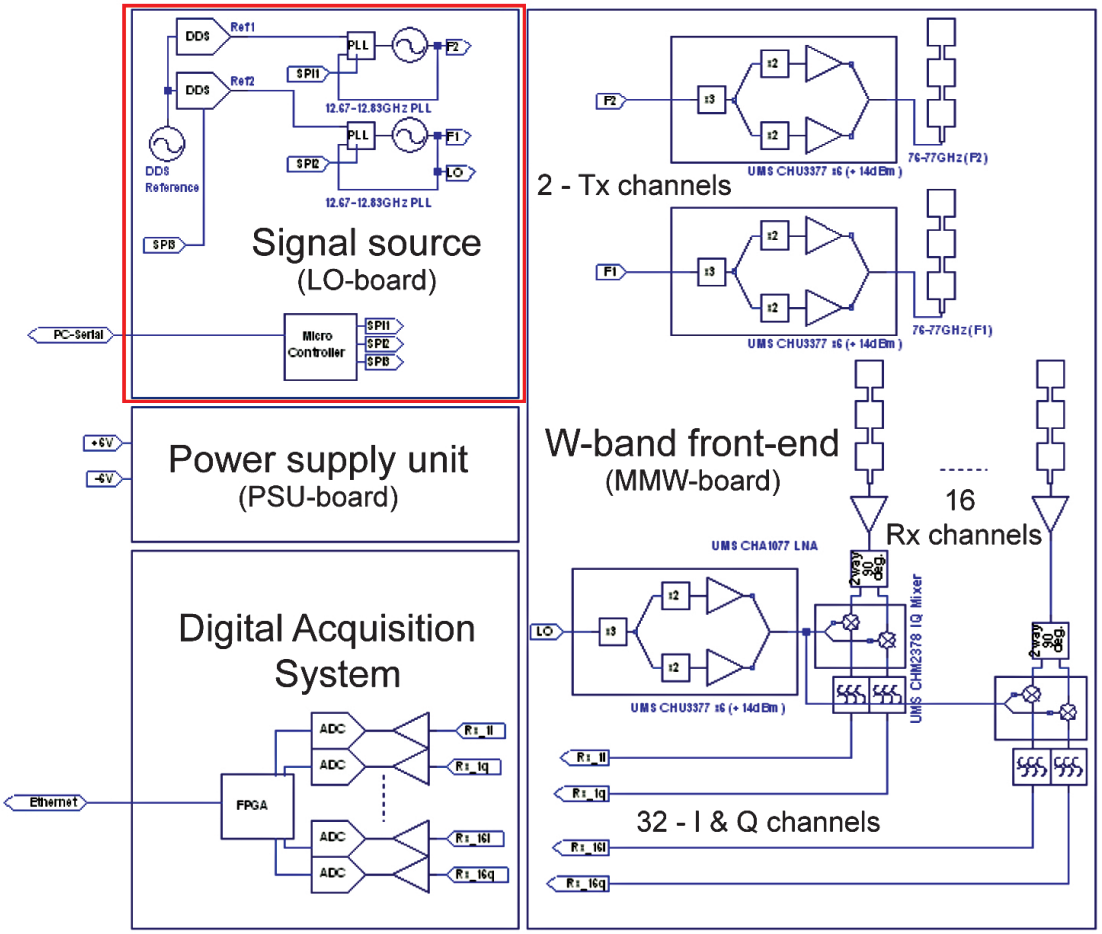

Figure 3.1.: General design concept of the experimental NORBIT FMCW W-band radar

Today many FMCW systems use direct digital synthesizers as main part of their signal source to generate high resolution and prescition FM signals under digital control. This

approach is preferable because of the synthesizers ability to yield highly stabil signals, agility in modulation and thus high linear frequency sweeps. However, today are no DDS capable of producing high frequency outputs directly to the typical radar bands (>X-band). Therefore must for instance linear frequency chirps be generated at lower frequencies and therefrom be up-converterted to the desired frequency band by mixing, frequency multiplication or PLL-frequency synthesis. The radar threated in this thesis, are designed to achieve a W-band (77 GHz) output at radar front-end by using a combination of low frequency DDS signal generation, PLL-synthesis and frequency multiplication.

The NORBIT FMCW 77 GHz experimental radar consist of four main parts, shown in figure 3.1. The signal source, which the is marked in *red*, provides a 12 GHz (X/Ku-band) signal to the rest of the circuit achieved by *direct conversion*. In all are two separate signal channels implemented to enable both automotive radar and harmonic radar features. The signal source, which from now on will be named *the LO-board*, are basicly controlled via a microcontroller which, again sets appropriate register values and timing to the fundamental DDS and its two supplementive PLL circuits. To achieve full W-band capability does the MMIC millimeter-wave front-end, named *MMW-board*, use frequency multipliers in combination with power amplifiers, which is further feed to two seperat transmitting antennas. Similarly are individual coherent LO-feeds applied to the MMW-board form each LO-board output channel. At the MMW-board are these feed to 16 individual quadrature Rx mixers, hence with supplementive frequency multipliers, PAs and feeding network. The radar utilizes the bistatic radar scheme, to achieve sufficient Tx-Rx isolation. Complete should the radar use two separate wide-azimuth Tx-antennas, two meet the dual radar features. At the receiver part are a 16 x 4 array antenna implemented, with 16 individual channels with each 4-element patch antennas. The signal received at each Rx channel is then feed to a 90° hybrid which splits the signal in to quadrature components. Form there on does a dual W-band mixer, down-converted the quadrature signal to base band (homodyn) with the coherent signal from the LO-board. In all are 32 channel utilized through the MMW-board, which has to be equally sampled in an not yet implemented DAS. Additionally does a power supply unit (PSU), supply the total circuit with sufficient power at the desired timing [5].

With the configuration shown in figure 3.1 can hence can both accurate angle measurements and synthetic Rx antenna beams be utilized in software. Since the radar use direct conversion with the combined DDS/PLL-synthesis will there additionally be no need for image-reject mixing or typical filtering of DDS/LO-image products. However are there a trade off to the benefits of this design scheme. Typically does the use of a PLL as a high order frequency multiplicatorin in combination with a DDS give more contribution to the overall phase noise. Along with the use of frequency multipliers at MMW bord is there an increased change of reduction of the radars low beat spectrum sensitivity. However as explained in section 2.6, should a matched bistatic noise leakage provide sufficient phase noise cancellation and minimized reduction of radar sensitivity, due to the PN correlation between the LO-feed and leakage. Further explanation of the design and the radar specifications can be reviewed in the radar documentation [7], [5] and [6].

3.1. LO-board

Figure 3.2 show the conceptual design of the LO-board with its main components, which will be the main focus of this thesis.

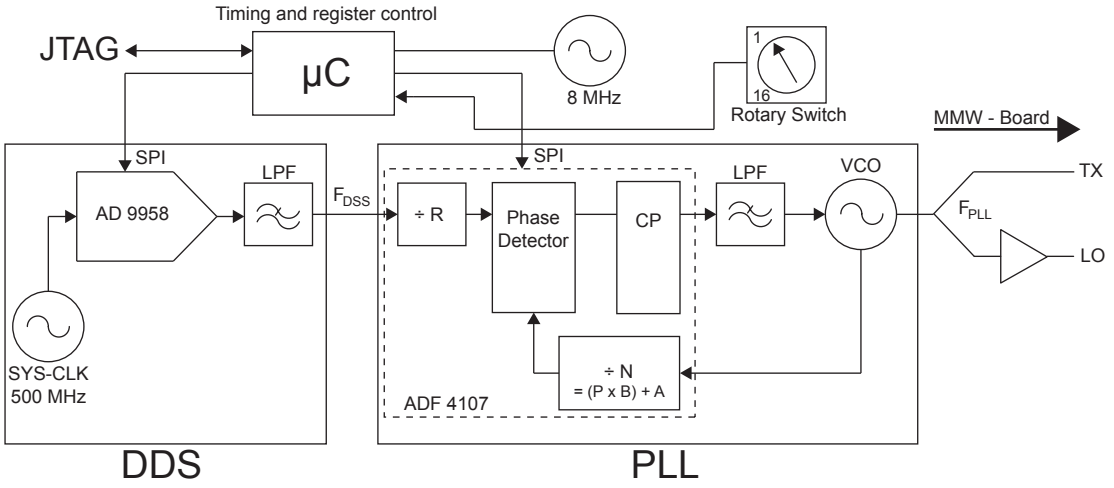

Figure 3.2.: Basic concept of operation with DDS, PLL and VCO on the LO-board

The signal source consist of one DDS (AD9958) which provides the fundamental frequency reference to the PLL-circuits, which is only shown as a single output channel configuration in figure 3.2. By the use of a 500 MHz oscillator as system main clock, can the DDS produce high quality signals beneath 125 MHz without comprimizing the output signal quality to increased spur output levels and excessive signal jitter [21]. The output of the DDS is hence further low pass filtered to smooth the staircase DAC signal output of the integrated DDS. With use of the DDS signal as reference and modulator, will the total PLL circuit function as a effective frequency multiplicator form DDS output to VCO output. This PLL is realized with an Analog Devices integrated circuit (ADF 4107), which yield functionality to create a integer-N PLL (with an implemented dual-modulus prescaler), through a digital programmable circuit. The ADF 4107 consist of a low noise phase/frequency detector (PD), in combination with to programmable reference dividers R and N. By matching the VCO output frequency by N and the DDS reference by R, can the PLL synthesize the DDS output at VCO output. However within proportions of the PLL's frequency lock time and the overall frequency response of the PLL. The frequency tracking is in this case enable digital with the phase/ frequency detector which yield the frequency error at output to the charge pump (CP). Defined by the VCO reference and PLL register setting would thus the CP give the desired discrete output as a correction current by its voltage sequential which is given by the PFD [3]. Further is then the correction error current filtered through a loop filter that is matched to the desired PLL frequency response. Inevitably must also this voltage match the VCO input, which in this design had to be achieved width an active filter. In addition did the VCO (12 GHz) in the current design yield an extra x2 multiplication to the PLL frequency reference. Which in total enables a total frequency multiplication of $\times 194$ form DDS frequency output, with appropriate PLL settings. The actual divider and additional register settings can be

reviewed in section 6.1 and the radar reference, technical note [34]. With an approximate DDS frequency output of 66 MHz, this brings the total LO-board output frequency at 12.8 GHz in Ku-band. By additional $\times 6$ multiplication performed in the MMW-board, the desired W-band is reached at 76.8 GHz. From the output of the VCO the signal is further divided by a Wilkinson power divider, which splits the signal in an amplified LO reference and a Tx output whci is matched to the MMW-board circuits. The specific power levels and additional circuits are not presented here, but can be reviewed in the radar documentation [5],[6],[7]and [34] or the design layouts provided by NORBIT.

Both the DDS and PLL can be controlled by the standard SPI serial programming interface to set timing and fuctionallity. However does the LO-board design enable control of both digital circuits through a microcontroller which accesses the SPI interface. With use of the microcontroller is hence the overall timing and register settings controlled by its on-board flash memory. The μC operates on an additional 8 MHz clock. A JTAG interface is hence used to access and reprogram the microcontroller. In this way all modulation and frequency word setting to the DDS controlled in this way. Hence also the timing of the modulation period (DDS profile pin) which is set by the μC in respect to its clock reference. Further programming of circuit to achieve FMCW modulation is explained in section 6.1 and appendix C.1. In addition to the control of DDS/PLL registers and timing through JTAG accessed programming, does the source code of the microcontroller enable control of DDS output through a mechanical 16-position rotary switch. Though a set of preprogrammed case-based DDS settings assigned to each switch position can different DDS settings be accessed through the switch.

Figure 3.3 show the real circuit, with identification of the fundamental components.

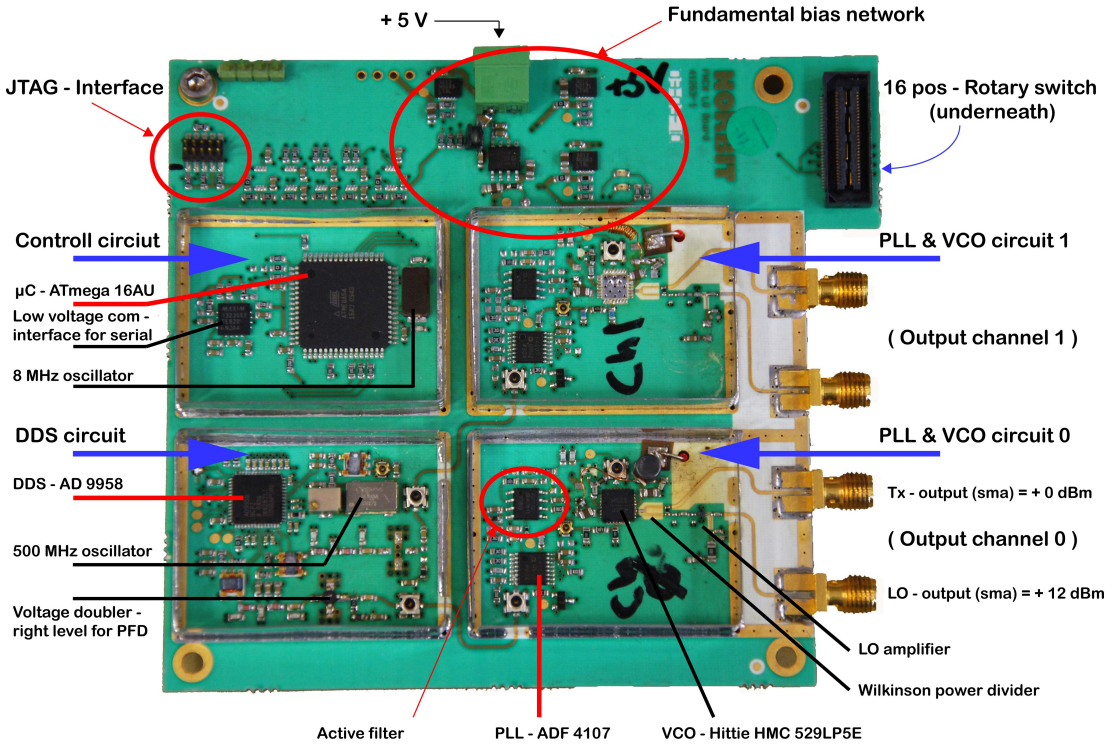

Figure 3.3.: Overview of the LO-board

Theoretically the combined DDS/PLL signal source should have improved chirp linearity compared to the isolated conversion schemes or older FMCW waveform synthesis methods, but increased phase noise as documented by [20] and [44]. However according to Stove [42], should most of the phase noise be correlated in the receive mixer due to the FMCW leakage problem, thereby in fact reducing the phase noise if the LO signal way equals the leakage signal way to mixer. In theory should this signal source be very beneficial for a FMCW test radar both in performance and waveform agility. Nevertheless should the quality parameters for the LO-board be further examined to fully understand its capability.

4. Initial Circuit Performance

The first step in the development process of the LO-board was to test the initial circuit performance, in order to validate the manufactors product delivery and foresee potential problems with the current design implementation. These measurements were also conducted to make a fundament for the further development of circuit/waveform test methods. The preprogrammed CW and LFM-waveform, were therefore to be tested for their spectral purity and output power achievements. Additionally were also the phase noise of the CW output to be measured. Hence to compared its real PN performance to the radar documentation, since this property can be vital for FMCW radar implementations. All these initial measurements were to be performed with an available spectrum analyzer, that had an additional application for phase noise measurements. The original design of the LO-board supports two channel transmission, for conducting both measurements as an automotive radar and a harmonic radar. However were only one channel to be tested, for its fundamental properties in this thesis. Since they both are equal circuits with the same signal performance and capability.

It was initially identified that further measurement methods had to be derived after the initial testing, in order to obtain more FMCW parameters form the desired LFM waveform. Thus were some desirable properties listed for the further investigation of the reference waveform. The desired properties were: The combined time/frequency plot of the waveform, a waveform chirp linearity characterization and the resulting beat frequency of the waveform. Available equipment were then to be obtained and matched as best suited to the purpose, in accordance with the finds in this chapter. The real implementation of the methods and measurements are hence shown in chapter 5, which were conducted after this initial part.

Thus were the general idea of chapter 4 and 5 to do testing of the delivered circuit in respect to the designed specifications, frequency spectrum properties and time-frequency properties, before any own programming of the circuit were to be executed. This was done to see the real outputs of the device, compared with the programming code and consequently reveal possible mismatches. Hence would this approach minimize the risk of erroneous programming and reduced de-bugging time, compared to a direct approach were the delivered circuit and theory could be taken for granted.

4.1. Initial Testing

In order to verify manufactures documentation and prepare for further development of the circuit, were initial measurements in chapter 4 and 5 done with the following equipment

- **Oscilloscope**: *Agilent*, MSO 9254A, 20 GSa/s, 2.5 GHz analog bandwidth.
- **Spectrum Analyzer**: *Rohde & Schwarz*, FSQ 40, (20Hz - 40GHz).
- **Power Supply**: *TTi*, EL302Tv.
- **Signal Generator**: *Hewlett & Packard*, HP 8672 A, (2 - 18 GHz).
- **Vector Signal Generator**: *Rohde & Schwarz*, VSG SMUA, (200 Hz - 6 GHz).
- **X/Ku-Band Mixer**: *RHG*, Doubled Balanced Mixer, mod DM1-18, (1 - 18 GHz).
- **Attenuator**: *Pasternack*, PE 7013, 10dB, 5W, (DC-18 GHz).
- **Power Amplifier**: *Microwave dB*, G=39dB, NF=5.5dB, P1=17dBm, (0.5-18 GHz).
- **Coaxial Waveguide**: *Huber & Suhner*, Sucoflex 104P, SMA (< 26.5 GHz).
- **Laptop**: *HP*, Elitebook 8540w, 8GB RAM, Intel i7 620M.
- **Software & Connectivity Drivers**: MATLAB®, IVI Agilent Infiniium driver, Agilent IO Libraries Suite 16.

4.1.1. Bias properties

To bias the LO-circuit board, were a single $+5V$ voltage applied. All additional voltage transformation were hence enable within the circuit, with distributed voltage regulators. However did the first start-up of the circuit resulted in an component burn-out. Possible sources of error were therefore tested. Since the initial start-up had been tested in an anti-static-environment lab with EMC precaution, were the possibility of an electro-static discharge, ruled out as a plausible source of error. Thus were measurements of grounding potentials between the PSU and the test instruments conducted with an DVOM. The measurements showed only small deviations in resistance, within the range of $3\ \Omega$,hence not sufficient to create great potential differences that could burn the circuit components. The most likely source of error seemed therefore to be high power transients from the PSU. Hence since the PSU power-to-circuit switch had been used. An oscilloscope test of the power-up of the curicuit by switching, showed however no significant overshoot of voltage. Nevertheless was this source seen as the most plausible cause of error. Therefore were the further circuit power-ups performed manually, by inserting the bias-cables in and out of the device, after PSU power-up. Hence to minimize the potential risk.

4.1.2. Output Power and Spectrum Properties

The output power from the supplied LO-board were measured for validation, before any own changes were made to the programming of the circuit. A midband CW frequency of 65.75 MHz had been preprogrammed by NORBIT to the DDS. The DDS output is theoretically further $\times 196$ frequency multiplied by the PLL circuit. Resultingly should the theoretical output thus yield 12.7497 GHz. Consecuently would the theoretical output of the operational radar at W-band further yield 76.498 GHz which would be the midband value, of the $76 - 77$ GHz automotive frequency band.

Tx-port CW Power Spectrum

First was the power spectrum of the Tx output-port measured with the *FSQ 40* spectrum analyzer.

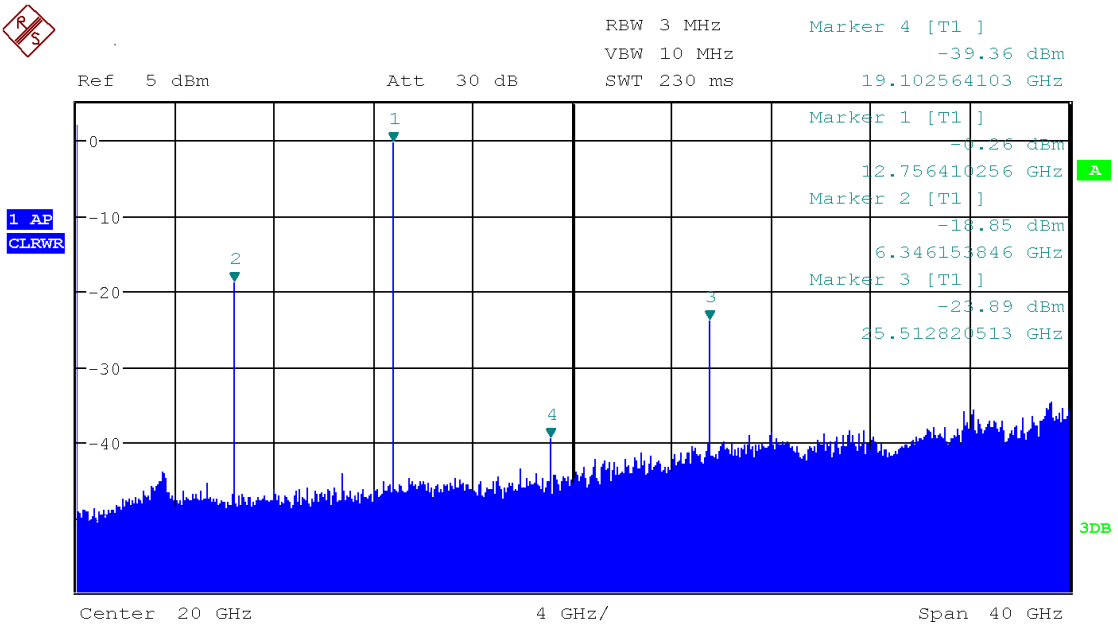

Figure 4.1.: Output power spectrum, Tx-port

Results:

Table 4.1.: Tx-port, ch 0, frequency output spectrum, $f_{cw} = 12.75$ GHz

Spectral component	Frequency	Output power
Fundamental	12.75 GHz	+0.7 dBm
2nd harmonic	25.52 GHz	-24.0 dBm
PLL-VCO-leakage	6.35 GHz	-18.7 dBm
Image frequency	19.10GHz	-39.9 dBm

Observations:
Figure 4.1 shows the fundamental frequency at 12.75 GHz and $-0.26dBm$, indicating a $+\mathbf{0.7dBm}$ on-circuit maximum output, with connector and cable loss added ($0.96dB$). Consequently showed the measurements good similarity between theoretical and measured fundamental harmonic in frequency, but a $3dB$ reduction in power, compared to the design specification [6, p.6]. Further did the spectrum reveal the PLL-through-VCO leakage at 6.35 GHz or one half of the fundamental frequency, with $-18.71dBm$ power. In addition did the 2nd harmonic appear at 25.52 GHz with $-24dBm$. The significant power levels from the other components did also combines in an IM product of ($f_{1st} + f_{leak}$) and ($f_{2nd} - f_{leak}$), at 19.10 GHz and $-39.90dBm$.

In respect to spectral purity, showed the measured output, great separation between the four observed components, none within the range of generating image components within the fundamental bandwidth in an FMCW operation. However were the 2nd harmonic and PLL-VCO-leakage components big enough to create confusion, if they sweep frequency of respectively 2 GHz and 500 MHz. If these component are later propagated through the output circuit, antenna or LO feed, could they be correlated in the mixer and synthesis beat frequencies, within the desired beat frequency region of the fundamental frequency. Hence creating false targets (ghosts). It is therefore important that the multipliers, amplifiers and antenna of the MMW-board have characteristics that suppress these out-of-band components.

Additionally did the initial test of circuit also revealed a start-up frequency error. Thus locking the CW-signal to 13.2 GHz and not at the desired 12.75 GHz. Therefore had repeated boot-ups of circuit, to be performed before the CW-signal could be locked to the preprogrammed one. No explanation to the cause of error were revealed during the LO-board test or by the correspondace with the design engineer at NORBIT. However did the nature of the circuit imply that the error was originating form the DDS-start-up, since the error gave a constant CW output. Thus excluding that the PLL locked to any start-up-spurs from the DDS.

LO-port CW Power Spectrum

Secondly was the spectrum of the LO port investigated.

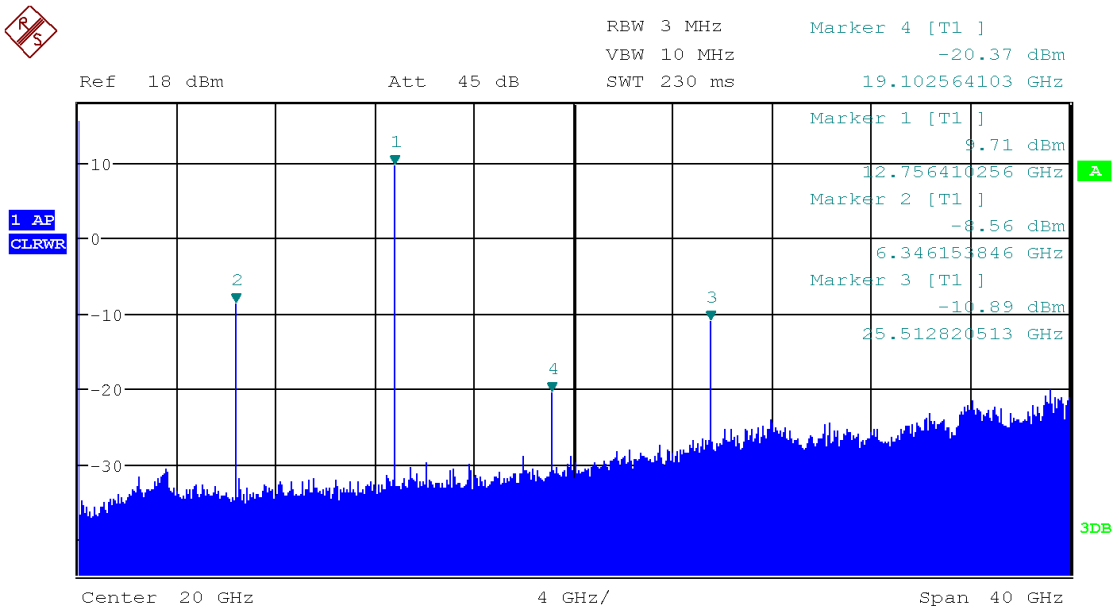

Figure 4.2.: Output power spectrum, LO-port

Results:

Table 4.2.: LO-port, ch 0, frequency output spectrum, $f_{cw} = 12.75$ GHz

Spectral component	Frequency	Output power
Fundamental	12.75 GHz	+10.7 dBm
2nd harmonic	25.52 GHz	-9.9 dBm
PLL-VCO-leakage	6.35 GHz	-7.6 dBm
Image frequency	19.10GHz	-19.4 dBm

Observations:
In figure 4.2 is it shown that the fundamental component was measured to $+\mathbf{10.7dBm}$. With reference to the output-port at Tx, did the fundamental frequency experienced an approximate gain of $+10dBm$ $(10.7dBm - (+0.7dBm) = +10dB)$. The real gain was however assumed to be a bit lower, since the signal at the input of the amplifier is always higher than the output of the connector. Hence due to the strip-line feeding loss. Similar to the fundamental frequency did, the noise floor, the 2nd harmonic and the vco leakage experienced almost the same gain. However did the image component, growed at a bigger rate. A gain of approximately $+19dB$ were measured. This were most likely caused by

dual the inherited power from the two image sources as indicated earlier, through the active amplifying circuit at this port. Nevertheless was this component still significatlly lower than the 2nd harmonic and PLL-VCO leakage.

LO-port FMCW Power Spectrum

After studying the circuit at mid-band CW frequency, was the module switched to FMCW mode and measured with the spectrum analyzer. The subject of investigation was a hard programmed waveform implemented by NORBIT. Hence given in table 4.1.2. The parameters were derived from the DDS programmed values supplied by Norbit and up-converted to the VCO output, by the PLL $\times 97$- and VCO $\times 2$ frequency multiplication. This part will hence present the waveform of interest, in relation to estimated theoretical waveform parameters, derived form the radar documentation [34]. Additionally will some basic quality parameter be given to yield as reference to further measurements of the waveform.

Preprogrammed Waveform:

Table 4.3.: Hard programmed NORBIT waveform at LO-board output [34]

FMCW type:	Triangular *Hold at chirp start and stop* *Symmetric up and down*
α	4.72 MHz /ms
Δf	188.762 MHz
f_{start}	12.666 MHz
f_{stop}	12.855 MHz
f_m	10 Hz
t_0	40 ms
t_{hold}	10 ms
t_m	50 ms

The theoretical signal would then without non-linearities, yield the quality parameters for static targets shown in figure 4.1.2. The table show the initial and degraded parameters for a theoretical radar implementation at Ku-band (Lo-board directly) and W-band (frequency multiplied to 77GHz). The maximal range were set to typical maximal automotive sensing distance(150m), assuming that the overall radar design provides sufficient SNR for detection at maximal distance, in relation to the radar equation. The signal was assumed processed over the modulation interval of 50ms, taking advantage of the hold periods as Doppler extractor. In relation to the $\mathbf{\Delta R_{eff}}$ would the theoretical waveform not suffer much loss in effective bandwidth, since the signal for filled the *Piper*, rule-of-thumb: $t_0 \geq 5 \times (\tau + t_{sr})$, where t_{sr} is the hold period. Thus would only 20% of the total bandwidth be lost. Likewise did the degradation of range resolution due

Table 4.4.: Theoretical properties of FMCW radar with NORBIT preprogrammed waveform

Parameters	**Ku-band** LO-board output	**W-band** MMW-board output
Initial theoretical parameters		
Δf	188.762 MHz	1.134 GHz
$\mathbf{\Delta R}$	**0.795 m**	**0.132 m**
t_0	40 ms	40 ms
t_{sr}	10 ms	10 ms
R_{max}	150 m	150 m
τ_{max}	1 μs	1 μs
$f_{b,\,max}$	4.72 kHz	28.35 kHz
$f_{s,\,min}$	9.44 kHz	56.70 kHz
N_{FFT}	512 (377)	4096 (2268)
$f_{s,\,opt}$	12.8 kHz	102.4 kHz
Initial theoretical parameters in relation to Δf_{conv} and R_{max}		
Δf_{rec}	25 Hz	25 Hz
Δf_{tar}	33.3 Hz	33.3 Hz
Δf_{conv}	41.6 Hz	41.6 Hz
$\mathbf{\Delta R_{conv}}$	**1.32 m**	**0.22 m**
Initial theoretical parameters in relation to Δf_{eff} and R_{max}		
Δf_{eff}	125.7 MHz	755.2 MHz
$\mathbf{\Delta R_{eff}}$	**1.19 m**	**0.2 m**

to $\mathbf{\Delta R_{conv}}$ not affect the performance much at maximum range. Thus could it be said that the corrected theoretical range resolution at MMW-band implementation would be **0.22 m** and yield sufficient range resolution at maximal range with the preprogramed waveform, if no nonlinearities take effect.

Another approach to processing the waveform could have been in relation to the up- and down-chirp period, thus yield a modulation period of 100ms. This would then be beneficial to direct extraction of Doppler to both hold-period and the difference in $f_b(up)$ an $f_b(down)$, minimizing the complexity of Doppler-extraction. However would the increase of t_m, decrease the processing time by an increase of $NFFT = t_m \times f_s$. Hence would this scheme not be preferable. Likewise could also the signal be segmented synchronized-sampled over just the chirp sweep, for primarily range extraction. However would it then be not suited for Doppler targets applications like automotive sensing. If the hold periods had been equal to the chirp period, could the signal be processed over the chirp sweep-time and hence both manage range and Doppler extraction. Nevertheless would the beat frequency output in this case be more pulsed. Thus yielding low detectability in range and reducing the overall reaction time of the radar sensor, in relation to tracking between range points. In order to compare the derived parameters the spectral properties and waveform appearance had to be closer examined both initially here in respect to frequency validity, but also in chapter 5 to reveal the modulation timing.

Results:
The *FSQ 40* spectrum analyzer, did however not sample as quickly as required, to capture the full bandwidth FMCW waveform. Therefore were an approximate measurement of the waveform conducted using the *max-hold* function of the spectrum analyzer, thus to visualize it and avoid the sampled nature of the analyzer. This function holds the maximal value during the measurement, thereby yielding an possible overestimate of average power. However should the distribution of power over the bandwidth and the power-gain tendency give an indication to the waveform properties in spectrum.

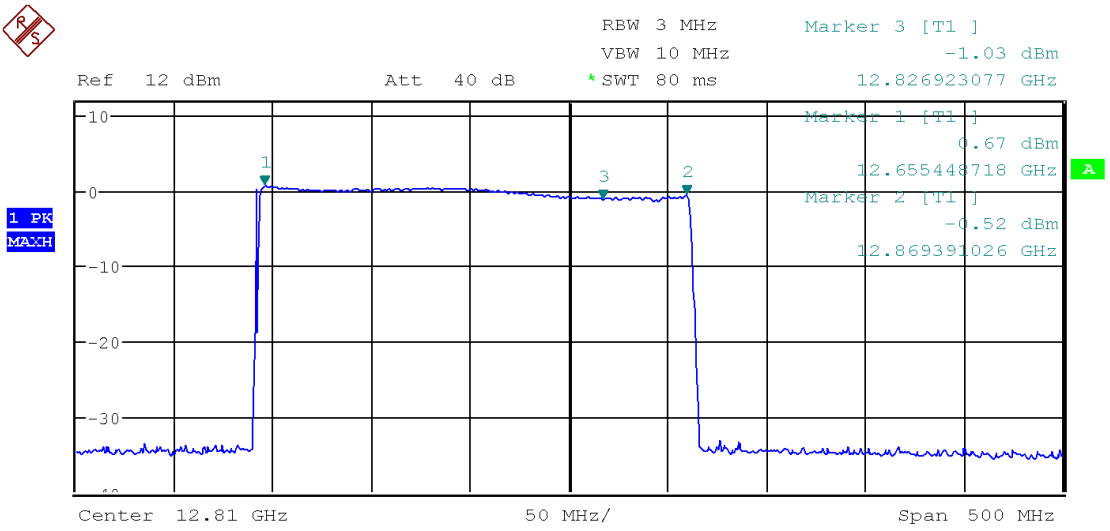

Figure 4.3.: Output waveform spectrum of triangular frequency sweep

Observations:
Figure 4.3 shows the measured spectrum with the max-hold function. The figure indicate a minimum-to-maximum waveform-ripple of $\mathbf{0.5dB}$. In addition was the bandwidth measured to be $\mathbf{213.94\ MHz}$, which is $\mathbf{25.18\ MHz}$ wider than the theoretical value. Since the waveform was so squared with reasonably low ripple, did it indicate that the waveform was probably a genuine capture. The mid-band CW measurement did also support this assumption. Hence showing no close image frequencies that could make an overlapping spectrum at the current FMCW bandwidth. Consecuently was the widening most likely to originating from an frequency drift over the long measurement period. These observation pointed towards a slow varying system instability. Therefore was an additional stability test of the CW mid-band frequency conducted to reveal its nature.

The stability test were conducted with the spectrum analyzer, set to max-hold peak detection for an hours duration. However did the test only reveal a small drift (<1.5 kHz) in the CW waveform. Thus indicating that the waveform only had large drifts in FMCW mode. Notably should the stability test have been conducted with an high analog bandwidth oscilloscope, however not available.

Normally does slow frequency drifts not imply big range errors in FMCW radars, since they synthesis the range from the bandwidth, independently of carrier frequency. This theory holds as long as the waveforms at Rx and LO are approximately equal in frequency

($f_r \approx f_0$), form ($Slope/linearity$) and delay as shown in A.13, 2.5.2 and 2.5.1. Sporadic frequency changes that mismatches the Rx and LO waveform, will however result in a shift in beat frequency depending of the degree of frequency shift between the two.

$$f_b = \alpha\frac{2R}{c} + (f_0 - f_{rx})$$

Nevertheless will this error will also be highly dependent of the nature of the drift over the signal round-trip-time. Note that this imperfection will yield a uncertainty to the true beat frequency, but not the effective processing bandwidth and hence the resolution. However can the combination of this error and receive-reference processing delay be devestaiting for high density target extraction. Thus dependent of the drift between the reference and received waveform, will the difference give the degree of correlated mismatch over the full bandwidth and sweep time. Depending of the degree of errorous radar range performance, either waveform synchronization and/or system stability precautions need to be taken care of.

But how does such a beat frequency error, affect the carrier dependent Doppler-response? It is apparent that big differences between reference and received start frequency, will complicate Doppler extraction, since an uncertainty have been added to f_b. However it will depend on which type of waveform is used and how the Doppler information is extracted. For single chirps or triangular extraction, will the bias error, certainly add an uncertainty to the Doppler estimate. On the other hand, if an hold CW is part of the waveform is used for extraction. Therefore does moderate changes in the carrier frequency, $< 1\,\mathrm{GHz}$ compared to W-band carrier, not complicate the estimation of Doppler targets. Hence because a changing carrier frequency within this limit, will give rise to small missinterpetations of real automotive target velocity. For instance a car at $80\,\mathrm{km/h}$ will have a Doppler frequency of $11.544\,\mathrm{kHz}$ at $78\,\mathrm{GHz}$ if a $1\,\mathrm{GHz}$ positive frequency drift occurs from a belived frequency at $77\,\mathrm{GHz}$. When extracting the Doppler frequency from the beat frequency, will a Doppler shift of $11.544\,\mathrm{kHz}$ be observed. Hence will the estimated velocity, believing $77\,\mathrm{GHz}$, yield $83.3\,\mathrm{km/h}$. Consecuently have only an error of $3.3\,\mathrm{km/h}$ been made by a $1\,\mathrm{GHz}$ drift of frequency.
Since the initial modulated drift, were measured to $\mathbf{25.18\,MHz}$, show the above example that Doppler estimation should not impose difficulties with the current modulation, as long as the range- and frequency resolution, and the bias error are within proper limits.

However for further investigation of this error and the not revealed waveforms time-dependence, need the waveform to be studied in the combined time-frequency domain and processed further to beat frequency domain. Hence to see if the frequency drift or its time-dependence impose any threat to the radar application.

4.1.3. Circuit Phase Noise

Since FMCW system performance is highly limited by the level of circuit phase noise and how the system suppress it, was the output phase noise from the Tx-port mid-band carrier, measured with the *FSQ 40* spectrum analyzer. Additionally were this measurement conducted to yield reference for future PN studies.

Results:

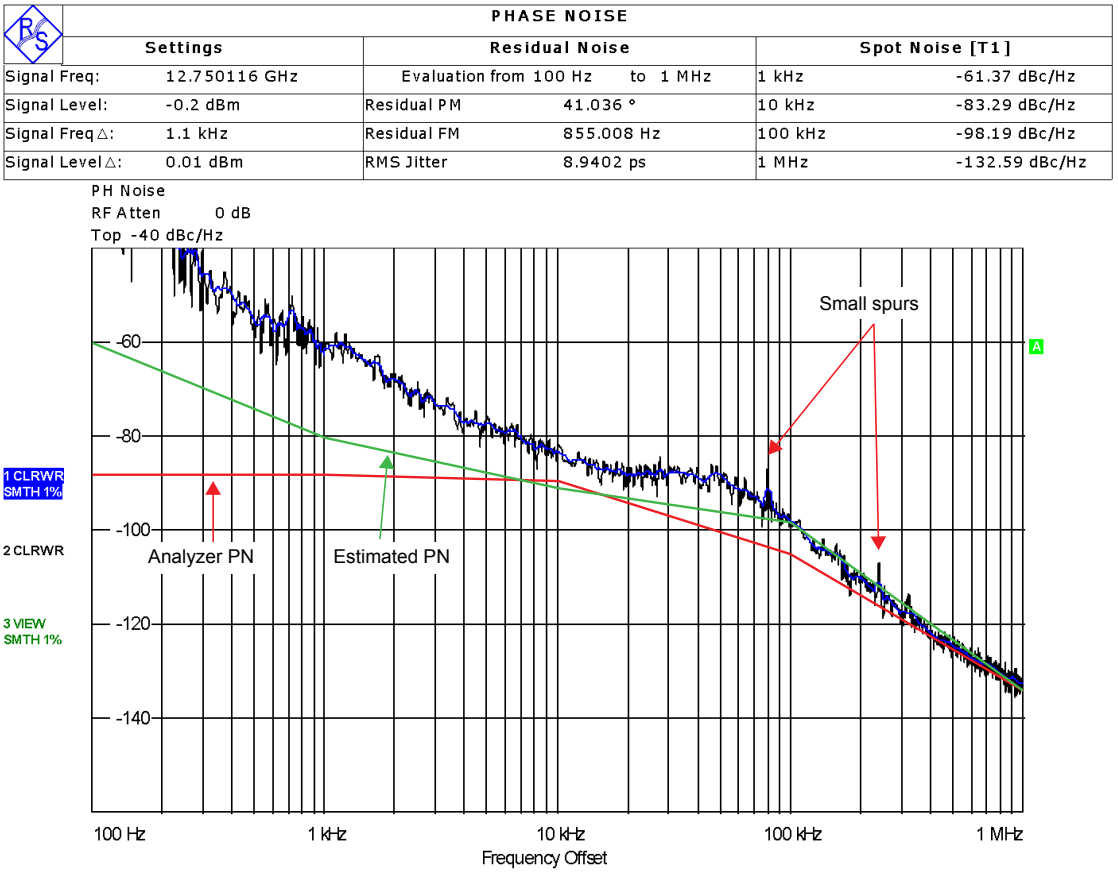

Figure 4.4.: Phase noise measurement of $12.75\ \mathrm{GHz}$ CW output

Table 4.5.: Phase noise measurement vs theoretical estimate, $f_{cw} = 12.75\ \mathrm{GHz}$

Offset	Estimate (PLL) [dBc/Hz]	Corrected (VCO) [dBc/Hz]	Measured [dBc/Hz]	Deviation [dBc/Hz]
100 Hz	-66.44	-60.46	-40	20.46
1 kHz	-86.63	-80.65	-61.37	19.28
10 kHz	-98.16	-92.18	-83.29	8.89
100 kHz	-103.6	-97.62	-98.19	-0.57
1 MHz	-139.4	-133.42	-132.59	0.83

Observations:
Figure 4.4 show the PN result of the measurement, with resulting PN levels at offset 100Hz,1 kHz, 10 kHz, 100 kHz and 1 MHz. Note that the measured $S(f)_{RF}$ will be the sum of both amplitude- and phase noise. However since the AM noise are normally small compared to the phase noise $\mathcal{L}(f)$, thus making the measurement still valid in most applications.

To investigate the circuit phase noise, was firstly a measurement of the self induced analyzer phase noise performed (indicated in red). In comparison does the figure indicates how the circuit-PN was predominant from frequencies belove 100 kHz. Compared to the analyzer noise the measurement also reveled two small spurs at 80 kHz and 220 kHz. The spur levels was however small, but in a mismatched down-converted spectrum, would these spurs still be within the typical detection range of the beat frequency. Note also the high level of RMS jitter and Residual PM in the CW signal. These high values were caused by the great PN noise variations in the 100Hz to 1kHz region, close to the center frequency. When evaluated belove 1kHz, the values reduced to correspondingly 0.354 ps and 1.6 degrees.

Compared to the design considerations in [5, p.39], where the DDS reference had been set to 66 MHz (equivalent 12.804 GHz IF band), did the phase noise of low frequency offsets belove 100 kHz prove to be underestimated, as indicated in table 4.1.3 and the figure (indicated in green). The table 4.1.3 shows a comparison between the measured and theoretical PN spectrum at corresponding offsets form carrier at mid-band frequency. To match the estimate and the measurement, was the PLL estimation degraded by

$$20 \cdot log_{10}(f_{output}/f_{input})$$

, but then further improved by mid-band to estimate-frequency deviation.

The design estimation was intentionally based upon that the DDS contributes mostly to low frequency PN and that the VCO and DDS phase noise is equal up to 1MHz [7, pp.13-14]. However did the table indicate that there was an unexpected contribution to the low frequency offset phase noise. Possible sources of the error could be the AM noise contribution was greater than expected, that the DDS frequency word processed more phase truncation, that the DAC quantization noise was high or that the oscillator phase noise was greater in the DDS or PLL circuit. Either way did increased PN at 1 kHz to 100kHz yield within the possible region of close target beat frequencies at down-conversion. Hence implying less sensitivity for such targets. Nevertheless when the FMCW waveform is correlated in the mixer, should a correct FMCW design however yield a great deal of correlation between the phase noise in the LO signal and the antenna leakage signal. Thus theoretically minimizing much of the observed phase noise at reception.

4.2. Initial Circuit Performance Discussion

The initial circuit performance proved in overall to be valid to the described radar documentation. In respect to CW spectral purity, did the circuit provided a minimum suppression of 18.3 dB to the closest spur component, which were the PLL-VCO leakage/spur. All discovered additional frequency components had large separation to the fundamental, with minimum separation of 6.35 GHz. Hence insuring minimal influence to the fundamental, also when the frequency was swept over the desired bandwidth at Ku-band, but also when later implemented at W-band. The fundamental power at Tx and LO port yielded correspondingly +0.7dBm and +10.7dBm, which had to be used for the design of the further waveform analysis in respect to power matching in the test setups.

The test of the FMCW waveform in spectrum, indicated a possible frequency drift of the waveform. However with the average power centered over the two hold frequencies. In addition did measurements with the max-hold trace also indicated a 0.5dB ripple over the waveform bandwidth. Hence were there some concern of the possible inflictions to the full radar implementation at W-band. Since the drifts will enhance when frequency multiplied and that the ripple would also be influenced more by the use of multipliers. Some possible effects of frequency drift were presented, with reference to the derived theory in section A.13. However was there great ambiguity to all the spectrum analyzer measurements of the FMCW parameters. Consequently since the waveform could not capture by the frequency sweep in a single run. Thus were the max-hold function used to get an approximation of the chirp in spectrum. Nevertheless did this analyzer mode also enhance spurious noise in the vicinity of the waveform. Thus was it impossible to say for certain that the appeared frequency drift, came from frequency drifts or from integrated out-of-band noise. Hence could the theoretical derived *bias-error* not be fully confirmed with this laboratory setup. Although the idea of errorous behavior is clear in the theoretical approach, would the real radar implementation, however enable the error to be minimized due to averaging over several measurement periods, although dependent of the nature of the drift between LO and Tx waveform. So it arises a unrevealed question to the performed measurements. In the initial LFM waveform measurements were it hence discovered that the used spectrum analyzer was not the best suited instrument to perform characterization of FMCW frequency quality parameters. The use of a high speed oscilloscope, to do further testing of waveform properties was then purposed as next step in the further characterization of the waveform. Additionally to the frequency spectrum property-test with the spectrum analyzer, were the performed stability test belived to suffer from the same source of error, yielding measurement accuracy. Hence should a high frequency oscilloscope instead have been used for such testing. However where such a oscilloscope not obtainable at Ku-band. Accordingly was there a great uncertainty to the measured 25 MHz frequency drift, at FMCW mode.

As a last initial test, were the phase noise of the CW mid-band frequency measured. Hence to yield as a reference to the further full radar implementation and future studies of the circuits ability to cancel phase noise at beat output. The phase noise proved to be significantly higher, than estimated in the radar documentation for offset frequency lower than 2 kHz, hence with maximal divation of 20.46 dB at 100 Hz offset. However

should this region not impose any great influence to the desired beat frequency spectrum after down-conversion, since minimal beat frequencies should be higher than 1 kHz for most applications using 1 GHz bandwidth and chirp modulation periods in order of milliseconds. Compared with the estimated PN spectrum in the NORBIT Design Note [5, p.42], showed the envelope of the descending noise figure, great resemblance in form, down to to 10 kHz offset, indicating that the noise consideration for high offsets were coherent with the estimated main PN noise sources. The region belove 10 kHz seemed to be mainly influenced by the used *Hittie* VCO, as indicated in Technical Note [7, p.12], were the PN level and slope are almost identical to the measured PN spectrum from 1 kHz to 10 kHz.

Nevertheless was the region between 1 kHz to 100 kHz identified as the critical to signal phase noise influence, yielding correspondingly $S_{RF}(f)$ from $-61.4\,dBc/Hz$ to $-98.2\,dBc/Hz$. When estimating a 77GHz output with 6 times frequency multiplication (15.5 dB) these PN levels becomes significant, correspondingly $-45.8\,dBc/Hz$ and $-82.6\,dBc/Hz$. A comparison were hence conducted to other similar designs that used combinations of DDS reference to PLL circuits like [20] and [44]. The estimated PN at 100 kHz, was seen as ,better in our circuit. However in the region from 1 kHz to 10 kHz yielded the measured circuit, significantly worse performance. Seen in figure 4.4, as the steep raising edge below 10 kHz. It was clear that the compared designs had a more flat noise region below 10 kHz, more similar to the estimated PN presented in the radar documentation [5]. Hence plotted as the green line in figure 4.4. However did the compared designs utilize fully integrated designs operated with correspondingly VCO's at 77 GHz in CMOS and SiGe architectures. Since the measured circuit was a distributed it was appropriate to assume that it would also be more noisy in respect to PN. Nevertheless should it be pointed out that NORBIT radar design have taken the transceiver Tx leakage to Rx antenna, into account. Hence imposing a beneficial scheme to cancel out much PN noise at these low frequencies. However must this property be tested when full the radar is fully implemented, to confirm validity to this assumption. In respect to the region above 100 kHz offset, could this region be seen as ideal since the PN descended appropriately and could be assumed to be mostly influenced by the receiver noise floor. Hence could the stable spur detected at 220 kHz be efficiently ignored. However in the case of the stabil small spur at 80 kHz, would it be more uncertainty to what influence this spur will have on beat frequency outputs at around this region. The noise floor were not studied in this thesis, since such measurements would only give meaning after the receiver and the full LO feed are implemented.

Furthermore had the experiment also revealed some additional problems with the *LO-board*. First the circuit had an initial component burn-out of channel 0's sensitive amplifier (voltage doubler). The test setup power supply and attached instruments were investigated for EMC properties. However where no apparent source of error found with measurements. Nevertheless were the start-up procedure altered to manual insertion of supply voltage pins to power supply, without using the power supply's power-to-circuit switch. This was done since the switch were identified as the most plausible source of error, although measurements never managed to confirm the hypothesis. After altering the prosedyre no more burn-outs occurred. Moreover did the experiments also suffered form a initial start-up error, that locked the circuit to a 13.2 GHz CW frequency. No

obvious source were identified in the experiment, but the long time stability of output indicated that the error came from the fundamental signal source, hence the DDS. Thus had the programming of the microcontroller to be reviewed in the further development to possibly de-bug the problem and to identify the problem more accurate. Nevertheless could the circuit be initialized correctly by the use of multiple boot-up's.

In this chapter was also the preprogrammed waveform presented and derived towards fundamental theoretical FMCW properties. Table 4.1.2 show that even with a non-ideal modulation period, in respect to pure range sensing, would the worst theoretical degradated range resolution yield 0.22 m at 150 m and 77GHz. This could be considered more than sufficient for the purpose of automotive radar applications with limited range. However did the estimate assume no nonlinearities in the waveform, since similar FMCW designs yield frequency errors on chirp in range of < 1MHz , which will be less than 0.1% of the desired 1 GHz chirp at W-band [15],[20],[40],[44]. By comparison should the design in theory, yield good linear properties. Hence with a combination of a low pass filtered DDS frequency sweep output, to a matched PLL circuit. Nevertheless would there be an unsertainty the further use of this waveform since such long chirp modulation would produce very low beat frequecies at short ranges. Hence had some further considerations to be made of its practical applicability. Nevertheless did the theoretical waveform presentation reveal, that the desired region between 76 - 77 GHz in the full implementation, would be exceeded. Hence had the upper frequency output from DDS 66.265 MHz, to be changed to 66.151 MHz. Hence to match a 1 GHz bandwidth at W-band, theoretically. With this property in mind and the ambiguities to the spectrum analyzer measurements, had the waveform to be further investigated before any reprogramming should be done.

5. Waveform Evaluation Methods and Waveform Measurements

In order to develop the radar signal source further, had the actual preprogrammed waveform to be confirmed. Hence to reveal if there was any mismatch between this waveform and the real output waveform, so that possible differences could be corrected. Differences discovered in this intermediate stage could be corruptive, when the waveform is further propagated through the MMW-board, with its multipliers, amplifiers and antenna. Although some waveform parameters had already been tested with the spectrum analyzer, could the FMCW characteristics in both frequency and time not be analyzed directly by this measurement instrument. Such test would then reveal the distribution of power over the waveform and possibly reveal how the linearity of the waveform were within the proper limits. Therefore were more investigations conducted, to exploring methods for obtaining frequency versus time plots and specific beat frequency quality tests for the current curicuit parameters.

Two main methods for further waveform quality studies were selected. First were the waveform to be investigated by visual inspection of the waveform spectrogram. Hence with the use of an oscilloscope as an real-time sampler, transferring the data to a laptop and analyze the spectrogram in MATLAB. Additionally in this part, were the waveform chirp linearity to be measured by extraction of spectrogram data. Secondly were the waveform to be investigated by the means of distortion of the beat frequency spectral resolution. The latter method were then be obtained by a simulated homodyn radar approach. Hence using the coherent outputs of the LO- and Tx-port and use them correspondinglly as a straight feed reference signal and a delayed feed to a down-conversion mixer. Thus making a simulated target response and a resulting beat frequency by the excessive delay of the Tx-signal path.

5.1. Obtaining Waveform Spectrogram

To capture the 12GHz FMCW waveform were there to main limiting factors. Firstly was the oscilloscope analog bandwidth limited to 2.5 GHz. Thus implying that a down conversion was needed. Secondly would the flickering noise at zero frequency corrupt the waveform. Hence setting the need for a down conversion to a new IF frequency with an appropriate zero frequency offset. As a consequence had this new IF, also to match the

maximum chirp component in accordance with the Nyquist requirement. Which again had to be set consistent with the oscilloscope sampling frequency and memory depth.

To obtain the waveform within the oscilloscope's bandwidth was the laboratory setup in figure 5.1 used. Hence with the specific components listed in the start of chapter 4.

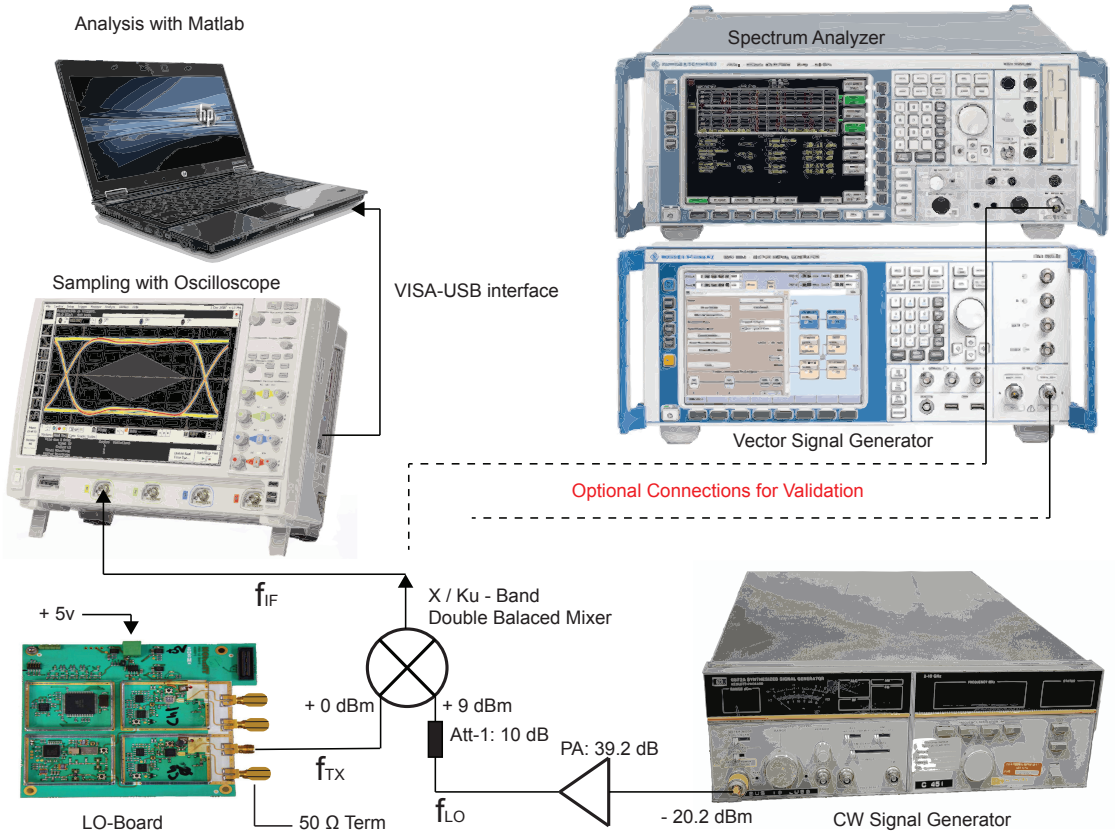

Figure 5.1.: Laboratory setup for waveform time-frequency analysis

Since this method heavily relay on the quality of down-conversion width minimal distortion, would the mixer and additional CW signal source, be of the most importance. Hence were the high quality *HP* signal source and the doubled balanced *RHG* mixer obtained. Unlike heterodyne transmitters, provided the LO-board a direct conversion to RF frequencies. Thereby removing the need for image-reject mixing. Although the double balanced mixer in general have worse RF input match than other mixers, does it in contrast have a excellent conversion loss to preserve the observability of the chirp waveform after downconversion. The RHG mixer provided the following properties for the laboratory measurement, shown in table 5.1.

Correspondingly to the mixer properties, could the conversion parameters then be derived (table 5.1). Additionally did the mixer give the power requirements for the surrounding instruments. Luckily provided the mixer also sufficient IF capability, for maximal waveforms components up to 500 MHz. Thus insuring that IF's could be set sufficiently away form the flickering noise and at the same time contain the full waveform bandwidth. Moreover were the LO-board Tx-port at +0 dBm, fitted to a LO drive of approximately

Table 5.1.: Mixer properties, RHG DM 1-18

Prop.	Typical	Min	Max
Frequency	—	1 GHz	18 GHz
IF Bandwidth	—	DC	500 MHz
Drive LO	9 dBm	7 dBm	11 dBm
CL	6 dB	—	9.5 dB
Iso,LO-RF	40 dB	22 dB	—
1 dB comp	4 dBm	2 dBm	—
VSWR(RF)	2.2:1	—	—
VSWR(LO)	1.6:1	—	—

9dBm, without violating the 1dB compression point. However did none of the available signal sources match a 9dBm output. A power amplifier and a attenuator were then issued, to match the mixer drive level and operated in a highly linear region. The PA gain were measured with an Agilent PNA (EB 8364B) to 39.35 dB and 39.09 dB at correspondingly 12.85 GHz and 12.95 GHz. Hence to insure unity between the measurements at different LO offsets. In addition were the frequency CW spectrum mesasurend from the PA and revealed no significant harmonics in addition to the fundamental were present. This proved thus a sufficient LO quality. Furthermore did the mixer's limited conversion loss (6 dB) give a corresponding **-8 dBm** power at the oscilloscope input. This were estimated by subtraction of a approximate cable loss of 2 dB and with a corresponding the LO-bord output at 0 dBm. Hence would the signal-to-ratio not be a problem, if the zero frequency flickering noise region was avoided. The bad VSWR relation at mixer input were also considered to not impose any threat to the laboratory setup. At respectively LO and RF port of mixer would the reflected power theoretically yield -3.75 dBm and -8.52 dBm. The LO signal path as described in figure 5.1, would with the applied attenuator and use of the high quality PA, terminate the reflected power efficiently. Likewise would the Tx signal path terminate the reflected power from RF mixer input port, in the Wilkinson power divider and the with the $50\ \Omega$ terminated LO-board LO output.

Table 5.2.: Conversion parameters

IF offset	$\mathbf{f_{LO}}$ $f_{TX}(\max) + \text{offset}$	**Max IF comp** $f_{LO} - f_{TX}(\min)$	**Nyquist Fs**
1 MHz	12.85641 GHz	189.762 MHz	379.5 MHz
50 MHz	12.90541 GHz	238.762 MHz	477.5 MHz
100 MHz	12.95541 GHz	288.762 MHz	577.5 MHz
	Chosen Fs Oscilloscope	**Memory depth** (Max)	**Acquisition time** Mem*(1/Fs)
1 MHz	500 MHz	20.5 Mpts	41.0 ms
50 MHz	500 MHz	20.5 Mpts	41.0 ms
100 MHz	1 GHz	20.5 Mpts	20.5 ms

Figure 5.2 shows the down-conversion scheme used to obtain the waveform within the oscilloscopes bandwidth and corresponding waveform image.

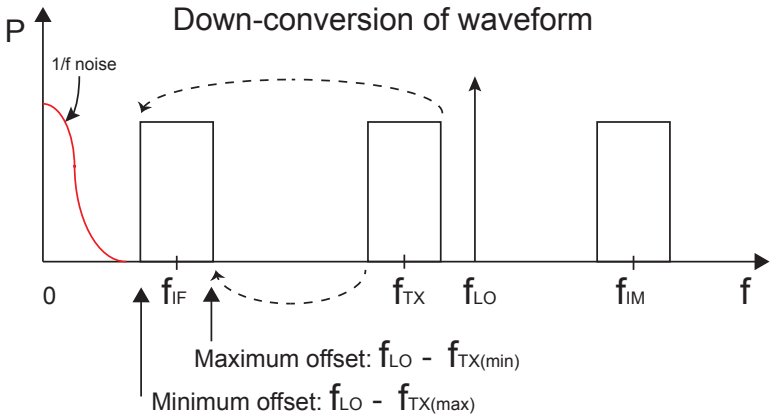

Figure 5.2.: Down-conversion of LO-board FMCW waveform to observable IF frequency

5.1.1. MATLAB Waveform Analysis Validation

Before any practical measurements were done, had the MATLAB analyzing software to be tested for its waveform computability. Thus to insure that the waveform could be analyzed properly with the available PC. Correspondingly were the FFT power estimation and spectrogram algorithms tested and optimized for the preprogrammed waveform.

Firstly had a theoretical FMCW waveform generator to be implemented. A set of complex FMCW signals were therefore implemented in accordance with the displayed waveforms in section 2.2, so different FMCW modulations could be studied on selection. Appendix B.1.1 shows the *waveform.m*-function, which takes the amplitude, chirp bandwidth, desired signal length, number of periods, desired waveform and sampling frequency parameters. The function then returns the complex time signal, its time vector and the used sampling frequency. By selection would the five different types of FMCW signals be generated as symmetric LFM waveforms.

In the case of the preprogrammed waveform analysis, did the string *WF5* generate a similar waveform with up-chirp, CW hold-period, and down-chirp. However dis the theoretical signal differ from the preprogrammed with a hold-period equal to the chirp-period. Nevertheless was this seen as an advantage in the MATLAB testing, since it would test a longer signal than the preprogrammed, thereby insuring computability for even longer signals. In addition was this preferable, since the real waveform generation and oscilloscope sampling would not be synchronized. Hence was a longer acquisition time in oscilloscope sampling needed, to insure that the full waveform could be captured. Thus was the long theoretical signal in MATLAB be perfered to insure handling of long measurement vectors.

Secondly was the signal analyzing code written. Appendix B.1.2 show the *theoretical.m*-script that set the FMCW parameters for the signal generation and call the *waveform.m*-function to obtain the wanted waveform. The FMCW parameters were set in accordance with a down-converted Ku-band LO-board output, to a 100 MHz IF. A

amplitude was then set from a theoretical output power of +0 dBm to insure amplitude similarity. Further were a chirp period of 40 ms and a 188.762 MHz bandwidth set similar to the theoretical output. The sampling frequency were then implemented as 1.5-*Nyquist* of maximal beat frequency to insure a good power estimate and tested of long measurement vector handling. However were the modulation only applied for one period. This was done, since a pre-tests of the measurement setup revealed that the memory depth of the available oscilloscope were limited to 20.5 Mpts. This meant that the real measurements could not obtain more than one period or parts of one waveform, for analysis. Already at this point it was obvious that a full waveform capture was impossible since

$$L_{signal} = t_m \cdot f_s = 50\,ms \cdot (3 \cdot 266.814\,MHz) = \ 43.3Msamples$$

Even with sampling at 1-Nyquist, would the number of samples be 29 Msamples. Hence were the waveform-acquiring-setup designed for both IF offsets at 1 MHz, 50 MHz and 100 MHz.
Nevertheless were the theoretical test, performed with full signal length to see the full signal appearance and MATLAB computabilliy.

The general theoretical analysis were then further performed in three steps, as intended for the real measurement. Hence time-signal analysis, FFT-spectrum analysis and spectrogram analysis. The time-signal were plotted to study possible time-signal anomalies, which could help to identify and isolated the chirp in time. Then the FFT power spectrum [17] were derived and plotted to study the resemblance to spectrum analyzer output. Furthermore were the MATLAB-provided, spectrogram-function [18], applied for 3D- and 2D- captures of the waveform in respectively power, time and frequency. The spectrogram is a algorithm that uses the Short-Time Fourier Transform (STFT) to generate a spectral estimation in relation to time. This algorithm uses segmented DFT estimation, to obtain 3D-measurement data. Although this algorithm is normally fast, had the extremely long signal vector ($L_{signal} = \ 104Msamples, t_m = 120\,ms$) to separated in three further segments. Hence to reduce the spectrogram computing time to belove one hour. Such signal segmenting would normally give an error to the frequency spectrum estimate. However dis the large number of samples reduce the error to a minimum. Further were the spectrogram parameters, then tuned for optimal performance and computing time.

After optimalization of the analyzing parameters, were simulated test results were obtained, shown in appendix B.2.1. Figure B.2 show the optimal, real part FFT spectrum. Figure B.3 present the 2D-spectrogram in the combined time-frequency-doiman. Hence showing the typical linear FMCW characteristics of the full waveform. In figure B.4 was the up-chirp part of the waveform, isolated as a shorter time vector (40 ms) of the total waveform. Thus revealing more details in the plot and how the distribution of power was descending out from each frequency segment in waveform.

To conclude did the trial for real signal analysis reveal that the MATLAB software in combination with the available PC, were well suited for large measurement data waveform analysis both in time, frequency and combined spectrum.

5.1.2. Obtaining Signal Data from Oscilloscope

When the MATLAB trial had been performed, was the work further focused on the sampling of measurement data and the transferring of sampled data between the high speed oscilloscope to the portable laptop. Different transfer protocols and interconnections were examined to yield the best transfer of sampled data between the Agilent MSO 9254A oscilloscope and the standard PC. However also considered in respect to simplicity.

After some trials, seemed the best suited transfer protocol, to be the USB-VISA connection. Hence both in respect to protocol standardization, simplicity and MATLAB compability. The general idea were to implement a simple protocol that could yield both high interconnectivity to standard laptops and high portability. hence to enable further mobile field measurements for the full scale radar implementation by the use of a standard oscilloscope.

The first step of implementation were to install the *Agilent IO libraries* (IO Libraries Suite 16), which enables the Agilent test instruments and similar modular instruments to be connected to a standard PC. From the included *Agilent Connection Expert* could the oscilloscope properties be set remotely. The provided software in the IO Libraries, did also enable test instrument programming in C to add wanted modes of operation. However since the analysis were to be done in MATLAB, were an additional Agilent MSO 9254A instrument driver ($AgilentInfiniium\_IVI.mdd$) added to MATLAB main path to control the oscilloscope from the MATLAB environment. In order to do so were the Agilent-.mmd driver imported via the *Instrument Control Toolbox* and the *MATLAB Instrument Driver Editor* (midedit), and further located as an IVI driver in the Instrument Control Toolbox. After suited driver had been imported, were the IVI driver configured with a logical name, driver session and hardware asset. Further was then a *Device Object* created from the AgilentInfiniium-driver by choosing the IVI drivers logical name as resource. When the Device Object had been created, was the connection to oscilloscope enable. Hence could all available functions and properties of the oscilloscope be viewed. By using this approach were all setting of properties and functions obtained via the connection, session-log without any direct MATLAB coding.

Furthermore were then the actual testing of the applied connection performed. To set the correct oscilloscope properties were hence the basic theory applied. The following relation yield to waveform sampling

$$Acquisitiontime = Memory\,depth \times \frac{1}{f_s}$$

thus showing that the a maximum memory depth had to be used to obtain as much of the waveform as possible. However did this relation also show that the waveform had to be converted as far down in spectrum as possible. Hence to minimize the f_s requirement and obtain as much of the waveform as possible without interfering with the 1/f-noise at low frequencies. Hence were the waveform down-converted to three different intermediate

stages. The actual used acquisition windows in the real measurements, are hence shown in table 5.1.
When the correct session-log for the actual waveform-acquiring was decided upon, was the session-log exported as a .m-script file to MATLAB main path. Hence could the m.-file be executed directly from MATLAB command window, performing the oscilloscope measurement by one click. The oscilloscope measurement data were then obtained directly in to the MATLAB Workspace, were further processing could be done. A general example of the oscilloscope session-log is shown in appendix B.1.3 were the data has been obtained by the *readwaveform*-function

$$[signal, start, inc] \; = \; invoke(groupObj,' ReadWaveform', \; 40e-3);$$

The measurement data obtained via the IVI-driver were given as oscilloscope Y-axis data, start of sample and increment between Y-data. Hence could the time amplitude data and sampling frequency be easily obtained and processed. From the measurement data set could then the sampling frequency be extracted as

$$f_s = 1/inc$$

Note that most of the agilent IVI drivers only are available as x86 drivers, hence had the Windows 64-bit PC to run XP-window as a virtual PC to obtain the oscilloscope data. During the trail for connectivity, were both oscilloscope parameters for the full waveform acquiring and beat frequency measurement tried out. The beat frequency measurement settings were tested first and passed the acquiring-test without problem. However did this measurement only need a low sampling frequency with relatively short measurement data vectors. In contrast did the acquiring-test of the full waveform **fail** when using the oscilloscopes full memory depth(78.2 MB bin-file measurement data).

Hence had another transfer scheme to be used for such measurements. Luckily could such an operation also be done manually, by operating the oscilloscope directly and transfer measured data by USB-pen into the MATLAB Workspace. However could not MATLAB read Agilent .bin-files and hence a to be converted before further data analysis. Nevertheless had Agilent provided such a script(importAgilentBin.m) making the conversion easy, thus by executing

$$[Y \;\; X] \; = \; importAgiletBin(X.bin);$$

By using .bin-files was the measurement data now provided as Y and X measurement vectors, implying a slightly different approach to extract the sampling frequency. Hence

$$f_s = 1/(X(2) - X(1))$$

When the oscilloscope was operated manually, were the sampling frequency set to the nearest value over Nyquist. Hence to obtain long time measurement of the waveform with the maximal memory depth of 20.5 Mpts. The acquire parameters were set manually to maximum memory depth, real time sampling and the desired sampling frequency.

In summary did the oscilloscope connectivity- and acquire-test, show the USB-VISA connection could be used successfully when used for radar measuments at low sampling frequencies. However did the connectivity fail when making use of the oscilloscope's full memory depth. Hence making it unusable for obtaining spectrograms of the full waveform. Hence were the manual transferring of oscilloscope data through the .bin-measurement scheme used, to enable such measurements and analysis in MATLAB.

The following references provided the used oscilloscope interconnectivity to PC:
(Listed her for convenience since bibliography mismatches long url-references)

Obtaining the Agilent IO Libraries suite:
$http://aaa.product.agilent.com/IOLibraries/Download\_IO\_Libraries.aspx$
Obtaining instrument .mdd-driver:
$http://www.home.agilent.com/agilent/redirector.jspx?action = doc\&lc = eng\&cc = SG\&id = 182728\&ltype = External\%20File$
Obtaining the .bin-file converter:
$http://www.home.agilent.com/agilent/editorial.jspx?cc = NO\&lc = eng\&ckey = 1185953\&nid = -536902447.0.00\&id = 1185953$
Tutorials used for oscilloscope connectivity and data extraction:
$http://www.mathworks.com/matlabcentral/fileexchange/?term = tag\%3A\%22oscilloscopes\%22$

5.1.3. Measurements and Processing of Oscilloscope Data

After the oscilloscope test, were the theoretical processing MATLAB-script adopted to extraction of Y and X data according to the use of .bin-file measurements. In addition were also the spectrogram parameters altered for better visualization for both long and short signal vectors.

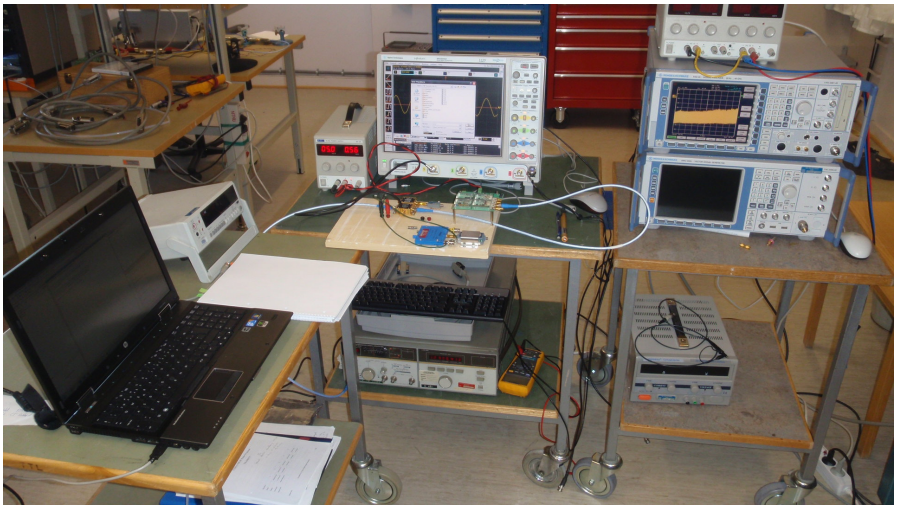

Figure 5.3.: The real setup of experiment, with wood board test bench

The measurements were then executed in accordance with figure 5.1 and table 5.1. However did the first mesurments only display the theoretical hold frequencies, both FFT and in spectrogram, at the different IF offsets. No 40 ms chirp were found, although several measurements were made. At least should a part of the chirp been present in spectrum, since the chirp period was longer than the hold peiode. The spectrogram showed that the hold frequencies were time segmented, but longer than the 10 ms diverging form the description in radar documentation[34]. The two initial thought was that the LO-board did not yield the correct output or that the oscillope did not sample as a real-time sampler. These initial FFT and spectrogram plots are displayed for a 100 MHz offset waveform measurement, in appendix B.3.1. However did the FFT spectrogram yield a slight increase in power between the high power hold frequencies. Thus was the properties of the waveform additionally measured again with the spectrum analyzer with the new setup, to see if there were some resemblance with the waveform observed at Ku-band.

The measurements conducted with spectrum analyzer with the new setup proved to be quite similar to the waveform observed at Ku-band, seen in figure B.7 and B.8. The max-hold trace of the signal, showed a waveform bandwidth 28 MHz wider than theory, but similar to the measurement at Ku-band (25 MHz wider than theory). This proved that some form of chirp transition were present, although not shown in the spectrogram. However as expected were the overall power lower, caused by the conversion loss in mixer, but still fully observable. In addition to the max-hold measurement where an average trace conducted to see the disturbution of power in relation to the observed spectrogram. This revealed that the average power were mostly distributed over the exact

theoretical hold frequencies at 100 MHz and 288 MHz, with a slight increase of average power in waveform midband. Compared to the obtained spectrogram, was hence the same relation observed, although distributed in time (figure B.6). The midband average was also seen as vaguely distributed over the same period as the low hold frequency at 100 MHz. Hence did the experiment confirm that there were great resemblance between the measurements conducted with the oscilloscope compared to the spectrum analyzer measurements in relation to frequency. However did the experiment also show that there were some ambiguity to the presens of the chirp. Compared to the spectrogram analysis, did the waveform time-relation diverge with theory, showing longer hold-periods and no presens of chirp in time. This discovery lead to a hypothesis which stated that the oscilloscope triggered on the hold frequencies and hence sampled only over these periods. Thus had the oscilloscope settings to be reviewed and further tested.

To do further testing of the oscilloscope setup, was the vector signal generator (VSG) implemented as a test signal source instead of the LO-board. Hence to find a setting that insured correct time data, in oscilloscope sampling. The VSG was therefore set up to sweep frequency from 1 MHz to 189.762 MHz, with oscilloscope parameters set equal to the 1 MHz offset test. The power output from the VSG was also matched to the LO-board output power to have unity of measurements. In addition was the oscilloscope operated at different trigger modes and additionally with the built in *Mask Test* to insure, that the oscilloscope sampled in real-time from test start to Memory depth maximum. Although the test were supposed to insure full unity to the real measurement, were the RF sweep in the VSG limited to segmented frequency steps of 10 ms per step. Nevertheless did the test still yield a known time relation, that would reveal if the sampling of the oscilloscope were correct in time.

After a lot of different oscilloscope testing, did experiment indicate that consistent time relation coul be enabled as long as the acquire-settings of the oscilloscope were set to *Real-Time sampling*, which was also the oscilloscope default. Figure B.9 in appendix show the spectrogram for a time-sampling confirmation test, with the VSG. The previous hypothesis had hence been proved to be wrong. A lot of time and effort had been put into the testing of the oscilloscope, but however now obvious explanation to the dissapeared chirp had been found.

As the next step towards a full waveform confirmation, were the LO-board setup as a simulated homodyne radar. Hence to study if the beat spectrum could reveal anything about the chirp sweep time. The test were conducted similar to the setup seen in figure 5.15, but diverged by use of the LO output from LO-board as single output and splitted by the use of a 3dB *Pasternack, Wilkinson power divider*. From splitter was the RF path delayed with a 12.5 m coaxial cable, yielding a synthesized range of 6 m to the mixer LO feed cable of 0.5 m.
Theoretically would this configuration yield a beat frequency of 188.7 Hz, if the chirp time was 40 ms. It was however clear that it would be difficult to see any real beat frequency at this low beat due to phase noise. Nevertheless were the test done to see if

the beat would appeared at other frequencies in spectrum. Thus maybe indicating another chirp sweep time. To maximize detectability in spectrum, in the study of anomalities, were the signal sampled for 100 ms to insure capture of chirp. Hence were f_s also set to 1 MHz to insure capture of all possible t_0 at 188.762 MHz signal bandwidth. Correspondingly were NFFT in set to 131072, matched to the next radix-2 of signal length, to insure high 'receiver' frequency resolution (7.6 Hz). Figure 5.4 show the resulting beat spectrum of this intermediate test, sampled with the oscilloscope.

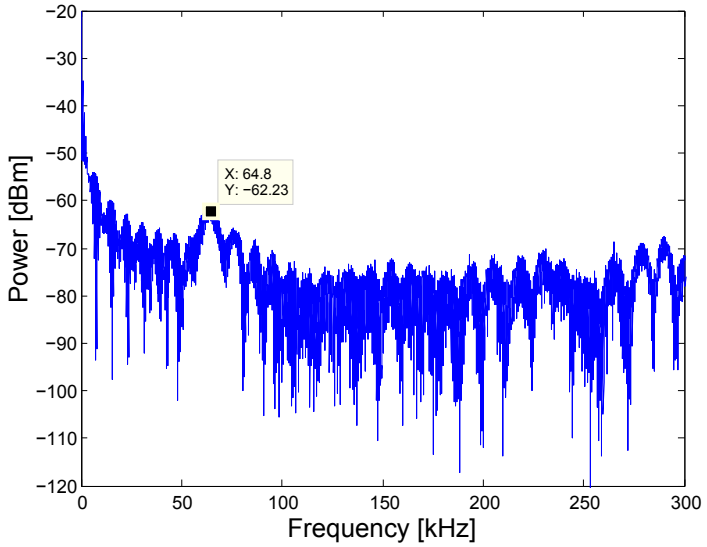

Figure 5.4.: Beat spectrum of intermediate waveform confirmation test

With a comparison between measurements done with the oscilloscope and the spectrum analyzer, were no beat signal discovered at 188 Hz as suspected. However did mesurments indicate that there were a small, but detectable beat output around **64 kHz**, shown in figure 5.4. If this was the real beat output, would this indicate a chirp sweep time of **117**μs. Hence 342 times shorter than the chirp described in the radar documentation and additional state that there were a significant programming error of the DDS. Nevertheless could the detected output beat, also have been some sidelobe from a low frequency Sinc(X) and hence the explain the low power. However since no other explanation to the divergens between test measurements and documentation had applied, were the chirp period thus expected to be significantly shorter than the hold periods. If true, could this explain the invisible chirp between the hold frequencies seen in spectrogram, due to the relative difference in signal length and observable power.

Additionally was the 3D spectrogram obtained to see if the chirp could be revealed, by observation from an other space angel. The 3D plot of spectrogram had not been studied earlier since it was belived that the chirp were in order of 40 ms, and hence be observable in relation to the shorter hold periods. Thus had the 2D spectrogram been initially be preferred since it would only show significant power elements in relation to time and frequency, and mean out the additional low power noise. However did this theory not hold if there were a strong mismatch between chirp time and hold time. Figure 5.5 show

the 3D-spectrogram of a down-converted waveform measurement done at 1 MHz offset. The plot reveal a clear the distributed power between the two hold frequencies. However did the plot also reveal a distorted power distubution in this region, which had to be looked further into. Additionally did the spectral plot at 1 MHz offset show that the low hold frequency was corrupted due to influence by the 1/f-noise at low frequencies. Hence where further tests not conducted at this offset as first planed. The two midband frequencies observed between max hold frequency and Zero frequency were identified as additional mixer harmonics.

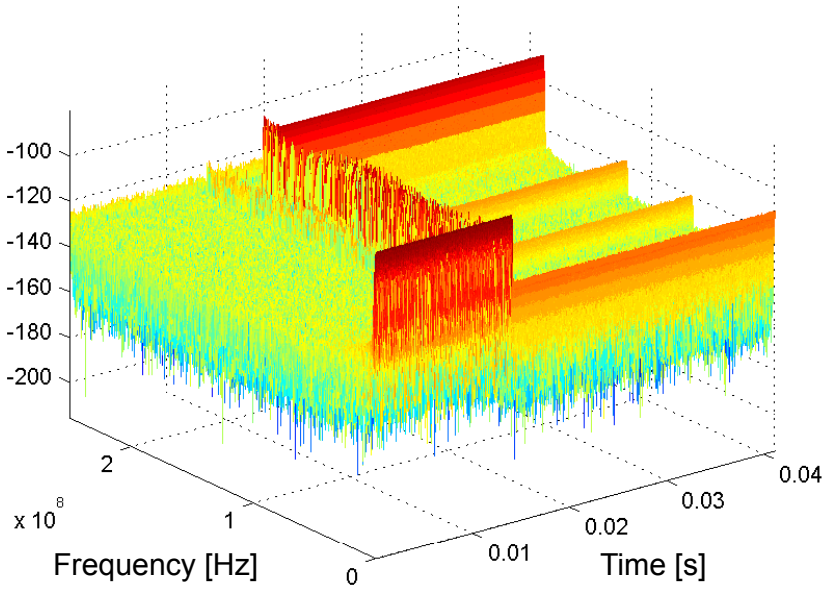

Figure 5.5.: 3D spectrogram of intermediate waveform confirmation test at $1\ \mathrm{MHz}$ offset

In summary had the hypothesis of a very short chirp in relation to the segmented hold frequencies, been vaguely confirmed. The long acquisition time in relation to the unexpected short chirp had possibly masked been in the 2D-plot. Hence to low power at each time bin, compared to the total record time.

To fully confirm the hypothesis, had the chirps in each measurements to be identified in time-plot and isolated as new processing vectors. The manual extraction of chirp measurement vectors are shown in appendix B.1.4, together with the full waveform processing. Additionally are example measurements containing chirp in time shown in figure B.10 and B.11 at respectively 50 and 100 MHz in appendix. All of the above processing of measurement data were done similar to the theoretical processing m-script, however implemented with reading of manually transfered .bin-files and X-Y data.

In this part of the confirmation of FMCW waveform properties, were the already captured measurement data analyzed in time domain in respect to amplitude anomalities that

would indicate frequency transition. The region of interest were then further identified as time points, marked as TL in script (App.B.1.4) and manually tuned to pick out the exact part of the measurement vector that would contain the chirp. This task was time-consuming, since the measurement vectors were long to insure that some part of the vector would contain the relatively short chirp. Since the maximal sampling window in both measurements at 50 MHz and 100 MHz offset, were shorter than the modulation period, did a lot of mesurment vectors not include the chirp at all. However did the time analysis reveal quite easily which measurements that included chirps. Hence since the transition from high hold-frequency to low appeared as a signal amplitude attenuation for high frequencies. The region in between high and low amplitude, could then be identified as the chirp region. The amplitude variation over the chirp could be identified as a single peak in the long time plot. Figure B.10 and B.11 show the described observation. In addition did also the time domain analysis reveal a negative DC component, that had to be removed. Ideally this component should have been removed before sampling either by a high pass filter or a capacitor DC-block. However had such an implementation, to yield 50Ω matching of components for the right the frequency band of interest. Hence were a digital HP filter instead implemented in MATLAB, by the use of FDATOOL for filter design. A high order FIR-filter were designed to insure minimal frequency distortion and preservation of real measured amplitude. The designed filter with magnitude and phase response can be reviewed in appendix B.1.5. By using such high order filtering could the measurements at 1 MHz offset still have been used. However since the 1 MHz measurements were similar to the ones at 50 MHz, were this still left out of the measurement set for conviniance.

After filtering of the amplitude data, were the FFT- and spectrogram-processing executed to study the isolated chirp, showed in the next subsection (*Spectrogram Results*).

5.1.4. Spectrogram Results of Measured Preprogrammed Waveform

Measurements were conducted in correspondence with figure 5.1 and table 5.1, except the measurements at 1 MHz offset to avoid 1/f-noise and 50 MHz resemblance as described in previous subsection. The amplitude data were also filtered with a digital high-pass filter to remove a discovered negative DC component, prior to signal processing.

Waveform chirp analysis at 50 MHz IF offset

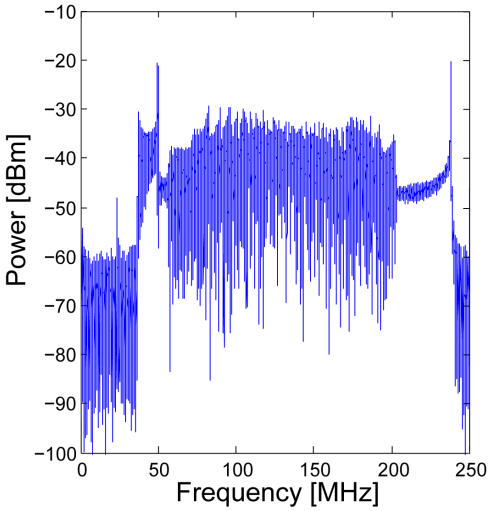

Figure 5.6.: FFT of chirp, obtained at $50\ \mathrm{MHz}$ offset

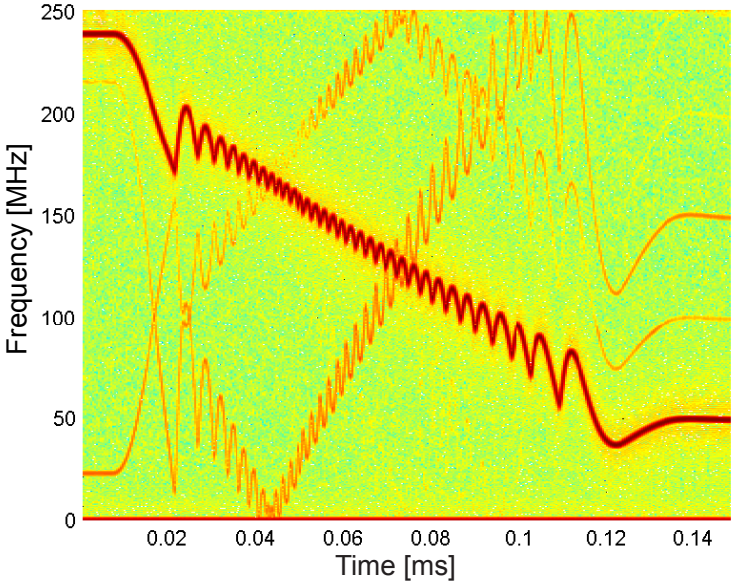

Figure 5.7.: 2D-spectrogram of chirp, obtained at $50\ \mathrm{MHz}$ offset

Waveform chirp analysis at 100 MHz IF offset

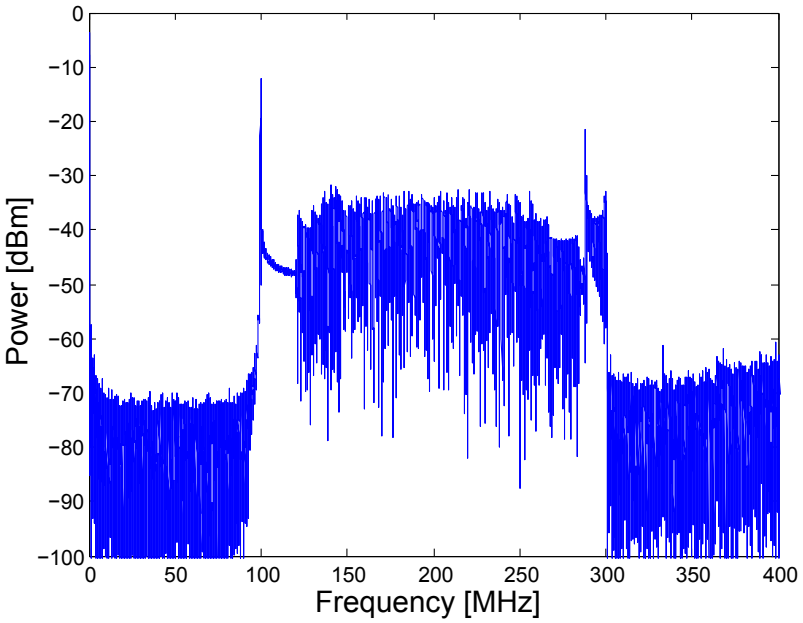

Figure 5.8.: FFT of chirp, obtained at $100\ \mathrm{MHz}$ offset

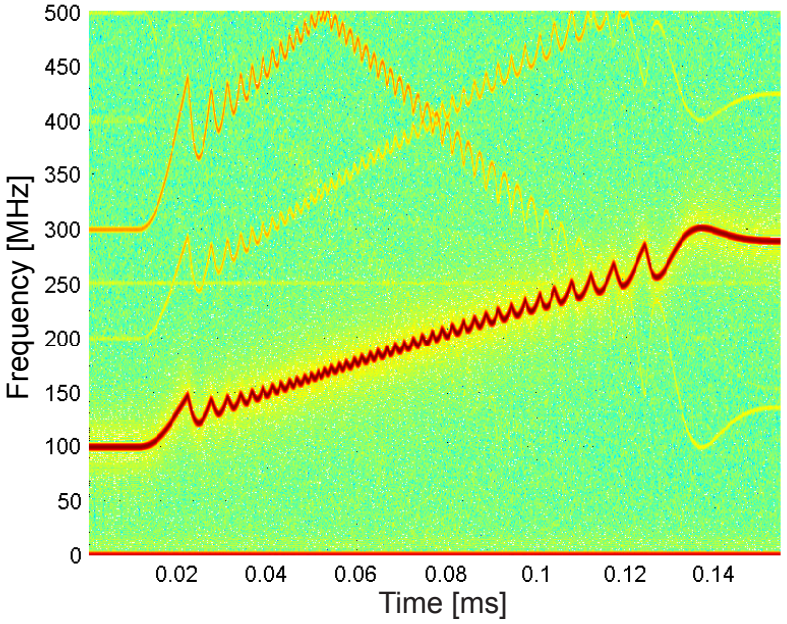

Figure 5.9.: 2D-spectrogram of chirp, obtained at $50\ \mathrm{MHz}$ offset

Observations

The analysis of the chirp confirmed the hypothesis of an extremely short frequency sweeping time, relative to the hold frequency period. Seen from the FFT-plots and

Table 5.3.: Measured chirp parameters and apparent waveform

Properties	IF=50 MHz approx	IF=100 MHz approx	**Apparent** approx
Chirp sweep time	130 μs	134 μs	132 μs
Hold time	49.87 ms	49.866 ms	49.87 ms
Chirp bandwidth	188.5 MHz	189 MHz	188.7 MHz
SNR chirp	15 dB	25 dB	-
Theoretical $\mathbf{\Delta R}$	-	-	0.795 m
f_b, (R=6m)	-	-	57.2 kHz

spectrogram-plots it was obvious that the reduced measurement vector helped to yield better power distribution to study the short chirp, in respect to the sampling window that were needed to capture it. The spectrogram results of the waveform chirp for both measurements are summarized in table 5.1.4. Hence concluded to an apparent waveform, yielding a chirp period of 132 μs. This indicated that there were a strong mismatch between the preprogrammed waveform and the real output, in relation to time properties. Not only were there an mismatch in chirp-time but also in respect to the hold frequency period which were significantly longer (49.87 ms). Thus did this indicate that the DDS modulation in respect to time were erroneous. This indicated the relation between DDS profile pin (modulation period), rising delta word (RDW), falling delta word (FSW) and raising/falling sweep ramp rate word (RSRR/FSRR) had to be reviewed. However did the experiment show that the frequency parameters for the start- and stop-frequencies, seemed to be set right according to documentation.

In relation to the performed spectrogram analysis and the difference of the two offset IF frequency measurement, proved the test inconclusive to which offset had been the best. It was not possible to say that any of the two were better than the other, but more supplementive to each other. The whole study had proven to be very important for reveling the true apparence of the waveform, that could not be studied with a normal spectrum analyzer. The measurements at 50 MHz, was preferable to look at more of the full waveform and see the chirp in relation to the hold period. Hence since it needed a lower sampling frequency and thus could sampled over a longer time interval. However as figure 5.6 and 5.7 indicate, did this measurement yield lower SNR over the chirp bandwidth and less spectral purity in respect to influence from harmonic waveforms and RF reflections. By increasing the IF offset to 100 MHz, were the spectral purity improved. However were the spectral purity traded for shorter glimpse of the full waveform.

Figure 5.7 and 5.9 show an linear like chirp appearance, but a large frequency error seen from the apparent linear chirp line. Such deviations in frequency over the chirp, could thus create large variation in beat frequency output over the sampling window for a full scale radar implementation and hence a degradation of beat frequency resolution. Since this is a non-desirable situation for FMCW radars, had the nonlinearity and frequency error to be investigated. Hence to acquire more accurate figure of merits of the current waveform. A method for frequency error extraction of the above measurement data

were thus developed and executed. Further did the spectrograms show the 2nd and 3nd harmonic waveforms whose images, was reflected back into the desired frequency region due to digital mirroring for frequency component outside the Nyquist bandwidth.

Although it was clearly seen a deviation to a imagined linear chirp, it was however not easy to determine the exact start and stop time-positions of the frequency sweep. It seem from the spectrogram that the PLL circuit was not optimized for this modulation. Hence in respect to frequency tracking over the sweep period and therefore hence struggling to get frequency lock between the hold frequencies. It was also clear that the theory of RDW/FDW-settings mismatched the wanted chirp period of 40 ms chirp. The uncertainty to the PLL performance with the current waveform, made hence a large ambiguity to the chirp sweep period. This indicated therefore that the circuit had to be reprogrammed with a longer chirp, to possibly match the PLL performance. Hence to get better accuracy of the frequency sweep. However would the purposed method of frequency error studies be help full for further development in determining the best FMCW modulation parameters, hence were this performed prior to any more work was done to reprogramming.

5.1.5. Estimating Chirp Linearity

Since the spectrogram analysis had reveal a frequency error in the measured preprogrammed waveform, was an algorithm developed in MATLAB to study the frequency error of measured waveform to the apparent theoretical chirp. This was done by means of curve fitting the apparent chirp to a theoretical linear frequency sweep, since the chirp time relation, did not match the radar documentation of the preprogrammed waveform.

By making a theoretical reference, could the frequency error be extracted by taking the difference from the theoretical frequency at each time segment, to the maximal power center of each time segment of the real waveform. Hence measuring the deviations in frequency to the theoretical chirp over time. With the waveform extracted as single point vector measurement data, instead of matrix data, could the waveform be mapped back to Ku-band by making an reversed ideal mixing in MATLAB. Hence by subtracting the measured waveform frequency to the LO-signal used for down-conversion. Hence would the waveform appear as it was originally output from the LO-board. By this metode could the frequency error be estimated at Ku-band. Additionally could also the W-band, real radar output be estimated. Hence with a x6 times frequency multiplication. Thus could this give a glimpse of the total system frequency error, however without additional dispersion errors made by Tx MMW circuit, antenna, propagation channel, target response and LO-feed.

Although there were great ambiguity to the settings of the theoretical chirp, could the method still give an indication to the current chirp linearity performance. Thus could this method be used as a quality test for new LFM modulations applied to the radar signal source.

Algorithm and Execution

In order to study waveform linearity, had the spectrogram data to be extracted as a single frequency vector, equal to the measurement time. To represent the waveform in relation to time and frequency, were the maximal power element at each time column found according to figure 5.10. Hence shown in the MATLAB script in appendix B.1.6. As described in the measurement of the spectrogram, had a high pass filter to be implemented prior to processing. This was also done here, since the low frequency components outmatched the maximum power of the desired chirp. Before the chirp could be extracted as a single frequency vector mapped from maximum power element at each time column, had the measurement vector to be matched to the apparent linear chirp length. Hence could the theoretical frequency vector be made by a linear function of the exact measurement time.

$$f_t(t) = f_{start} \pm \alpha\, t$$

Dependent of chirp rate (up- or down-chirp), was the sign changed accordingly. The maximum power element at each time sample coulum were then taken and mapped back to the corresponding frequency sample index. Hence were a frequency vector equal to sample time obtained, thus representing the waveform frequency over the chirp.

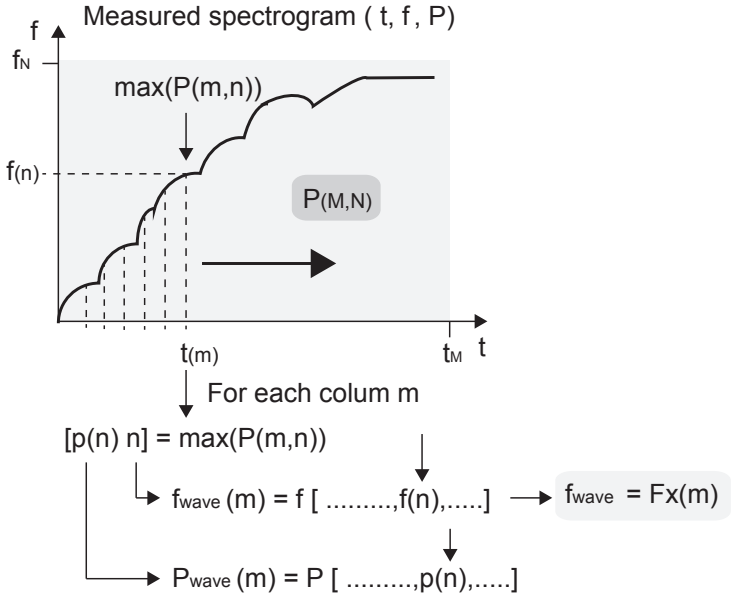

Figure 5.10.: Algorithm for separate vector waveform representation

Since the waveform had been downconverted by mixing to a low frequency IF, enabled the utilization of the single frequency vector up-conversion by reversed mixing with the same frequency LO. Thus could the waveform be represented as originally sent out from LO-board, which was a flipped version of the measured waveform.

$$f_{Ku} = f_{LO} - f_{meas}$$

Additionally it was also interesting to study the estimated frequency error/nonlinearity at 77 GHz output, similar to full radar implementation. Since the waveform were now represented as a single frequency vector could the measured estimate and the theoretical signal be easily multiplied by x6 to match the W-band output.

The frequency error were then obtained for both frequency estimates at the Ku- and W-band. Similarly were also the maximum deviation, root mean square error, effective maximum instantaneous linearity (L_{se}) and the range resolution estimate of L_{se} at 1 m and 150 m obtained (appendix B.1.6). However were the theoretical frequency chirp matched to the measured frequency apparent linear line. Hence not to the point were the frequency, were satteled to the CW frequencies. This was done to minimized the frequency error, since the slope fitting of the theoretical chirp to the start- and stop-CW's, produced a abnormal biased frequency error. Hence was the theoretical slope, fitted differently for the measurements at 50 MHz and 100MHz offset, to see the impact of the curve fitting error.

Linearity Results

The linearity-plots are shown for the 100 MHz offset measurement, upconverted to Ku-band and W-band. Additionally are the quality parameters for both measurements summarized in table 5.1.5.

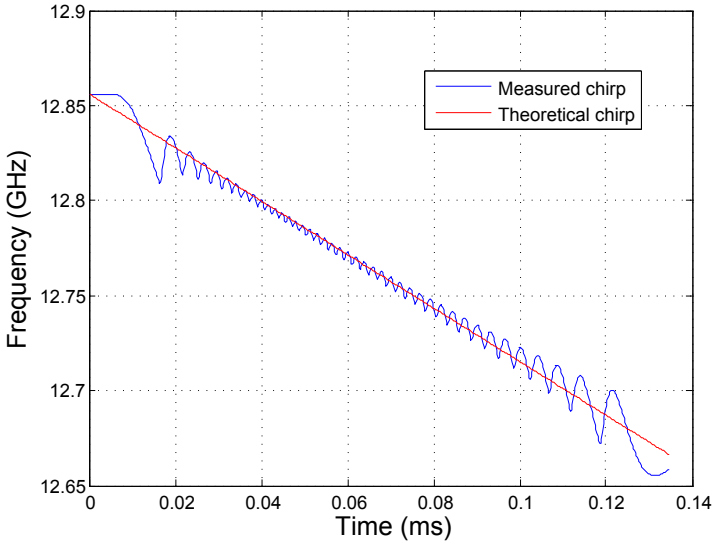

Figure 5.11.: Measured chirp vs theoretical, Ku-band, obtained form 100 MHz offset

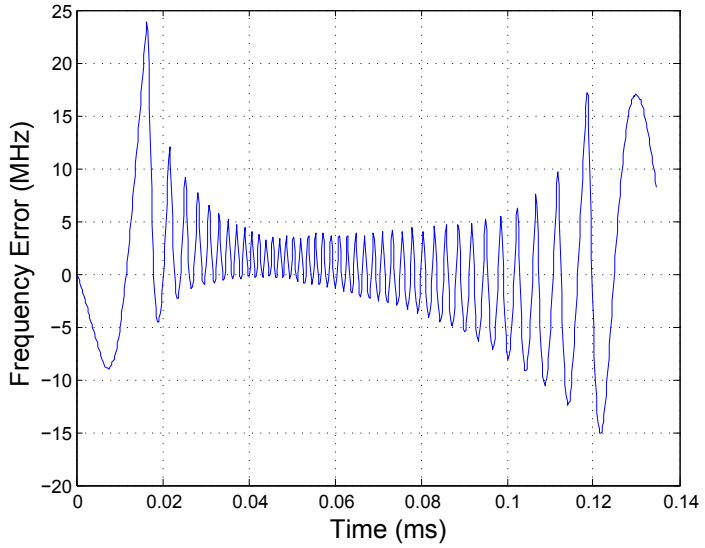

Figure 5.12.: Chirp frequency error, Ku-band, obtained form $100\ \mathrm{MHz}$ offset

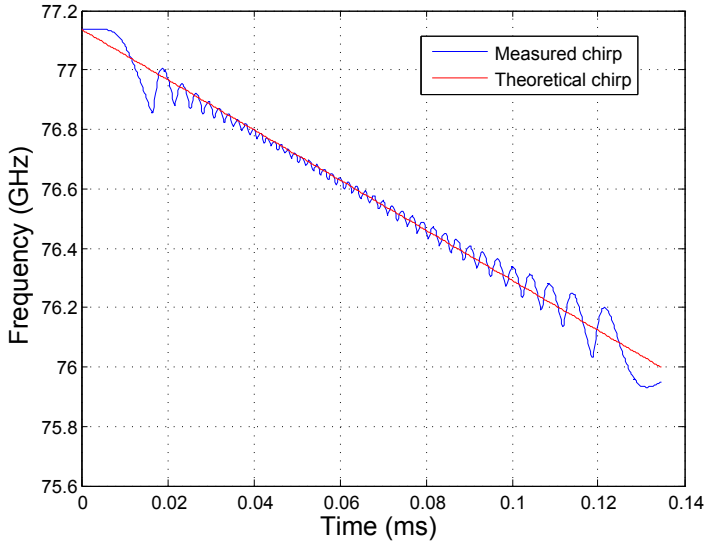

Figure 5.13.: Measured chirp vs theoretical, W-band, obtained form $100\ \mathrm{MHz}$ offset

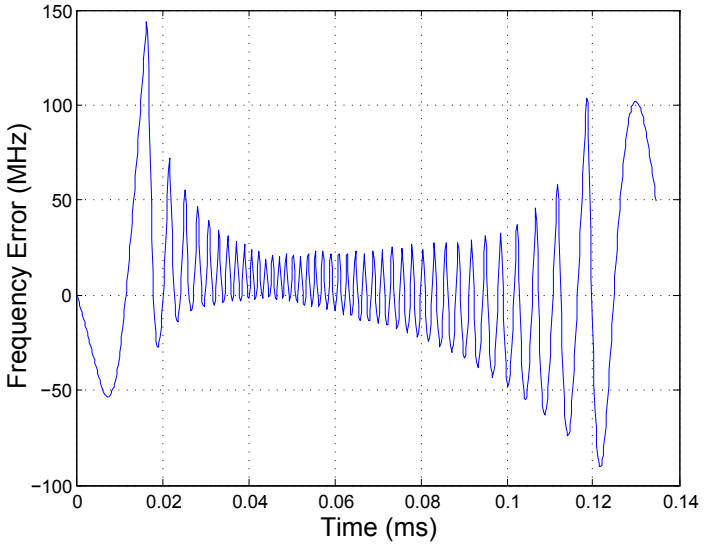

Figure 5.14.: Chirp frequency error, W-band, obtained form $100\ \mathrm{MHz}$ offset

Table 5.4.: Estimated chirp linearity parameters from analysis

Properties	**IF = 50 MHz**		**IF = 100 MHz**	
	LO-board Ku-band	MMW-board W-band	LO-board Ku-band	MMW-board W-band
Max freq. deviation	25.0 MHz	150.0 MHz	24.3 MHz	145.8 MHz
RMSE	8.89 MHz	53.39 MHz	6.68 MHz	40.00 MHz
L_{se}	4.56%	4.56%	3.53%	3.53%
ΔR_{theo}	0.77 m	0.130 m	0.79 m	0.132 m
$\Delta R_{RSS}(1m)$	0.77 m	0.140 m	0.793 m	0.137 m
$\Delta R_{RSS}(150m)$	6.88 m	6.85 m	5.35 m	5.29 m

Observations

As the slope- and error-plots indicate, was there a significant frequency error over the chirp period. When the error were upconverted to W-band did the maximal frequency error yield 150 MHz, which is 15% of the total bandwidth of 1 GHz. Table 5.1.5 summarize the measurements conducted at 50 MHz and 100 MHz offsets. In all were the difference between the two, due to different slope-fittings of the ideal chirp. Hence showing that different slopes would bias the frequency error differently, giving an ambiguity to the real chirp. Nevertheless was the variations in slope fitting, inevitable since the documented chirp were not known. Also did the use of single maximum values to represent the waveform, yield a source of error to the measurement. Although minimal compared to slope fitting. However did the experiment, with the described errors taken into account, yeild frequency errors significantly worse than similar designs [44], [20]. Compared with [44] that utilized and a linear chirp of 3 GHz bandwidth and 200μs, where the difference in maximum frequency error at W-band in fact 1000 times larger (150kHz to 150 MHz). Thus indicating that there were some significant mismatch to the generation of the chirp in the test circuit. Indicated from the chirp slope plots in figure 5.11 and 5.13, did it seem as the PLL has almost no track of the frequency sweep, wingling about until it reached the hold frequencies. These observations indicate that the PLL circuit was not matched to follow such short chirps. Furthermore did this indicate that the DDS circuit had be reprogrammed, in order to study the possible gain of longer chirp periods. To insure the validity of the measureuments, were the beat frequency output and its spectral resolution further measured in next section. Hence to see if any nonlinear anaomalities could be observed in beat spectrum.

Table 5.1.5 indicated how the measurements of the nonlinearity on waveform yield a untenable situation for implementation of the full radar system with the following nonlinear performance. With a RMSE ranging from 53.39 MHz to 40 MHz at W-band, did the effective normalized nonlinearity yield errors in correspondingly range of 4.56% to 3.53%. Hence were the convolved range resolution ΔR_{conv} at maximum range, estimated to be respectivelly 6.85 m and 5.29 m. As a consequence does this indicated that such nonlinearities will be devastating to the radar performance. This relation show in general that the range resolution will be influenced by nonlinearities as a function of range. Hence caused by the mismatch between waveforms which will increase with the relative to delay and further create variations in beat frequency during the chirp correlation.

5.2. Measuring Synthetic Beat Frequency

To make a validation of the previous test and results, were the beat frequency and its properties studied. By using the LO-board in combination with the same double balanced mixer as previously used, could a simulated homodyne radar be implemented. Hence with a delayed RF path. The main goal of the experiment were to confirm the short chirp by measuring the beat output. Further were also fundamental parameters of the beat frequency to be studied in relation to time and frequency. Additionally were it seen as important to examine how the beat was effected by the discovered nonlinearities and study how they affected the spectral resolution. The used laboratory setup is displayed in figure 5.15 with additional component specifications listed in start of section 4.1.

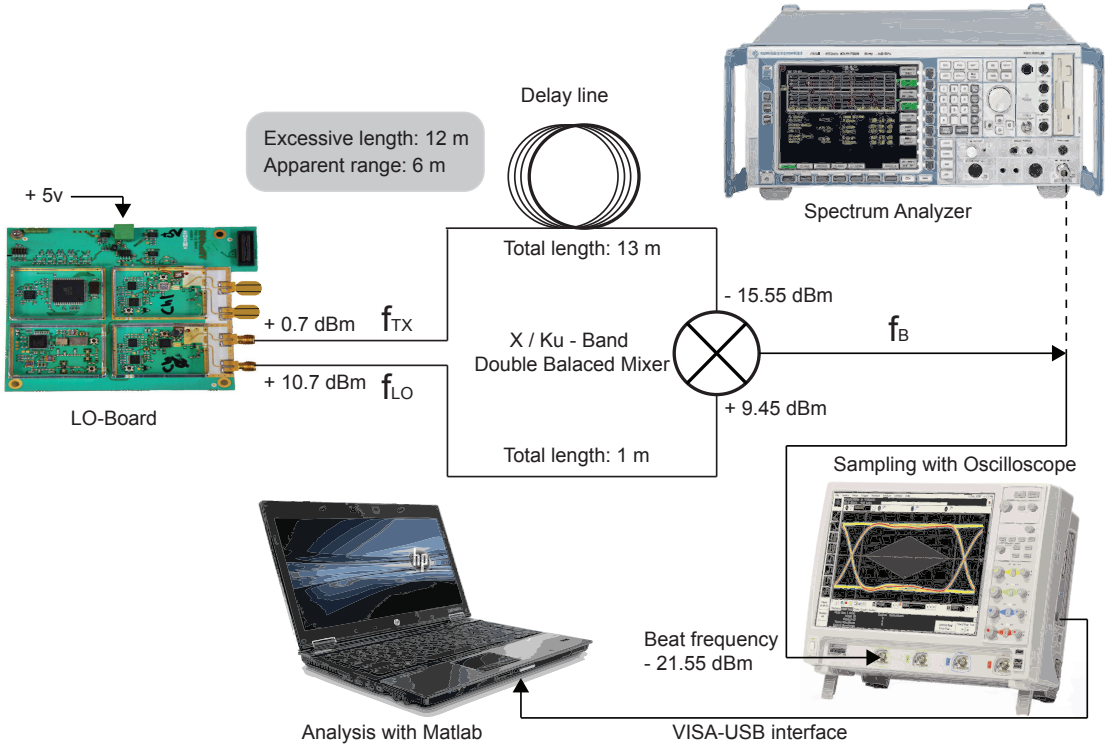

Figure 5.15.: Beat frequency spectral investigation

Before the experiment was initiated were some initial power calculations made to insure a good laboratory setup for the beat frequency studies. Table 5.2 gives the power calculations for the beat frequency investigation.

As in the previous laboratory setup was the RHG double balanced mixer used for down-conversion. The question to use of this mixer was the relatively high VSWR, which at both mixer inputs would be reflected power back at the PLL/VCO circuit. However was the Tx signal path long enough to theoretically insure substantial attenuation for the reflected power, yielding -24 dBm at mixer and -40 dBm at Tx output port, with VSWR = 2.2:1. At the LO mixer-port was the VSWR better (1.6:1), but the incident power also much higher. At the mixer port would the reflected power yield theoretically -3.29 dBm.

Table 5.5.: Power parameters for the beat frequency study

Parameters	**Path**	
	Tx	LO
$\mathbf{P_{OUT}}$	+ 0.7 dBm	+ 10.7 dBm
$\mathbf{L_{Coax}}$ $(1.25\,dB/m)$ $(12.5\,GHz)$	16.25 dBm	1.25 dBm
Mixer input	- 15.55 dBm	9.45 dBm
Remark	No violation of P1	Sufficient LO drive
Mixer CL	6 dB	
$\mathbf{L_{Coax}}$ $(0.03\,dB/m)$ $(< 1\,MHz)$	Neglected	
Oscilloscope input	- 21.55 dBm	

Which at the LO-port would be attenuated to -4.54 dBm. Nevertheless should the output amplifier (VMMK-2503) at this port, terminate most of the reflected power with a S12 of -17.6 dB together with the Wilkinson power divider at its input. Theoretically were it estimated that the working condition of the VCO/PLL circuit would not be affected by the used setup.

The data from the oscilloscope were then obtained by .bin-file manual transfer, to insure both long and short measurements. However should it be noted that the VISA-USB transfer scheme, were fully capable of making long measurements because of the lowered sampling frequency. Nevertheless were the .bin-scheme still used for conviniance to insure a good agility to the sampling frequency settings. Thus allowing the waveform to be obtained with a variety of sampling frequencies without thinking about the limitations to the data transfer. The transfer of data files were performed as described in section 5.1.2.

5.2.1. Beat Frequency Simulations and Processing

To study the resulting beat of the real measurement, were an ideal beat frequency generated in MATLAB to act as an reference to the real one. The simulated beat frequency were generated by initializing two separate waveforms with the measured power properties from section 4.1 and the results of the *apparent waveform* obtained in the spectrogram analysis (table 5.1.4). By using the previous *waveform*-function (B.1.1) with added functionality of signal delay and additional signal length, were a simulated theoretical reference generated. The beat frequency were theoretically enabled by complex conjugated multiplication as described in theory (section 2.4). The new functionality were added to simulate the excessive delay in the TX-signal path to mixer and to simulate the real signal length of the hold period. The source code for the new waveform function and mixing can be reviewed in appendix B.1.7. All other processing was performed as previously with done *FFT* and *Spectrograms*. However were the parameters for FFT precision and spectrogram resolution, changed.

During the measurement did the spectrograms suffer from low observability caused by the high noise level around zero frequency. Hence were a high pass digital filter implemented via MATLAB as previously done, to remove most of the 1/f-noise. A FIR filter with stop frequency at 10 kHz were implemented to do the job. However is this filter not taken into the thesis because of its resemblance to the last implemented filter and to reduce the overall length of the thesis.

5.2.2. Beat Frequency Results

The real measurement were performed with a variety of sampling frequencies and acquisition lengths, to study the impact of sampling window to beat observability. However did the experiment show as expected that the use of excessively large sampling frequencies compared to maximal beat frequencies will set unnecessarily high demands to FFT precision to obtain good spectral response. Thus were a sampling frequency of 1 MHz used, to obtain the beat output. However seen in relation to the parameter set in table 4.1.2 for static targets, were the sampling frequency considerably higher. Nevertheless were the following done since the oscilloscope had a limited choice of f_s-presets. However did this enable the possibility to see the impacts of different FFT precisions.

Beat Spectrum:

The initial measurement of beat spectrum were done with sampling frequency $\mathrm{f_s} = 1\ \mathrm{MHz}$ and $\mathrm{Acquisition\ time} = 2\ \mathrm{ms}$. The reduced sampling window compared to previous waveform studies, were now possible since the beat frequency appeared as an pulse in spectrum and thus enabling the beat to be triggered in the oscilloscope. The pulsed output expected due to the previously revealed mismatch between waveform chirp time and hold time. To match the FMCW properties in derived in table 4.1.2 were the NFFT set to 65536 to obtain a similar receiver resolution, hence $\Delta \mathrm{f_{rec}} = 15.3\ \mathrm{Hz}$. The theoretical

simulated beat were generated with the corresponding parameters to the real measure-measurement.

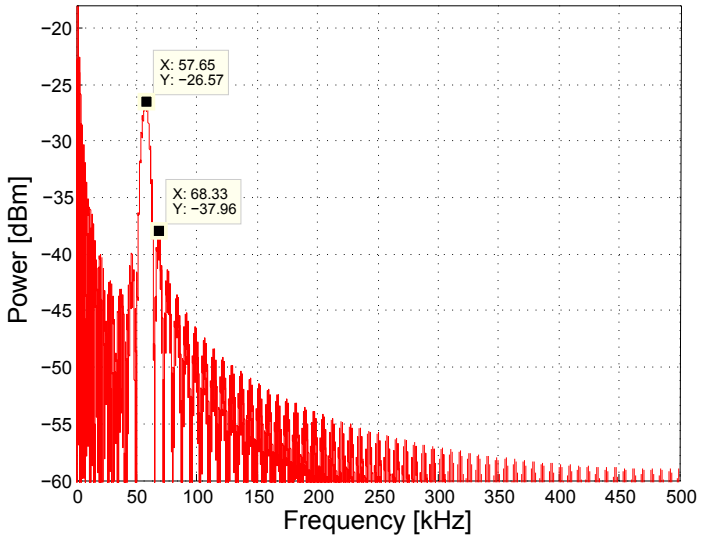

Figure 5.16.: Simulated beat spectrum, $\mathrm{t}_0 = 132\,\mu\mathrm{s}$, $\mathrm{t}_{\mathrm{hold}} = 1.868\,\mathrm{ms}$

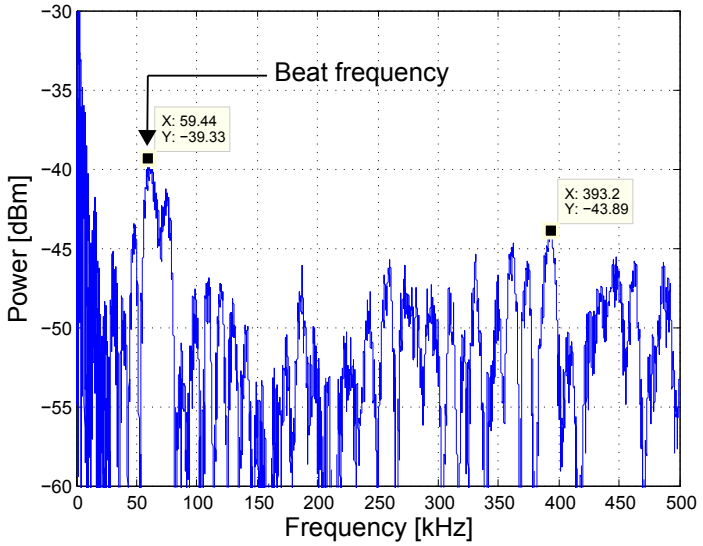

Figure 5.17.: Measured beat spectrum, $\mathrm{f_s} = 1\,\mathrm{MHz}$, Acq. time $= 2\,\mathrm{ms}$, $N_{FFT} = 65536$

The measured and theoretical spectrum's were then compared (figure 5.18). Since the were great ambiguity to the real chirp time the theoretical spectrum were shifted to match the real spectrum. Additionally were the power level also aligned so the two were comparable in form. To enhance the observability both spectrum's were applied a *hamming* window.

Observations:

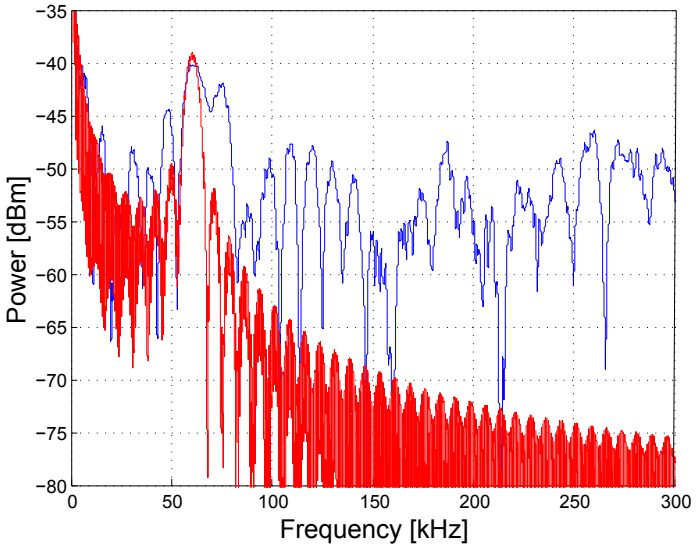

Figure 5.18.: Compared beat spectrum, Hamming, $\mathrm{f_s} = 1\,\mathrm{MHz},\ \mathrm{Acq.\,time} = 2\,\mathrm{ms},\ N_{FFT} = 65536$

Table 5.6.: Beat frequency properties of simulated and measured spectrum

Properties	Simulated	Measured	Deviation
f_b	57.65 kHz	59,44 kHz	1.79 kHz
R	6,05 m	6.23 m	0.18 m
$\Delta P_{sidelobe}$	11.40 dB	2.19 dB	9.21 dB
SNR	-	4.6 dB	-
Remark	Nearest sidelobe shifts due to shift of delay	High sidelobes Low SNR	

The theoretical beat frequency spectrum in figure 5.16, showed great resemblance with theory and were accepted as an valid reference. Compared with the theoretical RAF main lobe zero-to-zero bandwidth that yield 15.15 kHz with 132μs chirp time, the simulated yield 15.08 kHz bandwidth, that could said to be good anougth. However does the use of FFT always be a power spectrum estimation, but nevertheless valid for FMCW since FFT's are mostly used for spectral extraction. The deviation to the ideal spectrum can thus be seen as the small variations to the main lobe of the plot, and comes from FFT truncation and non-infinite resolution. As seen from the simulated beat plot and table 5.2.2, had the theoretical the beat frequency low sidelobes, with the closest at sidelobe-to-main lobe difference $\Delta \mathrm{P_{sidelobe}} = 11.4\,\mathrm{dB}$. The figure also illustrates how the mixing of waveforms with long hold periods and short chirp periods will result in more power around zero frequency. Hence seen in picture as the 1/f-like region. This would then yield less power to the desired beat, than if the waveform had been made only out of chirps or the receiver had allowed segmented processing only over the chirp peiodes.

Figure 5.17 show the real measured beat spectrum, processed with the same high receiver

resolution. The figure revealed the true noisy spectrum of a beat output, although the laboratory setup was quite idealized with the echo delay returning from a cabled synthesis. The beat frequency could be identified, but with a low margin to next highest peak in spectrum. Additionally was the beat frequency main lobe severely corrupted with high sidelobes (margin 2.19 dB), that yielded ambiguity to the true beat frequency. To compare the theoretical and measured spectrum, was the theoretical fitted to the real main lobe. Since there were great ambiguity to the real chirp duration and hence the true beat frequency. Furthermore were the power levels aligned to see resemblance of Sinc(X) output. Figure 5.18 show the great resemblance with main-lobe and sidelobes positions between the two. However were the noise level considerably higher in the measured. Additionally did the shift in delay done for comparison, also shift the highest sidelobe. Thus indicating that the ambiguity to chirp period was not as bad as first expected. Hence was there a possibility that the small shift in apparent main lobe, was induced by noise and nonlinearities, rather than a errorous estimation of the chirp period. Nevertheless were there a sinc-ed nature at the real spectrum, clearly affected by PN-noise as predicted in section 4.1.3. It was most likely that the laboratory setup with a 12 m cable had decorrelated the PN in TX and LO path anought to affect the signal within the observed spectral region. Hence giving the measured beat an additional low SNR, together with the non-ideal processing interval. Additionally did the compared plot illustrate the large corruptive sidelobes of the real spectrum compared to the simulated. By studies of the beat frequency response to nonlinear waveforms, in section 2.5.2, it was a large possibility that the nonlinearities discovered in the waveform analysis had caused the severe sidelobe levels. However seen from table 5.2.2 were the deviation in beat frequency and corresponding range to the simulated were not that intimidating. Nevertheless will nonlinear degradation of beat frequency resolution and range resolution, be a function of range. Thus implying that the beat main lobe would be fully interconnected with the closest sidelobes as the target gets farther away. Thus should the the test have been conducted with a much longer delay line to get clear of the most noisy PN region to exclude this source of error and confirm nonlinear effects on beat output. However were a much longer waveguide not available for these frequencies.

Although the laboratory setup had revealed small deviations in beat frequency to the simulated, were the SNR of the measured spectrum very low. Thus indicating that a real implementation would have difficulties to obtain the a consistent beat frequency from target responses degrading proportional in signal power with $\propto 1/R^4$. Hence did this show that the modulation needed to be altered, so much more desired beat can be observed for a longer time and hopefully yield more power. Additionally did the experiment also show that the nonlinear effects have to be minimized. Thus by finding a modulation that would possibly yield better conditions for the PLL to generate a more linear response.

Additional to the high resolution spectrum shown above, were the receiver resolution degraded to see the effects in beat spectrum. The experiment showed that the FFT presicion could be decimated down to NFFT=2048, with a $\Delta f = 488\ Hz$ before any notably big changes occurred in spectrum. Hence did this test show that the $f_s = 1\,MHz$ could be used without putting two much constrains to the DAS system, by using adjusted FFT precision.

Similar to the other experiments conducted in the thesis were also the spectrum analyzer used as second reference, hence showing no obvious beat output like captured with the oscilloscope. Nevertheless were a wage beat output obtained with the max-hold trace, but then with severely low beat frequency resolution. This find added to the earlier assumptions that the used spectrum analyzer were not well unsuited for studies of FMCW properties.

Beat Spectrogram

To confirm that the waveform produced a highly pulsed output caused by the extremely short chirp period, were the spectrogram obtained for two sampling windows at 2 ms and 32 ms. Since the spectrogram was dependent of the maximum power to set the color scale, were a HP-filter with stop frequency at 10 kHz used to remove the large noisy region belove and to insure observabilliy.

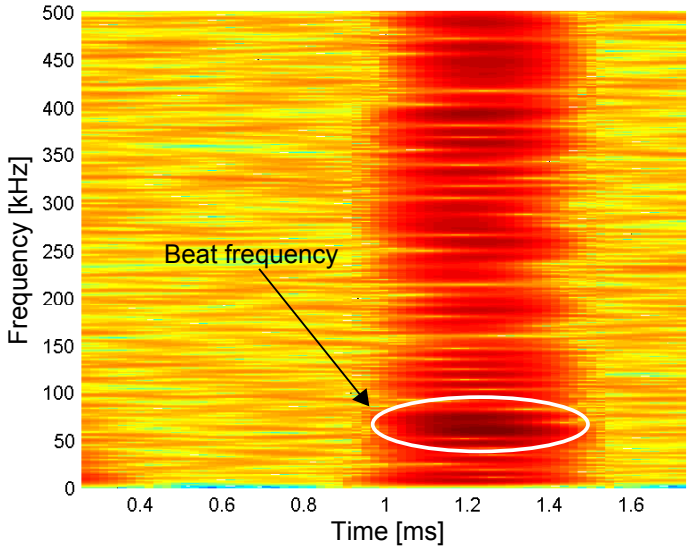

Figure 5.19.: 2D-Spectrogram of measured beat spectrum, processing interval 2ms

Observations:
The figures 5.19 to 5.21 show the beat frequency output in relation to time and frequency, and confirmed that the beat frequency was high pulsed compared with the total processing interval. Thus was the hypothesis of the extremely short chirp to the hold frequencies, finally proven. In relation to the different processing intervals, did the figures reveals that the it would be difficult to get much observable power out of the beat frequency, if the processing interval was long compared to the total modulation time (originally 50 ms). With the use of a shorter processing interval could the beat frequency be more observable. However suffering form low frequency resolution. It was no doubt that the signal source needed to be reprogrammed and hopefully yield better linearity with longer chirp duration.

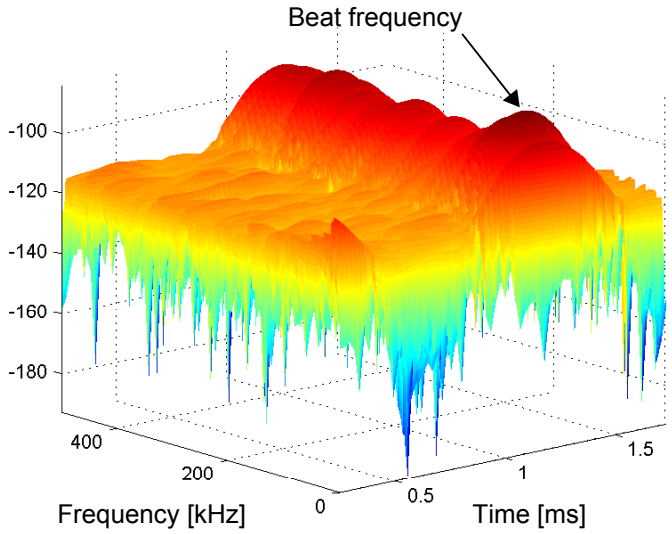

Figure 5.20.: 3D-Spectrogram of measured beat spectrum, processing interval 2ms

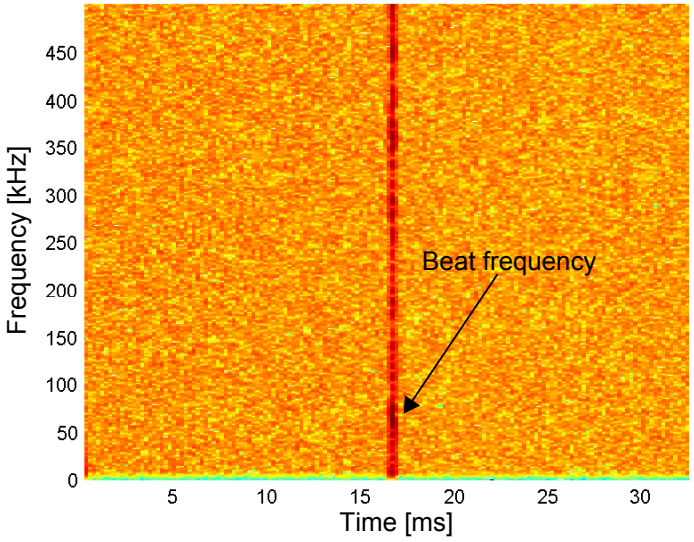

Figure 5.21.: 2D-Spectrogram of measured beat spectrum, processing interval 32ms

Beat Frequency Resolution

As a last and final experiment were the beat frequency resolution studied, to see possible impacts on resolution due to nonlinearities. This experiment were hence inspired by a similar one done by Jankiraman [13, p.338]. The general scheme was to utilize the computability of MATLAB to make an optimum receiver with approximately no contribution to the convolved degraded beat frequency resolution (equation 2.39). Hence to only study the targets response to nonlinearities as the deviation from simulated spectral resolution to the observed real measurement and since no additional truncation comes from reductions in effective bandwidth ($t_0 >> \tau$). However were a sufficiently long coaxial waveguide not obtainable to avoid the noisy region PN region and hence exclude this as an additional source of error. Nevertheless were the specific beat top examined in respect to -3dB resolution to see differences between simulated and measured results to get a figure of the general resolution degradation. The NFFT were set to radix-2 compatible 1052632 to get an optimum receiver frequency resolution of $\Delta f_{rec} = 0.95$ Hz. Further were the beat frequency top zoomed for close studies.

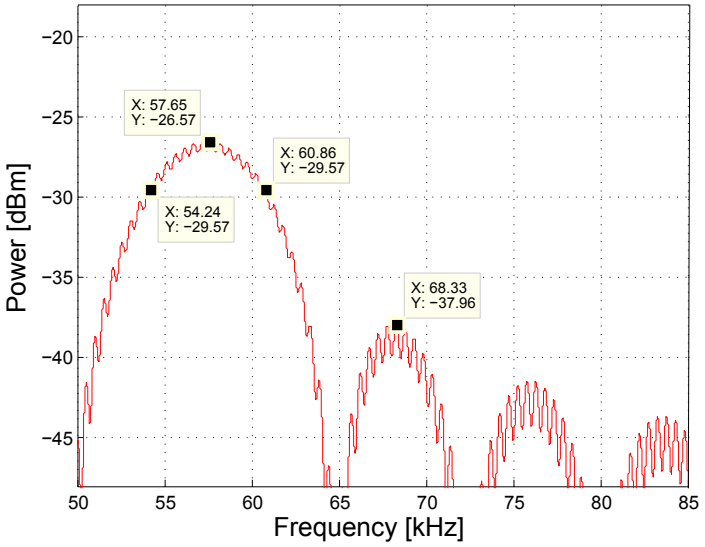

Figure 5.22.: 3dB beat frequency resolution, simulated

Observations:
Figure 5.22 and 5.23 show a large difference in near sidelobe levels. The real measured spectrum yield almost a unseperable main lobe with the closest sidelobe, which was clearly separated in the simulated, both in frequency and power. The simulated does show some distortion to its lobes, however caused by FFT truncation. Similarly did spikes appear at the measured, but however more random, possibly caused by the overall noise. From the studies of nonlinearities in section 5.1.5 and theory in section 2.5.2, showed the measured spectrum a typical nonlinear response in beat spectrum. By looking at the frequency error periodiosity and the large frequency errors at the start and stop of chirp, would in respect to sinusoidal NL be yield more response close to the beat

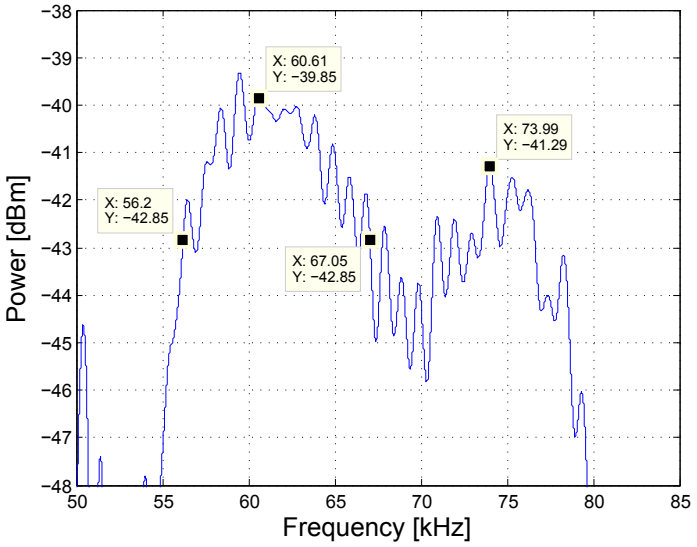

Figure 5.23.: 3dB beat frequency resolution, measured

Table 5.7.: Beat frequency 3dB bandwidth resolution

Properties	Simulated	Measured	Deviation
$\Delta f_b(3dB)$	6.62 kHz	10.85 kHz	4.23 kHz
$\frac{\Delta f_b(3dB)}{\Delta f} \cdot 100$	0.0035%	0.0057%	0.0022%
$\Delta R = \frac{\Delta f_b(3dB)\, t_0\, c}{2\Delta f}$	0.694 m	1.138 m	0.444 m

main lobe with large error amplitudes. Thus was it most likely that the sever frequency error of chirp would had been caused by the nonlinearity. If so, would this mean that the nonlinear effects will have significant degrading impact on the the range resolution further from the radar. With a W-band full radar implementation, would the frequency error also be further increased, proportional with the chirp bandwidth. Hence must the nonlienarites be reduced significatlly, before the full radar is finally implemented.

Table 5.7 show the 3dB main lobe bandwidth, relative bandwidth to frequency sweep and corresponding range resolution for the simulated and measured beat frequency. The table show that there was an notably difference in resolution between simulated and measured beat main lobe. The widening of the lobe were possibly caused by phase noise to main lobe, but also to a superposition of sidelobes to the main by an unidentified source of error. As the measured figure show, could the 3dB main lobe also have been draw across to the nearest sidelobe. If this sidelobe comes from nonlinearities it could be said that with a longer coaxial waveguide, the main lobe would be more degraded with a 'target' at a longer range. It was however obvious that the nonlinearities could **not** be measured directly by this method. Nevertheless did the analysis indicate the relative degradation on

the measured spectrum to the combined effect of noise and nonlinearities. Which again show that the total unideal conditions affected the beat even at 6 m synthesized range. If nonlinearities was a part of this combined degradation it was then likely to believe that the impact even further range would be quite devastating for long range targets. If the $\Delta R_{RSS}(6m)$ is calculated from the L_{se} of waveform, from section 5.1.5, it would yield a range resolution of 0.82 m. Compared with the degraded 3dB beat range resolution at 1.138 m. It seems as the beat main beam of the measured spectrum, will in fact be worse than first expected. Possibly accouring due to an unfavorable mismatch between the nonlinear reference chirp and the nonlinear echo chirp, when correlated in the Rx mixer. Summarized can it be said that this final study indicated that combined effect of PN and nonlinearities will probabilly affect the full scale implementation severely.

5.3. Waveform Evaluation Methods and Waveform Measurement Discussion

Many parameters of FMCW radar was tested in this part of the thesis, to reveal as much as possible of the real output of the LO-board signal source. The thorough work was done to insure a better implemtation of the fully implemented radar at a later stage of the *NTNU automotive radar project*. Experiences with a previous project that involved a tests of a 77GHz radar [35], had revealed that many sources of errors in the full scale implementation could be avoided with a more detailed study of the fundamental circuit and waveform properties. Hence were the focus of this section to examine as much of the fundamental properties as possible and look further into discovered problems.

First of all had the work in this chapter, showed that the use of standard medium performance spectrum analyzers was not the best way to study FMCW waveform properties. The use of high speed oscilloscopes like the Agilent MSO9254A in combination with MATLAB, had however proven to be a more appropriate analyzing tool. Although it was difficult to capture the full waveform with the spectrum analyzer, had the built in trace-functions indicated that the waveform were appropriate (chapter 4). Hence was there a possibility of excepting these results, first hand. However did this chapter show that it was highly relevant to obtain the waveform both in frequency and time, for a full analysis. If FMCW waveform are only studied through a spectrum analyzer, it would reveal nothing about the important time parameters, that would be of most relevance to confirm the relation between the output waveform and the utilized programming code of the radar. Additionally did the experiment also show that the use of spectrum analyzer can only give indications of nonlinearities in the waveform through its output at beat spectrum, but not how much the waveform actually suffers form nonlinearities. Hence would it be appropriate to purpose the two derived measurement methods of *waveform spectrogram-* and *beat frequency analysis* for further work with the radar, in respect to waveform developments. Even though the two derived methods were not fully optimized, would they either way give more knowlage of the true nature of the waveform than the spectrum analyzer and hence help to estimate the beat frequency more accurate. However in respect to the presented measurement setups did the use of VISA-USB connection

from oscilloscope to PC, prove to be inadequate for full memory depth data acquisitions, needed for full waveform analysis. However when used for live measurements of beat frequency output could this oscilloscope connection be recommended for further use in the project, when field measurements are to be conducted in absences of a DAS.

The most important find in this chapter were that the FMCW waveform deviated severely from the documented in respect to time. Thus were much time and effort where put into understanding and testing the oscilloscope settings. Hence since the 40 ms chirp and 10ms hold period that were supposed to be at the output, did not appear in the 2D-spectrogram. Initially was it belived that the oscilloscope triggered automatically on the high- and low hold-frequencies and did not act as an real-time sampler. However by studies of the beat frequency and 3D spectrogram was the extremely short chirp eventually found and isolated in time. Thus confirming that the setup had been correct all the way from the start. The measured chirp was determined to be 132μs, hence invisible when sampled over long time series as were first initiated, to capture the predescribed waveform. In relation to the documented hold frequency period of 10 ms, were this approximated to be close to 50 ms, thus implying that the total modulation time were programmed correctly. Hence was it belived that the chirp finished to early, to an incorrect setting of the rising/falling delta word (RDW/FDW) in the DDS. Logically did this indicated that the RDW/FDW were set too high, thus making few steps between the start and stop frequencies. This assumption could be made since the DDS time step was set to minimum (8 ns) initiated by the RSRR/FSRR-word set to 1, that could not be erroneous.

However did the experiment also reveal that the spectral components of the chirp, were difficult to analyze by FFT-estimates, if the sampling interval was large. This were similar to the finds obtained with the spectrum analyzer, with minimal sweep time of 2.5 ms. However had the start and stop frequencies been visual during all the experiments. Nevertheless when the chirp were identified in the time plot and isolated as an shorter measurement vector, were the true nature of the chirp spectrum revealed in figure 5.6 and 5.8. The isolated FFT analysis showed a severe distortion over the chirp bandwidth, indicating nonlinearities to the chirp. Hence did the isolated analysis illustrate the impotantance of matching the sampling/processing intervals to the FMCW waveform time properties. In the first initial experiments had the processing intevalls been matched to the supposed chirp period of 40 ms. Thus were the discrete power in each spectral component of the chirp, significantly lower than total signal power mostly distributed over the two hold frequencies. The chirp were then hence invisible in the full scale plots of FFT and spectrogram. This effect were also observed in beat spectrum analysis, were the long hold frequencies would yield much power to around zero frequency after down-conversion. Hence would the beat frequency be relatively low and more influenced by noise. This showed that the hold frequencies in such a modulation would have to be significantly shorter than the chirp period or that the sampling must be performed only over the chirp in a segmented fashion.

In chapter 4 did the initial experiment of spectral components revealed no problems of the preprogrammed waveform and it was hence stated that combined DDS/PLL design would not generally suffer from nonlinearities on chirp. However as the spectrogram

figures in section 5.1.4 show, were the examined chirp nonlinear suffering from large frequency deviations. By the looks of the spectrogram did it seemed that the DDS produced a chirp that were mismatched to the PLL working conditions. Hence the fast rolling change of frequencies over the chirp. Thus were it difficult to approximate the measured chirp time. Likewise did the observed spectrogram yield great uncertainty to the match between programmed frequency words in the DDS and the resulting output, since the PLL seemed to not function as it should.

Due to the observed frequency deviation were a linearity study initiated to get a figure to the frequency error and the mean nonlinearity for evaluation of the further waveform developments. Additionally did this test give the opportunity to compare the nonlinear performance against similar designs to estimate a quality of the performance. With the measured spectrograms at different frequency offsets, a metode were developed to extract the maximum power of the chirp signal to be represented as a single value frequency, at each time segment of the chirp. Hence enabling the frequency of chirp to be evaluated against an apparent theoretical slope fitted linear frequency sweep, and then deriving the frequency error of the waveform. Although the metode induced some ambiguity to the real signal max-value was this considered as an neglectable source of error. On the other hand did the selected parameter for the theoretical frequency chirp yield more deviation to the measured frequency error and the derived figures of nonlinearity. Nevertheless would the experiment give some indications to the circuit performance in respect to chirp frequency quality to be evaluated against other designs. When the spectrogram parameters had been applied to the derived algorithm and extracted as an single frequency vector, were the waveform reversely mixed in MATLAB to original Ku-band form the observations of the waveform at IF band. A conversion that had originally been done to overcome the limited analog bandwidth of the oscilloscope. After up-conversion, could the measured waveform be studied as an estimate of the direct output from the LO-board compared with a theoretical linear reference, shown in figure 5.11. From Ku-band could also W-band estimates be derived as an ideal frequency multiplication in MATLAB. Thus could the frequency error estimates at LO-board and MMW-board output be studied.

Although there were conducted few measurements of chirp nonlinearity hence yielding low statistical reability, were the deviations in frequency between each measurement unspereable, thus indicating sufficient validity to the measurements. The few meausuments of chirp spectrograms were caused by the impractical manual transferring of .bin-files. Hence induced by reading problems with the VISA-USB-connection for maximal oscilloscope memory depth, that was needed to capture the extremely short chirp in relation to the hold period. Nevertheless did the experiment indicate large frequency errors with both large variations in frequency-error amplitude and variations in error periodicity (table 5.1.5). Compared with frequency errors measured for other FMCW W-band DDS-PLL signal sources like [44] and [20] were the maximum frequency error lay in the region of 150kHz to 7MHz. In contrast did the tested circuit produced a estimated maximal frequency deviation around 148.5 MHz and RMSE at 40MHz. Although there were some unsertianty the the curve fitting, were the best estimate of measured maximal frequency error mismatched compared to [44] by a factor of 1000. Thus indicating that the circuit were operating under undesirable working conditions and that the beat frequency would be highly affected by the waveform nonlinearities. This important find

resulted in an further examination of the beat frequency. It was also assumed from the experiment that the PLL, did not match the current modulation. Hence implying that programming of the DDS had to be reviewed to obtain longer chirp modulations and hopefully better linear performance. If the linearities were to appear after reprogramming, does this indicate that the PLL circuit design needs to be reviewed or a syncroniced selective sampling should be enabled.

As a supplementive test to the discovered mismatches found in the waveform analysis, were the resulting beat frequency studied. The beat frequency were synthesized in a laboratory setup by delaying the TX output from the LO-board with a long coaxial waveguide, then mixed together with the LO-output. With a 12 m longer TX signal path than LO, an ideal target at 6 m range were synthesized. Although the chirp output from the LO-board were restricted to a sweep bandwidth of 188.762 MHz, hence producing beat frequencies far down in the 1/f-noise region for ms chirps at this range, did the discovered sweep time of 132μs would however yield a theoretic beat at 57.65 kHz. Thus enabling the beat to be visual. The measurement showed that the synthezised beat frequency appeared at 59.44 kHz, with a 1.79 kHz deviation to the simulated. Consequently were there only a 0.18 m mismatch to the simulated, with quite similar spectral positioning of measured sinc(X)-lobes to the simulated. However were the beat frequency main-lobe heavily affected by the closest side lobes, thus making an almost unseperable main-lobe between these.

Figure 5.17 to 5.18 and table 5.2.2, show that the sensitivity to the closest sidelobe were only 2.19 dB. Hence were there actually an ambiguity to the real beat main lobe by the curuptive sidelobes, only at 6 m synthesized range. Since the large side lobes showed great resemblance to waveform nonlinearity affecting the beat [27], were the effects on the full radar implementation with the current waveform were considered to be highly unperferable. Consequently due to the fact that nonlinearities on waveform will enhance the corruption of the beat output as a function of range. In addition did the experiment also indicate influence from phase noise to the beat spectrum, as random cancellations and enhancements within the sinc(X)-lobes. This find corresponded well with PN measurement done in chapter 4, which had predicted PN influence after down-conversion within the observed beat spectrum region. Nevertheless did the simulation of beat, show that the most noisy region around zero frequency were probably more influenced by the down-conversion of CW frequencies that would yield a significant contribution to the power in that region. Hence did this show that waveform need to minimize the duration of the hold frequencies or synchronize the sampling at the chirp. This problem were heavily indicated by the spectrogram study of the beat output, were frequencies belove 10 kHz had to be removed by filtering to allow the beat to be visual compared to the excessive amount of power around zero frequency. The spectrograms of the beat showed that the chirp time was too short compared to the hold periods and that the desired beat suffered from low SNR to the rest of the sinc(X)-output. Furthermore were also the beat frequency spectral resolution examined at the 3dB bandwidth of the beat frequency main-lobe. The experiment showed that the were a 4.23 kHz deviation between simulated beat main lobe and measured. It also revealed that it would be difficult to determine the beat as a singular frequency due to the closest sidelobe, in a real implementation when the target range is unknown. The 3dB range resolution were in this

part estimated to 1.138 m. Compared with the estimated RSS range resolution base on the RSME nonlinearity (0.82 m), were the measured 3dB resolution of the beat worse.

The observations of beat spectrum did not fully confirm which source of error, that produced the observed corruptive effects in spectrum, since the PN could not be eliminated by the used laboratory setup. However could it be said that the combined effect of probably PN and nonlinearities, resulted in a overall SNR to desired beat frequency by 4.6 dB, when the closest sidelobes were neglected. Thus indicating that both the design of waveform, PN and nonlinearities need to be improve before a full radar implementation. However in respect to PN the full radar design, as described in the radar documentation [5]. Should it however benefit the correlation of PN through a matched bistatic antenna noise leakage and thus reduce the overall PN. However can this not be tested before a full radar is up and running.

Summarized did this chapter indicate by the total analysis, that the preprogrammed waveform delivered from the industry partner were unmatched to the documented specification and hence possibly unmatched to the PLL circuit design. To further develop the signal source for a full scale radar implementation, had the programming of the DDS to be reviewed and correspondingly test possible new settings through the used analyzing methods in this part. Thus to yield validity to new programming and hopefully yield better performance of the circuit. The discovered problems with the tested waveform are summarized in figure 5.24.

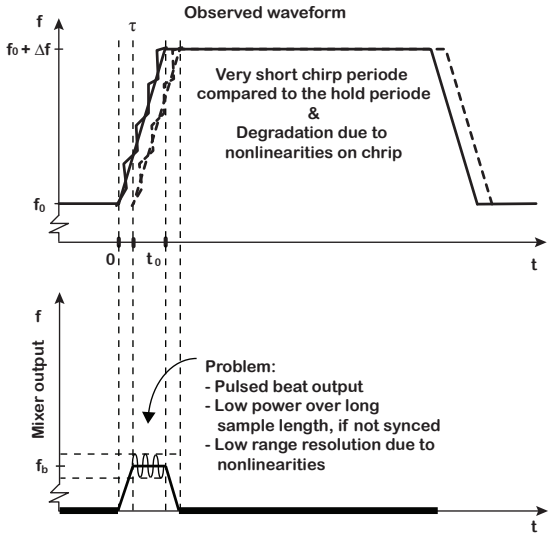

Figure 5.24.: Problems with preprogrammed waveform seen in frequency and time

6. Solving Erroneous Waveform Generation and Development of New Waveforms

Since the previous waveform analysis in chapter 5, had revealed large deviation between measured waveform properties and the radar documentation, had the circuit programming to be reviewed. Hence to confirm if the problem was software or hardware related. By making use of the same waveform analyzing methods as in the last chapter, could new developed programming and waveforms thus be tested and validated. The first goal of this next step of thesis were to find the source of error of the previous corrupted waveform and possible solutions to it. If so, would the next step be to also development of new applicable waveforms, implement them to circuit and test these to make the circuit suitable for a full scale W-band radar implementation. Thus by over holding the *ESTI* radar requirements [7, p.4] and finding modulations that would suppress unwanted nonlinear behavior and produce suitable beat frequencies for use at the automotive radar band.

In order to test out new programming, had this part of the thesis to involve studies of DDS and PLL programming and see how the supplied code from the industry partner were coherent with the circuit documentation, [10] and [9]. Additionally had also modification of the code to be programmed to circuit by the JTAG interface. Hence to test and validate new waveform properties. Thus had compatible software and interface hardware to be implemented as well.

The initial analysis of the preprogrammed waveform had implied that there were a possible mismatch of frequency modulation word settings (RDW/FDW) to the PLL circuit frequency lock time, thus making unfavorable conditions for linear chirp generation. Hence were much of the work concentrated in to quality assurance of the connection between DDS modulation settings and the real waveform output from LO-board. Thus in respect to time and frequency parameters. However were it in this part more appropriate to estimate the waveform output at full scale W-band. Thus were the previously derived method of obtaining waveform spectrograms, together with the maximum signal power method, used to estimate more interpretable frequency parameters at W-band by ideal MATLAB upconversion. Nevertheless would all the measured time properties be consistent at W-band output and had thus not to be considered as estimates. Additionally were also the synthetic beat frequency output to be tested to see the impact on hopefully better modulations than the periviously analyzed one.

6.1. Microcontroller Settings and Programming

Since the LO-board DDS and PLL's were controlled by the ATmega 64-16AU microcontroller, was a AVRDragon 8-bit de-bugger/emulator used together with the AVR studio 4 software, to compile and write new code into the microcontroller flash memory. Additionally were a suited 1,27 mm connector made, to fit the non-standard 'mini-JTAG' interface supplied on the LO-board. Hence shown in figure 6.1. To program the LO-board for new waveform modulations were the existing C programming code supplied by NORBIT used as fundment. Hence since minor changes to the overall code were supposedly needed. However were all programming theory for the DDS and PLL studied to understand the existing programming code and the following changes that had to be made.

The following software, hardware and documentation were use to perform the reprogramming of the LO-board:

- **LO-board**:
  NORBIT, Powered up to enable reprogramming, ATmega64-16AU, 8 MHz.
- **Emulator**:
  Atmel, AVRDragon,Emulator/De-bugger, 8-bit, JTAG.
- **Emulator Driver**:
  Atmel, AVRDragon USB-Driver.
- **Software**:
  Atmel, AVR Studio 4.
- **Programming Code**:
  NORBIT, C-code for timing/control and register setting of DDS and PLL.
- **Connector**:
  Harwin, M50-350-series, 1,27 mm, 10-pin (mini-JTAG).
- **Connector Cable**:
  Self made, JTAG to mini-JTAG interconnector (AVRDragon to LO-board).
- **Laptop**:
  HP, Elitebook 8540w, 8GB RAM, Intel i7 620M.
- **Programming Documentation-1**:
  NORBIT. Technical Note, Microcontroller Requirements,[34].
- **Programming Documentation-2**:
  Analog Devices. AD 4107 PLL datasheet,[9].
- **Programming Documentation-3**:
  Analog Devices. AD 9958 DDS datasheet,[10].

6.1.1. Microcontroller Setup

To add changes and new programming to the circuit microcontroller, were *AVR studio 4* used as software tool for building and compiling new assembler-code instructions from the existing C-code. Further were the AVRDragon emulator used to load the new instruction from the PC to circuit. With use of a customized JTAG-to-miniJTAG cable, the circuit interface were hence connected to the emulator as shown in figure 6.1. The order of operation were done in accordance with the AVRDragon documentation. Hence compiling code, connect emulator by AVR studio, then power up μC by normal circuit bias and then write to μC-flash memory. The existing C-code used the timing

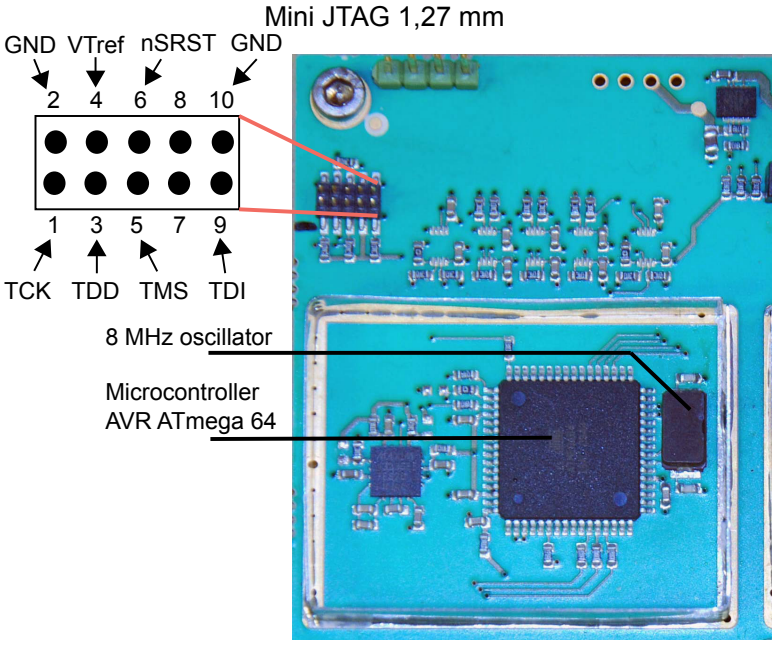

Figure 6.1.: Programming through mini JTAG interface on LO-board

of μC to control the DDS and PLL circuit. Hence to write desired register values to the specific integrated circuit at the desired timing intervals. The overall register settings and additional circuit operations can be reviewed in the radar μC programming documentation [34] and the DDS/PLL documentation, respectively [10]/[9].

Although the DDS and PLL circuits could be operated as autonome circuits by the use of direct SPI programing and full timing by own clock frequencies, the overall control by the μC enabled a easier interface to control all settings directly through the deliverered source code. The PLL circuit were hence fully controlled by the microcontroller since it only have to have appropriate register positions set high or low in order to operate correctly, at a suitable clock frequency supplied by the μC. However were the DDS operation in addition also dependent of the circuits external 500 MHz clock frequency, in order to produce high quality signals with low spurs and minimum influence from signal images, at the desired output frequency region from 65 to 66 MHz. Hence were the programming of the DDS differentiated in terms of timing and frequency references, using the DDS direct clock frequency for frequency word settings (f_{sys}), the fractional

synchronizing clock for time resolution setting ($f_{sync} = f_{sys}/4$) [10] and the μC timing for register updating and initiating timing of the frequency modulation (Profile Pin) [34].

The general idea of the provided microcontroller source code was to allow manual control of different modulations and frequency outputs by the use of the LO-board mechanical rotary switch. Hence were the program main file case-based, giving different control sequences to the DDS through each switch position by the use of methods that were setting the specific DDS registers. The used DDS and overall circuit design were originally provided with a two channel operation. However in this fundamental investigation of circuit and modulations the radar signal source were operated as a single channel. Hence were channel 1 (CH1) disabled via programming throughout the thesis.

The general concepts of DDS and PLL settings is described in the two following subsections. Additionally are the applied timing and methods further described in section 6.2 and appendix C.1 as some corrections were made to the delivered documentation and source code.

6.1.2. DDS Setup

To operate the DDS as described in section A.11 the desired frequency words needed to be set along with with the general operation register settings described in radar documentation [34]. In aspect of pure frequency modulation the most important DDS settings are the single frequency and frequency sweep settings, in order to define appropriate modulation.

Single Frequency Setting:
The output frequency from the current DDS, was predefined by the frequency tuning word FTW, the presicion of the phase accumulator (2^{32}) and the DDS main clock ($f_{sys} = 500\ MHz$).

$$f_{DDS} = \frac{FTW}{2^{32}} \cdot f_{sys}$$

By rearranging the above expression the FTW could be set to a desired DDS output frequency. By this relation were the CW set to the desired CW frequencies and the start/stop frequencies of the DDS in frequency sweep mode
($\mathrm{FTW0} = \mathrm{S_0(start)}$, $\mathrm{FTW1} = \mathrm{E_0(stop)}$).

$$FTW = \frac{f_{DDS}}{f_{sys}} \cdot 2^{32} \tag{6.1}$$

Frequency Sweep Setting:

Further more were the DDS programmed for different types of frequency sweep modes/ modulations. The AD9958 DDS allowed two general linear frequency modulations schemes, hence up-chirp modulation and triangular. The selection of modulation were enabled by setting appropriate register values. To operate the DDS as a LFM signal

source, two initial register positions needed to be set, CFR[23:22]=2 to enable frequency sweep and CFR[14]=1 to enable linear modulation. Additionally to assign the desired modulation of up-chirp or triangular mode the DDS had to be assigned a value to the NODWELL-register position, respectively high or low. The no-dwell-high yield that the frequency sweep are only performed one way, sweeping from a start frequency (S_0) to a stop frequency (E_0) and further reseting the modulation to start over again at S_0 at next initiation of sweep start. On the other hand would no-dwell-low yield both use of frequency sweeps both up and down, shown in figure 6.2, 6.3 and 6.4.

Figure 6.2 is taken from the DDS datasheet [10] to show the setting of frequency word that would make out the chirp/waveform.

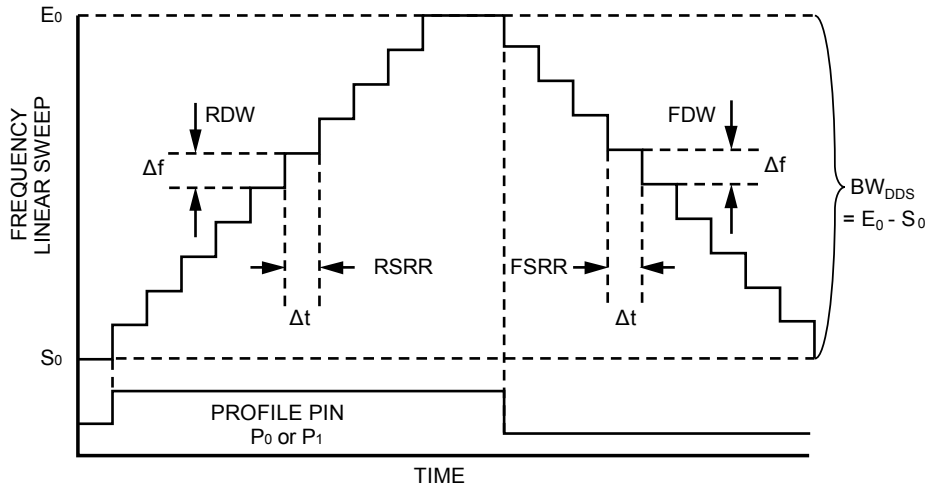

Figure 6.2.: DDS frequency sweep tuning words

The above figure show that the *profile pin* in the desired channel (P_0 *or* P_1), defines the modulation period of the waveform until the next sweep will be initiated. Thus was it important to align the sweep rate between S_0 and E_0 such that the sweep time were as desired and thus corresponding to the time were profile pin were set high, since the next sweep did not occur until the profile pin was set high again. However in the case of no-dwell enabled (up-chirp), would profile pin set to zero, yield immediate start-up after E_0 had been reached. Since the DDS had been overrided by the microcontroller, the profile pin timing had to be set appropriately through the source code ($TASK\_DELAY$).

In addition had also the sweep rate to be set appropriately to achieve the desired modulation in respect to frequency and time since the sweep would eventually stop after E_0 had been reached. The frequency step of DDS Δf, seen in figure 6.2, were depend of the defined raising delta word (RDW/FDW), the frequency word resolution of 32-bit (2^32) and the system clock.

$$\Delta f = \frac{RDW}{2^{32}} \cdot f_{sys} \tag{6.2}$$

Hence could RDW or FDW be obtained by rearranging the equation for a desired Δf. Also seen from figure 6.2 did the time step Δt have to be set, which together with the RDW/FDW defines the chirp rate of the sweep. Notably did the relation between Δt and

Δt also define the chirp time, since the sweep finishes when the f_{DDS} would reach the value of the stop frequency, seen in figure 6.2 as E_0. The time step was defined by the raising/falling sweep ramp rate word (RSRR/FSRR) and the DDS syncronisation clock $f_{sync} = f_{sys}/4 = 125MHz$.

$$\Delta t = \frac{1}{f_{sync}} \cdot RSSR \tag{6.3}$$

Since it is desired for FMCW radars to yield good frequency linearity the time resolution was set to a minimum, by RSRR/FSRR = 1. Thus implying that more and smaller frequency steps were needed to uphold the desired chirp time. With RSRR and FSRR set to 1 the resulting minimum time step were 8 ns.

Up-chirp modulation:

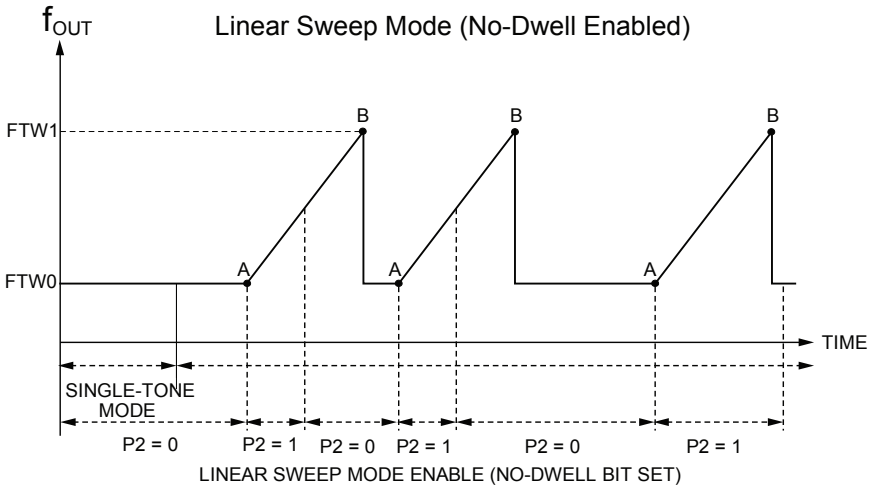

Figure 6.3.: DDS register setting, operating in up-chirp mode

Figure 6.3 show the basic operation of the DDS in no-dwell mode (up-chirp)[10], were A defines the start up of modulation (profile pin high). The point B is hence the point of modulation where the stop frequency have been reached ($FTW1 = E_0$), and the modulation starts over again at next profile pin high.

Triangular modulation:

Figure 6.4 show the scheme of the DDS operated as triangular modulation signal source. The point A still yield to the position were the up-sweep is initiated by the profile pin. However would the dwell now insure no start-up of down-sweep until pin have been disabled. Hence would the total time this pin were high make out the modulation period of chirp with hold until next modulation starts over sweep in another direction.

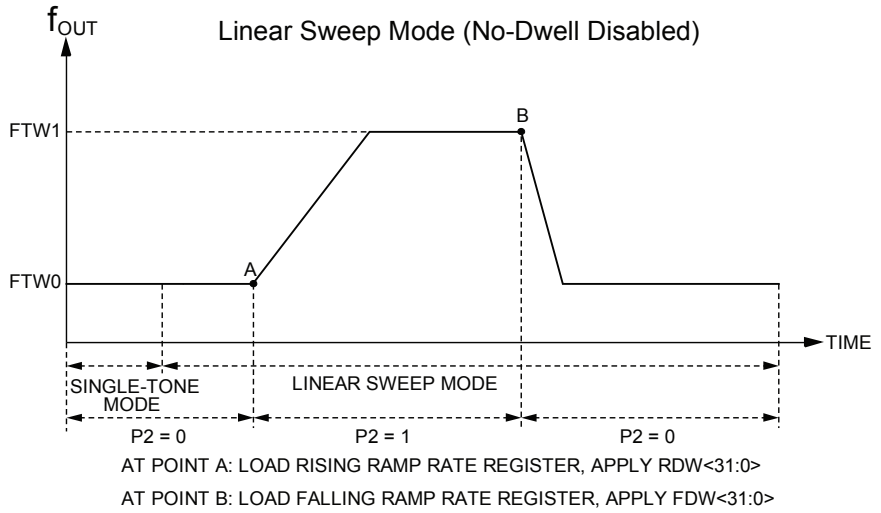

Figure 6.4.: DDS register setting, operating in pure triangular or hold mode

6.1.3. PLL Setup

The PLL circuit programming was not changed in this thesis, since the PLL after all seemed to functions as it should and that most work had to be done with the DDS to get the modulation right. The PLL control was initiated by register setting and timing control done by the microcontroller. The used register settings can be reviewed in radar programming documentation [34, p.3] with further reference to the Analog Devices PLL datasheet [9]. The used basic PLL parameters and desired functionality in the full radar implementation are hence shown in the following relations:

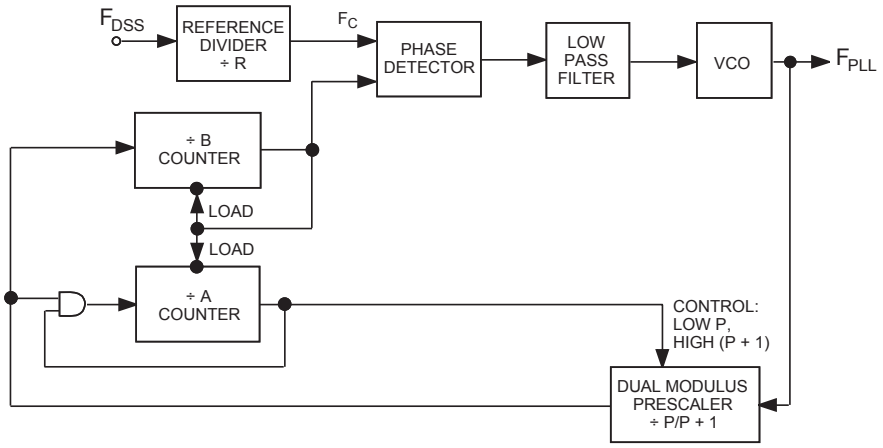

Figure 6.5.: PLL basic operation, [22, p.2]

The PLL would act as an efficient x97 frequency multiplier by setting

$$\begin{aligned} P =& 32 \\ B =& 3 \\ A =& 1 \\ R =& 1 \\ f_{PLL} =& \frac{((P \cdot B) + A)}{R} \cdot f_{DDS} \end{aligned} \tag{6.4}$$

By the use of the 12 GHz output VCO from LO board the output frequency will be

$$f_{LO-board} = f_{PLL} \cdot 2$$

In the further implementation will a x6 frequency multiplier also be implemented, thus

$$f_{MMW} = f_{DDS} \cdot 97 \cdot 2 \cdot 6 = f_{DDS} \times 1164 \tag{6.5}$$

To for fill the 1 GHz demand from 76 to 77 GHz at W-band, the DDS output would hence be restricted to

$$f_{DDS} = \{65.292\ ,\ 66.151\} \quad [MHz] \tag{6.6}$$

6.2. Corrections to Radar Documentation and Programming

In previous analysis of the preprogrammed waveform was it discovered that the output from the LO-board mismatched the predescribed programming documentation [34, p.5]. Hence were the programming code reviewed. The review of code versus output, seen in relation to figure 6.2, discovered that profile pin (P_0), were set correct with a total modulation time of 50 ms between each new sweep. However were the DDS frequency step Δf set to 200 Hz, matched to a total frequency sweep of 1 GHz. In contrast should the chirp rate instead have been matched to the bandwidth of the DDS output (BW_{DDS}), as the frequency sweep is automatically terminated at the stop frequency (E_0, at DDS output). When the stop frequency in contrast had been set correctly to 66.265 MHz matched to the DDS output, the chirp was supposedly terminated after the measured 132μs with the Δt set to 8 ns. As previously measured were also the chirp bandwidth to wide according to the ESTI requirement, making the stop frequency appear at 77.132 GHz. Thus were it appropriate to change the DDS stop frequency, in addition to new matching of the chirp rate for a correct chirp sweep time. However was the measured chirp time not consistent with the new derived theory. According to new theory the

measured chirp time should have been

$$\Delta f = 200\ Hz\ \text{(errorous)}$$

$$S_0 = 65.292\ MHz\ and\ E_0 = 66.265\ MHz$$

$$N_{steps} = \frac{BW_{DDS}}{\Delta f} = \frac{973kHz}{200Hz} = 4865$$

$$t_0 = \Delta t\ \cdot N_{step} = \underline{38.92\mu s}$$

From the sweep time estimate it seemed that the DDS feed a unfavorable chirp in to the PLL. Hence as the spectrograms in section 5.1.4 show did it seemed that the PLL were struggling to find some reference within the chirp and wiggling about with large variations in frequency until it finally got track of the hold frequency after 132μs. This indicated that the chirp time had to be at least set longer than 140mus. By looking at the design note [5, p.39], showing a simulated PLL lock time of 568μs to a 10kHz frequency step, it was decided that the minimum chirp time should be $\geq\ 1\ ms$ to yield a more favorable condition for the PLL, to produce linear chirps.

If the previous modulation should have been used, to generate a modulation of 40 ms chirp and 10 ms hold time, it had to be set accordingly as

$$N_{steps} = \frac{t_0}{\Delta t} = \frac{40ms}{8ns} = 5e6\ \text{time steps}$$

$$\Delta f = \frac{BW_{DDS}}{N_{steps}} = \frac{973kHz}{5e6}$$

$$\Delta f = 0.195\ Hz\ \approx \underline{0.23\ Hz}$$

Rounded to closest Δf which gives an integer RDW/FDW = 2

New t_0 due to rounding, choosing RDW/FDW=2

$$t_0 = 33.8\ ms$$

Additional t_0 due to rounding, choosing RDW/FDW=1

$$t_0 = 66.8\ ms$$

The derived relation show that the use of maximum time resolution(RSRR/FSRR=1), for long modulation periods would be difficult due to frequency word rounding and the fact that the setRDW()/setFDW()-function would only handle integer RDW/FDW. Hence had RSRR and FSRR to be increased if such modulations should be implemented in the further.

6.2.1. Corrected DDS Source Code Settings

From the above relations, section 6.1 and the DDS documentation [10], a general method were derived for correct DDS sweep settings, seen in relation to figure 6.2

First, insure that the modulation period controlled by microcontroller, match the total time of the desired waveform including both the chirp and eventual hold periods (*profile pin*). Set in the C-code as DDS_TASK_DELAY and matching $ROT\_SWITCH\_TASK\_DELAY$ as a decimal number that corresponds to number of ms. Hence the number 50 = 50ms modulation before new frequency sweep will be initiated.

Further derive the desired start and stop frequencies at DDS output in relation to W-band output (see section6.1.3)

$$E_0 = \frac{f_{MMW}(High)}{1164}$$

$$S_0 = \frac{f_{MMW}(low)}{1164}$$

Hence will the DDS chirp bandwidth be

$$BW_{DDS} = E_0 - S_0$$

The desired chirp sweep time will be defined by the DDS time step and number of steps

$$t_0 = \Delta t \cdot N_{step}$$

Thus will the desired chirp time yield the number of steps required

$$N_{step} = \frac{t_0}{\Delta t}$$

Finding the required DDS frequency step that overholds the time requirement

$$\Delta f = \frac{BW_{DDS}}{N_{step}}$$

The required RDW would then be given by equation 6.2

$$RDW = \frac{\Delta f}{f_{sys}} \cdot 2^{32}$$

$$\Downarrow \mathrm{C-code}$$

$$RDW = |RDW_{decimal}|_{HEX}$$

To use this relation in the C-code the decimal RDW needs then further to be converted to HEX-decimal values, to set correct register values. This method would yield for both raising and falling chirps. The used DDS frequency word setting and timing are presented in appendix C.1.

6.2.2. Additional Mircocontroller Source Code Corrections

After new DDS frequency words had been applied to the source code and instructions loaded to circuit, the waveform were analyzed with the spectrogram-method. However did these first tests yield no improvement to the waveform. The same problem with short nonlinear chirps appeared also after corrections to the DDS settings had been made. Several waveforms of different modulations where hence tested. However did the profile pin follow the desired programming, making the total waveform period consistent with programming. This led to a further investigation of the source code since it seemed that chirp were not initiated at all and that the visual chirp moreover could possibly be the frequency transition between large frequency gaps generated by the PLL with no reference within the gap.

After intensive testing of different programming approaches were it hence discovered that the used case-based structure of the source code main file laked a initialization of the RDW and FDW in each *case* switch position. By setting the RDW and FDW by the setRDW() and setFDW() methods within each *case* the new programming applied as it should. The new initialization of the case-based main file are shown in appendix C.1.1. The delivered code had hence initialized the sweep mode correctly but missed setting the ramp rate words at each position. With use of the mechanical switch had thus the previous ramp rate word been erased from μC memory and thus produced a 2-FSK modulation rather than a LFM. Since the DDS circuit was combined with a PLL, had the PLL produced a frequency transition with linear like properties. Seen with a standard spectrum analyzer had thus the transition produced enough power to be mistaken as the desired chirp. As the previous waveform analysis showed, had the transition contained anought linear characteristics to be mistaken for just a unfavorable chirp generation and hence produced a ambiguous waveform to real chirps, seen both in the spectrogram and the linearity test. The linear properties were in fact so 'good' that transition had produced a synthetic beat frequency, but with high nonlinear effects present as described in chapter 5.2. Thus had had source of error been found and all confusion around the previous waveform performance had been caused by a simple programming error. However had the previously derived methods been very essential to identifying that there actually had been a real problem of waveform timing and verification of the validity of new applied code.

After reprogramming with the need initialization, the new waveforms seemed to be flawless compared to the previous transition. However did the initial tests confirm the transition hypothesis, when pure Up-chirp modulations were initiated and closely examined. Figure 6.6 show the zoomed-in frequency transition between two 10ms up-chirp FMCW waveforms obtained with the spectrogram method, purified with the maximum power method and up-converted in MATLAB to W-band. The discovered transition showed great resemblance with the previously studied transition both in frequency deviation and time ($120\ \mu$s). Hence fully confirming the hypothesis and also indicating the circuits typical sweep recovery time (t_{sr}) to up-chirp waveforms.

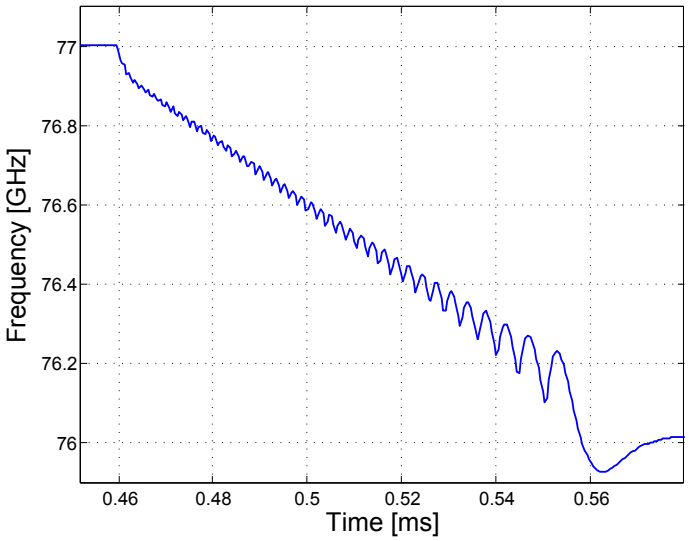

Figure 6.6.: Circuit frequency transition between large frequency gaps, 10ms up-chirp waveform, Upconverted to W-band

6.3. Choice of Beat Frequency and Waveform

Since much of the work in the thesis had consisted of finding suitable waveform evaluation methods and eliminating the source of errors in the delivered circuit, the development of new waveforms were limited to studies of two fundamental FMCW waveforms that could be used further in the full implementation of the radar system. It were then decided to implement the *up-chirp*- and *triangular* continuous waveforms to study LFM properties with previously derived waveform analysis methods. Hence to look at a desirable region of the beat frequency at different chirp rates. Additionally should the waveforms be maximized to exploitation of the preassigned 1 GHz bandwidth at W-band in the future full radar implementation. Although the two waveforms were not suited for multiple Doppler target extraction, they would still be highly preferable for initial range and single Doppler target trails of the full system.

Prior to implementation of the new waveforms were some basic consideration made to the resulting beat frequency at different chirp rates, as described in section 2.7, to have a meaningful measurement set. Since the bandwidth were to be optimized to fit the 1 GHz W-band implementation, the only remaining variable were the chirp time Since the basic property of near clutter influence had not been studied this consideration were left out. Additionally were it also difficult to predict the degree of phase noise cancellation achieved in the full system implementation, although the Tx CW mid-band phase noise had been measured. However would both of these limiting factors desire as high minimum beat frequency as possible. Nevertheless were a general assumption made from previous experience with measurements of bistatic FMCW radars at W-band [35], that the minimum beat frequency should be avoided below 1 kHz for pure ranging. Additionally in respect to Doppler targets sensed with the two chosen waveforms, should the lower limit be set much higher. If a maximum relative velocity between two

approaching cars, is considered to be in range of 200 km/h the resulting Doppler shift would be ±28 kHz. Thus indicating a minimum beat frequency at 29 kHz. However can the demand for minimum range detection be increased correspondingly, although this would then decrease the region of observation considerably for low chirp rates. In addition should also the maximum beat be considered in respect to the later implemented DAS, in respect to its capability to yield high sampling frequency ($2 \cdot f_{d,max}$), its intermediate data storage capacity and data rate handling. Both these limitations have to be reviewed at a later stage of implementation to tune in on the best suited modulation and chirp rate that yield the best radar observability. Additionally could also the later finds in this thesis set limits to the future beat frequency setting and hence modulation in respect to chirp linear quality and effective bandwidth reduction caused by for instance excessive sweep recovery time (HRR-systems 2.7). However had these quality to be measured before any prehand considerations could be made on the subject.

Hence were this thesis investigation restricted to the study the modulation of waveforms in aspect of signal source agility to moreover examine the performance of the fundamental waveforms at different chirp rates. Thus trying to identify the region of chirp rates where the circuit produces good enough waveform quality for LFM-CW beat frequency generation. With this goal in mind were hence a reasonable test region of chirp rates derived according to table 6.1, with 1 GHz bandwidth and the assumption that a desired region of observation were in range of 3 m to 150 m. The chirp time values in table 6.1

Table 6.1.: Beat frequency region at different chirp times

t_0	$f_{b,min}$	$f_{b,max}$
0.1 ms	200 kHz	10 MHz
1 ms	20 kHz	1 MHz
10 ms	2 kHz	100 kHz
20 ms	1 kHz	50 kHz
40 ms	500 Hz	25 kHz

were hence also selected by the limitations given by the ESTI requirements [7, p.4] for 1GHz maximum frequency modulations all within the maximum chirp rates belove or equal to 10000 MHz/ms. Although the perivious testing had alluded problems with short chirps in respect to the PLL lock time, the limits of the ESTI were still used for full confirmation with new programmed waveforms. In the last row of the table were the previously intended 40 ms chirp modulation listed. However as the table show would this waveform produce a unacceptable low beat well in range of the most noisy PN region. Additionally did a possible use of this waveform not be perfered for Doppler sensing applications due to the low minimum beat frequency and possible masking of fast approaching targets. Thus were the 40 ms chirp modulation left out of the test set.

In respect to the actual DDS programming for waveform generation, were there more variables that could be varied. The chirps of waveform could hence be made up of various combinations of DDS frequency steps and corresponding time resolution. However were it decided to limit the experiment further by the used of maximum time step resolution, hence setting RSRR/FSRR equal to 1 and time resolution at each frequency step to effectively 8 ns.

To achieve the desired continuous up-chirp modulation were hence the *nodwell*-enabled and the timing of the profile pin of figure 6.3, set to zero hence enabling a intermediate start-up of next frequency sweep. The actual modified programming for up-chirp modulation, are described in appendix C.1.1. To further set the DDS for triangular modulation as in figure 6.4 were the *nodwell* disabled. Additionally by setting RDW=FDW and RSRR=FSRR were a symmetrical triangular modulation achieved, where the profile pin period was matched to the total chirp modulation time, as described in 6.2. Hence were a pure triangular modulation with no excessive holding time created.

6.4. Time and Spectrum Properties of New Waveforms

After the first reprogrammed waveform failed as described in section 6.2.2. The RDW and FDW methods were initialized within each rotary switch case. Successively were then the time and spectral components of the new waveforms tested to see any changes that could reveal unfavorable conditions to the waveform by first hand examination and to insure a full capture of at least one of the chirps a specially for the long waveforms due to the limited memory depth. However to yield continuity to the last analysis and enable sampling with the oscilloscope, were the waveform down-converted to IF band as described in the method of spectrogram-obtainment(5.1). Hence to have comparable results to the previous analysis. The same LO down conversion frequency were hence used thus yielding new minimum IF offsets at 72 and 121 MHz due to the reduction of waveform bandwidth, from 188.762 MHz to 166.65 MHz, to uphold the overall ESTI requirement.

Figure 6.7, 6.8 and 6.9show the respectively time/FFT plots of a 20 ms triangular waveform and the FFT of a 20 ms up-chirp waveform.

Observations

As the time plot shows, did a quite different time signal appear on the oscilloscope with much smoother attenuations than periviously observed with the preprogrammed waveform (appendix B.11). Hence implying that the frequency dependent attenuation of the test setup, occurred over a longer duration with a approximate periodicity around the programmed modulation period. Additionally did the new programming resulted in a more uniform appearance of the frequency sweep in the FFT spectrum with an mean SNR about 15 dB. In the previous test of the preprogrammed waveform, the chirp had to be isolated in a shorter measurement vector to be visuable (figure 5.8). Now the frequency sweep were clearly visuable with full acquisition windows. Further did also the previous FFT spectrum show some large power variations over the sweep bandwidth, which did not appear in the new programmed waveforms. In contrast did the study of new waveforms yield more spurs in spectrum, however did the spur also appear at the previous FFT if the full acquisition window were applied as seen in figure B.5. Nevertheless

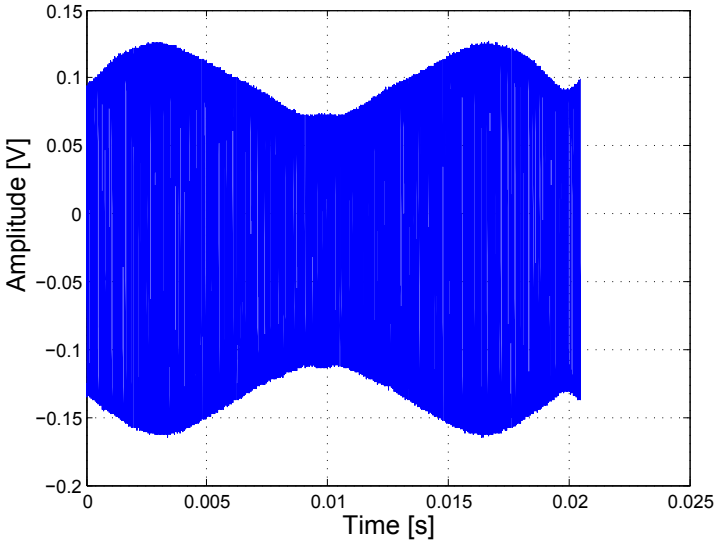

Figure 6.7.: Time plot of triangular waveform, 20.5 ms acq. window, 10ms chirps, 121 MHz offset

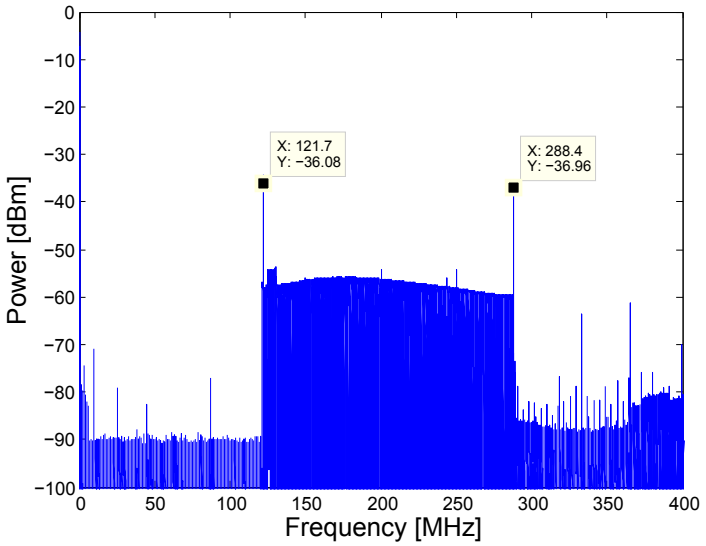

Figure 6.8.: FFT of triangular waveform, 20.5 ms acq. window, 10ms chirps, 121 MHz offset

were a there observed a difference between the newly implemented waveforms, were the up-chirp modulations seemed to have distortions at the frequency sweep endpoints. Seen in relation to the finds in the previous analysis were this a possible indication of end-point nonlinearity present at the up-chirp waveform. Additionally did also the FFT of both cases yield a increase of spectral power at the highest frequencies within the FFT window. This was propablly caused by the additional harmonics of both LO and waveform being mirrored back in to the observed spectrum due to insufficiently high sampling frequency, as observed in the previous spectrogram analysis.

In addition did a corresponding test with the spectrum analyzer, still prove ambigiuos. No capture of the full waveform were detected with a free running trace or operated

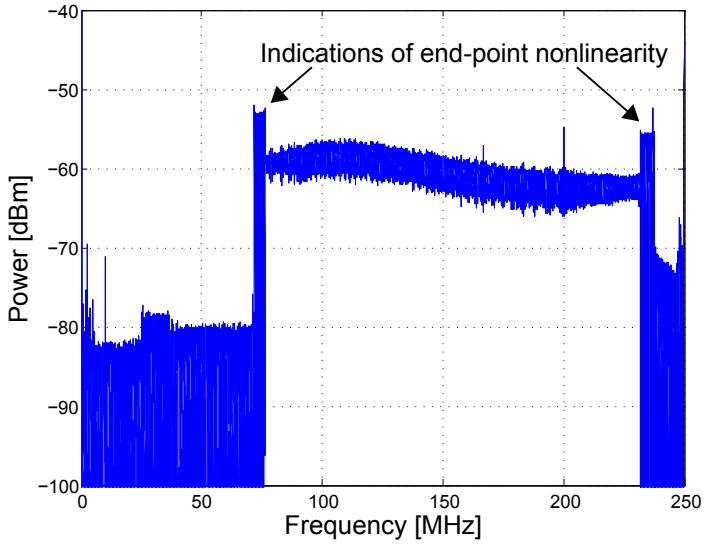

Figure 6.9.: FFT of up-chirp waveform, 41 ms acq. window, 20ms chirps, 72 MHz offset

at FFT mode. With the max-hold trace, did the frequency sweep of waveform still appeared as the preprogrammed one. On the other hand did the average trace deviated to the previous by showing no spectral components over the bandwidth. Hence did this possibly indicate that a fully sweeping waveform had been manage by equally spread frequency power over the linear modulation. However were the testing with the spectrum analyzer considered to still be somewhat ambigiuos to fully confirm that a redesigned good chirp had been implemented. Thus had the previously derived method of obtaining spectrograms, to be used, in order to fully confirm the exact quality and waveform properties after reprogramming.

6.5. New Waveforms Spectrogram and Linearity

The goal of the next step in the analysis of new waveforms, were to confirm their implementation by measurements of the waveform time and frequency properties. Additionally would such measurements yield the difference between the DDS programming and real signal source output. Thus helping to establish a first reference for future development of specialized waveforms for automotive radar applications.

The method of obtaining spectrograms, described in section 5.1, were used to measure the frequency and time properties of the new waveforms. By using downconversion with the same LO frequencies, were consistent waveforms with the identical bandwidth observed at two respective IF bands. The choice of LO frequency were fitted to the waveform modulation length, such that long modulations were converted further down in spectrum to ease the demand for oscilloscope sampling frequency and hence longer acquisition intervals in respect to the maximum oscilloscope memory depth. However were these low IF waveforms more affected by more lost of spectral purity due to the limited choice of oscilloscope sampling frequencies. Hence were therefore the highest

sampling frequency (1 GHz) used in to all measurements, except the 20ms up-chirp and 40 ms triangular waveforms (500 MHz).

However had also the first waveform analysis with the spectrograms also resulted in an method of extracting the maximum power elements of the waveform in order to look at chirp linearity (section 5.1.5). Hence were it seen as beneficial to use this method to yield more accurate estimation of frequency and time parameters, to the waveform centroid that would actually produce the beat frequency along with the possible detection of large frequency deviation power elements that produce nonlinear distortion. By such processing were it hence belived that more accurate information of the waveform could be extracted, that would help with better estimation of the true beat frequency. Additionally had the previous processing also enabled an ideal upconversion to LO-board output, by reverse mixing with the used downconverting LO frequency in MATLAB. Hence were this done in addition to ideal six times frequency multiplication up to W-band to estimate the waveform properties at more applicable frequency region to see the measurements in respect to full radar implementation. All measurements done at IF band are documented with the spectrogram in appendix C.2.1, whereas the W-band waveform estimations are presented in this section.

In addition were also the chirps of the new waveform isolated as in section 5.1.5, to study the linearity parameters. Thus to confirm LFM waveform quality at the part of the waveforms that creates the essential beat frequency. The results of the linearity measurmenst are presented in the latter part of this section.

However should some comments be made to the presented results prehandedly. First of all should it be noted that the programming of the DDS were limited by integer frequency word setting. Thus had the setting of RDW and FDW, that were supposed to fit the desired modulation time, to be rounded to the nearest integer. Hence would the modified resulting modulation time yield as the actual programming to circuit and that the measurements were thus compared to these parameters. Additionally did the implementation of 100 μs modulations fail in achieving full waveform bandwidths, as shown in figure C.4 for the up-chirp waveform. The figure does also show that the chirp is highly nonlinear and that frequency transition are acctualy longer than the desired chirp. The most feasible cause of error were belived to be the PLL ability to follow such fast chirps, as earlier indicated. Thus were the 100 μs chirp modulations of both waveforms seen as unachievable for the tested signal source with the current PLL design and programming.

6.5.1. Measured Triangular Modulation, Estimated at W-band

Triangular 2ms modulation

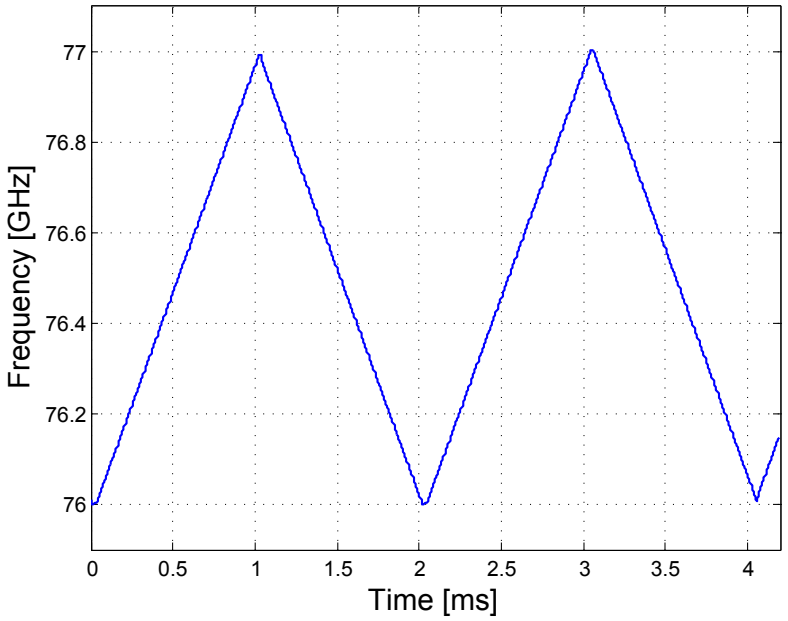

Figure 6.10.: Maximum power signal of triangular waveform, 4.2 ms acq. window, 1ms chirps, upconverted to W-band

Table 6.2.: Waveform properties of new 2 ms triangular modulation at W-band

Properties	**Triangular Modulation**		
	Desired	DDS round	Meas/Est
Δf	1 GHz	999 MHz	989 MHz
t_0	1 ms	1.005 ms	0.997 ms
t_{sr}	0 μs	8 ns	30 μs
t_m	2 ms	2.010 ms	2.024 ms
f_{start} (chirp)	76 GHz	75.999 GHz	76.001 GHz
f_{stop} (chirp)	77 GHz	76.999 GHz	76.990 GHz

Triangular 20ms modulation

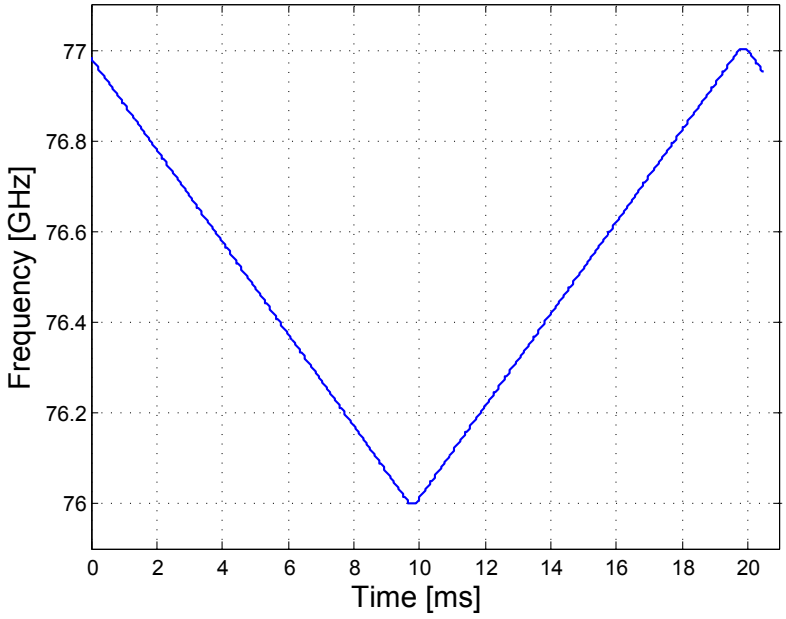

Figure 6.11.: Maximum power signal of triangular waveform, 20.5 ms acq. window, 10ms chirps, upconverted to W-band

Table 6.3.: Waveform properties of new 20 ms triangular modulation at W-band

Properties	**Triangular Modulation**		
	Desired	DDS round	Meas/Est
Δf	1 GHz	999 MHz	988 MHz
t_0	10 ms	9.84 ms	9.93 ms
t_{sr}	0 μs	8 ns	80 μs
t_m	20 ms	19.68 ms	19.94 ms
f_{start} (chirp)	76 GHz	75.998 GHz	76.002 GHz
f_{stop} (chirp)	77 GHz	76.999 GHz	76.990 GHz

Triangular 40ms modulation

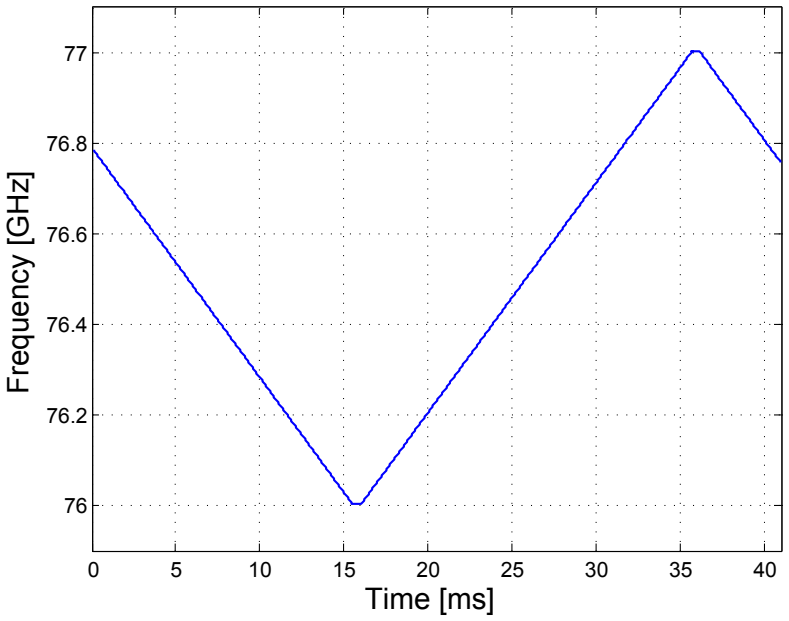

Figure 6.12.: Maximum power signal of triangular waveform, 41 ms acq. window, 20ms chirps, upconverted to W-band

Table 6.4.: Waveform properties of new 40 ms triangular modulation at W-band

	Triangular Modulation		
Properties	Desired	DDS round	Meas/Est
Δf	1 GHz	999 MHz	995 MHz
t_0	20 ms	19.6 ms	19.62 ms
t_{sr}	0 μs	8 ns	300 μs
t_m	40 ms	39.2 ms	39.24 ms
f_{start} (chirp)	76 GHz	75.998 GHz	76.001 GHz
f_{stop} (chirp)	77 GHz	76.999 GHz	76.996 GHz

Observations

As seen from the maximum power signal plots, extracted from the obtained spectrograms in appendix C.2.1, does the overall connexion between programmed waveform and its real output seem quite good. The best achievement were observed in respect to frequency, where a maximum deviation of 1.1% to the programmed bandwidth were observed from the W-band estimates. When compared to the time properties did the 20 ms and 40 ms waveform suffer initial DDS RDW/FDW rounding to the orginally intended. However seen in relation to the programmed did the waveforms seem to very presice in aspect of the chirp modulation time. Nevertheless did the waveforms suffer from more and more sweep recovery time, at longer total modulations. Surely did this observed phenomena

come from the fact that the rounding were more unfavourable for longer modulations and hence deviating more to the used profile-pin-high time that had been set on prior to the measurments equal to the desired modulation time. Seen in relation to the ESTI requirements did these estimate of the new implemented triangular waveforms to yield high exploitation of the allowed frequency modulation bandwidth. Additionally did all the waveforms appear as linear in respect to firsthand visual observarion of the plots and with great accuracy to the acctually programmed frequency words and timing. It should however be noted that the plots only are estimates of the real waveform output from the Ku-band, but the estimates seemed to show great unity to both general theory and programming. Hence were these finds considered to be good results, when compared to the relation between used programming and circuit output.

6.5.2. Measured Up-chirp Modulation, Estimated at W-band

Up-chirp 1ms modulation

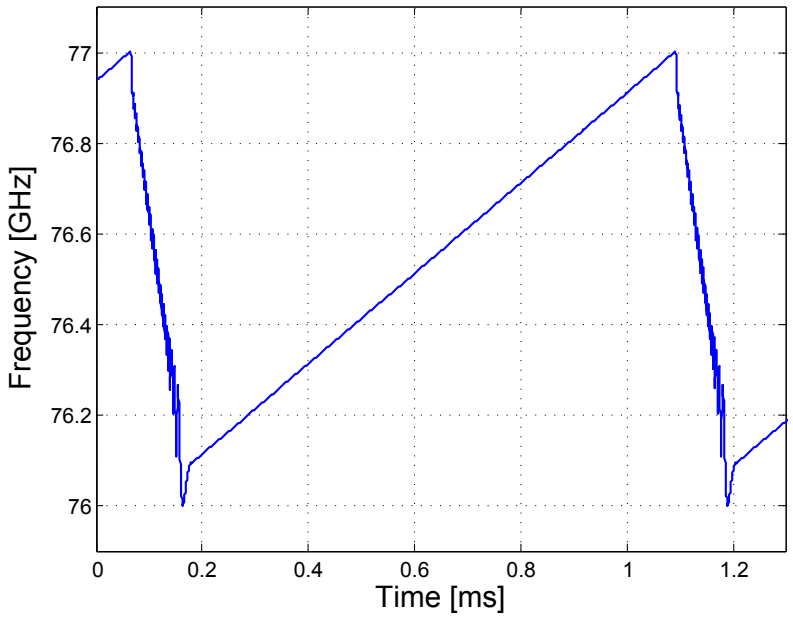

Figure 6.13.: Maximum power signal of up-chirp waveform, 1.3 ms acq. window, 1ms chirps, upconverted to W-band

Table 6.5.: Waveform properties of new 1 ms up-chirp modulation at W-band

Properties	Triangular Modulation		
	Desired	DDS round	Meas/Est
Δf	1 GHz	999 MHz	910 MHz
t_0	1 ms	1.001 ms	0.9037 ms
t_{sr}	0 μs	8 ns	116 μs
t_m	1 ms	1.001 ms	1.02 ms
f_{start} (chirp)	76 GHz	75.998 GHz	76.088 GHz
f_{stop} (chirp)	77 GHz	76.999 GHz	76.998 GHz

Up-chirp 10ms modulation

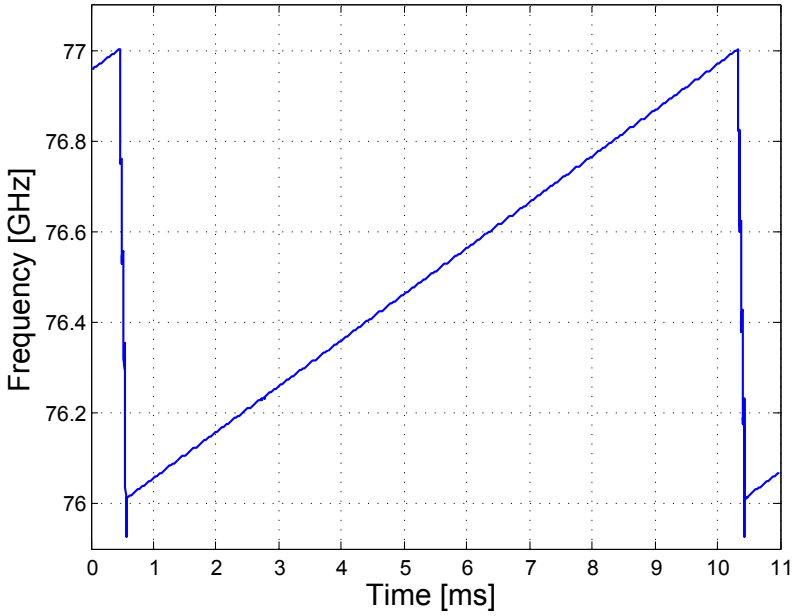

Figure 6.14.: Maximum power signal of up-chirp waveform, 11 ms acq. window, 10ms chirps, upconverted to W-band

Table 6.6.: Waveform properties of new 10 ms up-chirp modulation at W-band

Properties	Triangular Modulation		
	Desired	DDS round	Meas/Est
Δf	1 GHz	999 MHz	989 MHz
t_0	10 ms	9.84 ms	9.77 ms
t_{sr}	0 μs	8 ns	99 μs
t_m	10 ms	9.84 ms	9.87 ms
f_{start} (chirp)	76 GHz	75.998 GHz	76.009 GHz
f_{stop} (chirp)	77 GHz	76.999 GHz	76.998 GHz

Up-chirp 20ms modulation

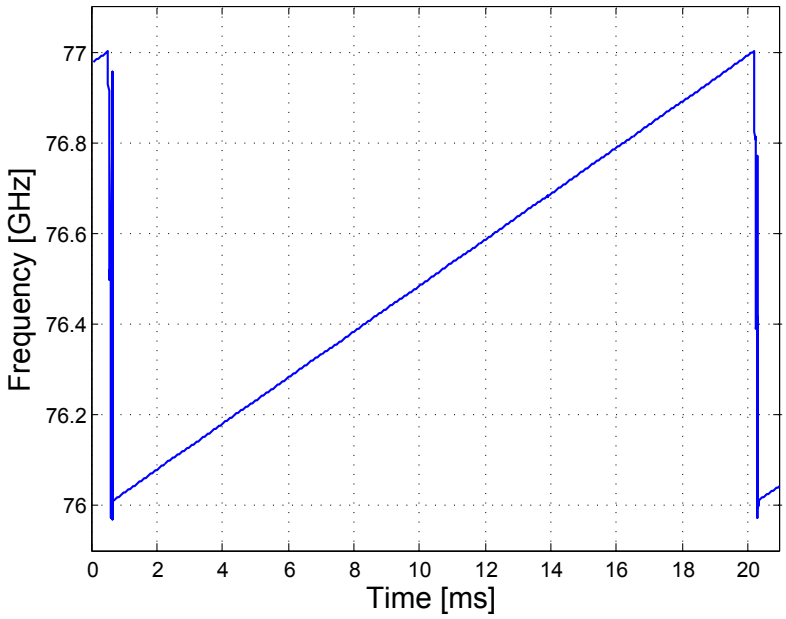

Figure 6.15.: Maximum power signal of up-chirp waveform, 20.5 ms acq. window, 20ms chirps, upconverted to W-band

Table 6.7.: Waveform properties of new 20 ms up-chirp modulation at W-band

	Triangular Modulation		
Properties	Desired	DDS round	Meas/Est
Δf	1 GHz	999 MHz	990 MHz
t_0	20 ms	19.6 ms	19.56 ms
t_{sr}	0 μs	8 ns	120 μs
t_m	20 ms	19.6 ms	19.68 ms
f_{start} (chirp)	76 GHz	75.998 GHz	76.009 GHz
f_{stop} (chirp)	77 GHz	76.999 GHz	76.998 GHz

Observations

The up-chirp modulation did deviate to the triangular in respect to observed linearity. Although the linear region seemed to be of similar quality as the triangular, the frequency transition between the sweeps did clearly eat into the waveform both in respect to efficient bandwidth and chirp time. Thus would this modulation yield less exploitation of the ESTI bandwidth. The worst case of nonlinearity affecting the waveform were the 1 ms up-chirp where the transition clearly influences the next chirp start-up. Although the nonlinear transition affects the waveform at all different chirp modulation times the influence decrease with at longer modulations. In addition should it be noted that the sweep recovery time seemed to vary between 99 to 120 μs which were quite similar

to the previous measured transition of the erroneous preprogrammed waveform, hence indicating that the circuit sweep recovery time, effectuated by the PLL frequency lock time , lay in this region and that up-chirp modulations belove 1ms should be avoided. In relation to the previous waveform analysis, where the single transition had produced a clearly visuable beat output. Were it hence desirable to further study the synthetic beat frequency output, especially the 1 ms up-chirp waveform. Thus to see if an ambiguous beat could impose any threat to the use of this in the real system implementation. However did the up-chirp waveforms after all produce large enough linear bandwidths to be used further in real radar range testing. Hence as long as the desired beat frequency would not be ambiguous, compared to the transition beat. Nevertheless did the pure triangular waveform seem at first hand to the most applicable choice of waveform, to is non-existing transients.

6.5.3. Chirp Linearity

As done in the initial linearity study of the preprogrammed waveform 5.1.5, were the maximum power element of each time-segment used to estimate the frequency error for the new waveforms as well. By identifying the linear part of a single chirp, that would create a consistent beat frequency output, were the linear frequency error studied. The first objective were to see the overall improvement to the previous chirp like transition studied in the last chapter and then to compare the new results to other documented designs. Additional would the derivation of frequency error also give an estimate of the expected range resolution over the desired observation range. The linearity results of the six valid reprogrammed waveforms are shown in table 6.5.3, derived at W-band. Additionally are three different frequency error plots shown in appendix C.2.2 to illustrate some problems with the used method, when the linearity of the waveform improves.

Table 6.8.: Estimated chirp linearity parameters at W-band, from analysis of new waveforms

Properties	**Triangular Modulation**		
	Chirp time ≈1 ms	Chirp time ≈ 10 ms	Chirp time ≈ 20 ms
Max freq. deviation	9.3 MHz	2.5 MHz	489 kHz
RMSE	700 kHz	935 kHz	211 kHz
L_{se}	0.0702%	0.0935%	0.0212%
ΔR_{theo}	0.150 m	0.150 m	0.150 m
$\Delta R_{RSS}(1m)$	0.150 m	0.150 m	0.150 m
$\Delta R_{RSS}(150m)$	0.183 m	0.205 m	0.154 m
Properties	**Up-chirp Modulation**		
	Chirp time ≈ 1 ms	Chirp time ≈ 10 ms	Chirp time ≈ 20 ms
Max freq. deviation	1.094 MHz	1.6 MHz	474 kHz
RMSE	429 kHz	848 kHz	212 kHz
L_{se}	0.0475%	0.0857%	0.0216%
ΔR_{theo}	0.164 m	0.152 m	0.151 m
$\Delta R_{RSS}(1m)$	0.164 m	0.152 m	0.151 m
$\Delta R_{RSS}(150m)$	0.181 m	0.198 m	0.156 m

Observations

Overall did the derived linearity parameters in table 6.5.3, yield moderate linear properties compared with the previously compared designs [20] and [44], over the linear chirp interval. Typical RMSE of frequency were under 1MHz and as good as 212 kHz for longer modulations. The worst maximum deviation were measured to 9.3 MHz and at best to 474 kHz. Compared to the two other designs the performance was seen as similar to [20] with a RMSE of 1.05 MHz, but worse than the UWB chirp in [44] which had been measured to have a maximum deviation of less than 150 kHz and RMSE significantly smaller. However where it difficult to compare the numbers directly since the compared

designs had little information of the used error extraction method and over which interval the linearity had been studied.

Nevertheless did the measured linearity confirm that the new waveforms were reasonable in respect to waveform quality and highly usable to generate beat frequencies when compared to the very nonlinear transition that had actually produce a beat output. However were the latter analysis of the transition now seen as useless, since it had actually been the a analysis of the frequency transitions, due to errorous programming, without any actual DDS chirp output. Additionally did the RRS range resolution estimates, show that the beat frequency output would be theoretically little influenced by waveform distortion, when the worst resolution estimate at 150 m, yield a resolution 0.205 m. Hence in respect to linearity did the experiment show that all the six presented waveforms in this part have more than sufficient linear characteristics to be used for real range measurements.

When the waveforms were compared to once another, it was difficult to draw the general tendency because the method proved to be inadequate for accurate prediction of waveform with such high linear parameters. The frequency error plots in appendix C.2.2 show that the linearity performance are highly determined by the selection of the part of the chirp that contains linear characteristics. As seen from the table does the cases of large frequency deviations come from bad selection of measurement vectors, thus also biasing the RMSE. This can be seen in figure C.8, which also reflects back at the one of the worst results in the table for the 1 ms chirp triangular waveform. In addition did also the theoretical slope fitting yield a lot to the linearity performance. Figure C.9 show an non-ideal fitting of theoretical curve, hence giving an unfavorable bias error which actually resulted in the worst linear results of the experiment, seen in table 6.5.3 for the triangular 10 ms chirp waveform. Hence did this find diviavte from the observation in the previous section were the triangular waveform showed an visual performance far better than the up-chirp since the up-chirp would have an large error around the frequency transition. Since this region were not taken into account, the over all performance proved thus to be more dependent of the utilization of the method. Hence could all the mesurments have been optimized more, as for the case in figure C.10. Nevertheless did a close-up study of the extracted frequency measurement reveal that the spectrogram resolution moreover produced much of the deviations from the theoretical linear frequency sweep (see figure 6.16). The limited resolution by the use of the spectrogram function created a staircase linearity which in respect to the linear line would always have a deviation of the magnitude as in figure C.10 which were fully optimized. The MATLAB spectrogram-function resolution were limited by its heavy computation, which were tried to overcome by the use of fast heavy computing servers at NTNU. However did this additional experiment show that the function it self could not produce much better resolution. Hence had the method for linearity studies, by the use of the MATLAB spectrogram function and extraction of maximum power elements, reached its applicable limit. Thus indicating that another more accurate method have to be used in future studies of the frequency error for such highly linear waveforms. The observed staircase chirp resembled the DDS output, but ideally should this form be smoothen by the DDS output LP filter and the use of the PLL which was not able to lock on to the 8 ns frequency steps of the DDS. By this observation it was reckoned that as long as the measured chirp follows the theoretical LFM there would be a large possibility that

the actual frequency deviation would be similar or less than RMSE of the optimalized cases observed for the 20 ms upchirp and triangular waveform. Note however that in both case of the 20 ms long chirps a systematic spur, as seen in figure C.10, was detected at the exact same time position. Thus indicating a natural DDS-to-PLL spur for such long chirps. Additionally was it observed from the 20 ms chirp cases in table 6.5.3, that the linearity were overall better for these long chirps. Hence was this consistent with programming since the DDS used smaller frequency steps for longer frequency modulations due to the fixed time resolution. However did the experiment show that this find were moreover a result of optimal vector selection, setting of theoretical reference and the limited practical frequency resolution of the spectrogram MATLAB function.

Since this problem were identified, no further optimalization were therefore performed, and the numerical results were hence de-emphasized to the quality description of the circuit performance. Although the method had proven to be insufficient for detailed characteristics of chirp linearity. The use of the spectrogram function together with the extraction of the maximum power elements had thus proven to give a good visual representation of the waveform and determination its time and frequency properties of the chirp, that would make out a better fundament for more accurate estimation of the true beat frequency. In respect to this statement, were the beat frequency studied as the next step in the analysis of the new designed waveforms.

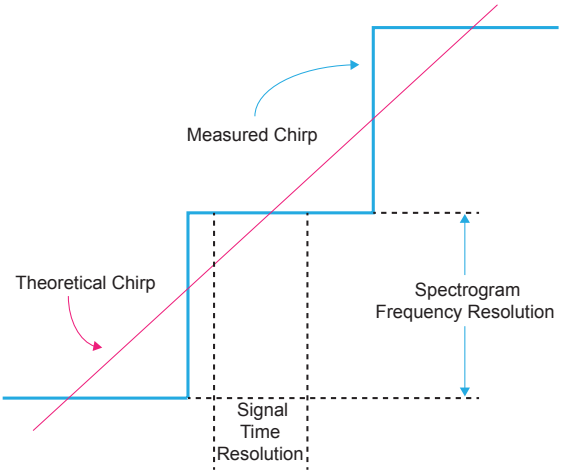

Figure 6.16.: Unavoidable frequency deviation limited by the use of the MATLAB spectrogram function and its limited frequency resolution

6.6. Synthetic Beat Frequency of New Waveforms

Since the reprogramming and implementation of new waveforms had been successful to much extent, within the chirp time region form 1 ms to 20 ms. The testing of the synthetic beat frequency seemed therefore to be the best final test of validation of the new generated waveforms, like previously done in section 5.2. Additionally were it also desirable to test the resulting beat frequency since the linearity test had not been as good as first expected and thus using the beat frequency as a signal quality reference. Since it had been discovered some possible problems of nonlinear effects, especially to the 1 ms up-chirp, were this waveform chosen as main focus in this test. Moreover were also a 20 ms triangular waveform tested as reference to the 1 ms up-chirp.

However, a problem with the use of the newly derived waveforms in respect to beat frequency synthesis, where that the modulation times were now considerably longer than the previously observed 'chirp' transition. Since the LO board output where 1/6 of the full implementation bandwidth and that the coaxial waveguide were limited to 12 m, were hence the theoretical beat frequencies quite low. Especially in the case of the 20 ms triangular waveform were the available synthetic range of the coaxial cable yielded a beat at 855 kHz thus belived to be non-observable, to the previously measured excessive phase noise in section 4.1.3. However where 10 ms case still tested to see how much the belived uncorrelated PN due to a 12m signal path divergens would affect the resulting beat spectrum. Although the method of the beat spectrum synthesis were highly idealized with the use of cabled signal path and optimum 'RCS', would it hence be to the general interest to see if this low beat frequency could be observed in the current measurement setup.

In addition to the triangular waveform, were it also interesting to study the beat output of the 1 ms up-chirp to its nonlinear behavior. Thus yielding a more favorable theoretical beat frequency at the current synthic range. Hence could the nonlinear effects be studied for further confirmation of the future use of this modulation. However were the beat frequency only synthesized with an medium bandwidth, from the intermediate stage output from the LO-board. Hence were an UWB case implemented, with the same 1 ms up-chirp waveform time properties, to enable studies of nonlinear effects at the beat spectrum of near 1 GHz bandwidth. Although worse signal purity were expected from the DDS output, were a quick Internet simulation performed on the Analog Devices ADIsimDDS design tool. Thus revealing that such implementation were possible, at least from the DDS's point of view. It were expected that the DDS low pass filter in combination with the PLL, would manage such output and hence yield good enough results. Hence to see some effects of nonlinearity at the radar output bandwidth, after an additional circuit frequency multiplication.

It was decided to study the beat frequency in three steps as previously done, with an initial FFT beat spectrum observation with a rectangular window. Then further study the FFT with a hamming window in comparison to a hamming windowed MATLAB simulated beat frequency. Hence aligned in power levels to closely examine the diviations in main lobe center point and overall SNR to main beam. Diverging from the last beat frequency studies were now the newly estimated/measured waveform frequency and

time properties implemented in the simulation to see how good the actual estimation had been in the previous section. The measurements were hence to be obtained with a sampling window similar to the waveform chirp time. As the last and final test were the spectrograms also to be studied to see if the nonlinearities would be manifested as they were in the study of the nonlinear transition and to confirm if a hopefully more consistent beat frequency would appear in respect to frequency and time.

In order to yield better estimates of the real beat frequency and the simulated, were the propagation velocity of the coaxial waveguide obtained from the coax datasheet [37]. With a typical propagation velocity at 12.5 GHz given as 4.3 ns/m, would thus the approximate delay through the 12 m waveguide yield 51.6 ns (τ). Hence were also the range estimated from this 'echo delay' and the new waveform properties from section 6.5. Likewise were also the previously derived method of beat simulations (appendix B.1.7) used, with the new estimated/measured parameters of the waveforms. Additionally were the frequency transitions of the up-chirp waveform implemented as down chirps between the desired ones with chirp times equal to the sweep recovery time, to yield resemblance to the real waveform obesevations.

The direct study of the beat frequency resolution were left out of this part, since the latter case-study did not yield any particular interpable answers. Thus were the overall focus more towards the beat frequency validity compared to simulated results and studies of nonlinear effects.

6.6.1. Beat Frequency of 20 ms Triangular Modulation

Firstly were the beat frequency of the 20 ms triangular waveform measured with a 250 kHz sampling frequency, set due to the relatively low beat frequencies observed at 6 m synthetic range. Combined with the use of a moderate NFFT of 4096 points, to yield fast computation, did the theoretical receiver resolution yield 61 Hz. However did the the MATLAB interpolation enable more accurate determination of the difference between measured and simulated beat. The same parameters were used though out the full experiment to yield comparable results. The measured waveform parameter obtained in the spectrogram analysis are listed in the figure captions, which also were the used parameters for simulated waveform generation. The spectrogram of the first beat frequency measurement were not presented due to impossible separation between beat and 1/f noise, caused by limited spectrogram resolution and non-obtainable digital filter designs that would not affect the beat in spectrogram.

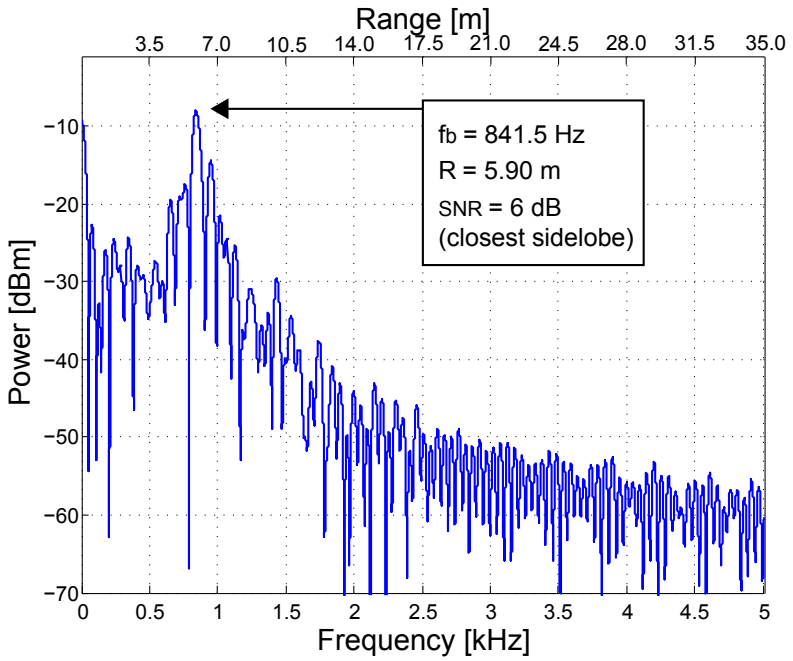

Figure 6.17.: Triangular Waveform, Rect-win, Δf=164.6 MHz, t_0=9.93ms, f_s=250 kHz, NFFT=4096, 10ms acq.window

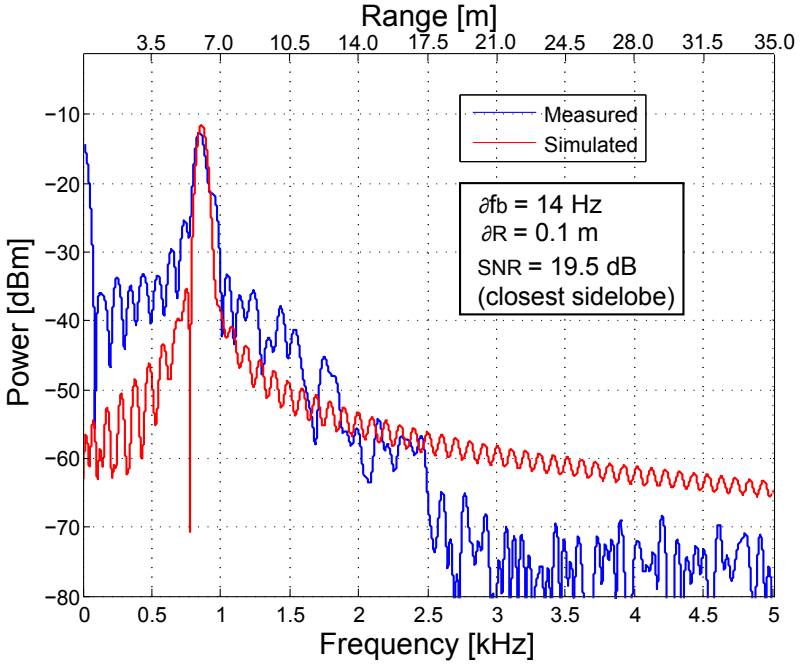

Figure 6.18.: Comparison, Triangular Waveform, Hamming, Δf=164.6 MHz, t_0=9.93ms, f_s=250kHz, NFFT=4096, 10ms acq.window

6.6.2. Beat Frequency of 1 ms Up-chirp Modulation

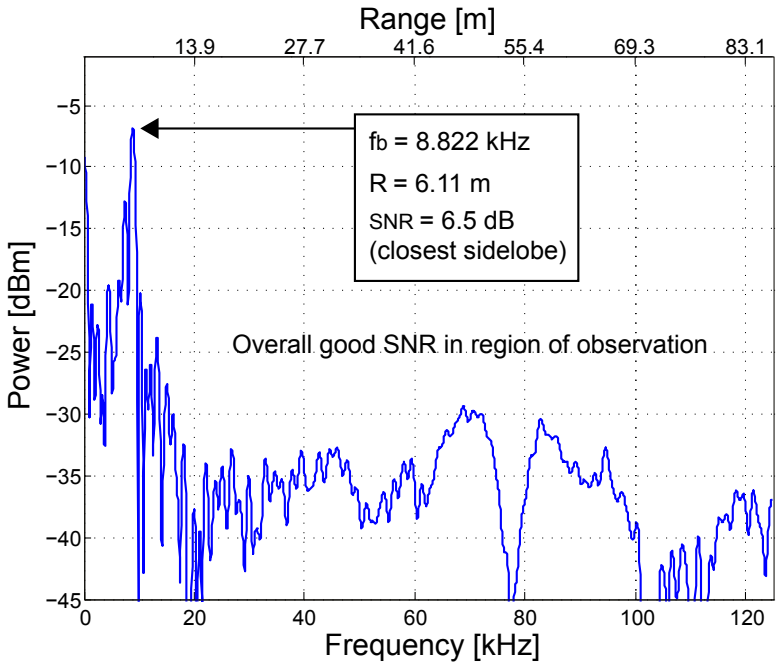

Figure 6.19.: Measured beat spectrum, Up-chirp, Rect-win, Δf=151.67 MHz, t_0=0.9037ms, f_s=250kHz, NFFT=4096, 1ms acq.window

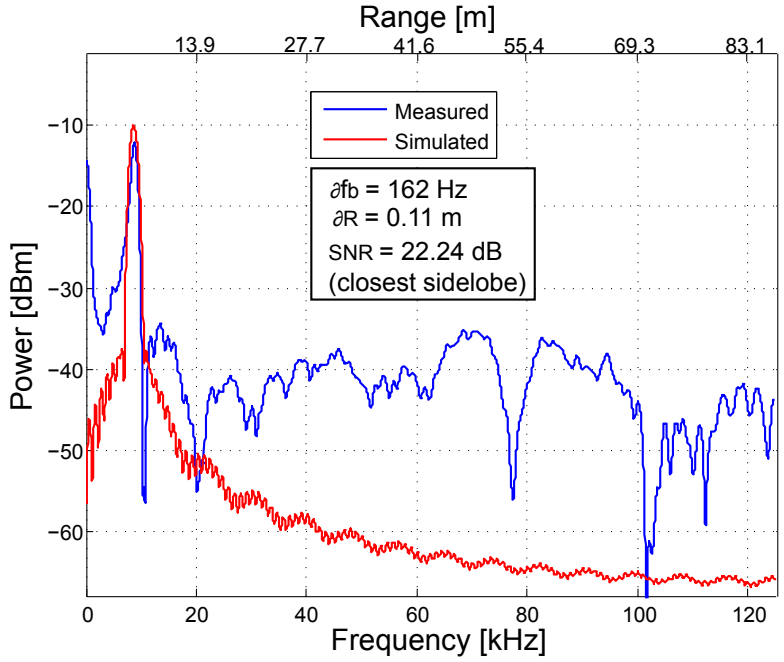

Figure 6.20.: Comparison, Up-chirp, Hamming, Δf=151.67 MHz, t_0=0.9037ms, f_s=250kHz, NFFT=4096, 1ms acq.window

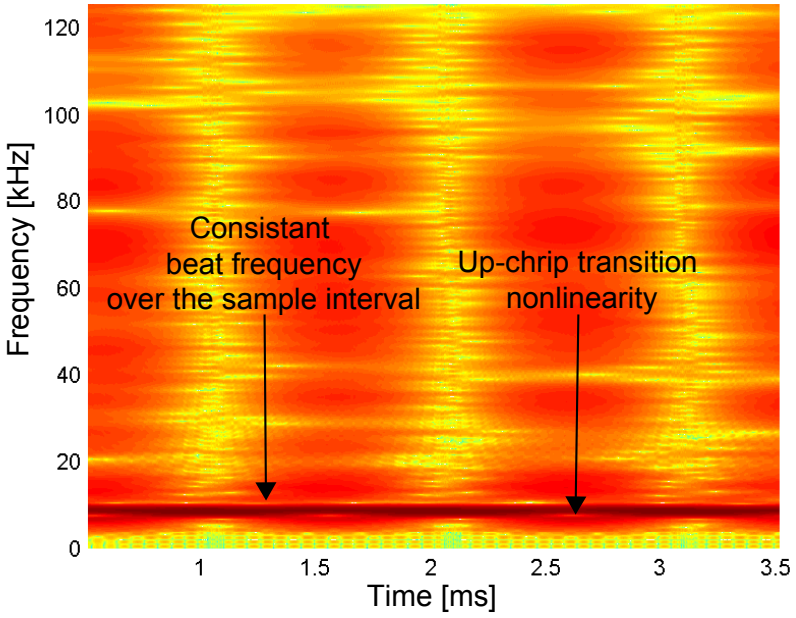

Figure 6.21.: Spectrogram of up-chirp, Δf=151.67 MHz, t_0=0.9037ms, f_s=250kHz, NFFT=4096, 3.5ms acq.window

6.6.3. Beat Frequency of 1 ms Up-chirp Modulation: UWB Special Case

To study the possible effects of the nonlinear transition in the 1 ms up-chirp and to see the beat appearance higher up in spectrum, were hence an additional reprogramming of the waveform done to alter the start and stop frequencies of the up-chirp waveform. By changing the start and stop frequencies in the DDS to respectively 61.855 MHz and 67.010 MHz should hence the LO-board output yield a 1 GHz frequency sweep from 12 GHz to 13 GHz. Thus were the theoretical limitations of the mixer frequency region met. However were this waveform not obtained with the spectrogram laboratory setup. Nevertheless was it assumed that the signal would be similar to the estimated W-band up-chirp, with t_{sr}, Δf and t_0, since it inherits a frequency error similar to the W-band signal.

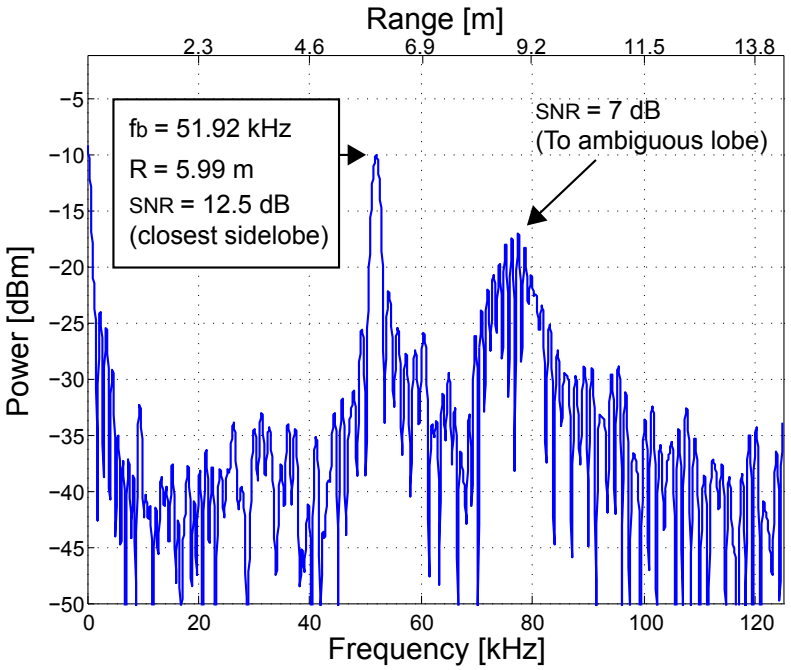

Figure 6.22.: Measured beat spectrum, UWB up-chirp, Rect-win, Δf=910 MHz, t_0=0.9037ms, f_s=250kHz, NFFT=4096, 1ms acq.window

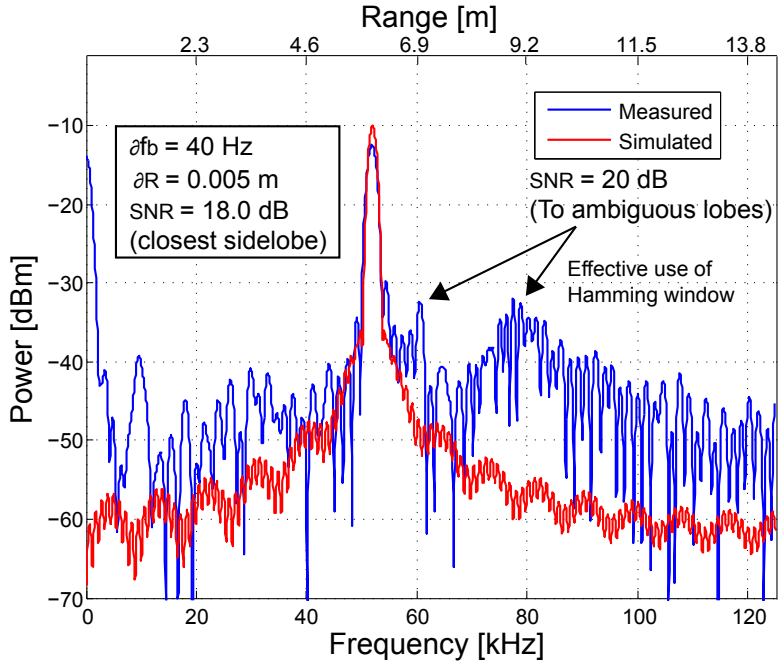

Figure 6.23.: Comparison, UWB up-chirp, Hamming, Δf=910 MHz, t_0=0.9037ms, f_s=250kHz, NFFT=4096, 1ms acq.window

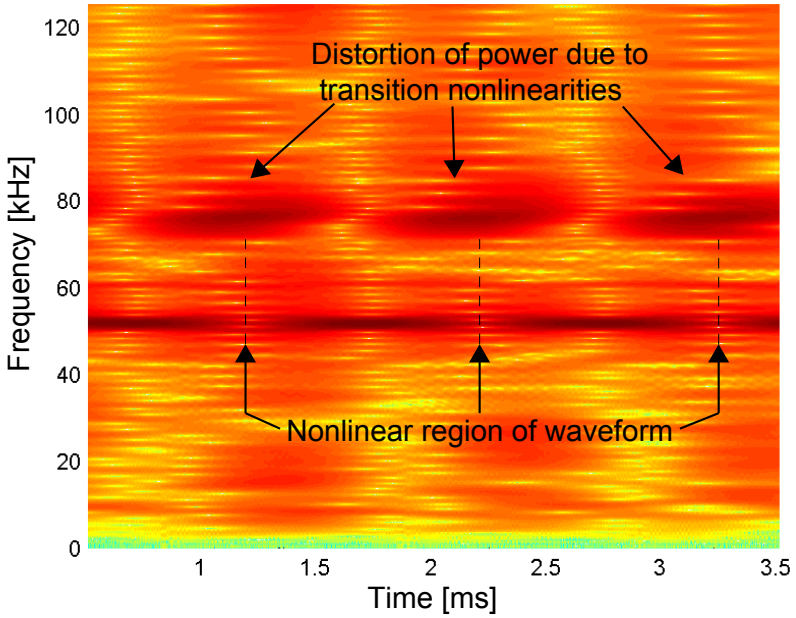

Figure 6.24.: Spectrogram of UWB up-chirp, Δf=910 MHz, t_0=0.9037ms, f_s=250kHz, NFFT=4096, 3.5ms acq.window

Observations

The first beat frequency case study of the 20 ms triangular waveform. Showed that the beat could be obtained although the desired beat was well in side the most noisy PN region, seen in figure 6.17. However was it obvious that the beat were affected by the noise with a low SNR of 6 dB to the closest side lobe. Within a fully implemented radar design at W-band, would probably the more noisy MMW components of such a design and the real RCS and signal path mask this beat output. Nevertheless would on the contrary a full design also move the beat further out in beat spectrum by a wider bandwidth, making the W-band utilization of this waveform highly plausible. As seen from the first figure did the beat yield a small deviation to the estimated range at 6 m. The figure does also indicate the PN seemed to influence the signal synthesis up to 2.5 kHz, quite consistent with earlier experiences were similar beat frequency experiments had been done with a real 77GHz radar system in an prior radar project [35]. Since the 20 ms triangular were considered to be one of the most linear waveforms implemented to the signal source, were thus the PN influence considered to be the most limiting factor for such low beat. Nonetheless could also some of the distortion originate from the unsynconized sampling of the beat frequency to the chirp start-up. Hence could some of the low frequency distorting power come from the sampling of the intermediate sweep recovery period between the up-chirp and down-chirp. Hence was it appropriate to state that future implementations of the circuit and full radar system should insure a syncronisation between the selected digital acquisition system and the DDS waveform start-up, by accessing the μC profile pin timing.

Figure 6.18 showed that the implementation of the Hamming window was highly effective

in reducing ambiguous sidelobes, although at the cost of main lobe resolution. The effective SNR was thereby reduced from 6 dB to 19.5 dB, which can be considered to very good improvement and hence had the great advantage of using Hamming windowing been proven. The comparison to the simulated showed a very good resemblance in respect to frequency validity, by the use of the prederived time and frequency waveform properties. With a beat frequency error of 14 Hz and range error at 0.1 m, did the beat at this noisy region of beat spectrum prove to be better than expected, compared to the initial PN measurements. Although the FFT power were difficult to estimate in the simulated case, was the frequency characteristics and form of the two very similar. Nevertheless did the region belove 2.5 kHz indicate that the combined noise contribution had raised the beat power main beam within the noisy region, but along with the additional noisy power contribution to the beat sidelobes. This indicates that the minimum beat frequency within this measurement setup should be higher than 2.5 kHz to overcome the most noisy 1/f region. Thus were it appropriate to estimate the beat frequency output of the 20 ms and 40 ms triangular at W-band and with a 6 m target, respectively at 5.2 and 2.59 kHz. This indicated that at least the 40 ms triangular waveform should be avoided in the full radar implementation, due to its overall low beat frequency. However will there be a unsertianty to how much of the phase noise that would be canceled in the full implementation to the bistatic PN leakage. This have hence to be tested further after the full design have been implementated, for a waveform usage confirmation.

Further was then the 1 ms up-chirp beat spectrum studied. Figure 6.19 show that the beat frequency was clearly observed in the beat spectrum even with a much wider total observation region. The SNR to the closest side lobe were however only 6.5 dB, but the overall SNR in the region of observation were considered to be very good. It was difficult to observe any nonlinear effects to the beat frequency synthesis. The range error were in the range of the previous case. Additionally did also this comparison of the measured and simulated yield good consistency, with an overall benift of using the Hamming window for range detection improvement. By studies of the beat frequency spectrogram over three modulation periods did the beat frequency seem very stable, unlike the pure transition beat observed in section 5.2.2. However were some small periodic anomalities observed in the spectrogram most likely to occur from the nonlinear transition between the up-chirps. Nevertheless did this not influence the FFT spectrum notably. Seen in relation to the sampling window unsertianty, was it in this case certain that at least a part of the nonlinear transitition had to be included in the FFT capture. Thus did this measurement show that the 1 ms up-chirp could be used as a practical modulation, however with the LO-board output bandwidth. Hence were there difficult to say something about the real nonlinear influence when the real radar implements a six times frequency multiplier. To get more insight to the 'full' bandwidth implementation were thus the up-chirp redesigned with a 1 GHz bandwidth output from the LO-board.

Figure 6.22 show the observed FFT plot for the reprogrammed UWB up-chirp. Although the beat main lobe yield outstanding performance with very good coherence to estimated range and good SNR (12.5 dB) to the nearest sidelobe, did the measurement show a large ambiguous lobe, 7 dB belove the beat main lobe at approximately 80 kHz. Several different approaches were considered as sources of error, but non fitted to the observed anomality. Thus were it belived to be the result of the the nonlinear transition

manifesting it self in spectrum as described in theory, section 2.5.2. However did the use of the Hamming window showed in the comparison plot, reduced the ambiguous lobe effectively to 20 dB belove the main lobe. This implementation with the incorporated Hamming window proved to be a very good modulation, showing the benefit of the increased bandwidth, observed through the range axis. By looking at the spectrogram in figure 6.24 it was clear that the observed ambiguous lobe came from the increased nonlinear transition at between the 910 MHz frequency gap. It was a clear periodic tendency over the three sampled modulation periods observed in the spectrogram, with the distorted power mid point aligned in the middle of the transition. Hence indicating that a part of the transition had been obtained within the beat sampling window. Consequently had the spectrogram illustrated that the beat output from the 1 ms up-chirp waveform, could be even further improved by synchronized segmented sampling aligned to the most linear region of reference waveform. Such a implementation could thus exclude more of the undesired nonlinearity and improving the overall radar sensitivity, to the cost of range resolution. In respect to the untested spectrogram appearance, were it by the beat mainbeam confirmed that there no obvious distortion to the LFM-part of the up-chip. Hence were the measurent although seen as valid.

Summarized did the experiment outline that the both modulations could be used further within the isolated chirp time region of 1 ms to 10 ms. Hence excluding the 40 ms triangular and 20 ms up-chirp waveform for further use, since they produce too low beat frequencies, in respect to PN interaction and Doppler target masking. If strictly used for ranging applications these modulations could be used, if a future test of the PN cancellation proves to be effective. On the other hand does also the use of the 1 ms up-chirp generate some unsertianty to its use. Since the nonlinear effects were clearly seen in the beat frequency experiment. Additionally would also the real implementation with more non-ideal circuit components would yield possibly more dispersion to the waveform and thus enhance the nonlinear behavior of the total waveform. By taking into account, the ideality of the beat frequency experiment, the appointed region of modulation to the two waveform yield even more validity.

6.7. Development Discussion

In this final part of the thesis were the erroneous waveform generation of the signal source solved, in addition to an implementation of two new fundamental FMCW waveforms that could be used for in the future work with the NORBIT/NTNU/TRIAD experimental automotive radar. This corresponded to the goals set for this part of the thesis, which included the identification of the source of error to the corruptive waveform that were analyzed in the previous chapter. Additionally were it also intended to correct the error if possible and further implement new applicable waveforms. Hence in relation to new waveform implementations, if managed, could the the previously derived methods for waveform and beat frequency analysis be used to confirm their validity for the further work.

The first step of this part of the thesis work, was to start off with experimental investiga-

tion of errorous performance at software level, hence to try to determine if the source of error were software or hardware related. Thus were the reprogramming initiated and corresponding studies of DDS/PLL programming thoroughly looked into. The initial observation at this part, when the previous waveform analysis and programming documentation had been compared, were the exceeded modulation bandwidth to the ESTI requirements. Hence had the DDS programming to be corrected, to yield a theoretical chirp bandwidth at W-band of 1 GHz. Additionally did also the preprogrammed chirp rate deviated to the intended modulation described in the radar documentation [34]. Hence were a general programming recipe worked out for correct DDS settings. Experimental waveforms according to new theory were hence implemented to the source code and implemented to the circuit microcontroller that were controlling the timing and register settings of the DDS and PLL. However did these initial waveforms also fail in aspect of chirp modulation, although consitant to waveform timing. Thus were the source code further tested. As a result were a source code error a last found. The waveform error were induced by a missed initialization of the modulation raising/ falling delta word (RDW/FDW). Hence had the modulation mode been set but no chirp rate had been initiated. Thus had the circuit modulated the waveform as an 2-FSK modulation between the chirp start and stop frequency. However had the PLL produced a frequency transition equal to the circuits sweep recovery time. Nevertheless had the transition enough linear resemblance to be mistaken for a nonlinear chirp with the ability to crate an observable beat frequency that were observed in the perivious waveform analysis. As a consequence had this erroneous waveform crated a lot of confusion to the identification of the main source of error.

Further were hence a the fundamental up-chirp and triangular waveform selected as main modulation schemes for further implementation and investigation. This was done to supply the experimental radar working group with two basic waveforms that could be used for initial testing of radar with the both ranging and Doppler sensing capability. Additionally were the two implemented to study the waveform quality and examine possible problems with nonlinear behavior at these waveform discontinuities in aspect of the circuits ability to crate LFM waveforms. Moreover were hence a test set of different chirp rates decided upon within the ESTI requirements. Since the 1 GHz chirp bandwidth had been desired for maximum range resolution, were only the chirp time defining the waveforms test sets. However were also some basic considerations made upon the resulting beat frequency. Hence were the previously desired 40 ms up-chirp and 80 ms triangular waveforms, excluded from the test set due to low beat frequency outputs that could reduce the radar sensitivity considerably for close targets, along with great chance of Doppler target masking. Additionally were also the 100μs up-chirp and 200μs belived to be erroneous due to the PLLs frequency locking time. However were these also included in the test to lock at the circuits full agility postensial, and hence yield a recommended region of modulation for the waveforms in aspect of LFM signal quality along with the resulting beat frequency. Thus were totally eight waveforms analyzed, 100μs - 20 ms up-chirp and the 200μs - 40 ms triangular waveform.

The new waveforms were measured, in two main test setups, sampled as amplitude data with a high speed oscilloscope and then further processed in MATLAB for its great processing agility as earlier done in chapter 5. First were the general waveform properties

studied in respect to frequency and time, through the spectrogram. By using a self developed algorithm (section 5.1.5) were the maximum power elements of the spectrogram extracted, thereby representing the waveform more accurately in frequency and time. Thus enabling easier determination of the waveform properties. Since the waveform had then been represented as an single frequency measurement vector, could the waveform be up-converted to 'real' LO-board Ku-band, by reverse mixing in MATLAB. However were it then easy to further convert the waveform to the radar W-band, by ideal frequency multiplication. Hence could the programming and real output of the LO-board be studied as an simulated full radar output, thus making the results more interpretable for the current and future waveform development. This experiment showed initially that the 100μs up-chirp and the 200μs triangular waveform could not be generated as desired, probably due to the limited PLL frequency lock time. Hence were these eliminated as possible waveforms for further work with this radar signal source. However should it be noted that there was no time during the thesis to do modifications to the PLL programming since the main goal were to implement a usable set of waveforms. Hence was there a large posiblllity that the PLL could be set to *fast lock mode* to improve the performance of the current unobtainable short modulations. However would there be a lower limit to the PLL lock time, due to the designed PLL low pass filter, although this was not further looked into. Nevertheless should some considerations be made upon a possible pursuit for shorter LFM modulations, in respect to Pipers rule-of-thumb, presented in section 2.5.1. To insure a minimum loss of efficient bandwidth, should thus a shorter chirp modulation for fill $t_0 \geq 5 \times (\tau + t_{sr})$. If the maximum range is assumed to be 150 m and the mean sweep recovery time will be similar for shorter modulations, would hence the chirp modulation have to match $t_0 \geq 5 \times (1\,ms + 110\,\mu s) = 0.555\,ms$, to avoid additional loss of range resolution.

The six remaining measured waveforms were hence studied in aspect of time and frequency properties, and showed that the divergence between the programmed triangular waveforms and the real outputs were minimal, with a maximum deviation in output bandwidth of 1.1$\%$ and great similarity in time. However were the DDS programming more limited by the frequency word rounding thus did the measured time properties deviate more to the initial desired test set. In addition was the sweep recovery time in the triangular waveforms longer than desired, but nevertheless more than sufficient with a max recorvery time of 300μs for the 40 ms triangular waveform. This observation in consistant with the fact at there will allways be an limited reaction time of a DDS/PLL combine circuit due to the nature of the PLL with a feedback lag. Overall had thus the derived DDS programming proven to be highly useble.

In respect to the more dicontineous up-chirp waveforms, did the experiment show that the large frequency gaps between two following frequency sweeps where affected by a nonlinear frequency transition that ate into the linear part of the waveform. Hence reducing both the linear sweep time and the effective linear sweep bandwidth. Intuitively was the 1 ms up-chirp mostly affected by the frequency transition, since the transitions were of quite similar durations (90 - 120 μs) independent of the total modulation time. Hence had the 1 ms up-chirp modulation a 116 μs reduction of sweep time and correspondingly 90 MHz reduction of chirp bandwidth at W-band (figure 6.13). Compared to the longer up-chirp modulations where the transition not that evident, due to the relative difference

to total modulation time. Hence were the 1 ms case treated as the lower limit for usable up-chirp modulations, among the tested.

Overall did the visual inspection of the estimated W-band waveform plots, did the waveforms seem to yield great linearity within their linear regions, although more reduced in the up-chirp cases. Since the frequency transition seemed unavoidable with the current programming and circuit design, did the triangular waveforms step forward as the most effective modulation in respect to bandwidth exploitation and minimal influence of nonlinearities.

To yield more specific information to the linearities of the waveforms, were the most linear part of the waveforms examined with a comparison to the theoretical linear frequency, like done previously in section 5.1.5. However did the study of the more linear waveforms show that the method it self were inadequate in determining frequency errors of less than 1 MHz, due to the limited spectrogram frequency resolution. Hence were the specific numerical linearity finds de-emphasized. Nevertheless had it been proven that the linear part of all new waveforms had linear properties in range of similar documented circuit designs, like [20] and [44]. Thus were the new waveforms condisered to be good enough in respect to chirp linearity, with estimated minimal loss of range and beat resolution. However needs the method of frequency error determination to be improved, if more accurate determination of linearity should be documented in the future.

As a final test of the new waveforms were a synthic beat frequency generated as done in the analysis of the preprogrammed waveform, section 5.2.1. The 1 ms up-chirp waveform had been identified as the waveform that were mostly affected by the observed nonlinear transition. Hence were the beat frequency analysis concentrated around this waveform. Additionally were also the 20 ms triangular waveform also tested, in aspect of comparison to the short up-chirp, but also to the study of synthesized radars sensitivity at very low beat frequencies. However were the generated waveforms fitted to a 166.65 MHz LO-board output bandwidth, matched to the full radar implementation with additional six times frequency multipliers up to W-band. Thus were an additional waveform implemented, by modifying the 1 ms up-chirp to yield an 910 MHz bandwidth at LO-board output. Hence enabling studies of nonlinear effects in the beat frequency generation similar to the full radar implementation.

Overall were all generated beat frequencies clearly visual and detectable in spectrum. However did the low frequency output at 841 Hz generated by the 20 ms triangular waveform, suffer from PN distortion compared to the 1 ms up-chirp at 8.822 kHz. Nevertheless did both the 20 ms triangular and 1 ms up-chirp waveforms generate beat frequencies with good consitancy with the theoretical range estimates, which were now derived from the more accurate waveform properties observed in the combined spectrogram/ max-power analysis. By comparing a simulated MATLAB generated beat, applied with the derived waveform properties did the simulated and the measured yield good resemblance in respect to frequency, with a maximum range error of 0.11 m at a 6 m synthetic target. The experiment did also illustrate that the use of Hamming windows improves the radar sensitivity, to the cost of minimal loss of beat/range resolution. In addition did a study of the 1 ms up-chirp beat spectrogram and FFT show no great influence of the earlier observed nonlinear transition, with a consistent beat frequency in

time and overall good SNR in FFT spectrum. Nevertheless should it be noted that the beat frequency sampling were not synchronized to the waveform generation, making some ambiguity to the validity of the beat frequency output. Hence not knowing if more or less of the internal transitions were included in the sampling, which will for curtain yield a difference to the beat frequency output. It was therefore appropriate to state that such synchronization would be beneficial to implement in the future radar development. Hence by interconnecting the DDS profile pin timing to the ADC of a later implemented DAS. Definitively must such a synchronization be utilized if the radar receiver should enable quadrature detection of the triangular waveform, since there would be differential beats to the up- and down chirps.

As a last test in the beat frequency analysis were the UWB 1 ms up-chirp measured. The beat frequency main lobe proved to be exceptionally good in reference to the estimated range, the simulated beat and the closest side lobes. However where a large additional ambigiuos lobe discovered in spectrum, only 7 dB below the main lobe (figure 6.22). By combined studies of the beat frequency spectrogram were hence the lobe identified as a distortion of power due to the nonlinear transition, which had been increased by the widening of the discontinuous frequency-gap between the 'continuous' chirps. Hence had the experiment proved the observations in previous waveforms analysis estimated to W-band, illustrating how the nonlinearities would possibly affect the beat frequency by the use of the 1 ms up-chirp waveform in the full radar implementation. However did also the use of the Hamming window in this case proven to be beneficial in reducing the nonlinear effect in the FFT spectrum. Nevertheless should it be mentioned that this experiment were conducted in a highly idealized test setup with a good relative SNR by the use of a coaxial waveguides as main signal path and full RCS reflection of signal power. In addition would also the full implementation moreover suffer from non-ideal noisy MMW components both in Tx and Rx signal path, thus decreasing the overall SNR. Further more will a future implementation also theoretically suffer more from dispersion effects both in full radar circuit signal path and air propagation, thus increasing the risk of nonlinearities affecting the desired beat output at the receiver. Nevertheless can this effect be reduced somewhat if a segmented synchronized sampling is implemented in the future, hence sampling only the most linear region of the waveform to increase the beat spectrum quality to the cost of a reduction in efficient bandwidth.

From these observations of waveform properties and beat frequency analysis of the LO-board output, and that worse general conditions expected in the full implementation of the radar, would it be recommended that the *triangular waveforms* should be used in the further work with the radar. Hence to insure minimal nonlinear influence and maximal exploitation of the allocated bandwidth. In respect to triangular waveform chirp time would thus the best region of further waveform development lay in the region between *1 ms* to *10 ms*, to insure maximum radar sensitivity, maximum range observation region and applicable sampling frequencies to the future DAS implementation.

However should it be emphasized that these recommendations were given from the observations done of the LO-board output and that the similar methods of investigation should be used after full implementation to yield better validity to the beat modulation for the radar system. Hence since no good assumptions can be currently be made of

both the real phase noise cancellation and the actual degradation of linearity to the real MMW-board implementation. In addition were also the PLL circuit not corrected in any way. Hence is there a possibility that further investigation of the PLL settings could be beneficial to improve the PLL lock time and reducing the nonlinear transitions in the up-chirp waveform. Likewise can also the DDS frequency steps be further examined to see the impacts of longer time-steps and fewer frequency steps. This scheme could be beneficial to ease the conditions to the PLL and possibly yield better performance to shorter chirp lengths.

The development of new waveforms showed that the combined DDS/PLL signal source could make accurate LFM waveforms with minimal divergens in both frequency and time, as long as the waveforms not are constructed with large discontinuities. The system showed a mean sweep recovery time of 110μs, that set a limit to the construction of short LFM waveforms. However did the circuit with the implemented DDS show a large frequency agility in respect to constructing large bandwidth signals, as shown int the 1 ms up-chirp UWB case. The experiments did also show that waveform analysis in both frequency and time are essential to yield waveform programming confirmation and that tuning of programming parameters are necessary to achieve desired modulations. In addition were it also shown that accurate measurements of waveform properties by the used methods were essential to achieve good range estimations, to the real beat frequency. However should it be noted that the real implementation could (and should) achieve the similar by radar reflector calibrations tests within the desired region of observation.

As a last comment to the development part of the thesis should it be noted that the earlier observed circuit boot up problem occurred also after reprogramming. However was there not enough time to pursue and investigate this error and that this problem have to be further looked into in the future development.

7. Summary Discussion

The task of this thesis was to realize a FMCW signal source, for use in an automotive experimental W-band radar. By using a programmable combined DDS/PLL circuit, supplied by the NTNU-projects industry partner, were new applicable waveforms to be implemented, along with a general confirmation of circuit properties.

7.1. Initial Circuit Performance

Due to lessons learned form a previous project, involving measurements of a W-band automotive radar [35], were the initial testing and confirmation of radar properties left much attention in the first part of the thesis. The earlier project had shown that small deviations in fundamental circuit performance could have large impacts of the radar performance at such high frequency circuits. Hence making the difference between full success or total failure, dependent of often small parametrical changes. Therefore were the fundamental circuit properties examined, as described in chapter 4. The measurements in this part were performed directly on the signal source output at Ku-band and observed with a 40 GHz spectrum analyzer.

The initial measurements showed that the general CW spectrum of both the Tx and LO outputs, were consistent with the described power properties in the radar documentation [5]. Additionally were the spectral purity of the CW output considered to be good, in aspect of additional harmonic and spur separation to the fundamental frequency. Hence imposing no threat to possible intermodulations of harmonics and spurs, when the LFM modulation were to be implemented. The frequency separation were considered good enough for both LFM-waveforms at both the LO-board Ku-band output and for the later full W-band radar implementation. Further were then the preprogrammed waveform tested. This waveform were documented to be a triangular waveform with 40 ms up- and down chirps, with intermediate hold frequencies at sweep start and stop of chirp modulation. However were it difficult to obtain any good capture of the waveform with the available spectrum analyzer. Hence caused by the analyzers limited sampling frequency. Nevertheless were the instruments *max-hold* trace-function used, to capture the spectral power within the predescribe LFM region. The measurements showed a clear distribution of power in between the two hold frequencies (figure 4.3). Thus consistent with the theoretical spectrum appearance of typical LFM waveforms. By contrast were the waveform bandwidth measured to be wider than predescribed waveform properties. Thus implying that the waveform drifted during the capture or that the waveform actually were wider than the documented. Nevertheless did the spectrum analyzer observations, yield an uncertainty to the real waveform spectrum properties. Hence caused by the

divergens between *max-hold*-function and normal sweep observations. The uncertainty implied that new waveform measurements methods had to be derived. Thus to capture the waveform spectral properties more accurately, but also the waveform time properties.

In addition to the signal sources fundamental spectral properties, were also the phase noise of the mid-band CW frequency measured. Hence to yield validity to the estimated phase noise, described in the radar documentation. In addition were this done to set a reference, for future studies of real PN cancellation in the full radar system. The measurement showed that the mid-band CW phase noise, was worse than the estimated for the frequency offset region belove 10 kHz. With the phase noise measurement yielding -83 dBc/Hz at 10 kHz, was it clear that the PN performance were limited. Thus implying that a homodyn down-conversion of the LFM radar signals could heavily suffer from phase noise within this region, if no cancellation of PN is provided by the MMW-part of the full radar system.

The initial circuit test did also revealed a boot-up problem, when the circuit was powered up from *cold* condition. Hence locking the output to a 13.5 GHz CW frequency, independent of the choice of radar mode. However were the problem solved intermediate, with repeated start-ups of circuit. In all were no explanation to this error found during the thesis. Nor were any changes to this error observed during the reprogramming of circuit. Hence did this observation yield that a solution to the boot-up problem needs to be further investigated and solved, before the radar is fully implemented.

7.2. Waveform Evaluation Methods and Waveform Measurements

In addition to the initial observations of spectral properties and circuit phase noise, had also the time and linear properties of the waveform, to be determined. As mentioned had the spectral properties to be more accurately determined as well. In all were these properties necessary to yield a validation of the signal source waveform generation. Moreover to derive the modulation quality, but also to enable a validation of the delivered programming against the real waveform output. Additionally were studies of the beat frequency seen as essential, to observe impacts of the waveform quality in respect to real radar measurements. Together were these methods of waveform analysis were seen as a necessary to insure a better implementation of new waveforms.

Obtaining Measurement Data for the Total Waveform Analysis

The next step of the signal source realization, were hence to implement the above described methods for studies of the preprogrammed waveform properties. Hence were it seen as beneficial to use a high speed oscilloscope to sample waveform amplitude data and utilize the great processing agility of the MATLAB software, to analyze the data further. In all were three methods of investigation utilized: Studies of the waveform spectrogram, determination of the chirp linearity through measurements of the frequency

error and studies of the beat frequency output through a synthetic homodyn radar setup. The three methods of processing had to be obtained by two different measurement setups.

The spectrogram and the chirp linearity data were hence obtained by sampling of the full waveform. However had the waveform in this case to be downconverted by mixing to an intermediate frequency band. Hence to overcome the limited analog bandwidth of the oscilloscope (section 5.1). This waveform measurement were not seen as ideal in respect to preservation of waveform power, by the use of mixing down to IF band. Nevertheless were the setup constructed to insure no severe attenuation of fundamental waveform components. By sufficient preservation of the waveform power properties, could the waveform be studied at IF-band as they appeared at LO-board output, however flipped in spectrum by the use of mixing. Nevertheless did the implementation of the oscilloscope show the the measurements limited by the maximum oscilloscope memory depth. Hence limiting the maximum acquisition time of the waveform. Therefore were the measurements conducted at different intermediate frequencies. As a result, were two different measurement approaches enabled. Firstly could long signal acquisitions be conducted at low frequencies with compatible low sampling frequencies. Secondly could then high spectral purity be achieved at higher frequency offsets from the 1/f noise, with higher sampling frequencies.

In order to study the beat frequency, had a synthesized radar to be implemented. This was achieved by making use the direct signal source output of Tx and LO. Further were the double balanced mixer used as a homodyne receiver to downconvert the two delay replica waveforms to base band (beat spectrum). With an excessive coaxial waveguide length of 12 m in the Tx path, were hence a synthesized ideal target at 6 m created (section 5.2). The use of the double balanced mixer were as sufficient, since the radar signal source enabled the a direct conversion scheme, thus without the need of image rejecting at Rx. The beat synthesis were not seen as optimal in respect to using other components than the later intended MMW components. Thus yielding a difference to the real implementation in relation to additional system noise and transmission dispersion. Nevertheless were the experiment seen as adequate. Hence to enable measurement data that could yield a sufficient qualitative analysis of the waveform through the beat spectrum.

Testing of Software, Signal Processing and Instrument Interface

Before any real measurements were conducted, had also the MATLAB software tool to be tested for its compatibility with the available PC's computional capacity. Hence to confirm that the needed measurement data, for a full waveform capture, could be processed and analyzed properly. Hence were theoretical LFM signals generated in MATLAB, to enable prehand developing of desired signal processing. The software testing, proved to be sufficient for full waveform signal processing and spectrogram analysis. However were the processing of the chirp linearity, not tested sufficiently on a theoretical signal, before the real measurements were conducted. As a consequence were it later discovered during the measurements, that the method of obtaining the frequency error though use of the spectrogram, were inadequate. This was caused by the limited spectrogram resolution, that were needed to obtain long signal aqcusitions. With the

limited frequency resolution, were an unavoidable stair-case like waveform obtained. Thus were there a constant frequency deviation in the measure waveform, compared to the theoretical linear frequency sweep. However was this only observed when the chirp linearity where good, as in the final waveform implementations. This proved however that the method should have been more thoroughly tested in this initial part of the thesis, prior to the measurements.

As a part of this work was also the oscilloscope interface possibilities tested and implemented. As a result were the measurement data obtained via the VISA-USB interface, directly into MATLAB. Hence to enable practical measurements of the beat frequency spectrum as an DAS alternative. However did the test of this interface prove to be inadequate for full waveform measurements, when utilizing the full memory depth of oscilloscope. As a consequence were an alternate method implemented, with the use of manual transferring of acquired measurement data. Nevertheless did the VISA-USB interface prove to be adequate for measurements of the beat frequency, at lower sampling frequencies. Thus were the original intention of the method met. Hence to yield an oscilloscope connection, that could be used in future radar measurements in absence of a full digital aqcusition system.

Measurements and Analysis of the Preprogrammed Waveform

Although much work had been done to insure good measurement setups, were the first measurements of the waveform spectrogram inconclusive. No chirp were found is spectrum. It seemed at first that there was an unfavorable sampling done by oscilloscope. Hence locking to the described hold frequencies and thereby masking the chirp both the FFT spectrum ans the 2D spectrogram. Nevertheless did studies of the waveform time sequences and the 3D-spectrogram, reveal a chirp-like behavior of region between the two hold frequencies. Although 300 times shorter in time, than described in the radar documentation. By identification and isolation of the very short time anaomality in the acquired measurement vectors, could the chirp be closely examined. The chirp spectrogram showed large frequency errors and overall unsufficient chirp linearity parameters. This proved a clear deviation in performance to other similar DDS/PLL documented designs [20],[44]. Although the method of extracting linearity parameters proved not to be optimal, did the visual spectrogram inspection in combination with the beat frequency analysis, show that the LFM waveform suffered from large nonlinear characteristics. Nevertheless did the waveform have linear-like characteristics and produce a beat frequency, similar to the measured chirp time and bandwidth. In respect to the documented description of the waveform, did the measurements yield a large deviation, to the chirp part of the total modulation. On the other hand seemed the total modulation time to be consitstant, together with the start and hold frequencies. Hence were it likely to assume that there first of all were an programming error of the waveform. Additionally did the appearance of the discovered 132μs nonlinear chirp, indicate that the PLL frequency lock time were not fast enough to handle such fast chirps, over the desired bandwidth. Moreover was it also observed that the preprogrammed waveform were exceeding the ESTI modulation requirements, regarding modulation bandwidth (deviation).

7.3. Solving Erroneous Waveform Generation and Development of New Waveforms

Since the first full analysis of the waveform indicated errors in the programming, was the first obvious choice of further work to examine the programming of the circuit. Although it could not be fully determined if the error were software or hardware related by the initial analysis, were the most obvious choice of action, to do further investigations by looking at the programming of the total circuit. Moreover had this to be done to firstly correct the observed frequency band violation, but then further try to correct the chirp modulation error.

Solving the Erroneous Waveform Generation through New Source Code Programming

The delivered circuit source code were firstly evaluated against the DDS and PLL datasheets. The investigation revealed that the DDS settings of the chirp modulation, raising/ falling delta words, were incorrect. Hence with too short chirp modulation time. As a consequence were a general method of DDS frequency word settings worked out in section 6.2. The PLL settings were on the other hand seen as sufficient. Further were then the corrections applied to the delivered source code and new microcontroller instructions uploaded to circuit, as described in section 6.1. However did the new implemented corrections to source code, produce similar short chirps as the preprogrammed. Hence with no reference to the new modulation, regarding chirp time properties. Consequently had the source code to be further tested and evaluated. The new investigation revealed however, that the RDW and FDW had not been initialized correctly. It was discovered that the previous code had initialized the different modulations through a case-based structure. Hence to enable different modulations, accessed by a mechanical rotary switch on circuit. Without the correct initialization, had thus this switching erased the RDW/FDW parameter settings in the microcontroller. Hence had the previous code implemented a 2-FSK modulation, between the start and stop frequencies, set to the DDS. The previously observed chirp-like modulation, had thus been the frequency transition produce by the PLL. Hence with no good frequency reference within the large frequency gap. However had the transition much LFM characteristics that it had produced a clearly visuable beat frequency. in the beat frequency analysis. Through this observation had latter case introduced a lot of confusion to the real source of error.

The modulation error were then corrected for valid chirp generation and tested with the previously derived methods. Further were two main types of basic LFM waveforms selected as test subjects for further waveform investigation and on circuit implementation. The countineous up-chirp and triangular modulations were hence selected to enable basic testing of range and Doppler measurements in the future implementation of the experimental radar. In addition were two different waveforms implemented to study their relative waveform property difference, in respect to bandwidth efficiency, waveform linearity and coherence with circuit performance. Since the two had theoretically different degrees of waveform discontinuity, were it thus interesting to study the circuits waveform

generation agility. Hence by the use the spectrogram, linearity and beat frequency analysis. An appropriate modulation test setup were derived, according to the ESTI standard. The bandwidth were hence maximized to the allocated 1 GHz bandwidth at W-band. Within the standard were four chirp times applied to the test set. However with an upper limit to the test set, limited up to the 20 ms up-chirp and the 40 ms triangular waveform. This was done to avoid low frequency beat outputs for longer chirp modulations. Which again were considered to reduce the minimum range observation region and possibly mask high speed Doppler targets in the full radar implementation. As a consequence were in all, eighth waveforms implemented. Hence at individual up/down-chirp periods at 100μs, 1 ms, 10 ms and 20 ms of the two waveforms.

Spectrogram and Chirp Linearity of New Waveform Implementations

The new implemented waveforms were firstly examined by use of the previously derived spectrogram method. However were it further refined by the use of the max-power method to extract a more accurate representations of the waveforms at W-band. By the use of software upconversion, were estimates of the waveform properties at higher frequencies enabled. Thereby yielding better determination of programming validity and improved estimation of the 'true' beat frequency/ range. Thus at the desired band of interest.

Figure 6.10 to 6.15, with the additional parameter tables, show the measument/estimation results of the new waveforms. However did the implementation of the 100μs up-chirp and 200μs triangular waveform, fail in respect to achieving respectable chirp bandwidth and overall waveform linearity. This were belived caused by the limited PLL frequency lock time. Hence setting a lower limit to the applicable chirp sweep time for LFM waveform generation. The enabling of better modulation of short chirps, were not further locked into, due to time limits of the total assignment. Additionally were also the Piper rule-of-thumb taken into account. Consequently indicating a that the lower limit to chirp time should be around 550μs, for the observed mean sweep time recovery time at 110μs and a maximum target delay time of 1ms at 150 m.

In all did the combined spectrogram/max-power analysis, yield great coherence to the programmed modulation parameters for the triangular waveform. Hence with good exploitation of the allocated bandwidth, with a maximum bandwidth loss of 1.1%. The waveform time paramters were also consistant with the programming. However with some additional modulation time, due to internal sweep recovery at the intersections of the up- and down-chirps. Moreover could not the exact desired chirp modulations be achived, due to integer parameter settings of the raising/ falling delta words. Hence was the overall modulation more restriced by the rounding of the DDS frequency words than the divergens to real output. The triangular waveforms were also observed as highly linear during the whole modulation periode.

In contrast did the up-chirp modulations yield a loss of chirp modulation bandwidth and time, to a frequency transition between corresponding chirps. The nonlinear intermediate transition were similar to the previously observed erroneous modulation. Hence were

there some unsertianty, to how much this would affect the desired beat frequency output. Since the transition was consistent in time, for all the up-chirp waveforms, was it desired to test the most affected waveform for beat frequency properties. As a consequence were the 1 ms modulation identified as the main subject of investigation for the beat frequency analysis. Hence to see if the nonlinear transition could decrease the performance of the synthesized beat.

In addition to the time/frequency analysis, were also the linearity parameters studied by the frequency error, as previously done. The measurements did in all show that the frequency error of the individual chirps were close to the frequency error of the earlier compared designs, [20] and [44]. However did this investigation the linearity, discover that the extraction of frequency error were limited by the spectrogram frequency resolution. Hence had the method of frequency error extraction proved to be inadequate for high linear chirps of RMSE errors of less than 1 MHz. Nevertheless had the analysis shown that the new waveforms had reasonably good linear properties within the generated chirps. However were there still some unsertianty to the impact of the nonlinear part of frequency transition in the up-chirp waveforms.

Synthetic Beat frequency of New Waveform Implementations

As final confirmation of the realized waveforms validity, were the synthesized beat frequency of the 20 ms triangular waveform and the 1 ms up-chirp waveform studied. As a result did the 20 ms triangular case prove to generate a low beat frequency well within the phase noise affected region, as expected. Hence since the beat were measured at the LO-board Ku-band output, with a chirp bandwidth less than 166.65 MHz and a beat frequency appearing at 841 Hz. Considered against the real W-band output, were it thus estimated that this waveform would yield a beat frequency in the vicinity of the 1/f noise region, for close targets. As a consequence were the longer modulations of the 40 ms triangular and the 20 ms up-chirp waveform, assumed to be inadequate for full radar use. Nevertheless should it be noted that the degree of PN cancellation in the real system could not be estimated or measured at this stage. Hence must the cancellation be determined at an later stage, if such long modulations would be desired in the future. In order to insure minimum reduction of radar sensitivity for close targets. Although the beat frequency were affected by phase noise, did the analysis show that the detectability of the 20 ms triangular beat, could be increased by the use of the Hamming window. Thus with a minimized reduction of beat/range resolution. This were a general tendency of all the measured beat frequencies. It was therefore recommended as an initial signal processing technince for target range determination. However a observation that is similarly documented in all other FMCW radar theory as well. More advanced windowing technices could however be implemented at a later stage, hence to compare their individual benefits to the overall unmasking of low RCS targets.
Further did the measured/theoretical comparison show that the use of the periviously derived waveform properties, were highly valuable in estimations of the 'true' beat frequency and range. In total did all measurements of the synthetic beat frequency show a minimal beat- and range error, with a maximum range divergens of 0.11 m at

6 m. Although this scheme were seen as beneficial to estimate the beat/range error in this laboratory measurement, would this method yield more uncertainty in a full radar implementation. Hence to additional waveform corruptions applied by the MMW components and additional propagation effects. It will therefore be appropriate to calibrate the radar after full implementation, for each applied modulation. Thus to set reference beats for the radar, obtained with reference targets measured at different ranges, within the region of observation.

The beat frequency output of the 1ms up-chirp modulation, showed however no evident effects of the previously observed nonlinear transition. The higher beat frequency output at 8.822 kHz yielded an overall good SNR within the observered beat region. With the additional use of the Hamming window, were the closet sidelobe decreased to 22.24 dB belove the beat main lobe. The beat frequency spectrogram showed a also consistent beat frequency in frequency and time, only with small periodic indications of nonlinear transitions. Although not observed in FFT beat spectrum. Nevertheless were the synthetic beat frequency analysis done under highly idealized conditions. Hence in respect to 'reflected' power form synthetic target and no noisy MMW components. Additionally had also the measurement been conducted at signal source output, which indicated a 1/6 reduction of frequency possible frequency errors.

To investigate the possible nonlinear effect at W-band, were hence an additional special case implemented and investigated. By setting new frequency parameters to the 1ms up-chirp modulation were a 910 MHz bandwidth implemented at LO-board output, similar to the estimated 1ms up-chirp at W-band. The measurement of this special waveform showed a beat frequency main beam at 51.92 kHz with good SNR (12.5 dB) to the close sidelobes, even without the Hamming window applied. However did an additional large ambiguous lobe appear in spectrum, 7 dB belove the main lobe. Although the introduction of the Hamming window, reduced the additional lobe to 20 dB belove the main lobe, did it still decrease the overall SNR in beat frequency spectrum. The beat spectrogram showed that the beat frequency were less consistent in time, compared to the previous 1 ms up-chirp implementation. Hence with the main beat appearing as long pulses, with intermediate gaps between the desired beat. The additional lobe were observed to be co-aligned with the intermediated gaps. Thus did this observation indicate that the ambiguous lobe were a direct result of the nonlinear transition. This corresponded to theory, which indicated that an increased bandwidth would also increase the frequency error of the nonlinear part of the waveform. As a consequence were the 1ms up-chirp not recommended for further use.

Furthermore should it be noted that non the beat frequency measurements, had been utilized with a synchronization between waveform modulation and sampling. Consequently giving some ambiguity to the results, in respect to the idealized sampling window. For example did the beat spectrum analysis of the UWB case, indicate that the beat frequency nonlinearity could be reduced by selective segmented sampling of the waveform. Such synchronization would also be beneficial, if the triangular waveform should be used together with quadrature sampling. Since the up- and down chirp will create diverging frequency spectrum's in quadrature. A syncronisation could be implemented in the tested design by interconnecting the microcontroller modulation pin (profile pin) to the ADC

synchronization interface. Thus enabling selective processing of the acquired data.

In addition did the analysis of the beat frequency show no effects of the possible frequency drift, that had been observed in the initial measurements with the spectrum analyzer. Although no drift-effects were obserserved, could it not be confirmed that no drifts were present.

Realized Waveforms Suited for further use

From the total analysis of the new implemented waveforms, were the following modulations recommended for further use. Hence to yield maximal explotaiton of the allocated bandwidth, minimal effect of nonlinearities within the waveform and applicable beat frequency regions:

- **Up-chirp: 10 ms** (t_0=9.77 ms, t_m=9.87 ms ,t_{sr}=90 μs, Δf=989 MHz)
- **Triangular: 2 ms** (t_0=0.997 ms, t_m=*2.024 ms*, t_{sr}=30 μs, Δf=989 MHz)
- **Triangular: 20 ms** (t_0=9.93 ms ,t_m=*19.94 ms* ,t_{sr}=80 μs, Δf=988 MHz)

The parameters within the brackets show the more accurate waveform properties, that were observed in the spectrogram/max-power analysis, estimated at W-band. The deviation to the desired parameters were caused by the combined effect of integer frequency rounding in DDS programming and real output deviations.

Among the implemented modulations, were the region between 1 ms to 10 ms chirp time, identified as the most favorable region of further waveform developments. In addition should also the *triangular* waveform be emphasized, as the most applicable modulation for Doppler extraction, but also in respect to overall linear performance. Nevertheless would the pure triangular waveform be insufficient in an real high density target situation. Hence if several Doppler targets should be extracted simultaneously together with range information. The limited time of the thesis prevented however implementation of more waveforms. Hence must further FMCW modulations be development in the future. However can the presented methods and programming yield as fundament for the future waveform realizations.

8. Conclusion

In this thesis was a DDS/PLL X/Ku-band signal source realized as an applicable linear waveform generator with two basic FMCW waveforms, accommodated for use in combination with a W-band radar front-end. The main achievements of waveform generation are shown in figure 6.10 to 6.15, presented as W-band signals in time and frequency.

To achieve a valid realization through reprogramming, were methods developed to enable accurate measurements and studies of the waveforms in time and frequency. Combined with studies of the resulting beat frequencies in a synthesized homodyn radar setup, were the development and evaluation of waveforms conducted. The use of a high speed oscilloscope as signal sampler in combination with the MATLAB engineering software tool, proved to be a good way of processing direct waveform and beat frequency data, thus enabling an overall fundament for implemented waveform characterization. As a consequence could thus more accurate estimates of *true* beat frequency and range be made. With use of the analyzing methods along with general beat frequency considerations, were the following three implemented waveforms specially recommended for further use in the experimental automotive radar:

- **Up-chirp: 10 ms** (t_0=9.77 ms, t_m=9.87 ms ,t_{sr}=90 μs, Δf=989 MHz)
- **Triangular: 2 ms** (t_0=0.997 ms, t_m=2.024 ms, t_{sr}=30 μs, Δf=989 MHz)
- **Triangular: 20 ms** (t_0=9.93 ms ,t_m=19.94 ,t_{sr}=80 μs, Δf=988 MHz)

Further were the core region of future LFM waveform developments, recommended for chirp modulation periods (t_0) between 1 ms to 10 ms, with additional full bandwidth utilization within the ESTI requirements. Thus to achieve a good trade-off between, radar sensitivity over the desired region of observation, waveform linearity and requirements for the future digital acquisition system. In addition were the triangular modulation identified as the most safe choice, regarding avoidance of nonlinear effects to beat spectrum. Nevertheless were all the recommended waveforms considered to be sufficient for future radar testing.

Unfortunately were the supplied circuit source code erroneous. Hence leading much of the work in this thesis to error source identification and solutions, rather than testing of more advanced FMCW waveforms and testing of the full signal source agility. However were the recommended waveforms successfully implemented and tested, such that the full radar could yield direct benefit of the realized waveforms for initial range and Doppler measurements in the further radar development. Although the source code contained an error, did the microcontroller in combination with the delivered source code, enable a good accessible interface with flexible control of the DDS and PLL.

In all, proved the signal source to yield good separation of harmonics and additional circuit spurs, hence good spectral purity. Moreover were it also shown that the circuit output power requirements, were well within the limits of the radar documentation. However did measurements of the circuit phase noise, exceed the radar documentation noise estimates considerably, for frequency offsets belove 10 kHz. Thus putting some unsertianty to the overall radar performance, since phase noise is considered to be one of the greater contributors to reduction of radar sensitivity for close target observations. Nevertheless have the phase noise problem been taken into account by the radar designer, documented in the radar design note. Hence was it assumed that much of the discovered dominant phase noise, would be canceled out through a matched bistatic transceiver noise leakage. However would this assumption have to be proven through future studies of this phenomena in the total system, to yield full phase noise cancellation validity.

To conclude was the NORBIT DDS/PLL signal source considered to be a good FMCW waveform generator for W-band automotive radar applications, within the described limitations and unplowed areas of testing. The signal source was also considered to be highly attainable for further implementations of more advanced FMCW waveforms, due to its reasonable agile design and possible future enhancements.

9. Recommendations for Further Work

Through the work in this thesis had two applicable LFM waveforms been implemented to a DDS/PLL signal source and tested. However had a erroneous source code curruped the preprogrammed waveform, that were intended to yield as reference to the work of thesis. As a result were most of the effort in this thesis focused on finding, analyzing and correcting errors. Thus were only small corrections made to the source code and a limited number of new modulations were tested. Hence in order to meet the basic need for functional FMCW waveforms, that could be used for initial testing in the experimental radar project. Consequently are there still a lot undiscovered ground to the further work with the signal source, as earlier described in the discussions. To emphasize on the further challenges and opurtinites, are hence some basic considerations to the further work made in the following chapter.

9.1. Waveform Development

Since only the up-chirp and triangular modulation were implemented and analyzed in this thesis, are there several types of modulation schemes that could yield more benefit to the full implementation of the experimental automotive radar. In addition were there not sufficient time to map the full potential and limitations of the signal source. Hence creating other, more advanced FMCW waveforms or possibly other complementary waveforms as well. Thus could a full agility test be further recommended for documentation of the signal sources ability to generate high quality signals. In that matter could perhaps additional functions as communication applications be tried out, due to the signal sources two channel modulation ability. Nevertheless would also further exploring of the ADOSE body tag radar application, be of the most concern, to yield benefit to one of the close industry partners in the radar project. Hence to make use of the two channel possibility, that were not examined in this thesis.

It was stated in the thesis, that the two main types of modulation that were impleneted, were not fully optimal for detection and tracking of high density targets. However is this ability needed for the real automotive radar applications. Thus is it be appropriate to recommend other modulation schemes as well. The easiest modulation to implement with the current source code, is hence two realize the triangular modulation with hold frequencies, as were supposed to be implemented in the preprogrammed waveform. Thereby to enable easier extraction of multiple Doppler targets. However is it highly

recommended to keep the internal chirp modulation within the 1 ms to 10 ms region to generate applicable beat frequencies. In addition should also the Piper rule-of-thumb not be exceeded, in aspect of the total waveform modulation period. Hence in relation to both chirp modulation period, hold frequency period and additional sweep recovery time. By making use of the highly agile DDS solution implemented on circuit, would it also be a possibility that SFCW waveforms could be implemented in the further work. Waveforms like the FSK-LFM, suggested by Rohling could especially be of interest, since this waveform can solve the range-Doppler ambiguity for multiple targets simulatanously [31]. In order to develop new modulations, could the derived methods of measuring and analyzing waveforms that were used in this thesis, be recommended to insure a good evaluation of new waveform property achievements.

In reference to the realized LFM waveforms, is there in addition a possibility of conduction more accurate measurements of the chirp linearity. Since the method used in the thesis proved to be inadequate. Furthermore accurate measurements of linearity could thus be used as qualitative documentation of the signal sources ability to generate quality LFM signals.

9.2. Signal Acquisition and Signal Processing

One of the most important tasks of the further work, is to implement a synchronization between the waveform modulation and the ADC-sampling, in the future implemented digital acquisition system. This could hence be done by interconnecting the DDS/μC-modulation timing(profile pin), to the sampling circuits sync-trigger interface. This scheme is essential to enable full exploitation of quadrature detection and processing. In addition could such synchronization enable selective sampling. Hence to avoid processing of corruptive nonlinearities in waveform and additionally allow more optimal sampling of desired parts of the implemented waveforms.

If the implementation of a DAS solution is further postponed, could the oscilloscope still be used as intermediate substitute for real radar measurements at a later stage. However with a limited four channel processing capability. In that matter could it be further recommended that a 'real time' session-log/MATLAB-script, should be worked out. Hence to utilize the oscilloscopes VISA-USB, GPIB or LAN connectivity. This would then enable direct live measurements of beat frequency data. Additionally could hence the oscilloscope be directly controlled from the PC and data simultaneous signal processing.

9.3. Signal Source Corrections and Optimalization

In respect to first hand corrections that should be to the signal source, must the discovered boot-up error be further examined and corrected. Thus in order to yield full signal integrity, since the frequency lock in connection to the boot-up error, can not be discovered

without measurements of the output spectrum.

Since only a few limited corrections where done to the overall source code, is then a large possibility that the over all performance could be increased by further investigation of the DDS and circuit register/mode settings. For instance can investigations of the PLL's frequency lock time and different combinations of RDW/FDW and RSRR/FSRR, be made to improve the circuits sweep recovery time. Such a achievement would possibly yield greater immunity to waveform discontiuties by the signal source. In addition could also further effort, be directed to investigations of source code. Hence to enable manual switching between different main-types of waveforms. Which in contrast had to be done by total circuit reprogramming, in this thesis.

It is obvious that more work could be done with the signal source, after the full radar have been implementated. Hence to tune the modulation and waveforms for optimum beat frequency response. Nevertheless should also the discovered high phase noise contribution, be payed further attention. Thus in order to determine the full systems, phase noise cancellation. This characterization would be highly valuable, since the degree of PN together with the near clutter response, would definitively yield new requirements back to the applicability of the implemented waveforms.

9.4. Intermediate Test Radar

The last beat frequency analysis of the UWB special case, proved that the signal source could produce waveforms with similar LFM properties as the intended W-band implementation. Hence can a intermediate X/Ku-band test radar, easily be constructed with tested signal source and available RF equipment at the university. This approach is suggested as an alternate method, for digital aqcusition system testing and evaluations of FMCW signal processing techniques on real range-Doppler maesurments, if the MMW part of radar is further postponed. Hence can the lessons learned, yield benefit to the later implementation of the complementary system. Such a test radar were partially built in this thesis, but the limited time in combination with the initial erroneous waveform generation, confined the total work of the thesis.

Bibliography

[1] AutoNOMOS. *Project web page, Autonomos Labs, Development of technology for driverless cars of the future.* Freie Universität Berlin, http://www.autonomos.inf.fu-berlin.de, 2011.

[2] Constantine A. Balanis. *Antenna Theory*. John Wiley & Sons, 2005.

[3] Dean Banerjee. *PLL Performance, Simulation and Design*. Dog Ear Publishing/ National Instruments, 4th edition, 2006.

[4] William David. *Research Report, FMCW MMW Radar for Automotive Longitudinal Control*. University of California, Berkeley, 1998.

[5] Laurens de Bruijn. *Design Note, 77GHz FMCW Radar, DN-090018*. NORBIT, 2009.

[6] Laurens de Bruijn. *Design Specification, 77GHz FMCW Radar, DS-090020*. NORBIT, 2009.

[7] Laurens de Bruijn. *Technical Note, 77GHz FMCW Radar Proposal, TN-090017*. NORBIT, 2009.

[8] Analog Devices, editor. *A Technical Tutorial on Digital Signal Synthesis*. Analog Devices, http://www.analog.com/static/imported-files/tutorials, 1999.

[9] Analog Devices. *Manual, ADF4107, PLL Frequency Synthesizer*. Analog Devices, 2007.

[10] Analog Devices. *Manual, AD9958, 2-Channel, 500MSPS DDS, with 10-Bit DAC*. Analog Devices, 2008.

[11] Adrian Fox. *Article, Pll Synthesizers*. Analog Dialogue 36-03. Analog Devices, 2002.

[12] Türker Ince. *Article, An S-band frequency-modulated continuous-wave boundary layer profiler: Description and initial results*, volume 38. Radio Sience, 2003.

[13] Mohinder Jankiraman. *Design of Multi-Frequency CW Radars*. SciTech Publishing Inc, 2007.

[14] John D. Kraus. *Antennas*, chapter 13, page 649. McGraw & Hill, 1956.

[15] Y. Liu. *Article, Linearity Study of DDS-Based W-band FMCW Sensor*. IEEE, 2009.

[16] Bassem R. Mahafza. *Radar Systems Analysis and Design using MATLAB*. Chapman & Hall/CRC, 2005.

[17] MathWorks. *Software Documentation, MATLAB FFT-function*. MathWorks, http://www.mathworks.com/help/techdoc/ref/fft.html, 2011.

[18] MathWorks. *Software Documentation, MATLAB Spectrogram function*. MathWorks, http://www.mathworks.com/help/toolbox/signal/spectrogram.html, 2011.

[19] Thomas A. Milligan. *Modern Antenna Design*. John Wiley & Sons, 2005.

[20] Mitomo. *Article, A 77 GHz 90 nm CMOS Transceiver for FMCW Radar Applications*, volume 45. IEEE Journal of Solid -State Circuits, 2010.

[21] Eva Murphy. *Article, All About Direct Digital Synthesis*. Analog Dialogue 38-08. Analog Devices, 2004.

[22] Paul O'Brian. *Article, Phase-Locked Loops for High-Frequency Receivers and Transmitters*, volume 3 of *Analog Dialogue 33-3*. Analog Devices, 1999.

[23] Paul O'Brian. *Article, Phase-Locked Loops for High-Frequency Receivers and Transmitters*, volume 2 of *Analog Dialogue 33-3*. Analog Devices, 1999.

[24] Paul O'Brien. *Article, Phase-Locked Loops for High-Frequency Receivers and Transmitters*, volume 1 of *Analog Dialogue 33-3*. Analog Devices, 1999.

[25] Jung Dong Park. *Article, An Efficient Method of Eliminating the Range Ambiguity for Low-Cost FMCW Radar Using VCO Tuning Characteristics*. IEEE, 2006.

[26] Samuel O. Piper. *Article, Reciver Frequency Resolution for Range Resolution in Homodyne FMCW Radar*. IEEE, 1993.

[27] Samuel O. Piper. *Article, Homodyne FMCW Radar Range Resolution Effects with Sinusoidal Nonlinearities in Frequency Sweep*. IEEE, 1995.

[28] David M. Pozar. *Microwave and RF Design of Wireless Systems*. Wiley, 2001.

[29] David M. Pozar. *Microwave Engineering*. John Wiley & Sons, 2004.

[30] Mark A. Richards. *Fundamentals of Radar Signal Processing*. McGraw & Hill, 2005.

[31] Hermann Rohling. *Article, Waveform Design Principles for Automotive Radar Systems*. Radar, 2001 CIE International Conference on, Proceedings. IEEE, 2001.

[32] Hermann Rohling. *Article, An Automotive Radar Network Based On 77GHz FMCW Sensors*. IEEE, 2005.

[33] Hermann Rohling. *Article, Radar Waveform for Automotive Radar Systems and Applications*. Radar Conference. RADAR '08. IEEE. IEEE, 2008.

[34] Jan Egil Ruud. *Technical Note, FMCW LO Board PR-31235-1 Microcontroller Requirements, TN-100008*. NORBIT, 2010.

[35] Martin Rygh. *Project Report, 77 GHz FMCW Radar, Simulation and Testing of a Millimeter-Wave Radar*. Department of Electronics and Telecommunications, NTNU, 2010.

[36] Martin Schneider. *Automotive Radar, Status and Trends*, volume 1. Article, GiMiC, Robert Bosch GmbH, Corporate Research, 2005.

[37] Huber & Shuner. *Datasheet, SUCOFLEX 104P*. Huber & Shuner, 2010.

[38] Merill I. Skolnik. *Introducion to Radar Systems*. McGraw & Hill, 2001.

[39] Merrill I Skolnik, editor. *Radar Handbook*. McGraw & Hill, 2008.

[40] Andreas Stelzer. *Article, High-Speed FMCW Radar Frequency Synthesizer With DDS Based Linearization*, volume 17 of *IEEE Microwave and Wireless Components Letters*. IEEE, MAY 2007.

[41] George W. Stimson. *Introduction to Airborne Radar*. SciTech Publishing Inc, 1998.

[42] A.G Stove. *Article, Linear FMCW Radar Techniques*, volume 139 of *IEE Proceedings-F*. IEEE, 1992.

[43] Yngve Thodesen. Mixer lecture, 15.05.10. General concepts of mixing, given in lecture series of "Microwave integrated circuits" at Radio Technology studies, NTNU, May 2010.

[44] Christoph Wagner. *Article, PLL Architecture for 77GHz FMCW Radar Systems with Highly Linear Ultra Wideband Frequency Sweeps*. IEEE, 2006.

[45] Z. Zhang. *Article, Analysis and Simulation of Land and Rain Clutter for PRC CW Radar at X-band*. Number 2 in Sonar Navigation. IEE, 1999.

A. Theoretical fundamentals

In this appendix of the thesis the fundamentals of radar are presented briefly as referance for the thesis and to connect the spesific theory and finds to an overall radar context.

A.1. Radar

Radio Detection And Ranging (RADAR) is a device that utilizes the RF/microwave/MMW-frequency part of the electromagnetic spectrum (3MHz - 300GHz) to conduct measurements of objects or an designated area. Typical sensable parameters is; range to target, radial and tagential velocity of target, space angles to target and object and area radar imaging. Today all parameters are obtained automatically in like for instance detection, tracking and pre-/post processing. To extract the wanted parameters in aspect of the surrounding environment and preferable radar plattform, different types of radars have been constructed. The most common way to classify operational radars is by their fundamental waveform, shown in fig A.1. Figure A.1 shows that radars are mainly

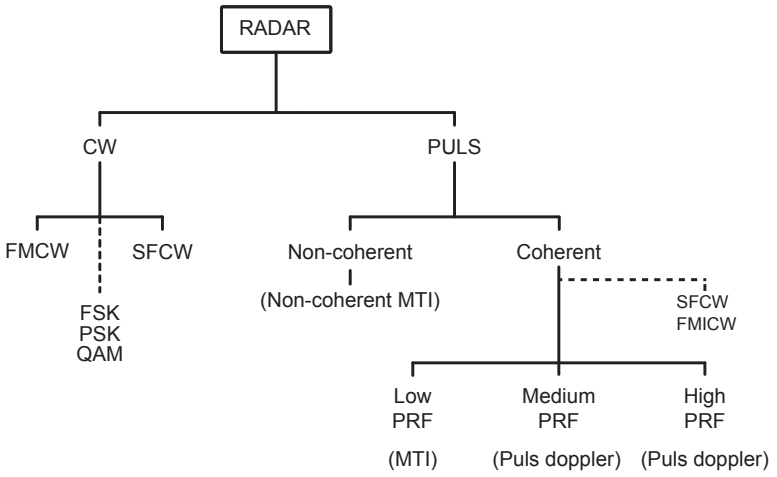

Figure A.1.: Classification of radars by waveform

separated by continuous wave and pulsed waveforms. Pure CW radars can only discriminate Doppler shifts, but with frequency modulation (FM), stepped frequency (SF) modulation or phase/frequency coded signal (PSK/FSK/QAM) compresion, range can also be extracted.
Pulsed waveforms are mainly divided between coherent and non-coherent pulses, where coherent pulses are mostly used for it's advantage with detection. Depending on interval between pulses (Puls Repetion Interval), mostly referred to as the puls repetion frequency

(PRF), puls radars are further divided in three categories: Low- , Medium- and High PRF. These different frequencies of puls repetion will give the puls radar different properties that can be exploited in different types of applications. The Low PRF scheme are used by MTI (Moving Target Indicator) radars, where echoes from moving targets are separated from unwanted echoes (background clutter) by signal variations given by Doppler shifted targets. Puls Doppler radars on the other hand uses high PRF's to get more preferable conditions for detection of high-speed head-on targets as in typical fighter aircraft applications. The medium PRF region is used by puls Doppler radars to utilize the advantages of low and high PRFs to a slight degradation in performance for some applications. However some coherent schemes like FMICW and SFCW are pulsed but utilizes some of the CW benifits and properties and can be seen as a kind of hybrid waveform. The most common types of radars in aircraft and ships are either MTI or puls Doppler radars. In vehicle applications and airborne altimeters FMCW and SFCW radars are mostly used. More advanced radars are also capable of operate with two or several modes of operations, for instance the AWACS airborne radar can operate in High PRF mode for long range air-target detection, but can also switch to 'maritime mode' and use a Low PRF mode to apply MTI signal processing to extract slow moving target from sea clutter. It is apparent that not only classification of radars by waveforms, but also classification by functionality. Typical functionalities are: 'Tracking radar','Searching radar','Track-while scan radars','Long range radars', 'Short range radars' and 'Navigation radars'. Hence radars can be described in many ways and only the basic ones are presented in this section. For further information about CW and puls radars a recommended reference is [38, chap.1], which also is used as a reference for this initial part.

A.2. Range Sensing

The easiest way to understand a ranging radar system, is by studying a puls radar. A

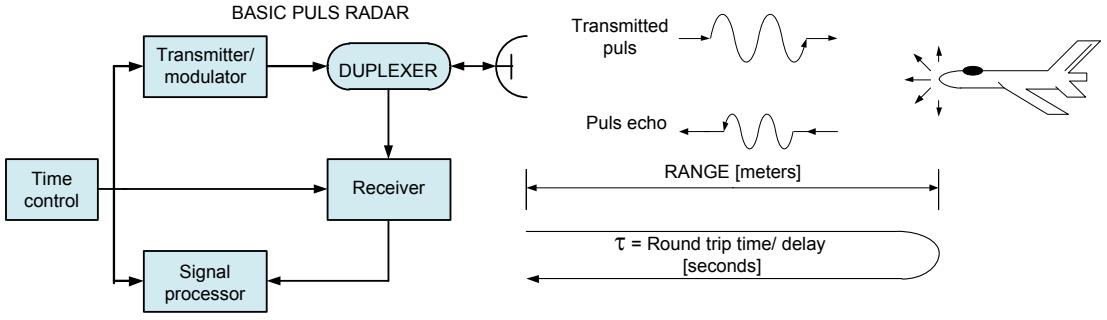

Figure A.2.: Basic puls radar, with single puls operation

basic puls radar configuration is shown in figure A.2, which is based on figure 1.5 from [16]. More comprehensive block diagrams for both puls and CW -radars are given in [38, chap.3] and [16, chap.3], for better understanding of the specific radar designs. The transmitter modulates a rectangular puls of length Δt with a sine wave and a duplexer

enables transmission through the antenna. Meanwhile transmitting the duplexer isolates the receiver which is optimized to receiving weak echoes. In this way the receiver is protected from the high power puls transmission. A antenna directs the puls in the wanted direction depending on its pointing direction and antenna directivity. The puls propagates until it hits a reflecting structure, that backscatters a part of the puls energy towards the radar. The weak echo puls is then intercepted by the same antenna structure and coupled through the duplexer to the receiver. This type of configuration that uses the same antenna for transmitting and after reception of the echo, the signal is processed by a signal processor. Thru the whole operation a timing device have control over the occurring events. By using the timing information between transmission and reception, one can sort out the delay (τ) from the reflection of target often called *round trip time*. Since electromagnetic waves travel at the speed of light, the *range* can be extracted.

$$\begin{aligned} \tau &= \frac{2R}{c} \\ &\Downarrow \\ R &= \frac{c\tau}{2} \end{aligned} \tag{A.1}$$

Extraction of range is also possible in CW-type radars but they have to modulate their waveform in order to make an time mark to obtain the round trip time.
To be able to follow the target and to detect new targets that arrives within the radars maximum range R_{max}, several pulses need to be send after another in pulsed radars. The time between transmitted pulses (PRI) needs to be such that the previous puls has been received by the radar. The rate (PRF) at which pluses are to be transmitted is determined by the longest range that targets are expected. This range will be given by the radar equation(A.24), that describes the systems performance to receive power or to gain a signal-to-noise ratio (SNR) at a specific range. A problem arise in pulsed radars when the PRI is to short and that echoes beyond R_{max} will arrive after the next puls is transmitted. This will lead to range ambiguity, and the radar can mistake earlier echoes as close targets. Such echoes are often referred to as *Second-time-around echoes* or even earlier transmitted pulses as *Multiple-time-around echoes*. Typical situations that could lead to such conditions is, bad radar design, big reflectors beyond R_{max}, unpredictable propagation conditions like *Ducting* or high-prf puls-Doppler radar, where this is a calculated disadvantage in order to achieve other preferable conditions. Figure A.3 shows the situation of a typical medium-range radar with rectangular modulated sine waves and the important puls parameters [38, p.4]. If the PRI is assigned variable T_p, it is defined by $T_p = \frac{1}{f_p}$, where f_p is the PRF. The *unambiguous range* is then defined as

$$R_{un} = \frac{cT_p}{2} = \frac{c}{2f_p} \tag{A.2}$$

In prospect of figure A.3 the *duty cycle* is given as the ratio of time transmitted over the time that could be used for transmission, *duty cycle* $= \frac{\Delta t}{T_p}$, where Δt is the puls width. Average power will show the effectiveness of the systems power utilization within a PRI and is therefore a perfered measurement of power compared to the peak power (P_t). To compensate for this, puls radars often use puls trains rather than a single puls to enhance

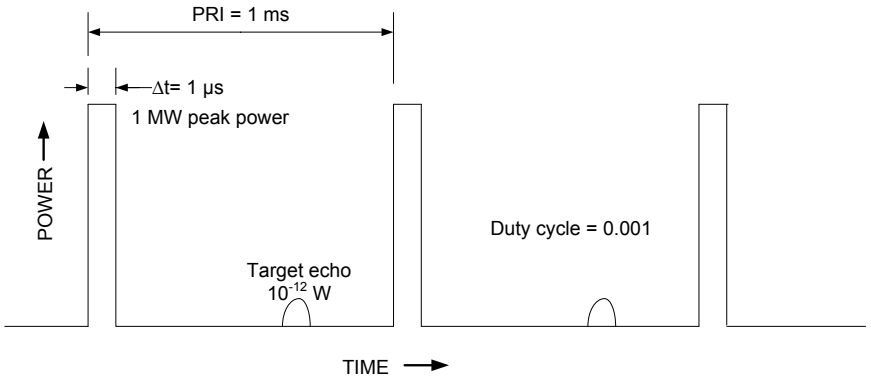

Figure A.3.: Typical puls configuration of a medium range surveillance radar

the *received average power* and thereby improve detection of targets.

$$P_{avg} = \frac{P_t \Delta t}{T_p} = P_t \Delta t f_p \tag{A.3}$$

Another consideration concerning the puls width and the use of puls trains, is the ability to discriminate multiple targets within the *unambiguous range*. To get a good *range resolution* a narrow puls is needed, which will decrease the average power if not puls trains are applied. *Range resolution* is defined in equation A.4. The receiver bandwidth, is in most radars designed such that $B \approx \frac{1}{\Delta t}$. The *range resolution* is the shortest distance between two targets that can be discriminated as singular targets.

$$\Delta R = \frac{c\Delta t}{2} = \frac{c}{2B} \tag{A.4}$$

Consequence the puls radar bandwidth needs to be large in order to get a good range resolution. Similarly this equation holds for CW type radars that enable ranging, and that they need to have a large modulated bandwith to have sufficient range resolution.

A.3. Radial and Tagential Velocity Sensing

It was shown that a simple puls radar can be an easy approach to understand the concept of ranging. In a similar way CW-radars if the simplest way to describe the sensing of radial and tagential velocity from moving targets by extraction of the Doppler shift. Puls radars can also sense doppler shifts by measuring the change of range over a period of time, but this requires more processing.
The CW radar is constantly sending the waveform, unlike puls radars. This means that CW radars transmit while they receive. As a consequence, such radars will have problems of isolating the strong transmitted signal from the weak target echo in a typical monostatic design. Although this occurs, a moving target will generate a Doppler shift $(\pm f_d)$ that will shift the echo signal away from the center frequency. Received signal will be shifted as $f_{Rx} = f_c \pm f_d$. Hence that enables these signals to be separated from

the strong transmitted signal by mixing the T_x and R_x-signals and using a Doppler filter or a Doppler filter bank. A basic theoretical block diagram of a CW radar is shown in figure A.4.
The Doppler frequency made by a moving target will be dependent of the targets vectorial velocity (v_r). A direct 'head-on' target will then produce a positive shift while a 'tail-on' target will produce a negative shift. When a target is following another track than the direct direction of the radar main beam, its relative velocity (v_0) will be given by the vectorial components of azimuth (ϕ) and elevation (θ) angles relative to the radar. If the target on the other hand travels in the same plane as the radar, the relative angle in the same plane ψ, will give the angel dependent relative velocity. The relative velocity components are thus

$$v_0 = v_r \cos\psi \tag{A.5}$$
$$v_0 = v_r \cos\phi \cos\theta \tag{A.6}$$

Further the Doppler frequencies are defined as

$$f_d = \frac{2v_r f_0}{c} = \frac{2v_r}{\lambda_0} \tag{A.7}$$
$$f_d = \frac{2v_r \cos\psi}{\lambda_0} \tag{A.8}$$
$$f_d = \frac{2v_r \cos\phi \cos\theta}{\lambda_0} \tag{A.9}$$

These defininitions will only be valid for a static radar with a moving target. If both targets are moving the distance change rate between the two moving object has to be taken into account.

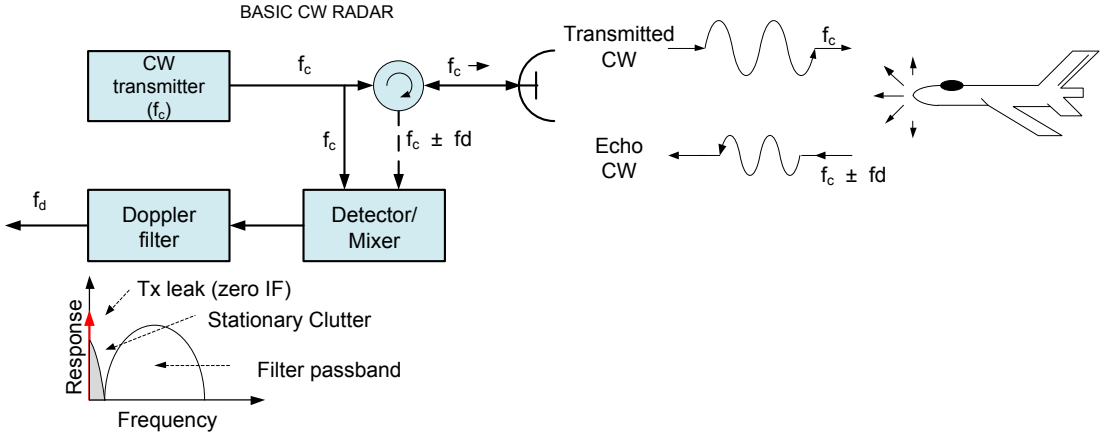

Figure A.4.: Basic CW radar block diagram

Figure A.4 illustrates the basic Doppler processing [38, fig. 3.3]. In Rx-mode the transmitter frequency is feed to the mixer/detector by direct leakage or by a coupler device. Here the Tx-frequency is mixed with the received echo and produces an Zero IF output. The Doppler filter will then have a lower cutoff response that remove the down-converted big Tx-component and stationary *clutter*. Stationary clutter is big reflections, often much stronger than the wanted echo, from non-moving zero Doppler big targets as mountains

etc. The upper cutoff of the filter response is determined by the radar application and how the maximum expected radial velocity from the targets in the specific application. A problem however in this design is that the mixing process removes the sign of the Doppler shift. As a result it is not possible of determine if the target is approaching or moving away from radar. In order to sense the sign, a common way is to use I and Q signaling, where the signal is splitted in two by an 90 degree phase shift. Dependent of the lag or lead of the two components the sign can be recovered [39, sec. 6.9] and [41, chap.18].
In Doppler sensing radars, it is common to use Doppler filter banks in order to sense shifts from multiple targets. To do this the signal is splitted in parallell to assigned overlapping narrow band filters. Ideally only the narrow band filters that have single Doppler frequencies within the passband will produce an output. But real filters will have some overlap in to other Doppler filters causing some respons in the adjacent filters. Never the less this will discriminate multiple targets by the accuracy/bandwidth of each applied filter. The concept is illustrated in figure A.5 and indicating that the filter bank can be implemented by digital filters.

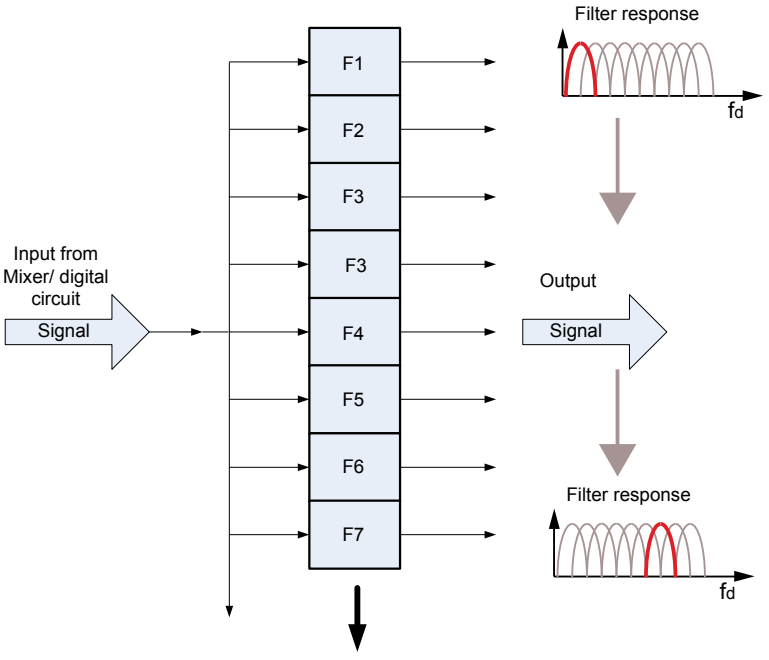

Figure A.5.: Doppler filter bank

In comparison with the P_{avg} in pulsed systems, CW radars have a similar the parameter termed P_{CW}, which is the average power over the *dwell time*. Dwell time is the interval where the received signal is observed by the Doppler filter. It is worth noticing that the dwell time is the inverse of the frequency resolution of the Doppler filter and that there will be a trade-off between the ability to get great accuracy in Doppler and high average CW-power. Compared to pulsed radars CW types can have appoximately $100\,\%$ duty cyle while transmitting, allowing a much lower Tx power to obtain the same target detectabillity. This is the reason why CW radars is often refered to as Low Probability of Intercept radars (*LPI*). Likewise will forinstance FMCW have the same property since it

utilizes the transmitted energy over a large modulation bandwith with a flat rectangular bandwith, making noncooperative intercepiton difficult in military ESM operations. The deterministic signal waveform makes it resistant to jamming, because the echo singal can be predicted allowing non-matching waveforms to be suppressed [13, p.4].

A.4. Antenna Parameters

The antenna is an important component of the radar since it acts as the interface between the radar transmission lines and the space propagation. Thereby it is defining the concentration of radiated energy in direction of the target (*Gain*) and the abillity to collect backscattered energy (*Antenna Effective Aperature*). In addition will the antenna give the radars abillity to measure the angle of arrival from echo signals in polar coordinates. Consecuently antennas acts as spatial filters to resolve targets in the angular domian and at the same time reject undesired signals outside the main beam. By the search/track operation of the radar the antenna parameters will define the volumic radar coverage and observation time per space bin [38, p.538]. A common way of extracting the target direction is by observing the angle at which the magnitude of the echo signal is at maximum from a scanning antenna. This requires an narrow antenna beam width (high antenna gain) and there by good angular resolution. To discriminate targets in one dimension the radar must use a two-antenna configuration with the main beams slightly displaced in pointing direction or the antennas slightly displaced but with same viewing angle. Then it is possible to monitor the respectively different amplitudes or phases received from the two antennas. Thereby the displacement can be extracted as a direction. If a full space observation is nessesary, four antennas must be used in the same way in order to extract direction in both azimuth and elevation. The main parameter of antennas is the *effective electrical size of the antenna*, which is related to the radars wavelength. There are many ways of getting large effective antennas but these technices are not described in this report. These thechnices can be reviewed in [41, Chap.8]. In this section only the main antenna parameters is treated.

Normally radar antennas are operated to sense targets in the *far field*. This is avoid influence on the antennas reactive near-field that will alter the antenna cracteristics. In addition the transmitted waveform will also not be properly created before it reaches the transversal electromagnetic (TEM) condition at the far field border. The far field is given as

$$R \geq \frac{2D^2}{\lambda} \tag{A.10}$$

In figure A.10 the far field will dependent of the aperture diameter (D) of the antenna and the wavelength (λ).
Another important set of parameters is the antenna beam width within θ(azimut) and ϕ(elevation) defining the main beam beamwidth in polar coordinates. For practical radar the 3_{dB} beamwidth (θ_{3dB}) is used in most considerations. This because its here most of the radiated energy lies and therefore is practical for target detection. Moreover the

waveform will experience the least distortion within this angle. In some applications although the null to null beam width is used (θ_0). The beam width is summarized in figure A.6 and following equations (Where D is referd to as the antenna dimension in λ).

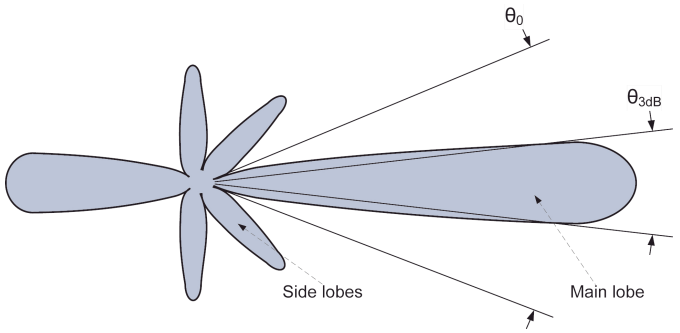

Figure A.6.: Typical high-gain antenna, 2-D-diagram

The additional side lobes can degrade performance of the radar considerably if this is not taken into account.

$$\theta_0 = 2\frac{\lambda}{D} \qquad [\text{radians}] \tag{A.11}$$

$$\theta_{3dB} \approx 65\frac{\lambda}{D} \qquad [\text{degrees}] \tag{A.12}$$

Note however that by using antenna arrays the beamwiths can be much more narrow.
In order to get a theoretical value of the antennas ability to direct power in main directions, its directivity or gain needs to be calculated. There are developed several types of gain derivations techninces, dependent of antenna type, structure and physical dimmentions, which can be reviewed in forinstace [2], [14] and [19]. However for a practical approach to radar implementation normally approximations of gain are needed, to get standard values for the most severe directions of energy emission, through the antenna. Both main lobe and sidelobe levels are important parameters, since sidelobes can cause illumination of large unwanted echo-sources, causing poor Rx conditions and false target detection. If sidelobe levels are acceptable, only the main lobe gain will be the parameter of subject. It is important to note that the directivity or gain of antennas yield for both transmission and reception since the all antennas are resiprocal of nature. Normally the gain and directivity are given as an functions of polar coordinates θ and ϕ. In the study of the antenna gain it is common among radar engineers to only use the *power gain* definition, which takes the antenna losses into account (impedance- and polarization mismatch)[38, sec. 9.2]. The power gain is defined as

$$G = \frac{4\pi\ (\text{Maximum power radiated per unit solid angle})}{\text{Net power accepted by the antenna}} \tag{A.13}$$

Or equivalent

$$G = \frac{\text{Maximum radiation intensity from subject antenna}}{\text{Radiation intensity from a lossless isotropic radiator with the same power input}}$$

In basic calculations of radar performance by the *radar equation*, the maximum gain of a lossless antenna is often used

$$G = \frac{4\pi A_e}{\lambda^2} = \frac{4\pi\eta A_p}{\lambda^2} \tag{A.14}$$

In equation A.14 A_e is the effective antenna area, while η is the antenna aperture efficiency and A_p the physical antenna area. Some times approximations is used when the 3dB beam widths in azimuth and elevation are known [38, p.77].

$$G \approx \frac{26}{\theta_B \phi_B} \qquad \text{(Skolnik)} \tag{A.15}$$

A.5. Radar Cross Section

The radar cross section (RCS) is a quantity (area in m^2), which gives the targets ability to reflect electromagnetic waves from the radars perspective. The most significant parameter in RCS-calcutaions is the characteristic dimensions of the object compared to the radar wavelength. This is because the wavelength will determine what kind of interaction mechanisms the radar wave experience at the target. In addition the RCS can vary with aspect and polarization. Therefore the reflections from a radar target is a very complex quantity and must not bee seen as a single number but more as an indication, with its values choosen with concern [38, sec. 2.7].
The RCS (σ) is the resultant from all individual infinitely small point scatterers that makes up the target. An vectorial addition of all contributing scatterers can be made by solving the Maxwell's equations if all boundary conditions known. This will mostly be applied for simple objects/ geometries, because of the big number of variables. The RCS from simple targets is often described analytically under simplified conditions For more complex targets only measurements of real or scaled modell targets, are possible to describe the targets backscatter. Often such measurements makes a database for statistical descriptions for target classes. Because the RCS is varying greatly with frequency, aspect and polarization the radar will experience *fading/ fluctuations* from complex targets. These considerations have to be taken into account to anticipate the performance of the radar. As a consequence many different probabillity density functions (*pdf*) have been developed to make conservative assumptions to the σ-parameter. For more details on fluctuating RCS's and RCS generally, see [38, sec. 2.7 & 2.8].
The backscattering from a radar target can be simplified defined as

$$\sigma = 4\pi R^2 \left| \frac{E_r}{E_i} \right|^2 \tag{A.16}$$

Figure A.16 shows how reflected power towards the radar per unit solid angle over the incident power density gives the RCS (under the TEM-wave assumption). E_r is the electrical field strength of the signal at the receiving radar, E_i is the electrical field strength incident on the target and R is the range to target.
To make initial measurements of radars, the *sphere target* and the *corner reflector* target is perfered to avoid uncertainties. The sphere target will have the great advantage because it will have the same backscatter characteristics from all points of aspect. Further more the sphere will have an rcs of approximately same size as its real viewed area, at wavelengths in typical radar frequency bands (if $(2\pi r)/\lambda > 10$) [38, p.51]. RCS of sphere of radius (r) under given conditions can be approximated as

$$\sigma \approx 2\pi r \tag{A.17}$$

Similarly a trihedral corner reflector is independent of aspect, within small angular variations. A trihedral corner reflector RCS can bee approximated when the objects dimmention $\gg \lambda$ [38, p. 53] and the frontal area of reflector is A.

$$\sigma \approx \frac{4\pi A^2}{\lambda^2} \tag{A.18}$$

For radar employed for automotive detection, cars can have quite large RCS. However the car design, material and angle of aspect may vary the backscatter significantly. Typical values from are within the region of $1 - 200\ \mathrm{m}^2$ [38, p.62].

A.6. Clutter

In addition to backscatter from targets that is desirable, the radar will receive unwanted reflections from objects as ground, sea, mountains and buildings etc known as *Clutter*. These reflections seen by the radar will degrade the ability to detect wanted targets because they can be much larger than the signature of the targets. Clutter will in addition to receiver noise and signal interference limit the performance of the radar. Like the RCS parameter Clutter has a statistical nature dependent of wavelength, observation angle, illuminated area/volume and the illuminated area/volume electrical properties and homogenity. Consecuently will different obsevation situations give several possible pdf's for clutter prediction.
Normally the clutter is divided in two main categories: *Stationary* and *Moving* clutter. Stationary clutter is typical ground, sea, mountains and buildings and will have no Doppler shifts and appears around zero frequency. This is partly true because the spectral components will have some extension in spectrum, caused by the finite signal lengths and/or radar plattform movement and antenna beam limits. Stationary clutter is also referred to as *area-clutter* and will be given by the illumanited area of the radar beam. To take this clutter type into account often a general normalized radar cross section

parameter is worked out form measured statistical data. RCS will the be given by $\sigma_c = Area \times \sigma_{norm}^{area}$. Never the less it is important state that stationary clutter can fluctuate like RCS's, but not as much as small targets. Figure A.7 from [38], shows how the illuminated surface for low grazing angles generates area clutter as the outlined area A. The figure shows the In addition to low grazing angles the radar can see objects and surfaces at different angles of aspect, shown in figure A.8 for the general nature of variations in surface clutter dependent of angle [38, p.409].

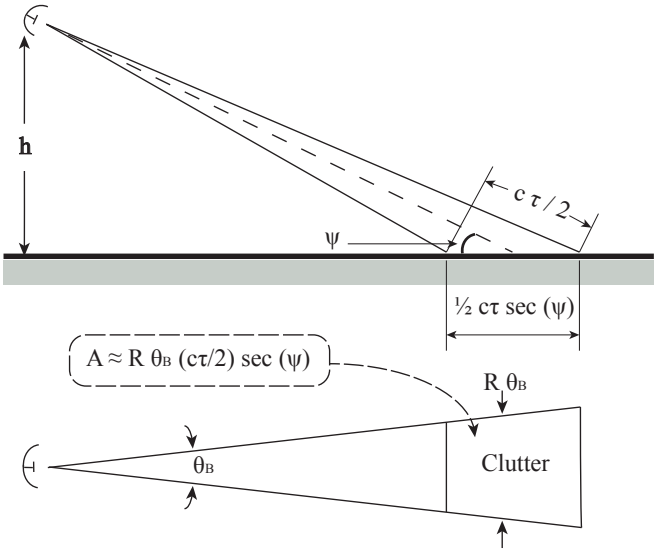

Figure A.7.: Low grazing angle area clutter geometry

The received clutter power can be estimated by the general radar equation described in section A.7, by substituting the real targets RCS, σ_t with the *area clutter cross section* $\sigma_c = Area\ \sigma_{norm}^{area}$

$$\begin{aligned} S_r &= \frac{P_t G A_e \sigma_t}{(4\pi)^2 R^4} \\ &\Downarrow \\ C_r &= \frac{P_t G A_e \sigma_{norm}^{area} (\theta_B (c\tau/2) sec(\psi))}{(4\pi)^2 R^4} \end{aligned} \tag{A.19}$$

If the stationary clutter is dominat over the receiver noise, the signal-to-clutter power ratio will be

$$\frac{S}{C} = \frac{\sigma_t}{\sigma_{norm}^{area} (\theta_B (c\tau/2) sec(\psi))} \tag{A.20}$$

In automotive LRR applications stationary ground clutter at low grazing angles would normally appear, if not suppresed by the antenna configuration or processing technics. A typical urban *road*-enviroment will in addition introduce the radar to undesired observed object or surfaces at other angles. Figure A.8 show the clutter variation, where

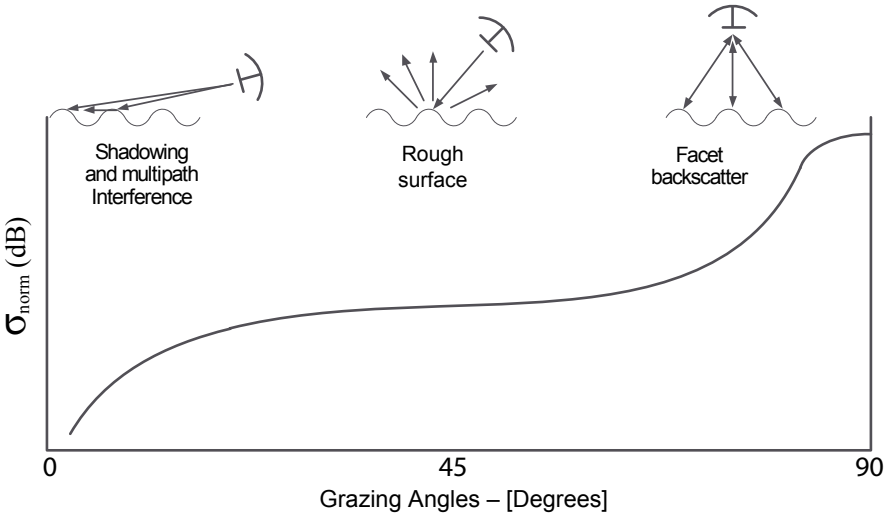

Figure A.8.: The three major scattering regions and variations in surface clutter over the grazing angle

high grazing angles may give severe backscatter from *facet* interaction. Likewise may intermediate grazing angles give rough surface backscatter, while low angles may give multipath effects reducing or enhacing backscatter dependent of the signal and surface wavenumber properties. In addition to stationary clutter, will clutter from undesired moving targets in the vicinity of the road create *non-zero-doppler* clutter. Together with the solid objects observed will rain, hail etc interact with the radar signal depenent of the frequency of choice. Typically will forms of precipitation attenuate the signal to some degree, but also bee seen by the radar as moving clutter.
When the radar observs moving non-zero-Doppler clutter like rain, hail, bird swarms or chaff, the clutter is referred to as *volume-clutter*. The biggest concerns here is that the clutter can mask moving targets at similar Doppler frequencies, typical MTI or Puls Doppler radars and that the volume expands at longer ranges from the radar. Volume clutter is calculated in a similar way as area clutter but with volume as main parameter $\sigma_c = Volume \times \sigma_{norm}^{volume}$. Compared with the signal strength received at radar, the area and volume clutter echo decreases as $1/R^2$ but the signal decrease by $1/R^4$.

The combination of all addable *noise*-sources will inflict upon the detection of desired targets, by raising the noise floor and thereby reducing the receivers sensibility and force the radar designer raise the detection threshold that will increase the possibility of a target *miss*. In addition to increased noise floor the clutter will contribute with clutter peaks that can totally mask targets or be a source of confusion to detection of real targets creating false targets. It should be noted that some types of radars senses clutter intentionally, like weather radars, ground mapping radars and SAR/ISAR imaging radars. [38, chap. 7].

Compared to a Low PRF MTI radar which sees clutter within only one range-angle cell of the radar pulse, CW radars sees clutter continuously only limited by the antenna properties [38, p.195]. However modulated schemes of the CW-waveform will practically see less clutter because smaller periodes of the signal is prosessed in segments and can be approximated in the same way as the pulsed scheme in figure A.7, [45, sec.3]. In every

different radar design the propagating frequecy(ies) needs to be investigated for levels of interaction and propagation attenuation in worst case scenarios. The use of MMW in signaling will have different effects on clutter backscatter, dependent of the type of illuminated area and its surface properties. However will small wavelengths result in less clutter compared to larger wavelengths because MMW will improve the antenna gain thereby reducing the illuminated area that is the source of unwanted backscatter. Additionally these wavelengths will also have greater attenuation in free space, thereby reducing the possibillities for multi-path interference and small sidelobes collecting clutter. The increased atmospheric attenuation of MMW contributes to immunity of unwanted detection and the overall interference immunity, thereby introducing an advantage in using MMW for automotive radar applications [4].

A.7. The Radar Equation

The radar equation is the radar designer or evaluators main working tool. It is a equation that anticipates the received power from target at the receiver or the signal-to-noise ratio at the output of the receiver front end. Often the equation is used to look at the maximum radar range for a specific design and to determine trade-offs in the design process. It is important to realize that the radar equation is an approximation. One can not fully take all reducing and enhancing factors into account. The basic radar equation, as presented in this section, is heavily overestimated. Therefore many different forms of the equation has been developed to account for special reducing factors for each radar application. The four main factors for correction is [38, p.31]

1. *The statistical nature of signal noise, mostly determined by receiver noise*
2. *Fading/ fluctuations of the RCS*
3. *Losses experienced throughout the radar system*
4. *Propagation effects caused by the Earth's surface or atmosphere*

The basic radar equation is derived as follows:
If the radar transmits a signal with the peak power (P_t) through a lossless fully matched directive antenna of gain (G), the received power density (ρ) at the target is

$$\rho_t = \frac{P_t G}{(4\pi)R^2} \tag{A.21}$$

The power accepted by the target with $\mathrm{RCS} = \sigma$ will then be

$$P_{acc} = \frac{P_t G \sigma}{(4\pi)R^2} \tag{A.22}$$

As a consequence the backscattered power density (assuming a isotropic scatterer) at the radar is

$$\rho_r = \frac{P_t G \sigma}{(4\pi)^2 R^4} \tag{A.23}$$

Hence the received power accepted by radar antenna of efficient area A_e, converted to gain by equation A.14 gives the basic radar equation for a mono static radar with respect to received power.

$$P_r = \frac{P_t G^2 \sigma \lambda^2}{(4\pi)^3 R^4} \tag{A.24}$$

To get the SNR at the output of the receiver, received signal power will be divided by the noise power ($N = kT_sB_s$).

$$\frac{S}{N} = \frac{P_t G^2 \sigma \lambda^2}{(4\pi)^3 R^4 k T_s B_s L_s} \tag{A.25}$$

In equation A.25 the signal is compared with its own receiver noise (kT_eB_s) and received noise from the antenna (kT_aB_s) that will make up the total system noise ($k(T_a + T_e)B_s = kT_sB_s$) within the receiver bandwidth B_s (see section A.8, for more details). In addition also a system general loss (L_s) is added to take other performance reducing factors as, wave guide loss, processing loss, mixer loss etc, into account. The independent system losses are seldom very high but the sum of all can be devestaiting. In many cases a radar designer wish to use the maximum range (R_{max}) to forfill the customers need. Therefore the radar equation is often defined in respect to R_{max}, and manipulated from the equations above. The equation will then be dependent on the *minimum detectable receiver signal power* (S_{min}) or *the minimum detectable signal-to-noise ratio* $(S/N)_{min}$. This will enable the designer to anticipate the receivers ability to detect targets in respect to a good noise-reduced design by manipulating the tweakable parameters like the transmitted power, antenna gain and wavelengths[38, Chap.2&3].

A.8. Distortion and Noise in Radar Circuits

Radar transceiver in general operate at high frequencies, typical in the microwave frequency region. Hence would a radar with internal microwave devices have multiple internal noise sources that will be superpositioned dependently of type, to both the transmitter and reciver output. The different sources are: *Thermal noise (Johnson noise), shot noise, 1/f - noise (Flickering noise), plasma noise and quantum noise.* In this text Thermal noise and 1/f noise mainly considered since these are the main contributing factors to reduction of radar performance. In relation to 1/f noise are also oscillator noise considered in the last subsection. Hence to its interconnected noise contribution to the typical flickering noise region when homodyne radar receiver used, like in the FMCW radar design threated in this thesis.

Thermal Noise

Thermal noise arise from the random motion of charges in lossy components or atmospheric attenuation resulting of random excitation of charges. The thermal noise power is often referred to as *white addative noise* because its independent of frequency within $0 < \mathrm{f} < 1000\ \mathrm{GHz}$. It will only be dependent of the temperature and the bandwidth. Remark that the other noise sources will have a different distribution than *white*-distribution of thermal noise. *Available Noise Power* is given as

$$P_n = N_0 = kTB\ \ [W] \tag{A.26}$$

Represented as *power spectral density* within the two-side spectrum between -B and B, will the frequency independent power spectrum density yield

$$S_n(\omega) = \frac{P_n}{2B} = \frac{kT}{2} = \frac{n_0}{2} \tag{A.27}$$

where n_0 is the noise spectral density constant. As a result in the frequency spectrum will thermal noise be observed as a flat noise spectrum with minor fluctuations, also know as the *noise floor*. If an arbitrary source of noise is white, it can be modeled as an equivalent thermal noise source, and characterized with an equivalent noise temperature. Noise temperature is defined by

$$T_e = \frac{N_0}{kB}\ \ [K] \tag{A.28}$$

Often $T_e = T_0 = 290K$ is used as referance for room temperaturated components (IEEE-standard). Note however that microwave componentens can be cooled for better noise performance or that antennas can be pointed towards objects, surfaces/ space which gives a different observable equivalent noise antenna temperature (T_a). If components have a signal gain, like an amplifier, this will also result in an gain of noise. An noisy amplifier can then be viewed as a noiseless amplifier with added noise temperature The

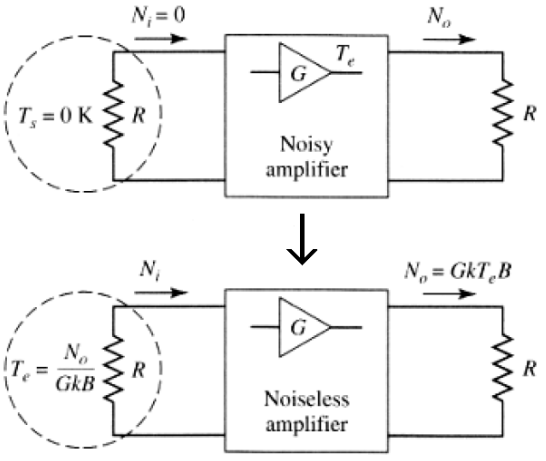

Figure A.9.: Equivalent noise temperature of noisy amplifier

the equivalent noise power at the input $N_i = kT_eB$ will then be $N_0 = kT_eBG$ at the

output. An alternate way of describing the noise enhancement of microwave components, is the *noise figure* (F). The noise figure can be interpret as *a measurement of the degradation of signal-to-noise ratio through the component*. If the input power (N_i) is from a matched load with $T_e = T_0$, the noise figure is defined as

$$F = \frac{\frac{S_i}{N_i}}{\frac{S_0}{N_0}} \geq 1 \tag{A.29}$$

In equation A.29 S_i and S_0 is respectively the input and output signal power. From this equation and the output noise power given as $N_0 = kGB(T_0 + T_e)$, will F be related to T_e by

$$\begin{aligned} F &= 1 + \frac{T_e}{T_0} \geq 1 \\ &\Downarrow \\ T_e &= (F-1)T_0 \end{aligned} \tag{A.30}$$

If on the other hand the component is *passive* and lossy, the relation is some what different. It is customary to denote the 'gain' of the component as *power loss factor* (L), which the inverse of the gain by definition. The result of the new definition will give the equivalent noise temperature, noise figure and special case when $T = T_0$

$$T_e = (L-1)T \tag{A.31}$$

$$\Downarrow$$

$$F = 1 + (L-1)\frac{T}{T_0} \tag{A.32}$$

$$\Downarrow$$

$$F = L$$

These above equations will hold for single component analysis. In the context of a transmitter/receiver made up of several components, is it useful to determine the total system noise performance. The equivalent noise temperature and noise figure can therefore be analyzed as and cascade of components with individual F and T_e.

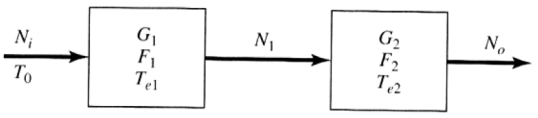

Figure A.10.: Cascaded system with individual F and T_e

The resulting cascaded system noise figure and equivalent noise temperature is given by

$$F = F_1 + \frac{F_2 - 1}{G_1} + \frac{F_3 - 1}{G_1 G_2} + ... \quad \text{(A.33)}$$

$$T_e = T_{e1} + \frac{T_{e2}}{G_1} + \frac{T_{e3}}{G_1 G_2} + ... \quad \text{(A.34)}$$

Flickering Noise

All semiconductor-based components, like amplifiers, diodes, mixers and oscillators, suffers from an additonal noise mechanism which is called *1/f-noise* or *flickering noise*. This is due to its spectral apperance, where the noise spectral density is inveresly proportional to frequency. In real spectrum this effect can be observed as the descending noise at zero frequency of fundamental harmonics in specturm. Figure A.11 show an typical spectrum where a sinusoidal signal is applied to a solid state device [29, p.569]. Hence is the flicering noise typically appearing around zero frequency and at carrier. The thermal noise floor will in addition be superior to the flickering noise for a certain offset frequency for zero-frequency and carrier.

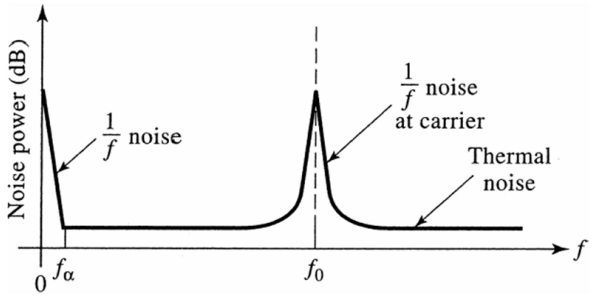

Figure A.11.: Noise power versus frequency for an solid state device with an applied sinusoidal input signal

Due to its noise characteristics, will the flickeing noise in most cases not be important to radar receivers that utilized the superheterodyne prinsipal, whose IF frequencies are grater than a few kHz. However this not apply to FMCW radars that use the homodyn radar configuration. Hence to the fact that a homodyn downconversion to baseband will reduce the radar sensitivity at low frequencies due to the descending 1/f-noise. For such systems will it be crutial to have an overall good 1/f noise performance to yield maximum performance or to enable higher beat frequencies in spectrum.

Oscillator Noise

In addition to the semiconductor 1/f-noise, will also FMCW radar systems be limited by the noise performance of the circuits local oscillator (LO). Hence to its phase- and amplitude noise. Allthough both AM- and PM-noise are associated with the oscillator, are the amplitude-modulation noise usuaslly small compared to the phase noise. Thus are

AM-noise in most cases not seen as a limiting factor to noisy oscillators. In relation to noise analysis, can hence both flickering noise and phase noise be modelled as a feedback amplifier and analysed with Leeson's modell for oscillator phase noise. This typical 1/f-noise and Oscillator modelling can be further examined in [29, p.594]. Like 1/f noise can phase noise mask weak target signals in homodyne baseband detection. Hence when a noisy oscillator signal is firstly upconverted to radar-band and then downconverted with the equal noisy LO signal. The PN will thus be decending from the zero frequency region. Nevetheless will there be some additional considerations in this matter since the mixing of 'equal' signals in the RX mixer will have a resulting phase noise output which will be dependent of the degree of relative PN-correlation between the RX target signal and the LO referance signal. More reading of the subject can be reviewed in [42] and [13].

Moreover in respect to the acctual phase noise, will oscillators or VCOs, both introduce *phase noise*. *Phase noise* arise due to the short-term random fluctuations in the frequency (phase) of an oscillator signal [28, p.280]. A typical phase noise affected signal is shown in figure A.12 [28, p. 281]. The figure illustrates that the phase variations can both be discrete and random. However will the typical spurs have distinct sources like mixer products or power line interference. The divergens to an ideal oscillator is hence illustrated with the center frequency *Dirac*-response at f_0.

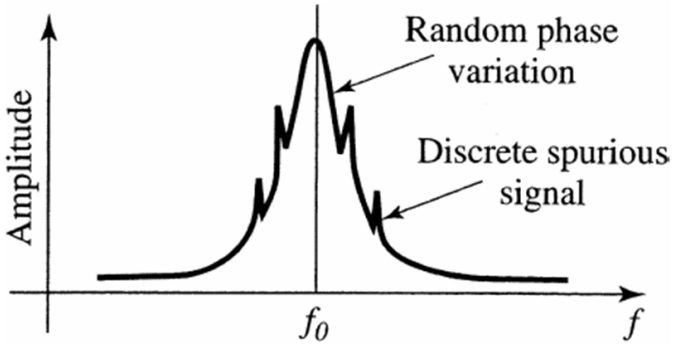

Figure A.12.: Typical noisy oscillator output spectrum

The phase noise is defined by Pozar as

> *the ration of power in a one phase modulation sideband to the total signal power per unit bandwidth at a given offset f_m from the frequency* [28, p.281].

This factor i denoted as $\mathcal{L}(f_m)$ and expressed as decibels in relation to the carrier per Hz of bandwidth at a specific offset(dBc/Hz at X Hz offset). Mathematically is the singel-sideband phase noise defined as

$$\mathcal{L}(f_m) = \frac{P_n}{P_c} = \frac{\theta_{rms}^2}{2} \tag{A.35}$$

where it will be the ratio of the noise power(SSB) to the carrier power (P_c), with the θ_{rms} which is the RMS value of the signal phase variation. This derivation along with Leeson's modell can be reveiwed in [29, pp.594-598]. The two-side power spectral density will by the latter be expressed as

$$S(f_m) = 2\,\mathcal{L}(f_m) = \theta_{rms}^2 \tag{A.36}$$

Leeson's Modell show that the phase noise can have characteristics of the type $1/f^n$. Where the different *n* arise from the different Q-factors of the oscillator designs. Typical spectral densities of two different oscillator output are shown in figure A.13 [29, p. 597], with typical low Q and high Q oscillators.

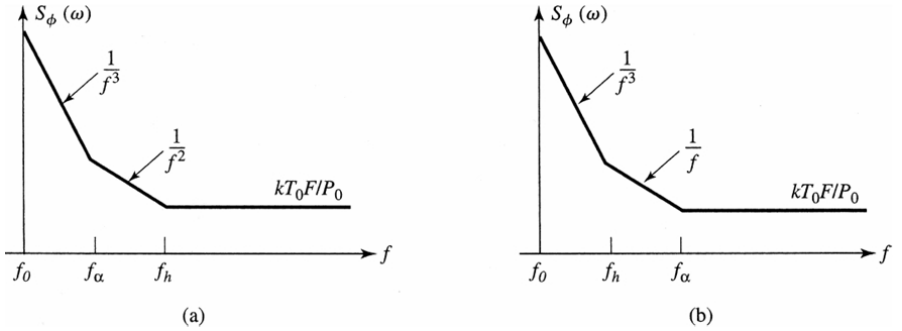

Figure A.13.: Power spectral density of phase noise at the output of an oscillator. (a) Response with low Q factor. (b) Response with high Q factor

The figure show that the dependence of oscillator design (Quality factors), will yield different noise spectral desisity curves between the to corner frequencies f_α and f_h. Hence different phase noise performance to the overall design, which can be a critical difference in an homodyne radar. Furhter does the figure show that the lower corner frequency will be determined by the total circuit noise temperature, hence the spectral desity noise floor, which in the illustration is represented with the circuit noise figure (F), $S_{floor}(\omega) = kT_0F \ / \ P_0$.

Dynamic range and intermodulation distortion

All nonlinear system components like diodes, amplifiers and mixers can yield additionall signal disstortion due to their nature. Normally the nonlinear circuits are used to utilized wanted functions as amplification, detection and frequency conversion. The problem however is that the nonlinearity can lead to undesired effects as *gain compression* and *intermodulation* distortion (spurious frequency components). This can result in increased loss, signal distortion and interference with other radio/ radar applications. If active devices such as diodes and transistors are operated beyond their desired working regions, high power levels can drive the components to degrading performance. Hence must allways nonlinear circuit inputs be matched belove the maximal recommended input power level of the spesific component. However for applied radio and radar systems, can unexpected signal amplification occur, that raises the input power levels such that the components still produce unwanted nonlinear effects. For components that contain diodes and transistors will the recomende power region be given as the *Dynamic Range*, were the component will yield the desired characteristics of the designer. If the device is operated beyond this region, *gain compression* and *intermodulation* distortion can occur. A nonlinear device with gain will output higher order harmonics together with the wanted fundamental amplified harmonic (termed ω_0), if a single tone input of the fundamental

tone is applied to the device A.37.

$$\begin{aligned} v_0 &= a_0 + a_1 V_0 \cos\omega_0 t + a_2 V_0^2 \cos^2\omega_0 t + a_3 V_0^3 \cos^3\omega_0 t + ... \\ &= (a_0 + \frac{1}{2}V_0^2) + (a_1 V_0 + \frac{3}{4}a_3 V_0^3)\cos\omega_0 t + \\ &\quad + \frac{1}{2}a_2 V_0^2 \cos 2\omega_0 t + \frac{1}{4}a_3 V_0^3 \cos 3\omega_0 t + ... \end{aligned} \tag{A.37}$$

As consequence the voltage gain will be limited by the third order harmonic coefficient $(3/4)a_3$ (which in most cases are negative) and the signal amplitude V_0^2 [28, p. 99]. In forinstance an amplifier will this parameter reduce the gain for large values of V_0. This effect is called *gain compression* or *saturation*. In real amplifier/active circuit implementations, this compression comes from a limited power supply to the circuit bias. Because amplifiers and similar devices are desired to be operated in the linear region to avoid nonlinear effects to the desired signal out, this region should be specified to each active componet by the *1dB compression point*. The effect of saturation is illustrated in figure A.14. By the nature of active components will the gain begin to vary, as the signal amplitude increases. Hence will gain compression in the end limit the output power of radar trasmitter by its active components. Consequently, in radar receivers, will this effect limit the dynamic range of the receiver. Thus must allways considerations of possible input signals be evaluated, to minimize the risk of active component saturation and an overall reduction of radar receiver sensitivity through nonlinear component behavior.

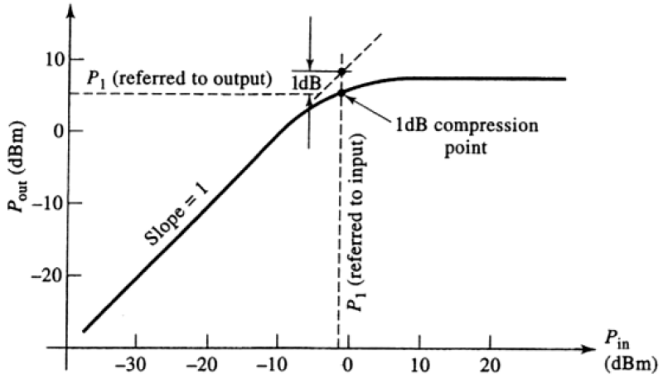

Figure A.14.: Gain compression of nonlinear amplifier

Equation A.37 show that nonlinear devices can make frequency conversions ($2\omega_0$, $3\omega_0$..). This effect is hence utilized by forinstace mixers to enable desired frequency stepping of the fundamental signal. However when an active device is pushed into saturation, will the additional harmonics increase in magnitude and increase the chance of *intermodulation*. Additioanlly will also intermodulation occur when other undesired signals, than the singel tone, are applied to the device through its input. To illustrate this effect is hence a two tone signal input to a nonlinear device shown in figure A.15. In a single tone case can other frequency components besides the fundamental be removed by filtering, due to the lagre separation of frequency harmonics. However in the case of the two tone signal (or more complex), will also the harmonics of sum and difference frequencies appear by *intermodulation*. Thus can undesired frequency components appear in near range of the tone signals. These components are however difficult to remove from the fundamental

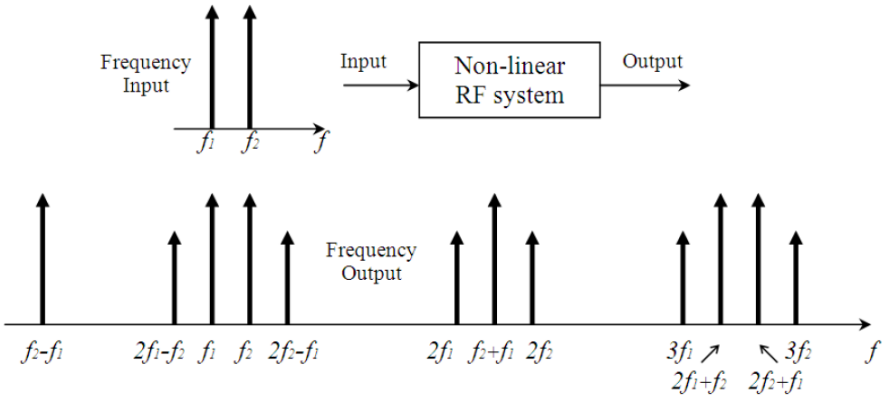

Figure A.15.: Output spectrum of a nonlinear device with a two-tone input

by filtering and will be a reducing factor if their magnitudes are high. In the case of the two tone singal conselation will such curruptive components be refered to as *third order intermodulation products*. If a mixer should be used to benefit the generation of sum and differance frequencies, must hence the additional tone be selected such that a maximum frequency sepearation is enabled (section A.9). This is also illustrated in figure A.15 where the difference frequency is greatly separated away from others components. On the other hand, can an increased waveform complexity, yield intermodulation effects. Hence must allways the signal conselation be considered agains the circuits linear properties. Typically will such passband intermodulation, come from the third-order-products, *third-order intermodulation distortion*. Hence can often a prehand signal analysis including the third-order-products be benificial to see the possible impacts in spectrum. A typical measured spectrum with likewise spurious components can be identified by distinct discrete peaks of the above mentioned harmonics. Dependent of the type of radar in use and what targets are desirable, spurious components can generate great confusion to the detection of real targets if not undesired components are remove.

A.9. Mixers

The section will give an introduction to mixers, how they can be utilized in a radar system and basic differences between different types. Since they are mostly made of nonlinear components like diodes and FET-transistors, they will influence the system performance as describes for nonlinear and active componentes in the Noise and Distortion section. The section has been written primarily based on [28, chap.3&7].

General

To exploit the high frequencies in the radar/RF part of the electromagnetic spectrum, baseband signals needs to be shifted up and down at the radar front-end. Often mixers are used to do this job,making them one of the key hardware components of a radar systems. A mixer is a device that uses nonlinear or time-varying elements to make waveforms

shift in the frequency domain. In general the mixer is a three-port device who makes an *frequency conversion* of two different frequencies. The output of a mixer is ideally the sum and difference frequencies from these two inputs. In a radar this is exploited to make the fundamental operation of *up-conversion* and *down-conversion*. Up-conversion is done in order to convert a radar signal from baseband up to a practical radio frequency(RF) for transmission and detection, often done in several steps via the use of intermediate frequencies(IF). Down conversion is done in the receiving part of an radar, by converting a RF-signal down to one or several intermediate frequencies, and back to baseband for signal prossesing of the received radar-echo. These two fundamental operations are illustrated in figure A.16, were (a) is the up-conversion and (b) is the down-conversion.

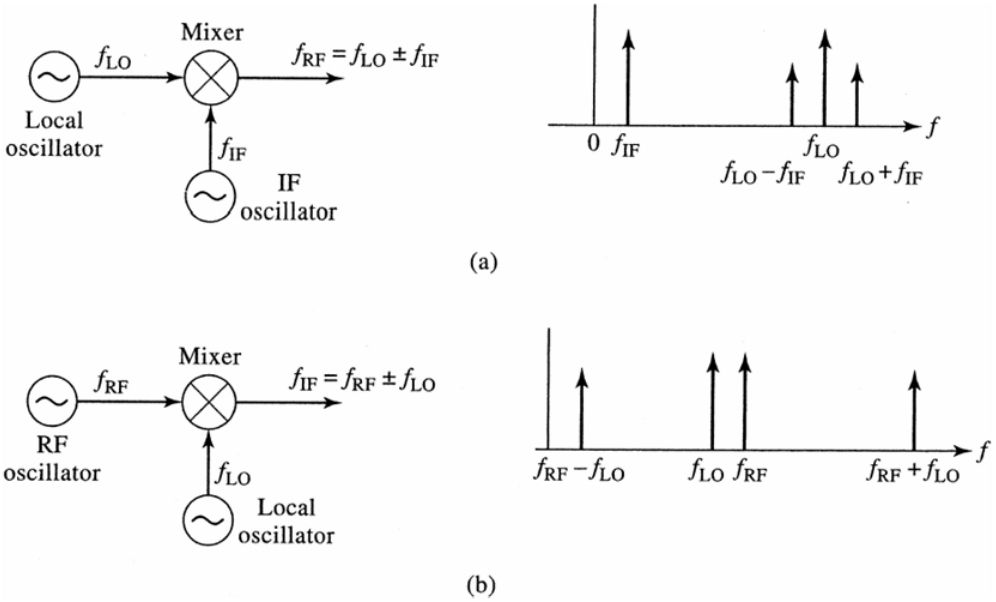

Figure A.16.: Frequency conversion by a mixer

Figure A.16 shows the idealized view of ta mixer but as mentioned i section A.8 the actual mixer outputs more harmonics than the desired ones due to the nonlinearity. The up-conversion occurs in a transmitter where a high frequency oscillator (LO) is mixed with the baseband signal or IF signal. Mathematically the up-conversion can be idealized described as

$$\begin{aligned} v_{LO}(t) &= \cos 2\pi f_{LO} t \\ v_{IF}(t) &= \cos 2\pi f_{IF} t \\ &\Downarrow \\ v_{RF}(t) &= K v_{LO}(t) v_{IF}(t) \\ &= \frac{K}{2}[\cos 2\pi (f_{LO} - f_{IF})t + \cos 2\pi (f_{LO} + f_{IF})t] \end{aligned} \tag{A.38}$$

K is a constant that takes the loss between the desired component (output) and the applied component (input), into account (Conversion loss). In up-conversion this is the loss from

f_{LO} to $f_{LO} - f_{IF}$. If both side bands are utilized by the mixer, the mixer percerves a *Double side band* signal ($f_{LO} \pm f_{IF}$) in respect to the carrier (f_{LO}). On the other hand a *Down-conversion* will be in a similar way but with the IF signal as output, converted down from RF. The resulting output is

$$\begin{aligned} v_{IF}(t) &= K v_{RF}(t) v_{LO}(t) \\ &= \frac{K}{2}[\cos 2\pi(f_{RF} - f_{LO})t + \cos 2\pi(f_{RF} + f_{LO})t] \end{aligned} \tag{A.39}$$

As is illustrated in figure A.16 (b) the desired component in baseband is $f_{IF} = f_{RF} - f_{LO}$, which can be separated with low pass filtering. Totally the mixer can generate *spurious components* for:

$$m f_{RF} \pm n f_{LO} = f_{IF}$$

A problem however is when the mixer is a part of the receiver in down-conversion. Since the antenna often see a wide band of frequencies, the receiver will receive two RF signals that where generated in the up-conversion (upper/lower sideband, seen in figure A.16 (a))

$$f_{RF} = f_{LO} - f_{IF} \tag{A.40}$$

$$f_{IM} = f_{LO} + f_{IF} \tag{A.41}$$

When down-converted, these two equations is in put into $f_{IF} = f_{RF} - f_{LO}$ as f_{RF} which will respectively give f_{IF} and $-f_{IF}$ after low pass filtering. The negative response from f_{IM} is known as the *Image frequency*. The problem is that the two responses are not indistinguishable at the IF part of the receiver front-end. This needs to be considered because undesired spectral component can be folded over to the positive side of spectrum, masking or distorting, the target in typical digital receivers.

Another important parameter of mixers is the *Conversion loss*. This parameter account for resistive losses and other losses that occur in the frequency conversion prosses. In up-conversion this will be from IF to RF and in down-conversion from RF to IF. The conversion loss for down-conversion is defined as

$$L_c = 10log\frac{\textit{Available RF input power}}{\textit{Available IF output power}} \text{ [dB]} \tag{A.42}$$

As other microwave components the mixer will have internally generated noise, generated by the diodes, transistors or the resistive losses. The noise figure of the mixer will be dependent of the mixer operation mode, if it uses the full double side band or only one single side band. Typical F_n of practical mixers are in the range of 1dB to 5dB. Generally the diode mixers achieve lower noise figures than transistor mixers. In addition mixers with nonlinearity will suffer from intermodulation. Normal values of third-order-intermodulation distortion will be in the range of 15dBm to 30dBm.
From figure A.16 it is shown a idealized picture of the resulting frequency spectrum of the mixer process, by contrast real mixers will not be able to decouple the applied signals. This will lead to leakage of power through the mixer from the oscillator. If this is not taken care of with filtering or other technics, strong signals like LO in up-conversion can be radiated by the antenna. The *isolation* of the input ports to the output port is therefore a important parameter.

Types of mixers

Generally two types of mixers are used, *diode mixers* and *FET mixers*. There can be several realizations of mixer types of the two main types. The different types of realizations is shown with typical values for the diode mixer approach in figure A.9 [28, p.245]. Note that there exist both active and passive mixers. More detailed descriptions of these types are given in [28, Chap.7].

Table A.1.: Summarized characteristics of several mixer realizations of diode mixers

Mixer Type	Number of Diodes	RF Input Match	RF-LO Isolation	Conversion Loss	Third-Order Intercept
Single-ended	1	Poor	Fair	Good	Fair
Balanced($90°$)	2	Good	Poor	Good	Fair
Balanced($180°$)	2	Fair	Excellent	Good	Fair
Doubled-balanced	4	Poor	Excellent	Excellent	Excellent
Image reject	2 or 4	Good	Good	Good	Good

The main difference between diode and FET-mixers can be observed from the typical values of single-end mixers in table A.9 [28, p.239].

Table A.2.: Difference between singel-ended diode and FET-mixers

Mixer Type	Conversion Gain ($1/L_c$)	Noise Figure	1 dB Compression	3rd Order Intercept
Diode	-5dB	5 to 7dB	-6 to -1 dBm	5dBm
FET	6dB	7 to 8dB	5 to 6 dBm	20dBm

FET-mixers have as diode mixers, several types of designs. Typical FET configurations is the use of dual-gate FET, where the LO and RF ports are separately FET gates. As a consequence there will be a high degree of RF-LO isolation, but very high noise figure. Another typical configuration is the use of two FET transistors in parallell as an differential amplifier, together with *balun*-networks. This design is shown in figure A.17. An often used extended design method of the differential type, is the *Gilbert cell*-mixer. This is very much used in integrated circuits. It has in addition to figure A.17 two differential stages which is an double balanced mixer. Because of this it achieves high dynamic range and high isolation between all ports. Another benefit is that it cancels all even-odd intermodulation products.

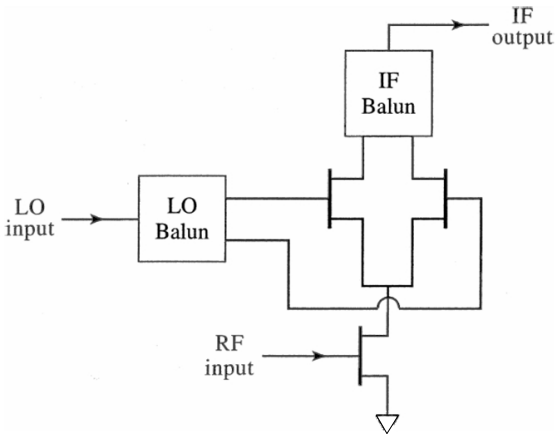

Figure A.17.: Differential mixer

Different FET-mixer designs for *balanced* and *image reject* mixers are shown in figures A.18 and A.19 with the resulting spectrum properties for upconversion. The illustrating figures are from the NTNU lecture series of the course Integrated Microwave Circuits [43].

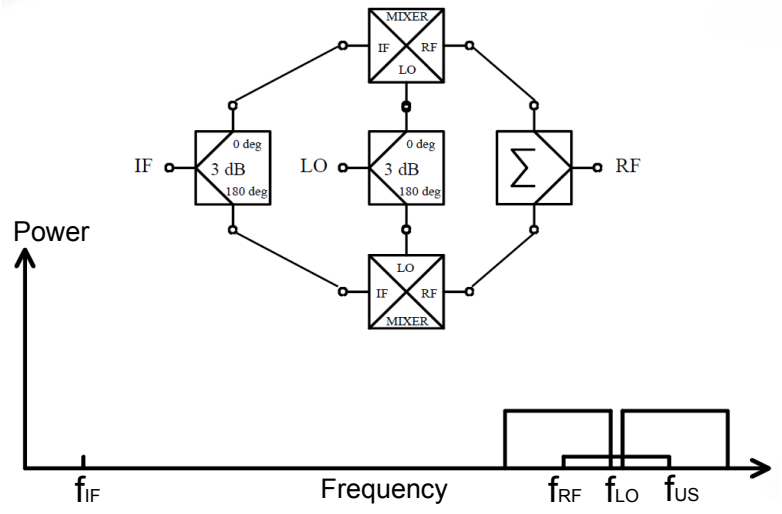

Figure A.18.: Balanced mixer

The balanced mixer will typically suppress the carrier and the IF output. The figure above consist of two parallell mixers in a balun configuration. Here the IF, RF, LO and Image frequency are denoted f_{IF}, f_{RF}, f_{LO} and f_{us}.

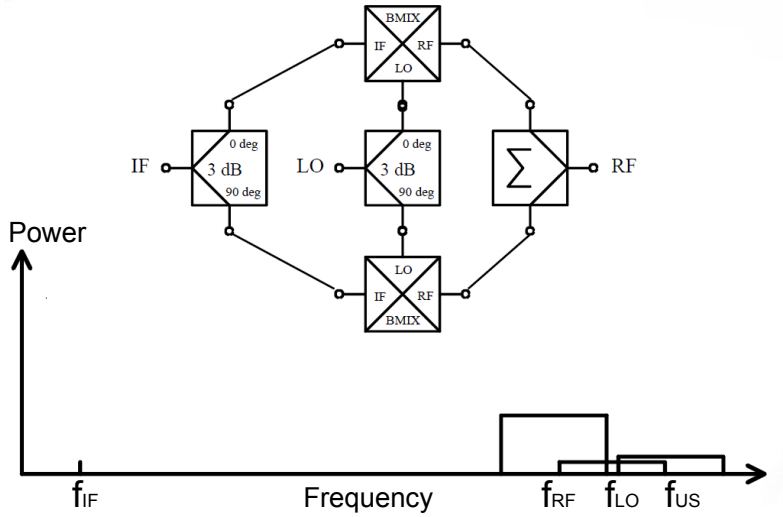

Figure A.19.: Image reject mixer

An image reject mixer will both suppress the carrier, the IF and the image component. This is done by two parallell balanced mixers with additional balun circuit. Note that the suppression is a very important property, since the output spectrum will overlap into another and distort the wanted signal, as shown in figure A.18 and A.19.

A.10. The Radar Ambiguity Function

This section is primarly written on the basis of the excellent derivation of the radar ambiguity function done by B.R.Mahafza [16].

The goal of most radar designs is to achive the best conditions for detection of targets in presens of noise. Therefore it will be nessesary to implement a receiving filter or circuit characteristic that can acheive the highest possible instantaneous SNR. It has been proven that a *matched filter* will achieve the maximum instantanous SNR at its output when a signal plus addative noise is present at the input [16, ch.6].

$$SNR(t_0) = \frac{2E_0}{N_0} \tag{A.43}$$

Equation A.43 show that the peak instantaneous SNR will be given by the signal energy and the input noise power. The equation therefore states that the used waveform will have no direct connection to the radars sensitivity. However will the matched filter be of most importance when studing waveforms, since its implementation will imply the best possible conditions for reception and hence a *best case* scenario as referance to the real world radar implementation with the spesific waveform. Mahafza [16, pp.233-236] proves that the matched filter can be implemented by using the matched filter impuls response in the causual case as

$$h(t) = K \cdot s_i^*(\tau - t)$$

or in frequency domain

$$H(f) = K \cdot S_i^*(f)e^{-j(2\pi\tau)}$$

where the filter is a mirrored and delayed version of the transmitted waveform $s(t)_i$ and $S(f)_i$. The filter operation will be the cross-correlation of the transmitted and received waveform with output $y(t)$

$$y(t) \;=\; \int_{-\infty}^{\infty} s(t)_i s^*(t-\tau)\, dt$$

In many radar designs the Tx waveform is computed stored in memory to acheive a digital match filter implementation. When using the matched filter implementation for waveform analysis. It is interesting to study the influence of the transmitted waveform when it inflicts on the target, targets or clutter with different type of dopplershifts and ranges at Rx. But how does the matched filter operation affect the range resolution and the doppler resolution, besides giving the best SNR conditions? It is however proven that the MF operation perserves these waveform properties making the matched filter implementation a good tool for theoretical waveform analysis [16, pp.237-243]. To make the analysis more complete it is usefull to study the two fundamental properties of time delay τ and Doppler frquency f_d combined out of the matched filter as a pair of variables (τ, f_d), forming the combined range and Doppler correlation function or 2-D correlation fuction [16, p.244] and [30, 170].

$$\chi(\tau, f_d) \;=\; \int_{-\infty}^{+\infty} s(t)s^*(t-\tau)e^{j2\pi f_d t}\, dt \tag{A.44}$$

The $\chi(\tau, f_d)$ will then represent the MF output, obtained from the cross-correlation between the complex signal and a time- and Doppler-shifted version of it self. All combined the output of the matched filter still obtain the most achievable Doppler and range/time delay resolutions. To study the resolvability in both time delay/ range and Doppler the squared magnitude of $\chi(\tau, f_d)$ is taken, representing the *Radar Ambiguity Function*.

$$|\chi(\tau, f_d)|^2 \;=\; \int_{-\infty}^{+\infty} \left|s(t)s^*(t+\tau)e^{j2\pi f_d t}\right|^2\, dt \tag{A.45}$$

A generic 3-D radar ambiguity function plot is plotted in Matlab as an example for a single pulse of $3\ seconds$.

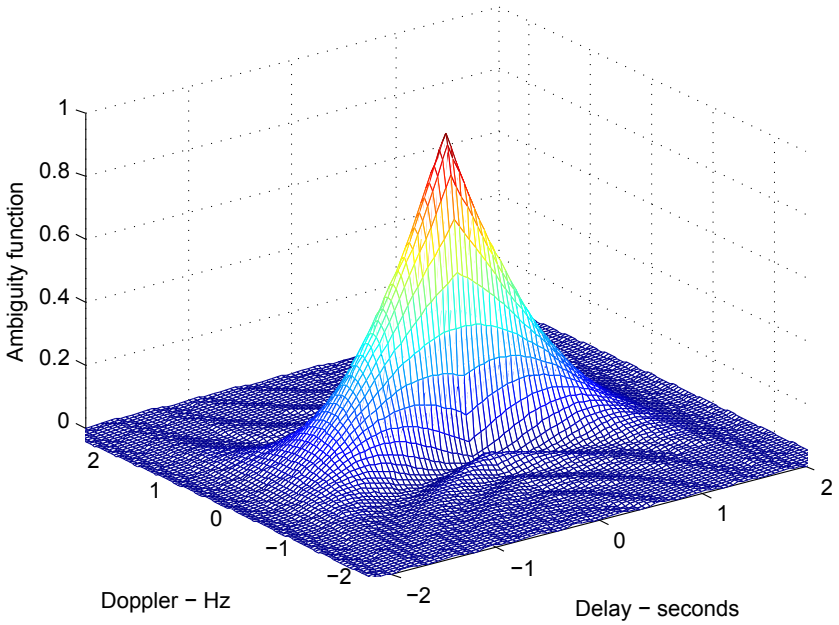

Figure A.20.: The radar ambiguity function for a $3\ seconds$ CW puls

The radar ambiguity function has been defined as follows by Mahafaza:

> *The radar ambiguity function represents the output of the matched filter and it describes the interference caused by the range and/or Doppler shift of a target when compared to a reference target of equal RCS* [16, p. 244].

Consecuently will the returns that are non-Zero time delay or Doppler, represent backscatter deviating from the nominal target. Hence can the Radar Ambiguity Function be useful to study different waveforms for spesific radar applications or to determine the Doppler/ range resolution, side lobe behavior and ambiguities in the two domains.
To understand the RAF and how changes to the waveform will affect the output, its set of properties must be described

1. The maximum value of the RAF occurs at $(\tau, f_d) = (0, 0)$

$$max\left\{|\chi(\tau, f_d)|^2\right\} = |\chi(0,0)|^2 = (2E)^2 \tag{A.46}$$
$$|\chi(\tau, f_d)|^2 \leq |\chi(0,0)|^2 = (2E)^2$$

2. The RAF is symmetric

$$|\chi(\tau, f_d)|^2 = |\chi(-\tau, -f_d)|^2 \tag{A.47}$$

3. The total volume is constant

$$\int_{-\infty}^{\infty}\int_{-\infty}^{\infty} |\chi(\tau, f_d)|^2 \, d\tau \, df_d = (2E)^2 \tag{A.48}$$

4. If $S(f)$ is the Fourier transform of $s(t)$, then

$$|\chi(\tau, f_d)|^2 = \left| \int S^*(f) S(f - f_d) e^{-j2\pi f t}\, df \right|^2 \tag{A.49}$$

The teoretical referance for the waveform analysis is described as the ideal ambiguity function which is a theoretical non-realizable construction. Figure A.21 shows the ideal response as an infinitedesimal thick single peak at the origin. As a result the resultant waveform synthesis would result in an non-ambiguous response both in Doppler and range. All targets present could then be resolved no matter how close they are in both domains and reject all clutter elsewere than at the origin.

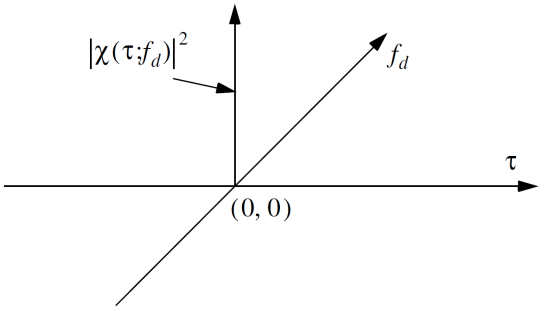

Figure A.21.: The ideal theoretical ambiguity function

Often in the study of the ambigiuities the *Uncertainty Function* is derived in cuts of the different domains in order to veiw the limits of the unambiguous regions. Equation A.50 shows the uncertainty function while $|\chi(\tau, 0)|$ and $|\chi(0, f_d)|$ will be the correponding Zero Doppler cut and Zero delay cut of the function.

$$|\chi(\tau, f_d)| \;=\; \int_{-\infty}^{+\infty} \left| s(t) s^*(t + \tau) e^{j2\pi f_d t} \right| \, dt \tag{A.50}$$

The uncertainty cuts for a single puls of width $\tau^{'}$ is displayed in figure A.22(a) and A.22(b) and shows that two targets whould be unambiguous if they are separated $\tau^{'}$ seconds apart in time delay and $1/\tau^{'}$ in doppler [16, pp.248-250].

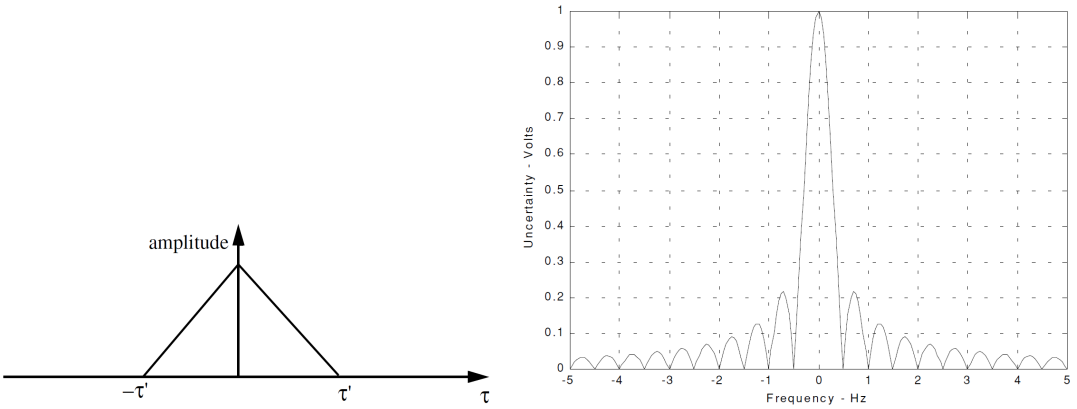

(a) Zero Doppler cut (b) Zero delay cut

Figure A.22.: The uncertainty fuction-cuts of a single puls of $\tau^{'} = 3sec$ pulswidth

Although these cut-representations give us valuble information isolated, the can be missleding to interpet the range-Doppler coupling hence the trade-off between range and Doppler resolution. At the same time the 3-D ambiguity diagram can be difficult to produce and to interpet. Therefore it is most common to view the properties of the waveform as 2-D contour plots of frequency and time. The generalized contour plots of a CW-puls is shown in figure ref, which also show the typical trade-off of puls length versus bandwith and the resulting properties of domain resolution. Consecuently displaying that a short puls will enhance the resolution in range/delay and that a long puls will resolve better in Doppler-domain [16, p.264].

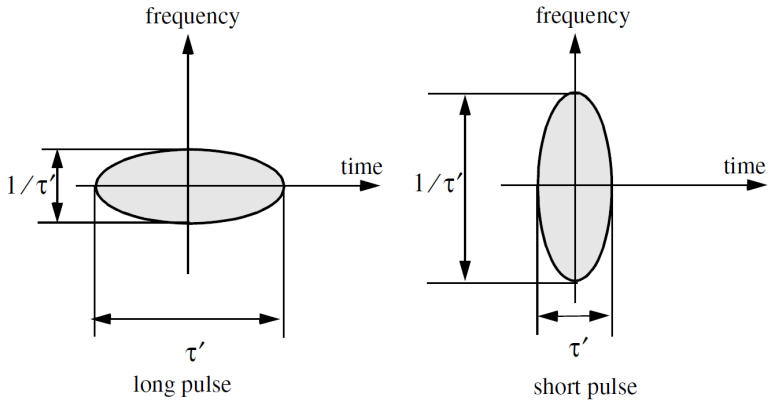

Figure A.23.: The generalized single CW pulse ambiguity contour

Summarized would the waveform analysis using the radar ambiguity function, be the initial study of the compatibillity of the waveform in the desired radar system. Thereby giving the theoretical analysing tool to understand the properties of the current waveform and its effect on accuracy, resolution, range and doppler ambiguities, and its response to clutter. Note that the real implementation of a matched filter will only be an approximate one, since the waveform would be distorted during transmission. Hence would difficulties discovered in the radar ambiguity function analysis further increase in practical implementation and therefore be of the most importance when choosing the right waveform for a radar application.

A.11. Direct Digital Synthesis

Direct digital synthesis is a method of generating accurate and harmonically pure digital sequences. These sequences are high resolution representations of analog signals that can be generated by an DAC in combination with a low-pass reconstruction filter. Basic block diagram is shown in figure A.24. With all components incorporated, the total cuircuit is known as a *Complete DDS* or *Direct Digital Synthesizer*. The fundamental DDS circuit uses digital data processing blocks to generate a frequency- and phase-tunable output signal, referenced to a precision clock source. The clock referance frequency is multiplied or divided within the DDS architecture by scaling factors set by programmable binary tuning words. This allows significant frequency precision in accordance to the tuning word presition. In addition does the digital operations enable fast switching between output frequencies and broadband frequency operations. More over are the advantages, compared to other sythesis methods, listed below and show why the DDS is often used as a precision signal source and to generate different types of signal modulations [39, sec.6-13], [8, p.5].

Advantages of direct digital synthesizer:

- Micro-Hertz tuning resolution of the output frequency and sub-degree phase tuning capability.
- Flexibillity of applying several operation modes or fequencies with out the need of manual tuning or change of components, all remotely controlled by the digital control interface of the DDS architecture.
- Digital control increase process stabillity by enabling rapid monitoring and tuning for temperature changes, frequency drifts and removes the need of automatic gain controll.
- Phase continuity preservation whenever the frequency is changed.
- Improved phase noise compared to PLL synthesis.
- Precise control of the output phase across frequency switching transitions.
- DDS integer arithmetic implementation allows control by microcontrollers.

However the advantages, these must be seen up against the greater DDS system noise and spurious signals compared with other synthesizing technices, see section A.11.3.

A.11.1. DDS Fundamentals

The fundamental components of the a complete DDS include a *phase accumulator*, a *phase-to-amplitude* conversion device (usually a sine look-up table) and a *digital-to-analog Converter*. The basic components are shown in figure A.24 [8, p.7].

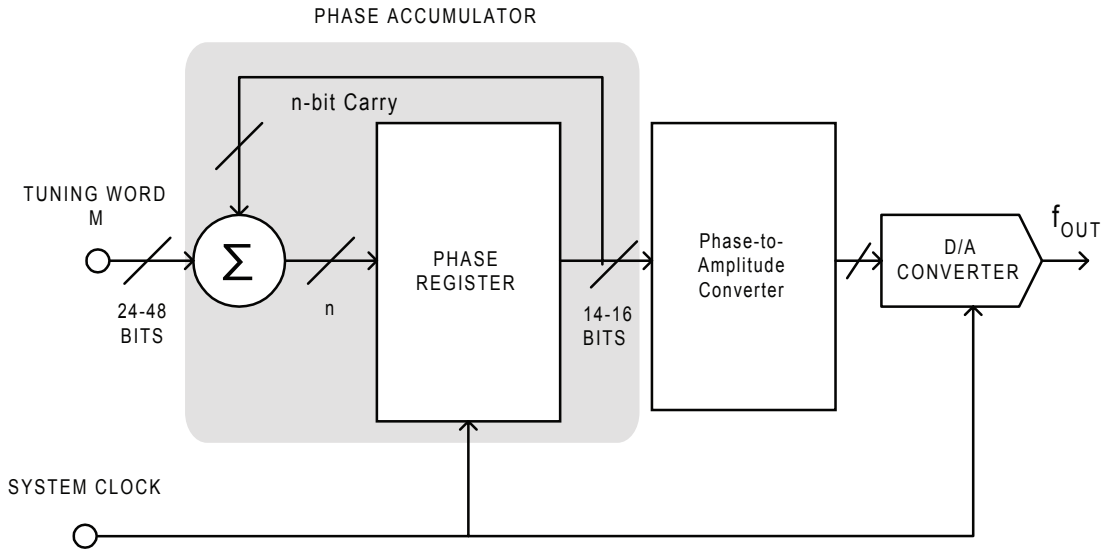

Figure A.24.: Components of a direct digital synthesizer

The basic DDS seen in figure A.24, produce a harmonic wave on the basis of two parameters, the dds *oscillator source/ referance clock* and the phase *tuning word* (M), which is a binary sequence programmed into a frequency register. The figure does not show the frequency register, but only the output from it, which is the input to the phase accumulator. Typical bit-lengths for Analog Devices DDS's are shown in the figure. The phase accumulator generates angle information for the phase-amplitude conversion cuircuit on basis of the phase tuning word (M). If a *sine look-up table* is used for the phase-to-amplitude discrete-time transformation, the phase accumulator provides a phase address for the table. Further will the address correspond to a amplitude value of the wanted fundamental harmonic in discrete time. The output sequence will then be feed to the DAC, which turns the amplitude number to a analog voltage/current value. In addition, will a low-pass anti-alias filter, applied out side the DDS, smoothen the sine-squared output (figure A.32) from the DAC and remove the possible aliased signals in fundamental lobe output (section A.11.2).

To understand the concept of operation, the generation of a fixed harmonic can be exemplified. In order for the DDS to produce a single frequency a constant phase increment (M) is added to phase accumulator at each clock cycle. Intuitively would a large phase increment, let the phase accumulator push quickly through the sine look-up table, generating a high frequency. Likewise will a small increment, result in a slower execution of the look-up table and a lower frequency output. The phase accumulator with the *n-bit carry function* can be seen as a *Phase Wheel* in the DDS architecture. This shows the connection between the repetitive nature of the digital representation in discrete-time and in countinuos-time. The phase wheel can be thought of as a vector that rotates around the analog phase cycle, seen in figure A.25. The different points in the circle represents equivalents amplitude points of the analog sinewave. In the figure, these values are assigned as angles of phase and by a binary number at the start and stop.

The sine look-up table will generate a discrete time representation before the analog signal

is generated in the DAC. Figure A.26 illustrates how the assigned tuning word determines the steps at equally spaced intervals in the phase weel and how the corresponding discrete amplitudes build the sine wave. The analog envelope output from the low-pass filter is visualized between the discrete values. With such waveform build-up, are the amplitude vaules updated every clock cycle thereby giving the DDS output frequency (f_{out}) from the ratio between used binary step-size (M) and total phase accumulator size (2^n). The value n is the length of the phase accumulator and the ratio is multiplied by the clock frequency (f_{clk}) [21, pp.1-2].

$$\boxed{f_{out} = \frac{M}{2^n} \cdot f_{clk}} \tag{A.51}$$

Form this equation it is given that the agility of the DDS depends on the resolution of the phase accumulator (n) seen as available points in the phase wheel and the number of bits to address the sine look-up table. The tuning word resolution (M) will further give the abillity to acess the overall DDS capabillity to create frequencies. However are these parameters subordinate to the referance clock in respect to outputng the desired frequencies. Allthough figure A.25 show equally spaced points to generate sine waveforms, will the referance to the look-up table give the coupling to the output waveform, thereby enabling also other waveforms as triangular and square waveforms. In addition would the generation of e.g chirp waveforms, need to be sett in the phase accumulator hence allowing a exponetial growth of the phase vaules and at the same time access the sine look-up table.

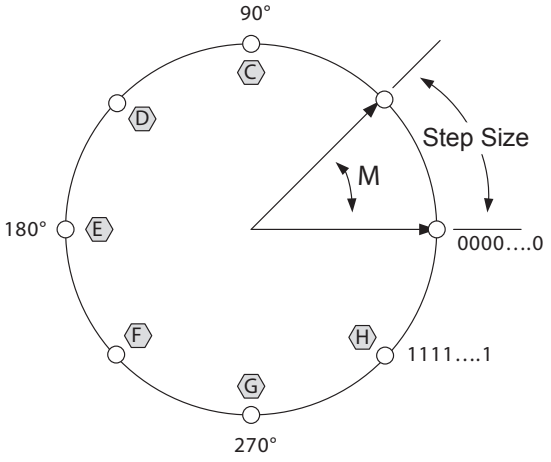

Figure A.25.: Digital phase wheel representation of the phase accumulator

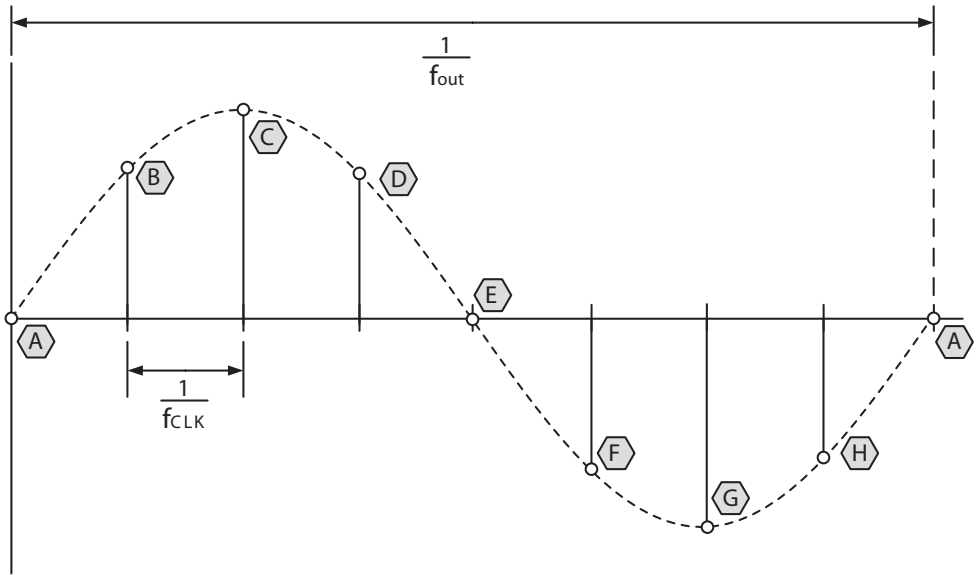

Figure A.26.: Sine discrete output from phase to amplitude conversion

In addition to the DDS good abillity to generate fine frequency resolution, can the value M be changed immediatlly, thereby yielding immediate and phase-continuous changes in the DDS output frequency. Allthough these eminent advangtages , is there an upper limit for high frequency outputs, when the number of samples per accumulator cycle decreases. The limitation arise from the sampled nature of the DDS where at least two samples per cycle is needed to construct the output analog signal. Hence given by the *Nyquist* criterion. Therefore is the maximal theoretical frequency output is given by $f_{clk}/2$. However in paractice, will the frequency output be limited even more, due to the desire for high signal quality and due to practical filter requirements. A upper limit for frequency generation is purposed by [28, p.270].

$$f_{max} = \frac{f_{clk}}{4} \tag{A.52}$$

hence to generate 4 samples per periode to obtain sufficient signal quality. In addition have [13, p.299] suggest a enven higher output frequency

$$f_{max} = \frac{f_{clk}}{5} \cdot 2 \tag{A.53}$$

or 40% of the clock frequency, to yield maximal signal purity. Either way will the use of lower frequencies than the maximal limit, increase the quality of the analog signals and ease the problems of sampled aliased components of the output spectrum. At the same time would the minimum output frequency be given by the 2^n sine look-up table sample values, and a minimum tuning word $M(1)$ [28, p.271].

$$f_{min} = \frac{f_{clk}}{2^n} \tag{A.54}$$

Additionally there will be other limitations than the frequency constraints, e.g DAC quality which will determine the level of spurs out of the system, and the compatibility of the phase word which will give the level spurs caused by phase truncation in the digital circuit. These and other limitations are given in the next sections.

A.11.2. The Sampled Output

Since the DDS architecture uses an digital to analog converter will the frequency output be dependent of its sampled nature. To illustate a typical output, is the theoretical spectrum from the used AD9958 DDS, with maximal clock frequency (500 MHz) and wanted fundamental frequency of 66 MHz, displayed in figure A.27 modified from [8, p.12].

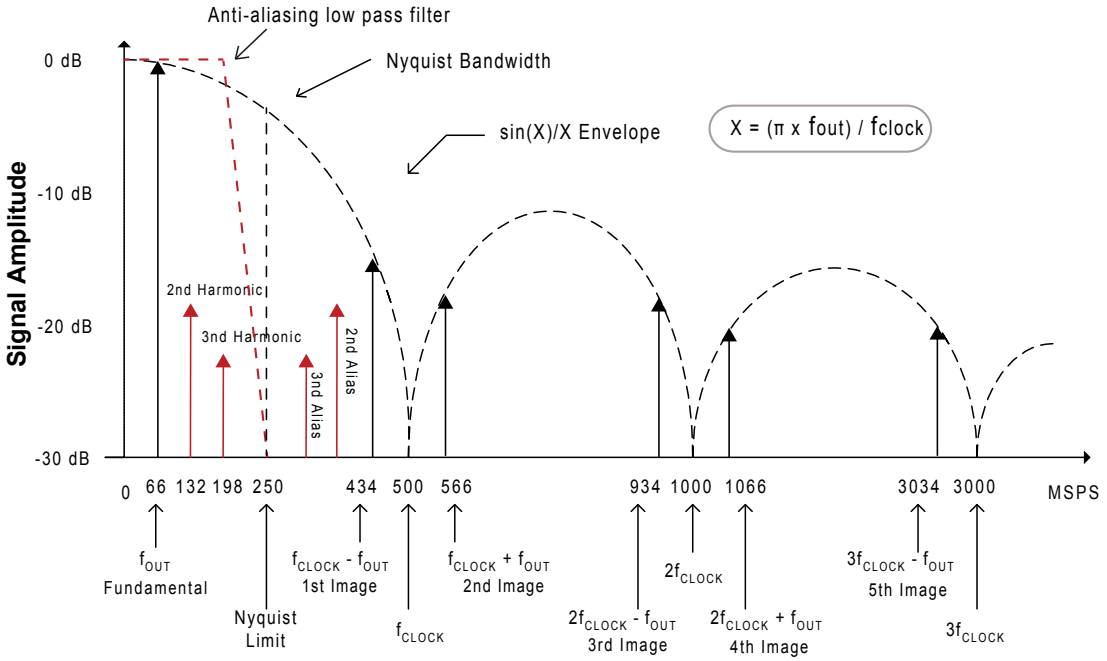

Figure A.27.: Sampled theoretical output from the AD9958 DDS, max clock frequency

This typical spectrum shows the CW operation mode of the DDS used in this thesis. The spectrum in figure A.27 illustrates how the nonlinearities of the DAC, produce image frequencies and mirror components of the clock and the generated frequencies. In addition will the output be limited by the envelope of the sinc(X)/X roll off response, due to the quantized nature of the sampled output [8, pp.12-13]. The first additional harmonics and alias components are only shown within the first clock roll-off. This illustate how the output of the DDS will be currupted by additional frequency components. As illustrated will it be benificial to have a large clock frequency in respect to the desired output, to yield a high power to the fundamental component and further reduce the impact of images to DDS total spectrum. Nevertheless does a antialias-filter need to be implemented to remove high componets within the nyquist lobe beond the nyquist limit, hence to achive high spectral purity. Allthough such filters can remove components that is natural to the digital signal output, will anomalities that arise from the forinstance the DAC not be remove by such filtering. Hence would it allways be nessesary to invesigate the DDS spectrum in relation to natural additional harmonics, images and spurs, both in relation to amplitude and frequency poistion. Hence to determine the best fundamental output suited to the DDS clock, but also to fit the best possible anti-alias/ reconstruction filter. Allthough the it in most cases are benificial to have a low DDS in respect to the

DDS clock, will there be a lower limit to the minimum frequency output from the DDS (equation A.54). Additionally will there be an trade-off in the DDS settings, since signals from 5 MHz and above are easier to handel to their fast slew rates in respect to jitter management [8, app.E]. Allthough higher frequency signals as such, will have higher harmonic influence, would this not be bad until the fundamental harmonic is aliased into the passband. If so will hence the apperance of the additional harmonic generate a nonharmonically related product, within the comparator and thus start to increase the jitter contribution.

Figure A.28 show that the DDS spectral purity would be of the most importance since the ideal filter respones is not realizeable. Hence must the actual antialias filte be suited for best possible alias and additional harmonic suppression, along with the analog signal reconstruction.

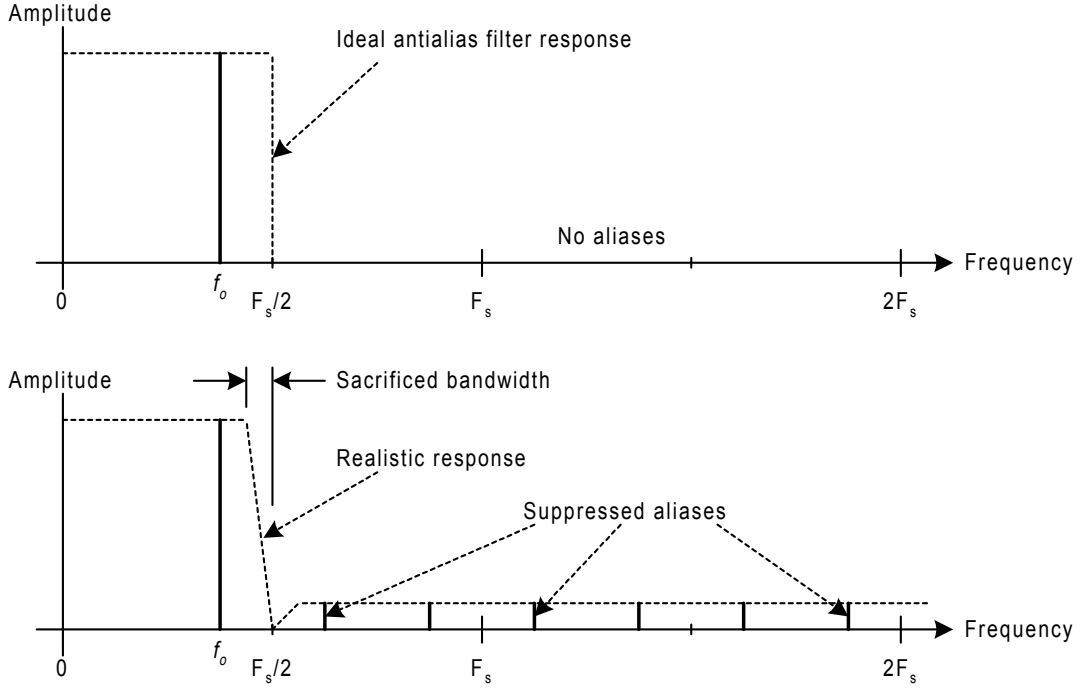

Figure A.28.: Theoretical DDS anti-alias filter respons

A.11.3. DDS Noise Contributions

The last section showed that there will be different types of noise contributions to the DDS signals. This section will give a brief introduction to the main noise contributions of DDS noise.

Generally will the general noise floor of a DDS device be determined by the superpositioned effect of substrate noise, total circuit thermal noise, circuit ground coupling and a the total contribution of all random noise within the DDS. sources of low-level signal corruption. The noise floor, spur performance, and jitter performance of the DDS is

greatly affected by the quality of the total circuit power supply, its surronding circuit layout and the quality of the input reference clock/ oscillator. It is however difficult to determine all sources of error through observations, since there is a lagre interconnection between some different noise sources in the Digital-to-Anlog design, like forinstance the connection of system jitter, which through the DAC will produce output phase modulation. Nevertheless are most of the DDS noise contributions deterministic[39, sec.6.49].

Spurious Components:
Typical DDS output spurs can to much extent be determined from their source. Spurs that originates from phase trucation, DAC quantization and nonlinearity, and sine look-up table divergens, can all be predicted [13, p.306]. However is it more difficult to predict their magnitude, sine they all are a function of DAC nonlinerity.

A general spur situation can be shown to a CW waveform generation, where the DAC repeats it self after 2^K samples, where 2^K kan be approximated to the most usual divisor of 2^n and M. Hence will the spurs be at succesively

$$f_{spur} = \frac{i\, f_{clk}}{2^K} \qquad i = 0, 1, 2.....$$

In typical cases with high f_{clk} and high precision accumulators would the typical spruious spacing be less than 1 Hz. Hence can the spurs not be differentiated from noise. The impact of DDS spurious signals to radar performance will be dependent of the spur nature and the type of radar processing. For applications like FMCW radars using chirp waveforms with large bandwidth products, will the radar be less sensitive to spurious DDS outputs. This comes from the fact that DDS spur signals, chirp at a different rate than the desired LFM signal. Hence will the spurious signals be rejected during LFM compression/ mixer corralation [39, sec.6.49].

In relation to spur effects present within the DDS, is the *spurious-free dynamic range* (SFDR) used as a figure of merit to the overall spur effect. The SFDR refers to the ratio between fundamental frequency and the highes level of any spur, including alias and additional harmonics in output spectrum. This figure would hence be an important spesification to the DDS within the total system. Hence since additional large frequency components can affect the systems signal output, if they are not taken care off by filtering or other suppression technics. Tyical implications is such as violation of allocated frequency band, thereby increasing the change of adjecent channel interferance. Additionally will also an high SFDR enhance possible risk system intermodulations.

In addition to typical spurious signal curruptions, are there two main nondeterministic errors. The internal clock jitter in combination with the additive thermal noise and the oscillator phase noise, will both yiled output noise through their influence on the DAC, inevitably coupled to the the DAC performance.

Quality of DAC:
The digital-to-analog converter would determine much of the DDS output noise, since its performance would define to what extent the digital sequnce could be interpet to an analog signal. With its additional dependence to oscillator background phase noise and

DDS internal generated jitter, would all effects combine to the total degradation of signal purity. However can some grips be taken to reduce the overall noise. The most obvious choice would offcource be to have great DAC resolution to minimized the quantization error, which will directly give less spurs and noise in spectum[8, p.16]. In addition can also the DAC sampling frequency be increased. Figure A.29 show the scheme of reducing the noiselevel in spectrum of the allready existing quantization error through DAC oversampling.

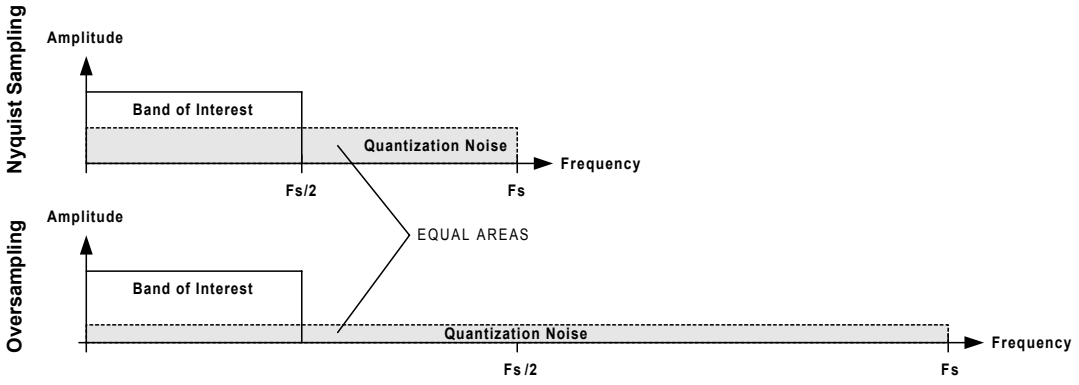

Figure A.29.: Reduced quantization noise from oversampling [8, fig.4-3]

Jitter:
As earlier stated would the use of nonideal oscillators, thermal noise, ground potensials and external output connections, yield an overall contribution to the distortion of digital signal edges within the DDS. Jitter is thus measured as the dynamic RMS displacement of digital signal edges, from their long-term average posistions. The internal sequence jitter will be added to the DAC which in turn add a phase modulation to the output signal, proportional to the output frequency. The isolated oscillator phase noise level will however be reduced to the DDS output, since the DDS is an feed-forward sytem, unlike forinstance a PLL. The DDS reduces the isolated oscillator phase noise by

$$R \;=\; 20\,log(f_{out}/f_{clk})$$

since the DDS output is a fractional division of the clock/oscillator. Hence will the referance ocillator phase noise add to the total system jitter and yield as phase modulation at DDS output. However will this jitter be a smaller procentage of the total output periode, as shown by the above relation. The jitter effect is summarized in figure A.30, showing the relation between DDS referance clock, DAC output, filtered DDS output and the effective DDS phase noise output region (interpet as jitter).

A.11.4. DDS Chirp Signal Generation

To generate FM modulations with the DDS can a second accumulator be implemented before the phase accumulator of the basic DDS cuircuit, shown in figure A.24. Hence

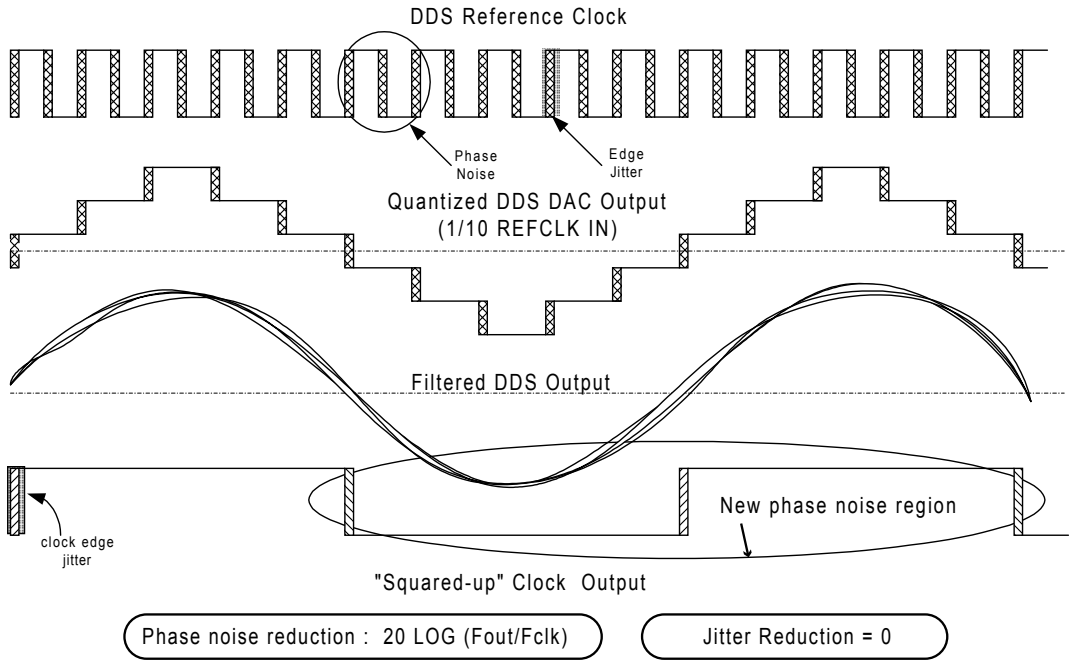

Figure A.30.: Reference clock jitter affecting DDS output signal purity [8, fig.5-1]

frequency chirped waveforms be created with a added *frequency accumulator* which will enable the user to apply a constant chirp slope word to the accumulator input, resulting in a quadratic phase sequence out of the phase register. A chrip generating DDS configuration is illustrated in figure A.31, which also show the sequence register outputs.

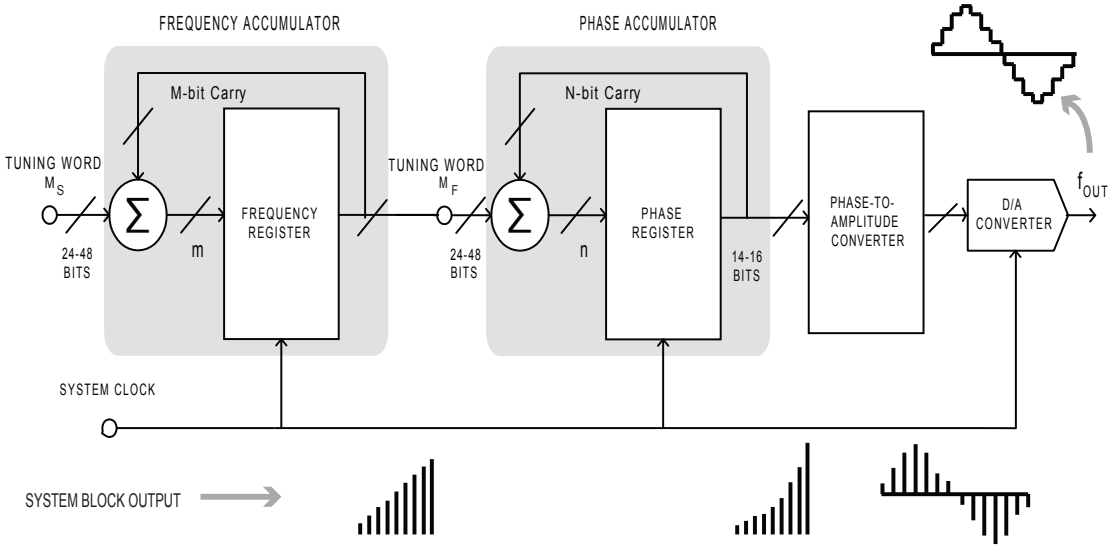

Figure A.31.: DDS fundamental components of a frequency sweep configuration

Figure A.32 show the the overall conversion of discrete sequences, from frequency accumulator output to DAC output.

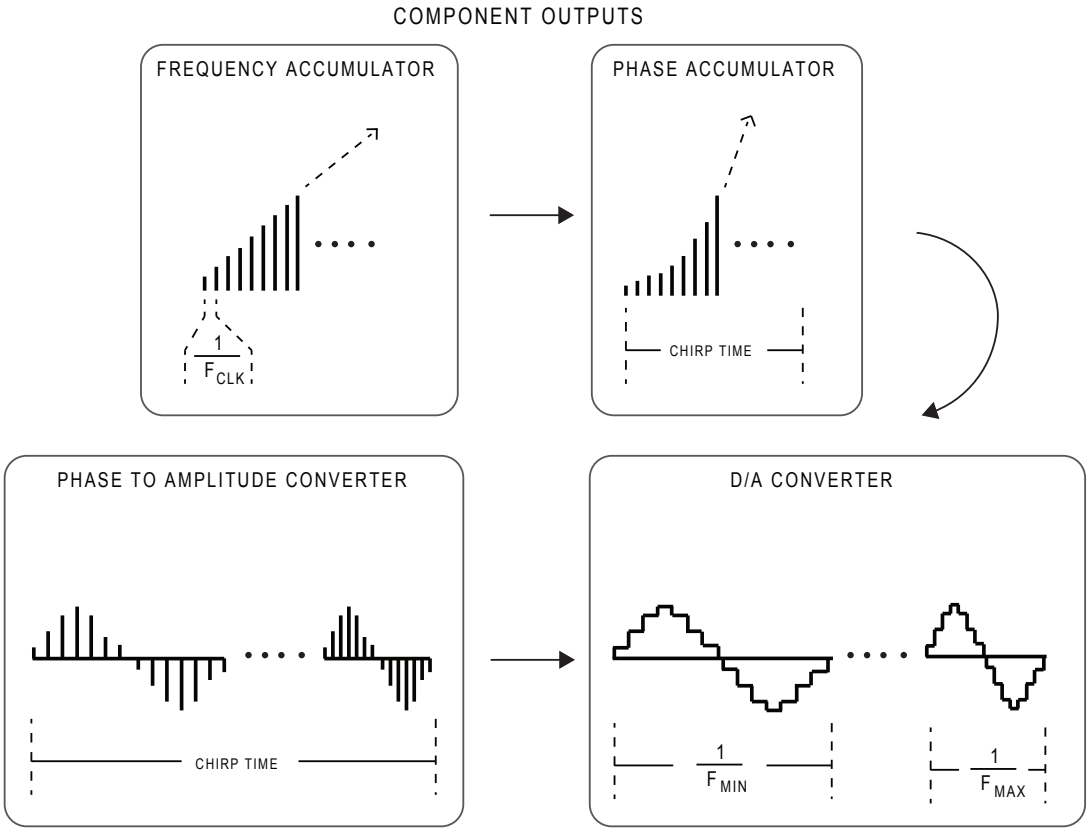

Figure A.32.: DDS component output signals with applied chirp tuning word

In order to apply such modulations must a set of logical commands be added to the DDS. Hence to define the start and stopp frequencies, but also the chrip rate (ramp rate) and additional modulation timing. Figure A.33 show the linear frequency modulation definitions that has to be set for the AD9958 DDS used in this thesis, as an example.

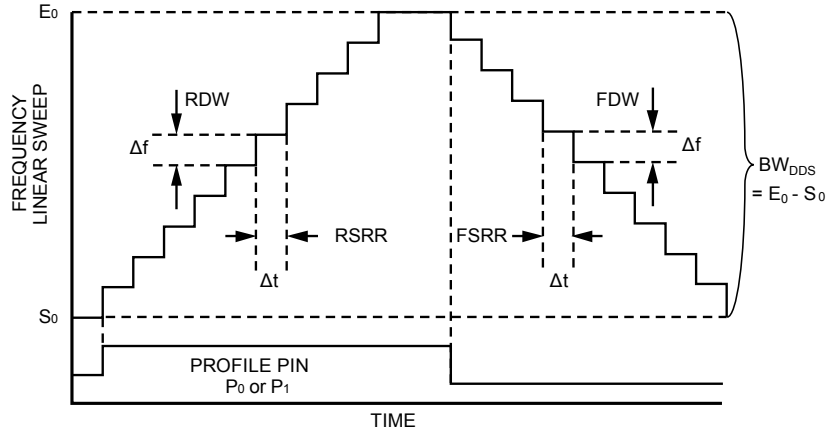

Figure A.33.: Linear frequency sweep parameters of the AD9958, DDS [10]

The above figure defines the fundaments for the DDS register settings, which will yield the logical operation performed as shown in figure A.34. The AD9958 defines the start

and stop frequencies by respectively S_0 and E_0, which is set as frequency tuning words to the desired frequency output f_{DDS}:

$$FTW = \frac{f_{DDS}}{f_{sys}} \cdot 2^{32} \tag{A.55}$$

The f_{sys} is hence the referance oscillator frequency, and the nominator is defined by the accumulator resolution. By starting the chirp at S_0, initiated by the modulation timing (Profile Pin) will the frequency sweep be conducted until the value of frequency stopp word is reached. The total chirp time and frequency step resolution would hence be set by the chrip rate, defined by the raising/falling delta word (RDW/FDW) and the raising/falling sweep ramp rate word (RSRR/FSRR). Which for the AD9958 case will be set accordingly by

$$[RDW, FDW] = \frac{\Delta f}{f_{sys}} \cdot 2^{32} \tag{A.56}$$

$$[RSSR, FSRR] = f_{sync} \cdot \Delta t \tag{A.57}$$

It should be noted that the definitions presented here are the spesific definitions made by Analog Devices, and that these are not univeral. However will the basic consept of operation yield for all DDS circuits.

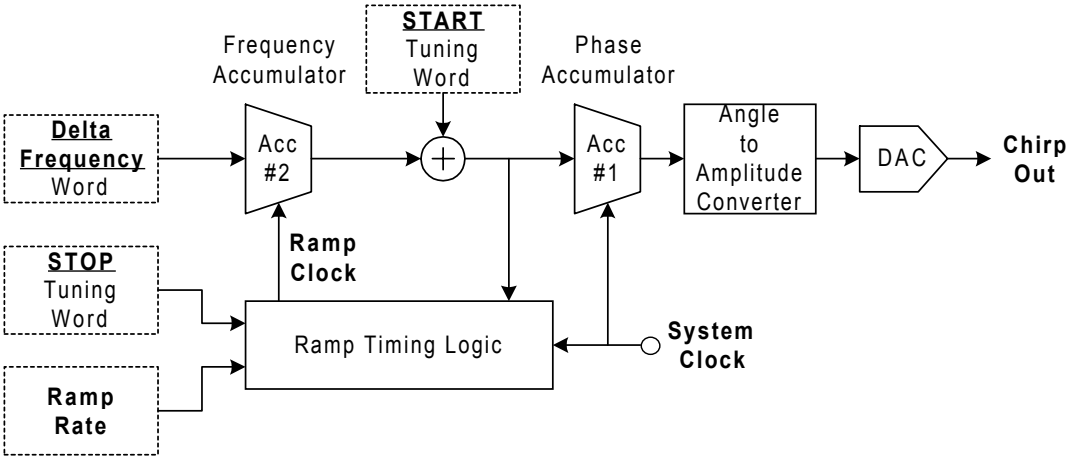

Figure A.34.: DDS block diagram of chirp mode execution [8, fig.11-3]

A.12. Phased Lock Loop Synthesizers

Phased locked loops are circuits which utilizes a feedback control loop to enable a voltage controlled oscillator (VCO) to be tracked with referance to a stable oscillator. With use of a phase comparator within the loop, will the VCO maintain a constant phase angle to its referance. This feature will hence allow the output VCO to run at multiples of the input oscillator frequency. Thereby can PLLs be used as frequency synthesizers for both modulation and demodulation. Very often are such circuits also used as FM demodulators, to recover unknown carriers of the signal in radio receivers [28,

p.271]. In this thesis, does the radar signal source utilize a PLL as an effective frequency multiplicator, also known as a *PLL synthesizer*. Since the radar should enable linear frequency modulation, is a DDS implemented as modulating signal referance. This sets however some requirements to the PLL which has to follow the everchanging frequency within its working bandwidth. The following section will give an brief introduction to digital PLL circuits. Additional PLL analysis and designs can be further investigated in [3], [11],[24] and [22].

A typical PLL synthesizer block diagram is shown in figure A.35, using an integrated circuit synthesizer. The typical block diagram show partly IC PLL with external lowpass filter and VCO, often refered to as a *integer-N* PLL. An input frequency divider/IC counter (R) can reduce the input referance to fit the phase frequency compartor's desired frequency, along with the N-counter/divider from VCO feedback. By scaling the VCO and referance via programming the PFD can output the frequency error from output frequency to referance as an voltage sequence. The digital signal is then converted by the charge pump as an correction current which can further lowpass filtered externally by the LPF. The output of the filter would then yiled a suited voltage to the VCO, which by its voltage-to-frequency characteristics result in an output frequency [3],[11]. At equilibrium, will the two frequencies be equal and the output frequency would be at the desired multiple frequency

$$F_{out} = N \times F_{PFD}$$

To give the best PLL frequency resolution, are often the feedback counter (N) implemented as an Dual-Modulus prescaler. The DM-prescaler uses two additional counters A and B, along with a implemented single prescaler P. Hence will the integer-N feedback defined by $N = (P \times B) + A$. More reading of digital PLL circuits can be reveiwed in [3], which threat this subject extensively.

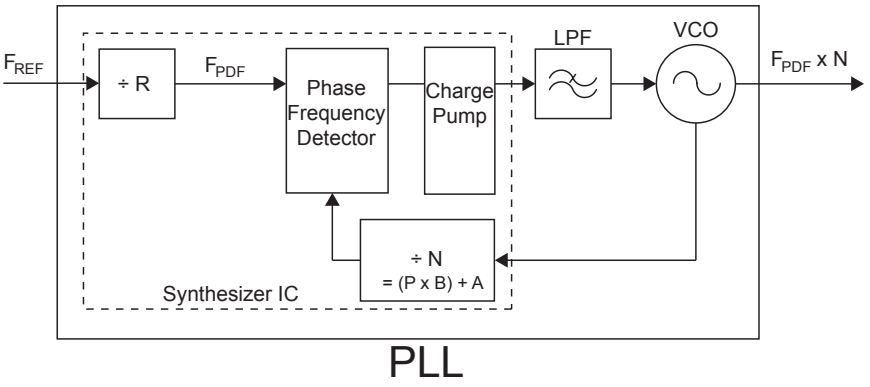

Figure A.35.: Basic block diagram of a PLL

It is however clear that the total circuit must be matched according to the desired application, regarding closed loop gain and transient response. Hence is PLL circuits modelled as a voltage-based reverse feedback system and analysed in Laplace-plane ($s = j\omega$). A typical analysing modell of the above design, without the fractional R counter is shown in figure A.36

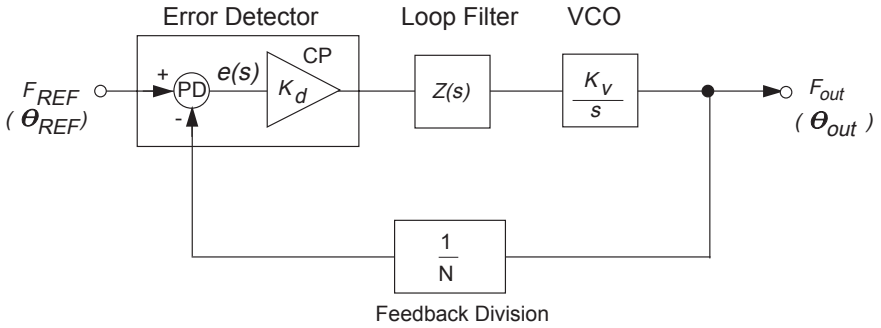

Figure A.36.: Basic PLL analysing model

The frequency error of the signal comparison would be proportional to the, diverging phase of the VCO feedback and the referance input. Thus will the average output of the PFD be constant at equilibrium. By applying the standard negative feedback relations would the typical loop gains be given by

$$\begin{aligned} Forward\,gain &= G(S) = K_d \times Z(S) \times \frac{K_V}{S} \\ Loop\,gain &= G(S) \times H(S) = K_d \times Z(S) \times \frac{K_V}{S} \times \frac{1}{N} \\ Closed-loop\,gain &= \frac{G(S)}{1 + (G(S) \times H(S))} = \frac{V_o}{V_i} \end{aligned}$$

Hence will both the charge pump gain, the loop filter function, the feedback divider ratio and the VCO sensitivity, contribute to the overall loop gain. In respect to frequency the PLL could be analysed according to the derivative of the phase error

$$\frac{d}{dt}\, e(s) = \frac{d}{dt}\left(\theta_{REF} - \frac{\theta_{out}}{N}\right)$$

When equilibrium is reached between the phase VCO fraction and phase referance, the error output will be constant. Hence will $F_{out} = N \times F_{REF}$. With phase divergance will the charge pump send current pulses to the low-pass filter, which smoothes them to a voltage, which again drives the VCO. Dependent of the VCO sensitivity (K_V [MHz/V]) will the output frequency be directed in the right way towards new equilibrium. In respect to LFM will the above relation, never be setteled and the PLL must be matched such that the frequency sweep will be followed linearly, only with a slight additional time lag. Moreover will the transient response of the loop be highly controlled be the filter design, with the other dependecies as additional paramters. There must hence be a trade-off in the filter design between wide bandwidth(fast transient response) and referance spur attenuations [24]. The the loop filter design will in such way set the main parmeter to the PLL *frequency lock time*, which is the time the PLL uses to lock the output frequency to a spesific change of referance frequency step at a given tolerance. However must the bandwith be kept belove the point were the loop turns unstabile. Moreover can the filters bandwidth be additionally adjusted by the PFD frequency or the charge pump current. A problem however in PLL circuits is the possible lagre variations of loop bandwith, to great variations of VCO sensitivity in typical wideband systems. If the monotonic tuning

sensitivity of the VCO (K_V) diverges in large proportions of the nominal sensitivity, will there be a greate chance of loop instabillity. Nevertheless can lagre K_V variations be compensated by decrasing or increasing the charge-pump current through circuit programming.

In addition are there two basic key features that must be considered regarding PLL circuits. Hence the circuit output *phase noise* and the circuit *spur levels*. In respect to minimizing phase noise, must the circuit fist of all inherite a good PN relation from its referance frequency source. This will futher also reduce the internal digital signal jitter. When analysing the phase noise with the above loop gain relations, is it shown [23] that the phase noise of the synthesiser in all will dominate low frequency offsets from carrier, while the VCO PN contibution will be dominat at lagre frequency offsets. Hence must considerations regarding application, be used in order to deside upon how the VCO phase noise relation should be reduced. The synthesizers phase noise will however be directly dependent of the frequency multiplication form F_{PFD} to F_{out}. Hence will the synthesizer phase noise at low frequency offsets be given by $20 \cdot log(N)$. Therefore will a reduction of N yield a direct contribution to the reduction of phase noise output. Thus is it always desireable to used the highest possible F_{PFD}.

The spurious output of the PLL is on the otherhand unwanted discrete frequency components that are generated in the IC conunters and in the charge pump operation. Spurs will be generated in the charge pump by missmatched up and down currents, additional charge pump leakage and inadequate grounding. The spurs are in all nondesireable since they will be mixed directly to the wanted signal creating intermodulation effects in the desired output spectrum. Thus will referance spurs appear at multiples of the F_{REF} [23].

A.13. Ambiguity from Waveform Frequency Drift

Normally will a good FMCW radar design more or less match the Rx and LO waveforms into the mixer giving $f_{Rx} = f_{LO}$ due to the overall circuit stabillity, by matching the two waveform start-frequencies in receive-correlation mixer. In *stretch processing* [13, p.63] these two start frequencies could be missmatched, but still know, thereby also yield an easily solveable ambiguity. However if the design have constant or rapid time-dependent frequency drift during the round trip time, could the beat frequency be constant biased or smeared out, by the nature of the drift and mismatched when mixed at the receiver. Figure A.37 shows how a constant start difference, could give an added ambiguity to the real beat frequency by an vertical displacement waveform in frequency and time. Hence resulting in a bias beat error. Nevertheless will this not change the effective bandwidth.

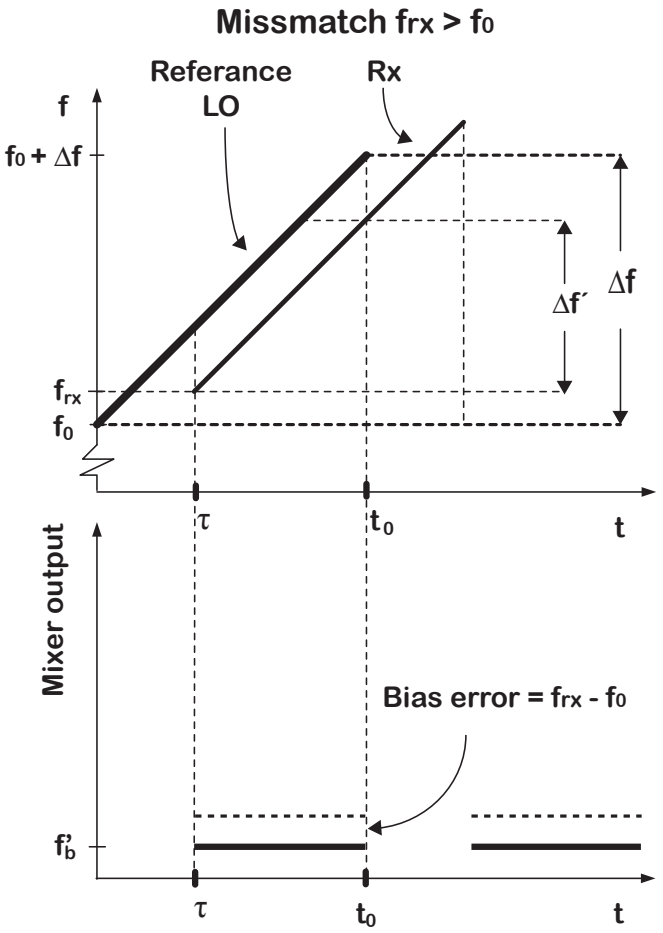

Figure A.37.: Mixer output with biased beat frequency

If $f_{Rx} \neq LO$ the sweep start is unequal $f_{rx} \neq f_0$.

$$
\begin{aligned}
s(t)_{bb} &= s(t)^*_{LO} \cdot s(t-\tau)_{Rx} \\
&= A_{LO}\, e^{-j2\pi(f_0 t + \frac{\alpha}{2}t^2)} \cdot A_{Rx}\, e^{j2\pi(f_{rx}(t-\tau) + \frac{\alpha}{2}(t-\tau)^2)} \\
&= A_{LO}\, A_{Rx}\, e^{-j2\pi\left(f_0 t + \frac{\alpha}{2}t^2 - f_{rx}(t-\tau)\frac{\alpha}{2}(t-\tau)^2\right)} \\
&= A_{LO}\, A_{Rx}\, e^{-j2\pi\left((f_0 - f_{rx})t + f_{rx}\tau + \alpha\tau t - \frac{\alpha}{2}\tau^2\right)}
\end{aligned}
$$

Substituting τ and α

$$
= A_{LO}\, A_{Rx}\, e^{-j2\pi\left((f_0 - f_{rx})t + f_{rx}\frac{2R}{c} + \frac{\Delta f}{t_0}\frac{2R}{c}t - \frac{\Delta f}{2t_0}\left(\frac{2R}{c}\right)^2\right)}
$$

Assuming that sweep time, $t_0 >> \frac{2R}{c}$ last term can be neglected

$$= A_{LO}A_{Rx}\, e^{-j2\pi\left((f_0 - f_{rx})t + f_{rx}\frac{2R}{c} + \frac{\Delta f}{t_0}\frac{2R}{c}t\right)}$$

However utilizing a real signal in the positive side of spectrum

$$\begin{aligned} s(t)_{real} &= Re\left\{s(t)_{bb}\right\} \\ &= A_{LO}A_{Rx}\,\cos\left(2\pi\left((f_0 - f_{rx})t + f_{rx}\frac{2R}{c} + \frac{\Delta f}{t_0}\frac{2R}{c}t\right)\right) \end{aligned}$$

The instantaneous frequency (*beat frequency*) is then

$$\begin{aligned} &\Downarrow \\ f_b &= \frac{1}{2\pi}\frac{d}{dt}(\psi) \\ f_b &= \frac{1}{2\pi}\frac{d}{dt}\left(2\pi\left((f_0 - f_{rx})t + \frac{2f_{rx}R}{c} + \frac{\Delta f}{t_0}\frac{2R}{c}t\right)\right) \\ f_b &= \underbrace{(f_0 - f_{rx})}_{\text{BIAS ERROR}} + \frac{\Delta f}{t_0}\frac{2R}{c} \end{aligned} \tag{A.58}$$

If the referance f_0 is rapidly changing with time $f_0(t)$, compared to the transmitted waveform f_{rx}, the beat frequency will be smeared out in the received spectrum reducing the range resolution. However dependent of the nature of the change $\frac{d}{dt}\left\{f_{LO}(t)\right\}$, and would be averaged out if the drift is pice-wise stable over more chrip periodes. It should be noted that this is not stretched processing or PN added to the echo signal during transmission, but can be merely seen as a erruptive unexpected frequency shift of the whole waveform during the Tx transition time. Hence does this lead to a frequency shifted missmatch between LO referance and previous Tx signal, however still holding the same time-dependent stabillity.

B. Waveform Evaluation Methods and Waveform Measurements

B.1. MATLAB Code

B.1.1. Generating Theoretical Waveform

```
% ------------ Function Waveform -----------------

% Generates a complex waveform by entering
% FMCW parameters, and returns the wavefrom,
% time vector and sampling frequency used
function [wave sfs time] = waveform(AM,F0,...
    DELTA,L,P,WF,Fs)
% --------- Signal-duration vectors: -------------
                            % Fs = Sampling frequency
                            % L = Signal length
Ts=1/Fs;                    % Sampling intervall
t=(0:L-1)*Ts;               % Discrete time vector
signal=zeros(1,length(t)); % Signal/wave-vector
% ------------ Choice of waveform: ----------------
% Initializing Up-chirp:
if strcmp(WF,'wf1')
  signal=AM*exp(1i*2*pi*((F0*t)+((DELTA/2)*t.^2)));
end
% Initializing Down-chirp:
if strcmp(WF,'wf2')
  signal=AM*exp(1i*2*pi*((F0*t)+(BW*t)-((DELTA/2)...
      *(t.^2))));
end
% Initializing Triangular-chirp:
if strcmp(WF,'wf3')
  signal=AM*exp(1i*2*pi*((F0*t)+((DELTA/2)*t.^2)));
  signal1=AM*exp(1i*2*pi*((F0*t)+(BW*t)-((DELTA/2)...
      *(t.^2))));
  signal=[signal signal1];
end
% Initializing Triangular w/incorporated hold low CW:
```

```
if strcmp(WF,'wf4')
  signal=AM*exp(1i*2*pi*((F0*t)+((DELTA/2)*t.^2)));
  signal1=AM*exp(1i*2*pi*((F0*t)+((BW)*t)-((DELTA/2)...
      *(t.^2))));
  signal2=AM*exp(1i*2*pi*F0*t);
  signal=[signal signal1 signal2];
end
% Initializing Triangular w/incorporated hold high CW:
if strcmp(WF,'wf5')
  signal=AM*exp(1i*2*pi*((F0*t)+((DELTA/2)*t.^2)));
  signal1=AM*exp(1i*2*pi*((F0*t)+((BW)*t)-((DELTA/2)...
      *(t.^2))));
  signal2=AM*exp(1i*2*pi*(F0+BW)*t);
  signal=[signal signal2 signal1];
end
% ----- Making the total signal of P periods:-----
total_signal=repmat(signal,1,P); wave=total_signal;
time=(0:(length(total_signal)-1))*Ts;
sfs=Fs;
return
```

B.1.2. Theoretical Processing

```
%%%%%%%%%%%%%%%%%%%%%%%%%%%%%%%%%%%%%%%%%%%%%%%%%%%%%%%%%%%%%%%%
%                     Theoretical Processing                     %
%%%%%%%%%%%%%%%%%%%%%%%%%%%%%%%%%%%%%%%%%%%%%%%%%%%%%%%%%%%%%%%%
% Waveform variables:
Pt=0;                          % Power of Tx signal in dBm
A=sqrt(2*10^((Pt-30)/10));     % Amplitude of Tx waveform
f0=100e6;                      % Start frequency
fmax=288.762e6;                % Maximal frequency (stop)
df=fmax-f0;                    % Bandwidth
tau=40e-3;                     % Time of up-chirp/down-chirp
delta=df/tau;                  % LFM-ratio coefficient
fs_s=fmax*3;                   % Sampling frequency
Le=tau*fs_s;                   % Length of one period
Pe=1;                          % Number of periods
% wf1=up-chirp, wf2=down-chirp,
% wf3=triangular, wf4=triangular w/hold,
% wf5=triangular w/hold DDS-style.
% ------------------------------------------------------
% Initializing and comfirming time signal,
%         chirp BW=188.762MHz
% ------------------------------------------------------
[wave fs t] = waveform(A,f0,delta,Le,Pe,'wf5',fs_s);
% Plot of time signal for waveform confirmation
```

```
figure; plot(t,wave);
title(['Tx Waveform "Up-chirp", ploted for '...
      num2str(max(t)) ' seconds']);
xlabel('Time (seconds)');
ylabel('Envelope of waveform');
% Clearing temporary variables:
clear A f0 fmax df delta fs_s Le Pe;

% ------------------------------------------------
% Power spectrum estimation
% ------------------------------------------------
% Finds the real values of complex wave signal
w=real(wave);
% Seperates w in to chuncks in order to ease
% computability for spectrogram function.
overlap=0;
w1=w(1:(round(length(w))/3)+overlap);
w2=w(-overlap+(round((length(w))/3))...
    +1:2*(round(length(w))/3)+overlap);
w3=w(-(2*overlap)+2*(round(length(w))/3)...
    +1:3*(round(length(w))/3));
% Clearing temporary variables:
clear wave t;
% Number of points in the FFT-algorithm.
% To gain good frequency resolution, NFFT needs
% to be in the range of the number of samples
% per sweep.
NFFT=2^(nextpow2(length(w)));
% Digital frequency vector.
f=linspace(-0.5,0.5,NFFT);
% Execution of the FTT:
FREQ=fft(w,NFFT)/length(w);
% Plot of the one-side spectrum in MHz and dBm.
figure;
plot(f*fs/(1e6),20*log10(fftshift(abs(FREQ)))...
    +30+10*log10(lenght(w)/2));
axis([50 300 -5 5]);
xlabel('Frequency [MHz]');
ylabel('Power [dBm]');
% Clearing temporary variables:
clear FREQ f;

% ------------------------------------------------
%           Waveform confirmation;
%      Frequency vs Time spectrogram:
% ------------------------------------------------
```

```
% w = The amplitude of sampled signal.
H_n=256;     % Hamming window number.
O_n=64;      % Overlap number (Spectrogram resolution).
S_n=512;     % Oversampling, gives smoother frequency.
S_f=fs;      % Sampling frequency to display f in Hz.
ax='yaxis'; % Defines the frequency axis.
% Executes the code on chuncks of signal array:
[y1,fi1,ti1,p1]=spectrogram(w1,H_n,O_n,S_n,S_f,ax);
clear y1;
[y2,fi2,ti2,p2]=spectrogram(w2,H_n,O_n,S_n,S_f,ax);
clear y2 ti2 fi2;
[y3,fi3,ti3,p3]=spectrogram(w3,H_n,O_n,S_n,S_f,ax);
clear y3 ti3 fi3;
% Total processed variables:
ti=[ti1 ti1+(ti1(length(ti1)))...
    ti1+(2*(ti1(length(ti1))))];
clear ti1;
p=[p1 p2 p3];
clear p1 p2 p3;
% Spectrogram plot/ FMCW waveform plot:
figure;
surf(ti,fi1,10*log10(abs(p)),'EdgeColor','none');
axis xy; axis tight; colormap(hot); view(0,90);
xlabel('Time (s)');
ylabel('Frequency (Hz)');
```

B.1.3. Reading from Oscilloscope

```
% ---------------  READ_AGILENT ------------------------
%      M-Code for communicating with an instrument.
%
%  Session log created from T&M tool in the
%           Instrument Control Toolbox:
%
%  AgilentInfiniium_IVI.mdd must first be imported with
%  the driver editor (midedit).
%       1. Create a device object
%       2. Connect to the instrument
%       3. Configure properties
%       4. Invoke functions
%       5. Disconnect from the instrument
%   To run the instrument control session, type the name
%   of the M-file, read_Agilent, at the MATLAB
%   command prompt.
% -------------- Create a device object ------------------
deviceObj = icdevice('AgilentInfiniium_IVI.mdd',...
    'AgilentMSO9254A');
% Instantiate the device object from the .mdd-driver placed
% in the MATLAB-path, and configured IVI-configuration
% 'AgilentMSO9254A'
% -------------- Connect device object to hardware. ------
connect(deviceObj);
% -------------- Query property value(s). ----------------
get30 = get(deviceObj, 'Initialized');
get31 = get(deviceObj.Acquisition(1), 'RecordLength');
get32 = get(deviceObj.Acquisition(1), 'SampleRate');
% More parameters can be viewed from the get()-command and
% set by the set()-command. All available instument
% properties and functions that could be get() or set(),
% can be veiwed in the created Instrument Object, in
% Test and Measurement tool.
% ------------- Execute device object function(s). -------
groupObj = get(deviceObj, 'Measurement');
groupObj = groupObj(1);
[signal,start,inc] = invoke(groupObj,...
    'ReadWaveform', 40e-3);
invoke(deviceObj, 'Close');
% ------------- Delete object. ---------------------------
delete(deviceObj);
% Delete object and closes the connection.
% --- Execute the further processing of the waveform:-----
% agilent_processing;
```

B.1.4. Measurements and Processing of Oscilloscope Data

```
%%%%%%%%%%%%%%%%%%%%%%%%%%%%%%%%%%%%%%%%%%%%%%%%%%%%%%%%%%%%%%%%
%                    Waveform Analysis                           %
%%%%%%%%%%%%%%%%%%%%%%%%%%%%%%%%%%%%%%%%%%%%%%%%%%%%%%%%%%%%%%%%

% ------------- Full waveform processing -------------
% ---------------------- & --------------------------
% ----- Indentification and Isolation of chirp -------

% -------------------- Import data --------------------
% Import X and Y oscilloscope data from MSO 9254A, via
% manual .bin-file transfer.
% Converting Agilent .bin-file to Matlab readable
% data vectors.
[X1 Y1]=importAgilentBin('waveform.bin');
% Transformation of colum to row vectors to fit script:
X1=X1';
Y1=Y1';
% Extraction of sampling intervall used in scope.
 increment=(X1(2)-X1(1));

% ------------ Time Domain Analysis ------------------
% Creating measurment time vector.
t=0:increment:increment*(length(Y1)-1);
% Plot of time-signal as displayed in oscilloscope.
plot(t,Y1);
% Chirp Indentified in time plot and Isolated as new
% measurment vector.
% (Time Limits set by visual inspection of time-plot)
% % ------------ 50MHz offset --------------------
% TL1=0.01781; % Obseved region of interest.
% TL2=0.01796; % Obseved region of interest.
% 50MHz offset to linearity:
% (Slope-fit)
% TL1=0.01780166; % Obseved region of interest.
% TL2=0.0179414; % Obseved region of interest.
% % ------------ 100MHz offset: ------------------
% TL1=0.001935; % Obseved region of interest.
% TL2=0.00209; % Obseved region of interest.
% % 100MHz offset to linearity:
% (Slope follow frequency start and stopp)
% TL1=0.00194776; % Obseved region of interest.
% TL2=0.0020827; % Obseved region of interest.
% 100MHz offset to linearity: (follow slope)
TL1=0.00194066; % Obseved region of interest.
```

```
45 TL2=0.0020756; % Obseved region of interest.
46 % ------- New Index ----------------------------
47 l1=TL1/increment;
48 l2=TL2/increment;
49 % New signal vector of the identified chirp:
50 Y1_1=Y1(l1:l2);
51 % Clearing time variable analysis.
52 clear t;
53
54 % -------------- FFT Analysis -------------------
55 % Number of points in the FFT-algorithm.
56 NFFT=2^(nextpow2(length(Y1_1)));
57 % Sampling frequency, as in oscilloscope.
58  fs=1/increment;
59 % Digital frequency vector.
60 f=linspace(-0.5,0.5,NFFT);
61 % Seperates Y1 in to chuncks in order to ease
62 % computability for spectrogramfunction.
63  overlap=0;
64  Y_1=Y1_1(1:(round(length(Y1_1))/3)+overlap);
65  Y_2=Y1_1(-overlap+(round((length(Y1_1))/3))...
66      +1:2*(round(length(Y1_1))/3)+overlap);
67  Y_3=Y1_1(-(2*overlap)+2*(round(length(Y1_1))/3)...
68      +1:3*(round(length(Y1_1))/3));
69 % Execution of the FTT:
70 FREQ=fft(Y1_1,NFFT)/length(Y1_1);
71 % Plot of FFT spectrum in MHz, one-side
72 % spectrum capture.
73 figure;
74 plot(f*fs/(1e6),20*log10(fftshift(abs(FREQ)))+30);
75 axis([0 400 -100 0]);
76 xlabel('Frequency [MHz]');
77 ylabel('Power [dBm]');
78 % Clearing temporary variables:
79 clear FREQ f;
80
81 % ----------- Spectrogram Analysis -------------
82 % % Parameters for whole signal:
83 % % Y1 = The amplitude sampled signal.
84 % H_n=512;       % Hamming window number.
85 % O_n=64;        % Overlap number.
86 % S_n=2048;      % Oversampling (num).
87 % S_f=fs;        % To display f in correct Hz.
88 % ax='yaxis';    % Defines the frequency axis.
89
90 % Parameters for isolated chirp signal:
```

```
% Y1 = The amplitude sampled signal.
H_n=512;          % Hamming window number.
O_n=300;          % Overlap number.
S_n=4096;         % 512; %2048;
S_f=fs;           % To display f in correct Hz.
ax='yaxis';       % Defines the frequency axis.
% Executes spectrogram function, 3D-plot:
figure;
[y,fr,tr,pr]=spectrogram(Y1_1,H_n,...
     O_n,S_n,S_f,ax);
surf(tr*1e3,fr/1e6,10*log10(abs(pr)),...
     'EdgeColor','none');
axis xy; axis tight; colormap(jet);
grid on;
xlabel('Time (ms)');
ylabel('Frequency (MHz)');
% Executes the code on chuncks of signal array:
[y1,fi1,ti1,p1]=spectrogram(Y_1,H_n,O_n,S_n,S_f,ax);
clear y1;
[y2,fi2,ti2,p2]=spectrogram(Y_2,H_n,O_n,S_n,S_f,ax);
clear y2 ti2 fi2;
[y3,fi3,ti3,p3]=spectrogram(Y_3,H_n,O_n,S_n,S_f,ax);
clear y3 ti3 fi3;
ti=[ti1 ti1+(ti1(length(ti1))) ti1+...
    (2*(ti1(length(ti1))))];
clear ti1;
p=[p1 p2 p3];
clear p1 p2 p3;
% Executes spectrogram function, 2D-plot:
% (Optimized computation time for whole signal)
figure;
surf(ti*1e3,fi1/1e6,10*log10(abs(p))+30,...
    'EdgeColor','none');
axis xy; axis tight; colormap(jet); view(0,90);
grid on;
xlabel('Time (ms)');
ylabel('Frequency (MHz)');
% Clearing all memory for further processing:
clear p ti FREQ f ;
```

B.1.5. Filtering of Captured Waveform

```
function Hd = filter_HP_1
% ------Methode of Executing:-------
% Hd = filter_HP_1;
% Y1 = filter(Hd,Y1);
% ---------------------------------
% All frequency values are in MHz.
Fs = 500;  % Sampling Frequency
% Parameters designed with FDATOOL:
Fstop = 1;                % Stopband Frequency
Fpass = 10;               % Passband Frequency
Dstop = 0.0001;           % Stopband Attenuation
Dpass = 0.057501127785;   % Passband Ripple
flag  = 'scale';          % Sampling Flag
% Calculate the order from the parameters
% using KAISERORD.
[N,Wn,BETA,TYPE] = kaiserord([Fstop Fpass]/...
    (Fs/2), [0 1], [Dpass Dstop]);
% Calculate the coefficients using the FIR1
% function.
b  = fir1(N, Wn, TYPE, kaiser(N+1, BETA), flag);
Hd = dfilt.dffir(b);
```

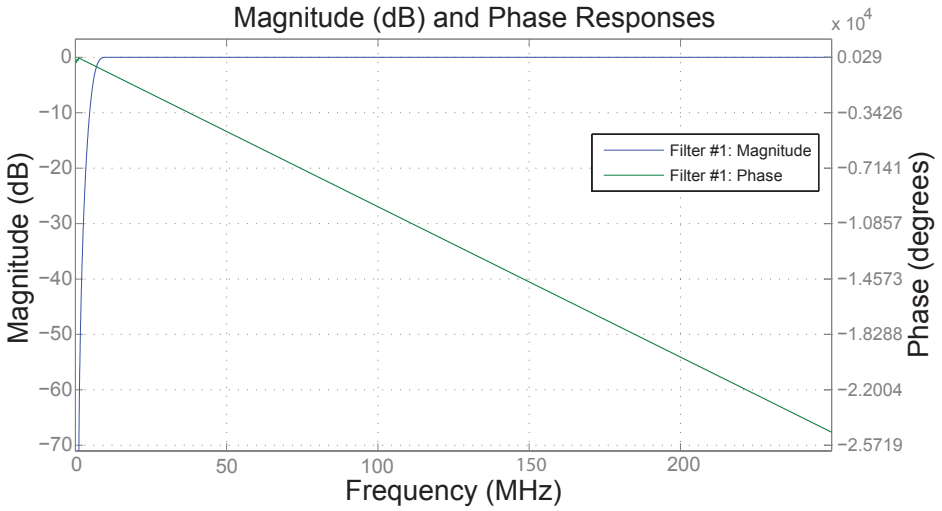

Figure B.1.: Magnitude and phase response of digital HP filter

B.1.6. Linearity Studies

```
%%%%%%%%%%%%%%%%%%%%%%%%%%%%%%%%%%%%%%%%%%%%%%%%%%%%%%%%%%%%%%%%%%%%%%%
%                      LINEARITY OF CHIRP                               %
%%%%%%%%%%%%%%%%%%%%%%%%%%%%%%%%%%%%%%%%%%%%%%%%%%%%%%%%%%%%%%%%%%%%%%%
% Use variables obtained from transfered .bin-file and
% processed by the spectrogram function in
% process_agilent_from_bin.m

% Finds max(P) values for each time index,
% matching the find to the corresponding frequency index
% pn(J,I)-Power matrix obtained from spectrogram processing
p=zeros(1,length(tr)-1);     % Maximum of each time column
I=zeros(1,length(tr)-1);     % Frequency position index
pn=zeros(1,length(fr)-1);    % Temporary column vector
for i=1:length(tr)
   for j=1:length(fr)
       pn(j)=pr(j,i);
   end
   [p(i),I(i)]=max(pn);
end
% Frequency vector corresponding to the max power element
% in Power matrix.
f=zeros(1,length(tr));
for n=1:length(tr)
    temp=I(n);
    f(n)=fr(temp);
end
%%%%%%%%%%%%%%%%%%%%%%%%%%%%%%%%%%%%%%%%%%%%%%%%%%%%%%%%%%%%%%%%%%%%%%%
%               UP-conversion  to Ku-band                               %
%%%%%%%%%%%%%%%%%%%%%%%%%%%%%%%%%%%%%%%%%%%%%%%%%%%%%%%%%%%%%%%%%%%%%%%
% Up-mixing with used LO-frequency:
% (50MHz offset=12.90541e9, 100MHz offset=12.95541e9)
fLO=12.95541e9;
% Waveform frequency at LO-board output:
f_u=fLO-f;
% Time vector:
t0=max(tr)/1000;     % Sweep time
time=0:t0/(length(tr)-1):t0;

% ------------------ Theoretical chirp ------------------
% Creating the theoretical frequency-time relation,
% in respect to chrip parmeters:
% Set by datatip inspection of measured spectrogram
% in IF-band:
% 100Mhz: df=189.3e6
```

```
% 50MHz: df=195.5e6
f0=f_u(1);    % Start frequency
df=189.3e6;   % Desired/ apparent bandwidth
a=df/t0;      % Chirp rate
% Creates a theoretical linear chirp within the
% measured chirp parameters:
%ft=f0+a*time;
ft=f0-a*time;
% --------------- Comparison --------------------------
figure; plot(tr*1e3,f_u/1e9); hold all;
plot(tr*1e3,ft/1e9,'red');hold all;hold off; grid on;
h = legend('Measured chirp','Theoretical chirp',2);
xlabel('Time (ms)'); ylabel('Frequency (GHz)');
% ----------- Frequency error: ft-fmeas: --------------
er=ft-f_u;
figure; plot(tr*1e3,er/1e6); grid on;
xlabel('Time (ms)'); ylabel('Frequency Error (MHz)');
% --------------------- RMSE: -------------------------
% Standard deviation will yield same results
RMSE=sqrt((1/length(er)).*sum((abs(er)).^2));
% -- Effective root mean square error linearity in %:---
Lse=(RMSE/df)*100;
% ------- Range resolution, with nonlinearity ----------
% Ideal range resolution:
deltaRt=3e8/(2*df);
% Contribution to range resolution by the nonlinearity
% of chirp.
% Estimated by RSS and at typical Rmin and Rmax:
% Example at range = 150 m and 1 m
Rmin=1; Rmax=150;
deltaRmin=Rmin*Lse/100; deltaRmax=Rmax*Lse/100;
% Effective range resolution to Lse contribution :
deltaRss_min=sqrt((deltaRt^2)+(deltaRmin^2));
deltaRss_max=sqrt((deltaRt^2)+(deltaRmax^2));

%%%%%%%%%%%%%%%%%%%%%%%%%%%%%%%%%%%%%%%%%%%%%%%%%%%%%%%%%%%%%%%%%%%%%%%%%%%%
%                  Conversion to 77 GHz                                      %
%%%%%%%%%%%%%%%%%%%%%%%%%%%%%%%%%%%%%%%%%%%%%%%%%%%%%%%%%%%%%%%%%%%%%%%%%%%%
% Further must the up-mixed signal be x6 multiplied up to
% 77GHz, to simulate to MMW-board.
% Multiplication factor x6 to MMW:
f_mmw=f_u*6;
ft_mmw=ft*6;
df_mmw=df*6;
% ---------------- Comparison --------------------------
figure; plot(tr*1e3,f_mmw/1e9); hold all;
```

```
plot(tr*1e3,ft_mmw/1e9,'red');hold all;hold off; grid on;
h = legend('Measured chirp','Theoretical chirp',2);
xlabel('Time (ms)'); ylabel('Frequency (GHz)');
% ----------- Frequency error: ft_mmw-f_mmw: ------------
er_mmw=ft_mmw-f_mmw;
figure; plot(tr*1e3,er_mmw/1e6); grid on;
xlabel('Time (ms)'); ylabel('Frequency Error (MHz)');
% ----------------- RMSE_mmw: -------------------------
RMSE_mmw=sqrt((1/length(er_mmw))...
.*sum((abs(er_mmw)).^2));
% -- Effective root mean square error linearity in %: --
Lse_mmw=(RMSE_mmw/df_mmw)*100;
% ------ Range resolution, with nonlinearity -----------
% Ideal range resolution:
deltaRt_mmw=3e8/(2*df_mmw);
% Contribution to range resolution by the nonlinearity
% of chirp.
% Estimated by RSS and at typical Rmin and Rmax:
% Example at range = 150 m and 1 m
deltaRmin_mmw=Rmin*Lse_mmw/100;
deltaRmax_mmw=Rmax*Lse_mmw/100;
% Effective range resolution to Lse contribution :
deltaRss_min_mmw=sqrt((deltaRt_mmw^2)+(deltaRmin_mmw^2));
deltaRss_max_mmw=sqrt((deltaRt_mmw^2)+(deltaRmax_mmw^2));
```

B.1.7. Beat Frequency Studies

```
% ------ Function New Waveform from TX and LO --------
function [wave sfs time] = waveform_new(AM,F0,DELTA,...
    L,Lh,P,WF,Fs,delay,f_doppler)
% Signal duration vectors:
Ts=1/Fs;           % Sampling intervall
t=(0:L-1)*Ts;      % Discrete time vector of chirp-period
th=(0:Lh-1)*Ts;    % Discrete time vector of hold-period
%Choice of waveform:
if strcmp(WF,'wf1')
        signal=AM*exp(1i*2*pi*(f_doppler*t+...
            (F0*(t-delay))+((DELTA/2)*(t-delay).^2)));
end
if strcmp(WF,'wf2')
        signal=AM*exp(1i*2*pi*(f_doppler*t+...
            (F0*(t-delay))+((DELTA/2)*(t-delay).^2)));
        signal2=AM*exp(1i*2*pi*(f_doppler*th+...
            F0*(th-delay)));
   signal=[signal signal2];
end
% Making of the total signal of P periods:
total_signal=repmat(signal,1,P);
wave = total_signal;
time=(0:(length(total_signal)-1))*Ts;
sfs=Fs;
return
%%%%%%%%%%%%%%%%%%%%%%%%%%%%%%%%%%%%%%%%%%%%%%%%%%%%%%%%%%%%
%           Mixing signals to beat output                 %
%%%%%%%%%%%%%%%%%%%%%%%%%%%%%%%%%%%%%%%%%%%%%%%%%%%%%%%%%%%%
% --------- Theoretical Parameters: -------------------
% Set equal to oscilloscope settings and measured
% waveform chrip and hold parameters.

% ----- Power at LO-board, initial measurements:-------
Pm_tx=0.7; %dBm at Tx LO-board
Pm_lo=10.7;%dBm at LO LO-board
% ----- Loss contribution to mixer: ------------------
% RF path:(cable=13m)
cable_tx=16.25; % 1.25 dBm/m, 12.5 GHz datasheet SUCOFLEX
% LO path:(cable=1m)
cable_lo=1.25; % 1.25 dBm/m, 12.5 GHz datasheet SUCOFLEX
% ----- Power at mixer: ------------------------------
% RF path:
Po_tx=Pm_tx-cable_tx;
% LO path:
```

```
45 Po_lo=Pm_lo-cable_lo;
46 % ---- General theoretical parameters ----------------
47 A_tx=sqrt(2*10^((Po_tx-30)/10));    % Amplitude Tx.
48 A_lo=sqrt(2*10^((Po_lo-30)/10));    % Amplitude LO.
49 bw=188.762e6;          % Bandwidth at Ku
50 Fc=12.66e9;            % Ku band.
51 T0=132e-6;             % Modulation time for up waveform.
52 t_meas=2e-3;           % Oscilloscope acqusition time.
53 Thold=(t_meas)-T0;     % Hold frequency periode.
54 DELTA=bw/T0;           % Chirp ratio.
55 FS=1e6;                % Sampling frequncy.
56 Sign_l=(FS*T0);        % Signal segment chirp.
57 Sign_h=(FS*Thold);     % Signal segment hold.
58 period=1;              % Number of modulation periods.
59 Range=6.0;             % Set in accordance with real meas.
60 Delay=(2*Range)/3e8;   % Excessive Delay of TX path to mixer.
61 % -------------- LO waveform to mixer ---------------
62 % Generates LO waveform:
63 [wave_lo sfs_lo t_lo] =...
64     waveform(A_lo,Fc,DELTA,Sign_l,Sign_h,period,'wf2',FS);
65 %The conjungate of LO waveform.
66 wave_lo_conj=conj(wave_lo);
67 % ------------- Tx waveform to mixer ----------------
68 [wave_tx sfs_tx t_tx] = ...
69     waveform_rx(A_tx,Fc,DELTA,Sign_l,Sign_h...
70     ,period,'wf2',FS,Delay,0);
71 % ----------- Mixing of LO and Tx signal: ------------
72 wave_base=wave_tx.*(wave_lo_conj);
73 %----------------- Real signal as observed -----------
74 % Real value of signal:
75 wave_base_real=real(wave_base);
76 % Further processing: (as earlier)
```

B.2. Simulations

B.2.1. Simulated Theoretical Waveform

Theoretical signals, processing and results where obtain to see if the long preprogrammed waveform by NORBIT, was possible to capture and analyze by Matlab.

A theoretical signal of $120\ ms$ was generated to get a an triangular FMCW modulation with high hold frequency. Because of the long signal lenght and the need for high sampling frequency, the approximated NORBIT waveform made it ideal as an upper-limit test for Matlab analysis of FMCW waveforms.

The resulting frequency spectrum obtained by FFT estimation (figure B.2), of an $0\ dBm$ triangular waveform with $166.814\ MHz$ bandwidth from $100\ MHz$ to $288.762\ MHz$. Maximal offset frequency of 100MHz was implemented according to the real experiment, to avoid the flickering noise descending from Zero frequency and test maximum computabillity.

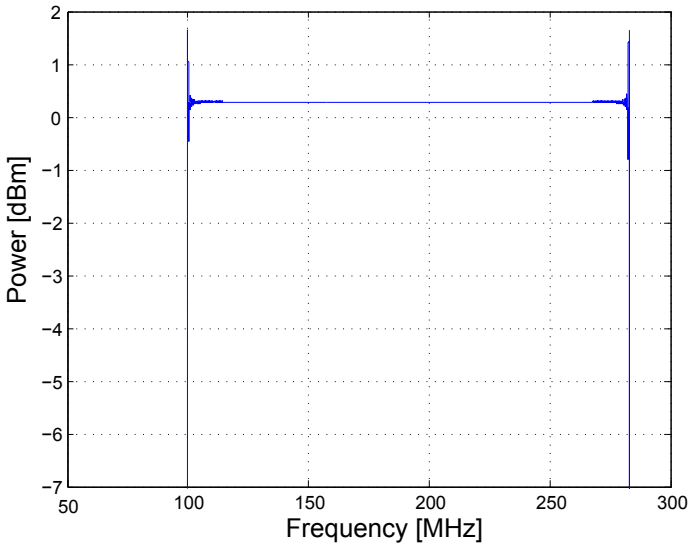

Figure B.2.: FFT spectra of triangular waveform, 0 dBm, 120 ms and Δf =188.762 MHz

The resulting 2D-spectrogram (figure B.3), of an $0\ dBm$ triangular waveform, with $188.762\ MHz$ bandwidth and 40 ms chrips. The figure yield imperfections due to low frequency resolution in spectrogram fuction, hence used to avoid long computaion time.

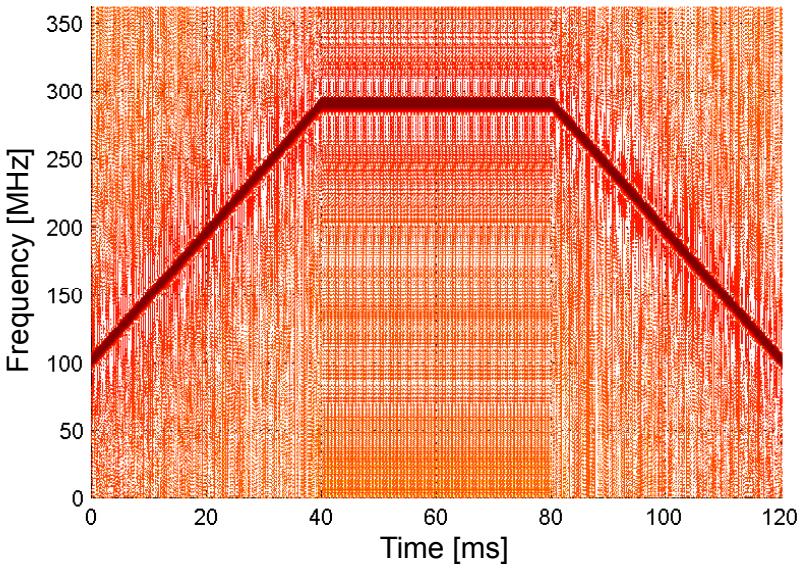

Figure B.3.: Spectrogram of triangular waveform, 0 dBm, 120 ms and Δf = 188.762 MHz

Zoomed in up-chirp of theoretical waveform (figure B.4) in combined time- and frequency domain.

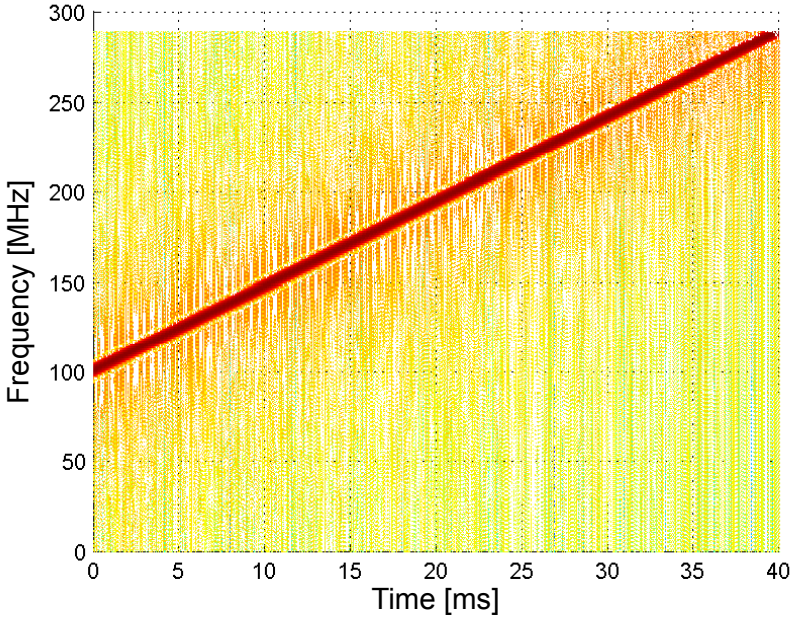

Figure B.4.: Zoomed Up-chirp of triangular waveform, 40 ms and Δf = 166.8 MHz

B.3. Measurements

B.3.1. Obtaining Preprogrammed Waveform Spectrogram

Initial Waveform Analysis

Initial test results for processed sampled data, in the waveform analysis of the preprogrammed waveform.

Figure B.5 shows the FFT spectrum in the initial waveform measurment of the preprogrammed waveform, with slight increase of spectral componets between the large hold frequencies at 100 MHz and 288.762 MHz.

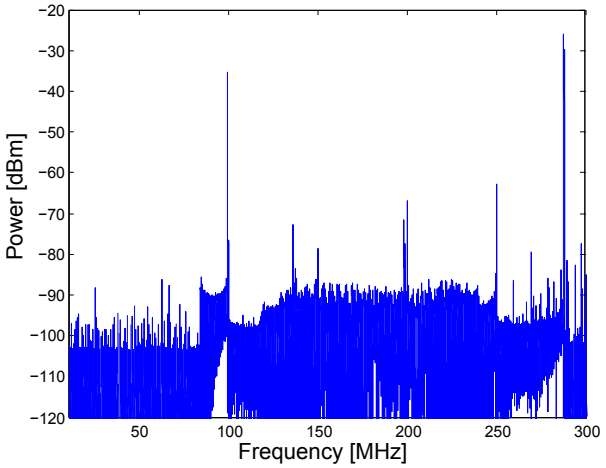

Figure B.5.: FFT plot, Acq.time: 20.5 ms, Δf: 188.762 MHz, Offset: 100MHz

Figure B.6 shows initial measurment of the preprogrammed waveform, with segmented hold frequencies in time. No chrip of 40 ms is seen in spectrum.

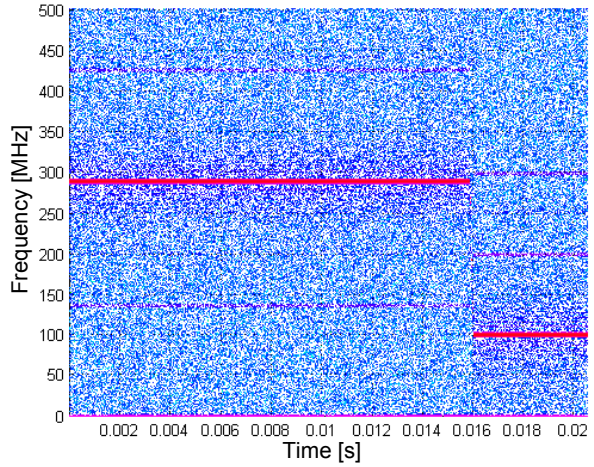

Figure B.6.: 2D-Spectrogram plot, Acq.time: 20.5 ms, Δf: 188.762 MHz , Offset: 100MHz

Figure B.7 and B.8 show the spectrum analyzer confirmation of the preprogrammed waveform, tested due to errorous results of the spectrogram in relation to radar documentation.

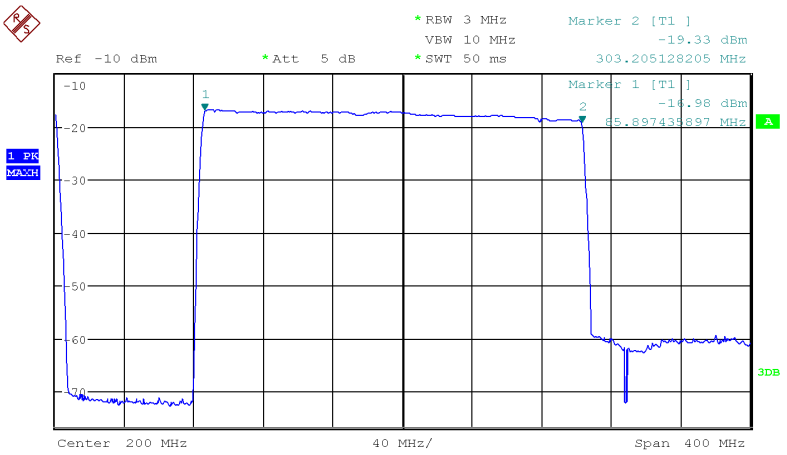

Figure B.7.: WF waveform captured with spectrum analyzer, Max-hold trace, Offset: 100MHz

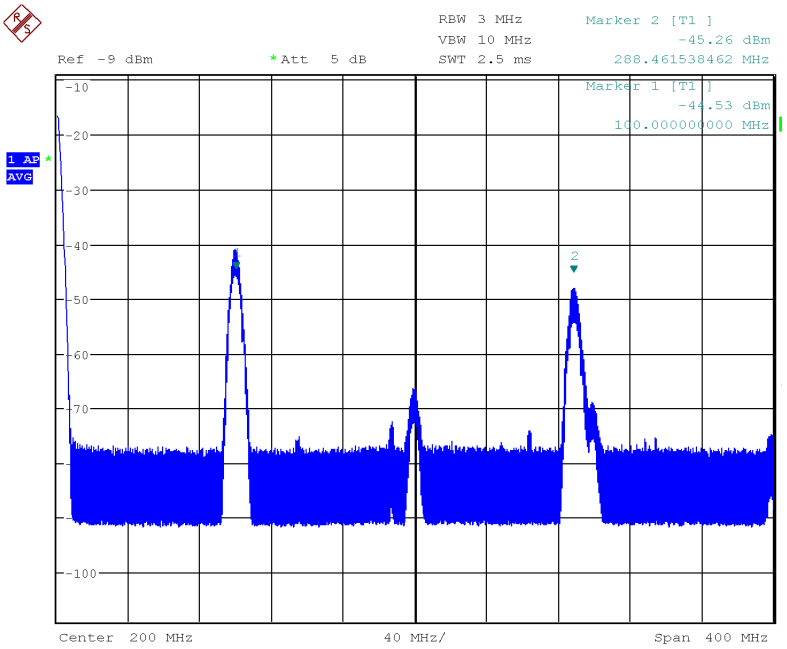

Figure B.8.: Waveform captured with spectrum analyzer, Average trace, Offset: 100MHz

Figure B.9 show the time-sampling test for the confirmation of correct oscilloscope setup, with VSG as signal source.

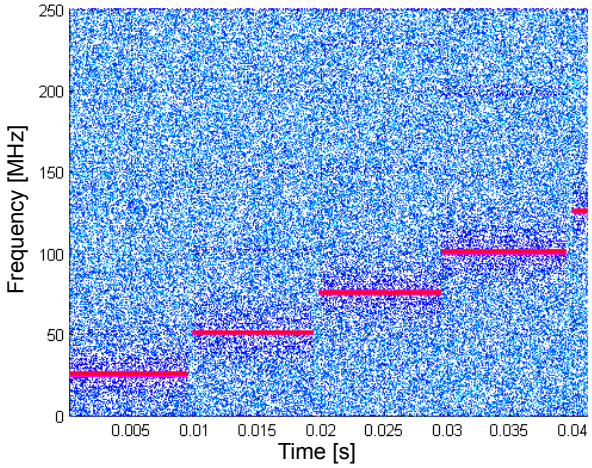

Figure B.9.: Spectrogram of oscilloscope time-sampling test, with VSG

Figure B.10 and B.11 show the time plots of captured short chirp at 50 and 100 MHz offset.

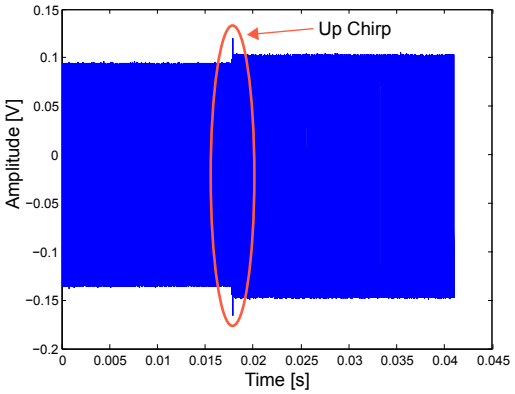

Figure B.10.: Time plot of measurement at 50 MHz offset, and chirp capture

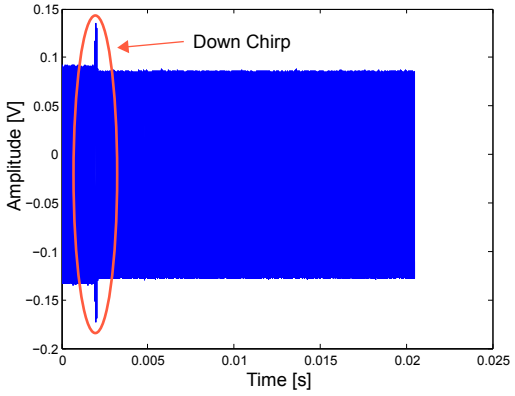

Figure B.11.: Time plot of measurement at 100 MHz offset, and chirp capture

C. Solving Erroneous Waveform Generation and Development of New Waveforms

C.1. Microcontroller program modifications

Note that the full code is not provided in the appendix to protect the property of NORBIT. Hence are only modifications to the existing code described here to document the work done in the thesis and to assist the further development of the radar for NORBIT and co-workers of the MMW radar project. The modified C-code have been handed over to the thesis co-supervisor at end of thesis and are available on request.

C.1.1. New Frequency Sweep Region

Since the ESTI requirement [7, p.4] of maximum 1GHz frequency modulation/deviation were exceed in the delivered microcontroller programming code, were the stop frequency (E_0) altered, and the new frequency region were set by

$$\begin{aligned} &\#\text{define S0\_65292kHz 0x216DF3F9 (Start frequency at DDS)} \\ &\#\text{define S0\_66151kHz 0x21DE9209 (Stop frequency at DDS)} \end{aligned}$$

By this new definitions the LO-board output would thus yield

$$\begin{aligned} f_{start}(LO) &= 12.666648\,GHz \\ f_{stop}(LO) &= 12.833294\,GHz \end{aligned}$$

Further at automotive W-band

$$\begin{aligned} f_{start}(MMW) &= 75.999888\,GHz \\ f_{stop}(MMW) &= 76.999764\,GHz \end{aligned}$$

Instantiated at each ROTARY SWITCH position, within each *case* in fmcw_lo.c by

$$\begin{aligned} &\text{ddsSetS0(S0\_65292kHz, 0);} \\ &\text{ddsSetE0(S0\_66151kHz, 0);} \end{aligned}$$

C.1.2. Modifications to Modulation Settings

Enabling both Up-chirp and Triangular Modulation

To enable switching between pure up-chirp modulation (nodwell=enabled) and triangular (nodwell=disabled), the setting of DDS variable NODWELL to CFR[]-DDS-register were set in the ddsSetModeSweep();-function, through the dds.c-file. Hence new variable had to be altered to allow switching between DDS modulation mode

$$\begin{aligned} \text{dds.CFR\_CH1.val.sweep\_nodwell} &= 1; (Up - chirp) \\ \text{dds.CFR\_CH1.val.sweep\_nodwell} &= 0; (Triangular) \end{aligned}$$

Different Timing in Up-chirp and Triangular Modulation

Since the timing of modulation in AD9958 DDS is dependent of modulation scheme utilized, the microcontroller timing had had to be altered between Up-chirp and Triangular modulation, but also between different Triangular modulations. The current C-code sets the timing by fractioning the AVR clock-frequency and hence data rate (BAUD). With the current code the *Profile Pin* [10] (new sweep interval or modulation period) is set in the fmcw_lo.c-file by the two global variables, DDS_TASK_DELAY and ROT_SWITCH_TASK_DELAY. The desired modulation time between new frequency sweep is assigned by **integer** decimal numbers, that equal time in milliseconds (derived by the fractioned AVR clock).

Up-chirp modulation:
DDS_TASK_DELAY = ROT_SWITCH_TASK_DELAY = 0, will allow 'immediate' start-up of modulation after the stop frequency have been reached. However note that the system have a sweep recovery time (t_{sr}) when switching between large frequency gaps in the region of 100μs that will eat into the total up-chirp sweep time. See section 6.5 for the tested modulations.

Triangular modulation:
DDS_TASK_DELAY = ROT_SWITCH_TASK_DELAY = integer (ms), will define the total modulation time between initiated raising modulation (RDW) and next falling modulation (FDW) in the triangular modulation scheme. If a pure triangular modulation is desired the DELAY's have to be matched to the sweeping modulation time, thus insuring immediate start of falling modulation after the raising modulation has ended. Calculations to achieve pure triangular follow the same principals as in section 6.2.

Setting New Modulations to Each Rotary Switch Position

To enable several different modulations at each mechanical switch-position the desired parameters needs to be set at each *case* since the AVR erases a part of memory when switching. Thus must new RDW/FDW and S_0/E_0, be set at each *case* at the desired channel (CH0). Additionally must the *DELAY*-timing be altered between different

triangular modulations to get the desired waveform modulation time. A example of one position case is presented her for a 1 ms up-chirp modulation, with use of the predefined methods provided through the dds.c-file.

$$
\begin{aligned}
&// \, Pos\, 3 : Sweep\, mode\, for\, CH0\ (t = 1ms)\\
&case 0x03 :\\
&\qquad ddsSetModeSweep(DDS\_CH0);\\
&\qquad ddsSetS0(S0\_65292kHz,\ 0);\\
&\qquad ddsSetE0(S0\_66151kHz,\ 0);\\
&\qquad ddsSetRDW(59,\ 0);\\
&\qquad ddsSetFDW(59,\ 0);\\
&\qquad break;
\end{aligned}
$$

Note that the ddsSetRDW/ddsSetFDW-methods are set by **decimal** RDW and FDW, and not hexadecimal numbers as needed if the current code are executed without the *case* rotary-switch positions. Additionally should it be noted that the zeros indicate that the other channel are not programmed, but can be set if a two channel operation is desired in the future.

Used Modulation Parameters

Table C.1.: Used modulation DSS parameters in C-code

	Up-chirp Modulation			**Triangular Modulation**		
Param.	t_m:1ms	t_m:10ms	t_m:20ms	t_m:2ms	t_m:20ms	t_m: 40ms
RDW	59	6	3	59	6	3
FDW	don't care	don't care	don't care	59	6	3
RSRR	1	1	1	1	1	1
FSRR	don't care	don't care	don't care	1	1	1
DELAY	0	0	0	1	10	20
nodwell	1	1	1	0	0	0

C.2. Measurements

C.2.1. Spectrograms

Triangular Waveform Spectrograms

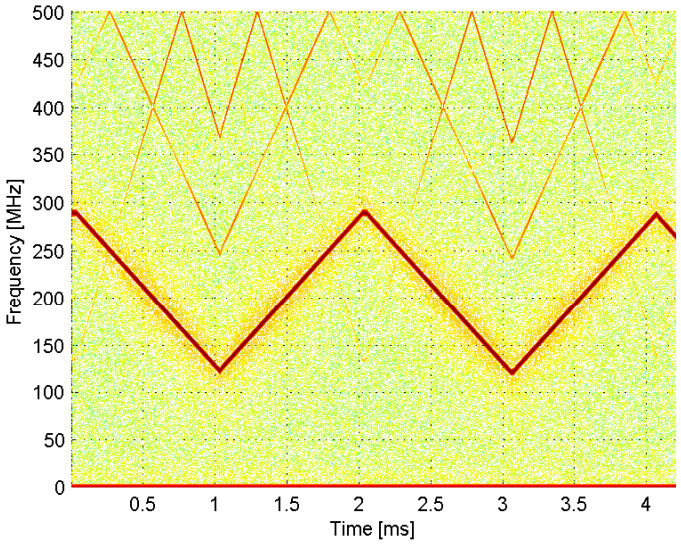

Figure C.1.: Spectrogram of tringular waveform, 4.2 ms acq. window, 1ms chrips, 121 MHz offset

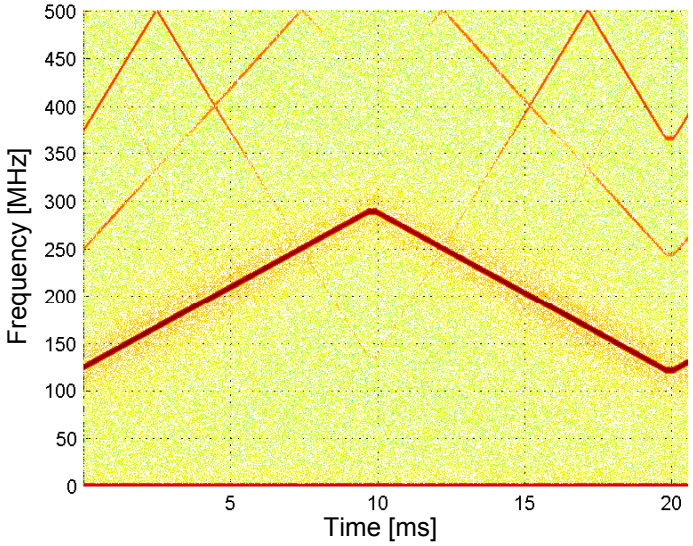

Figure C.2.: Spectrogram of tringular waveform, 20.5 ms acq. window, 10ms chrips, 121 MHz offset

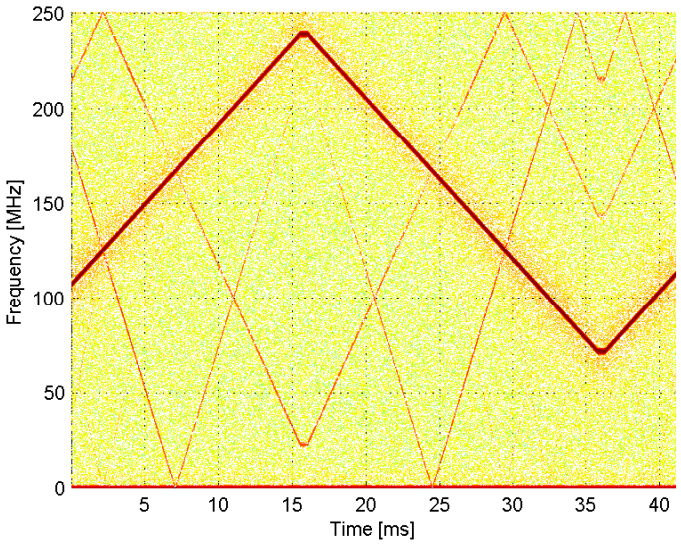

Figure C.3.: Spectrogram of tringular waveform, 41 ms acq. window, 20ms chrips, $72\ \mathrm{MHz}$ offset

Up-chirp Waveform Spectrograms

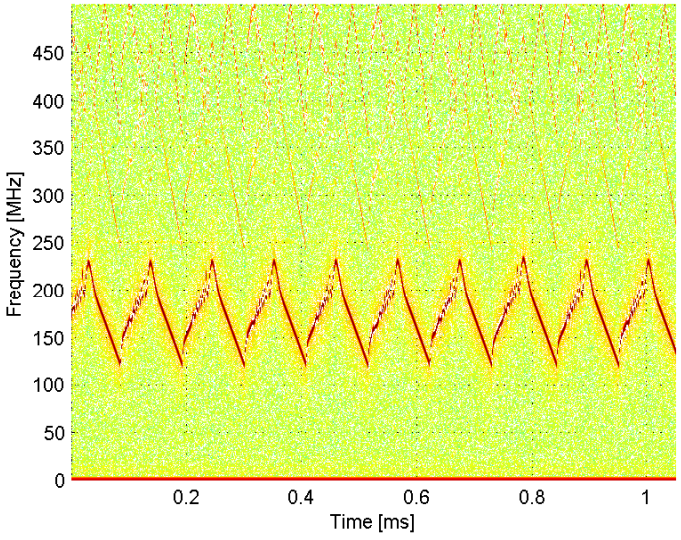

Figure C.4.: Spectrogram of up-chirp waveform, 1.02 ms acq. window, 0.1ms chrips, $121\ \mathrm{MHz}$ offset

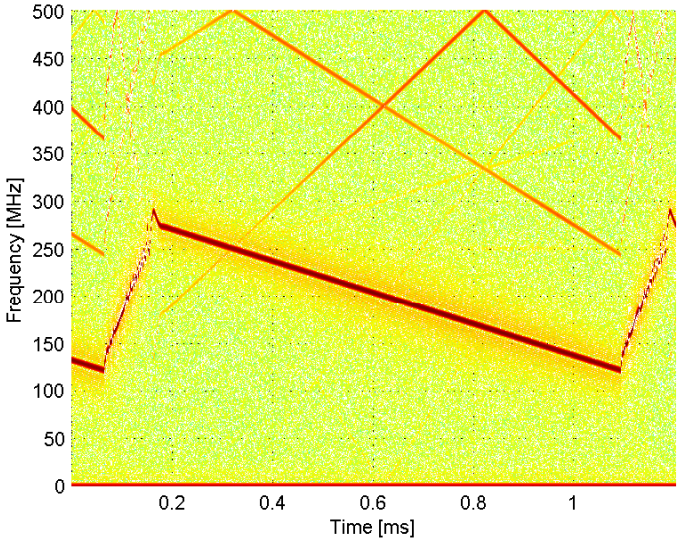

Figure C.5.: Spectrogram of up-chirp waveform, 1.2 ms acq. window, 1ms chrips, 121 MHz offset

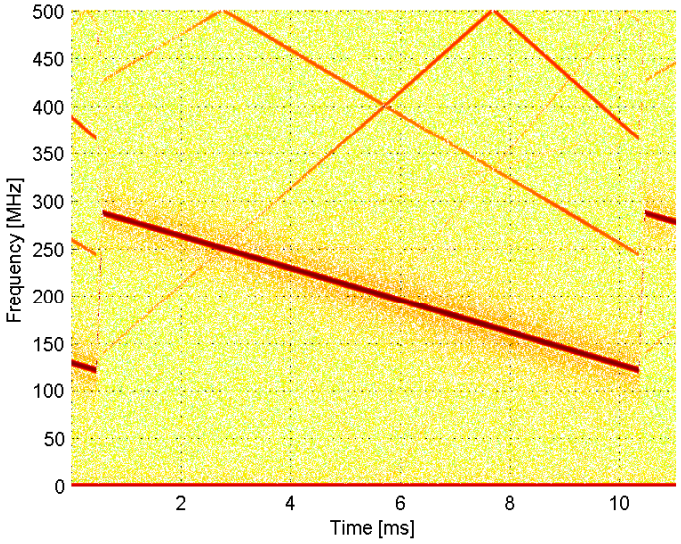

Figure C.6.: Spectrogram of up-chirp waveform, 11 ms acq. window, 10ms chrips, 121 MHz offset

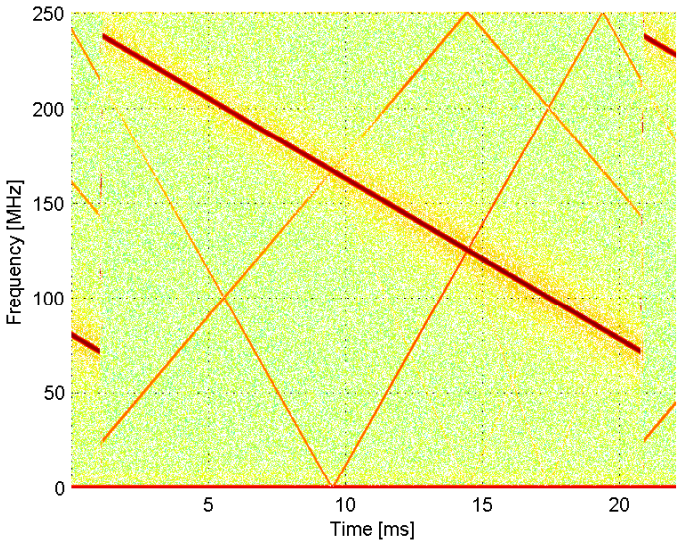

Figure C.7.: Spectrogram of up-chirp waveform, 22 ms acq. window, 20ms chrips, $72\ \mathrm{MHz}$ offset

C.2.2. New Waveform Linearity

The belove frequency error plots at W-band, represent a selection of the different waveforms. Additionall do they show the methodical error of measurment vector length in respect to the most linear part of chirp and difference to theoretical referance.

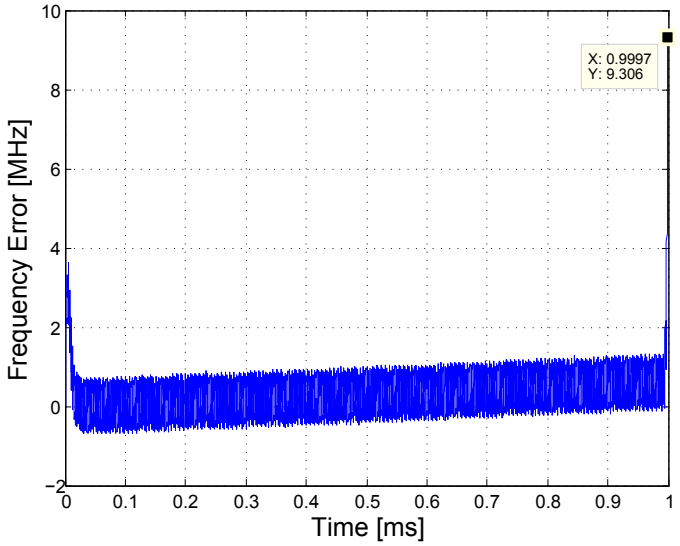

Figure C.8.: Frequency error of chirp, 2ms triangular waveform, 1ms chrips, Up-converted to W-band

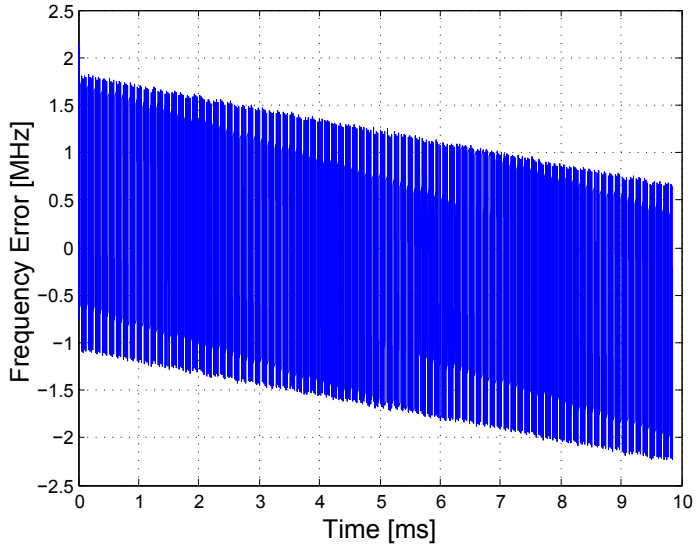

Figure C.9.: Frequency error of chirp, 20ms triangular waveform, 10ms chrips, Up-converted to W-band

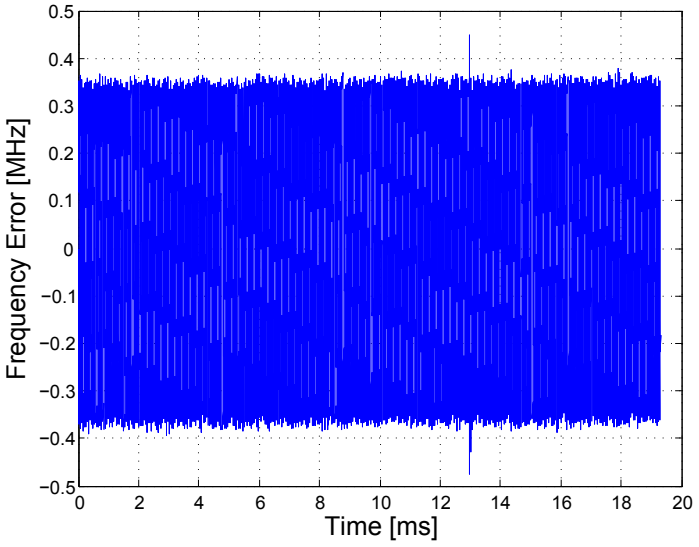

Figure C.10.: Frequency error of chirp, 20ms up-chirp waveform, Up-converted to W-band

D. MATLAB Code: Visualization of the Radar Ambiguity Function

D.1. RAF.m

```
%------------ Radar Ambiguity Function ---------------
%--- Generating the two dimentional fuction of the RAF
% Variables:
% t=sweep time,BW=bandwidth,
% sign={-1(down chirp),1(up chirp)}
function X = RAF(t, BW, sign)
eps = 0.000001;     % float presition
n = 0;
mu = sign * BW / 2. / t;
for tau = -1.1*t:(.005*1.1*t/2):1.1*t
%-1.1*t:.05:1.1*t
n = n + 1;
m = 0;
for f = -BW:(.005*BW/2):BW
%-BW:.05:BW
m = m + 1;
fac_1 = 1. - abs(tau) / t;
fac_2 = pi * taup * (1.0 - abs(tau) / t);
fac_3 = (fd + mu * tau);
res = fac_2 * fac_3;
% The RAF
X(m,n) = abs( fac_1 * (sin(res+eps)/(res+eps))).^2;
end
end
```

D.2. RAF-plots.m

```
%--- Plot of the Radar Ambiguity Function -------
% Defining the waveform parameters:
BW=1e9;          % [Hz]
delay=2e-3;      % [sec]
sign=1;          % {1=up-chirp , -1=down-chirp}
```

```
6  eps = 0.0001;    % floating point precision
7  % Initializing the ambiguity function:
8  X = RAF(delay,BW,sign);
9  % Defining dimensions:
10 time = -1.1*delay:(.005*1.1*delay/2):1.1*delay;
11 %-1.1*delay:.05:1.1*delay;
12 f =  -BW:(.005*BW/2):BW;
13 %-BW:.05:BW; -BW:.05:BW;%
14 %---------- Ploting the RAF ----------------------
15 figure; mesh(time,f,X);
16 axis([min(time) max(time) min(f) max(f) 0 1 0 1]);
17 grid on; xlabel ('Delay - seconds');
18 ylabel ('Doppler - Hz');
19 zlabel ('Ambiguity function');
20 %--- Ploting the RAF countour
21 figure; contour(time,f,X); grid on;
22 xlabel ('Delay - seconds');
23 ylabel ('Doppler - Hz');
24 % Finding the Uncertainty Function (UF)
25 U = sqrt(X);
26 %--- Ploting the UF
27 figure; mesh(time,f,U);
28 axis([min(time) max(time) min(f) max(f) 0 1 0.2 1]);
29 xlabel ('Delay - seconds');
30 ylabel ('Doppler - Hz');
31 zlabel ('Uncertainty function');
32 %--- Ploting the UF contour
33 figure; contour(time,f,U); grid on;
34 xlabel ('Delay - seconds');
35 ylabel ('Doppler - Hz');
36 %---Ploting the domain views
37 figure; surf(time,f,U,'EdgeColor','none');
38 axis tight; colormap(hsv); view(90,0);
39 ylabel('Delay - seconds');
40 zlabel ('Uncertainty function delay-view plot');
41 figure; surf(time,f,U,'EdgeColor','none');
42 axis tight; colormap(hsv); view(0,0);
43 xlabel('Doppler - MHz');
44 zlabel ('Uncertainty function Doppler-view plot');
```

E. Indexing

List of symbols

α	.....	Chirp sweep ratio	$[Hz/s]$
A_n	.....	Sinusoidal non-linearity amplitude	$[Hz]$
B	.....	Bandwidth	$[Hz]$
BW_{DDS}	.....	DDS Output Bandwidth	$[Hz]$
c	.....	Speed of light in vacuum $(3 \cdot 10^8)$	$[m/s]$
f_0	.....	Sweep start frequency	$[Hz]$
f_b	.....	Beat frequency	$[Hz]$
δf_b	.....	Beat frequency error	$[Hz]$
Δf_b	.....	Beat frequency spectral resolution	$[Hz]$
f_c	.....	Carrier frequency	$[Hz]$
f_d	.....	Doppler frequency	$[Hz]$
f_m	.....	Waveform modulation frequency	$[Hz]$
f_n	.....	Sinusoidal non-linearity modulation frequency	$[Hz]$
Δf	.....	Sweep frequency bandwidth/ DDS frequency step	$[Hz]$
$\Delta f'$	.....	Effective processing bandwidth	$[Hz]$
F	.....	Noise Figure	$[dB]$
ΔF	.....	Frequency resolution	$[Hz]$

G	.....	Gain $(power gain/\ antenna\ power\ gain)$	$[dB]$
k	.....	Boltzmann's constant $(1.38 \cdot 10^{-23})$	$[J/K]$
L	.....	Power loss/ Total Radar loss	$[dB]$
$\mathcal{L}(f)$	.....	Phase noise $(dBc/Hz, at\ xHz)$	$[W/Hz]$
L_{win}	.....	Windowing loss	$[dB]$
N	.....	Noise Power	$[W]$
N_{FFT}	.....	Number of FFT points	$[Num]$
P	.....	Power	$[W]$
P_{CW}	.....	Average CW power	$[W]$
$\widetilde{P}(f)$	.....	Estimated frequency spectrum	$[W/Hz]$
ρ	.....	Power density	$[W/m^2]$
R	.....	Range to target	$[m]$
δR	.....	Range error	$[m]$
ΔR	.....	Range resolution	$[m]$
σ	.....	RCS	$[m^2]$
S	.....	Signal power	$[W]$
$S(f)$	.....	Spectral power density	$[W/Hz]$
$S(f)_{RF}$	.....	Total sideband noise $(AM + PM)$, $(dBc/Hz, at\ xHz)$	$[W/Hz]$
Δt	.....	DDS time step	$[s]$
T	.....	Noise temperature $(20° = 290K)$	$[K]$
τ	.....	Signal round-trip time/ time of flight	$[s]$
t_0	.....	Chirp sweep period	$[s]$
t_m	.....	Waveform modulation period	$[s]$

t_{sr}	.....	Frequency sweep recovery time	$[s]$
T_{Dwell}	.....	Dwell time	$[s]$
v	.....	Target speed	$[m/s]$

List of Figures

List of Tables